ALL OPTICAL MAGNETOMETRY WITH NITROGEN VACANCY CENTERS IN DIAMONDS

Ludwig Horsthemke

A dissertation submitted to

in partial fulfillment
of the requirements for the degree of
Doctor of Science

Doctoral Programme in Information and Communication Technologies
(Tecnologías de la Información y de las Comunicaciones)

Universidad de Granada
November 2024

Supervisors:
Ignacio Rojas Ruiz
Peter Glösekötter

Editor: Universidad de Granada. Tesis Doctorales
Autor: Ludwig Horsthemke
ISBN: 978-84-1195-767-0
URI: https://hdl.handle.net/10481/103267

Abstract

This thesis explores advancements in all-optical magnetometry using nitrogen-vacancy centers in diamonds, with a focus on fiber-based sensor systems. We begin by providing an overview of current sensing and magnetic field sensing technologies, highlighting the need for compact, high-sensitivity solutions. After introducing the physics of NV centers and discussing various readout methods, we present an all-optical setup for magnetometry, for which we developed a compact and low-cost phase-sensitive detection system. This system achieves a performance comparable to commercial laboratory equipment while significantly reducing size and costs.

We further investigate the fluorescence lifetime of high-NV-density microdiamonds. This offers a non-intensity-based approach for magnetic field sensing, providing greater immunity to intensity fluctuations and enhancing robustness. Additionally, we analyze the complete frequency response of the system. By training an artificial neural network on the raw response, we improve the system's accuracy, resolving low-field ambiguities and minimizing temperature sensitivity.

Compared to state-of-the-art NV-based sensors, our all-optical system offers a non-conductive and non-magnetic sensing head, simpler implementation, and functionality over a high magnetic field range. These advancements demonstrate the potential for low-cost, portable magnetometry systems suitable for practical applications where traditional methods face challenges due to metallic or microwave components. The integration of fluorescence lifetime sensing and frequency domain analysis positions this technology as a promising alternative for future quantum sensing developments.

Resumen

Esta tesis explora los avances en la magnetometría totalmente óptica, utilizando centros the nitrógeno vacante en diamantes, con un enfoque en sistemas de sensores basados en fibra óptica. Comenzamos brindando una descripción general de las tecnologías actuales de sensores de corriente y sensores de campos magnéticos, destacando la necesidad de soluciones compactas y de alta sensibilidad. Tras introducir la física de los centros NV y discutir varios métodos de lectura, presentamos una configuración totalmente óptica para magnetometría, para lo que hemos desarrollado un sistema de detección sensible a la fase, compacto y de bajo coste. Este sistema alcanza un rendimiento comparable al de los equipos comerciales de laboratorio, reduciendo significativamente el tamaño y los costes.

Además, investigamos más a fondo el tiempo de vida útil de la fluorescencia de los microdiamantes de alta densidad de NV. Esto ofrece un enfoque no basado en la intensidad para la detección del campo magnético, lo que proporciona una mayor inmunidad a las fluctuaciones de intensidad y mejora la robustez. Además, analizamos la respuesta de frecuencia completa del sistema. Mediante el entrenamiento de una red neuronal artificial en la respuesta bruta, mejoramos la precisión del sistema y resolvemos las ambigüedades de campo bajo y minimizando la sensibilidad a la temperatura.

En comparación con los sensores basados en NV de última generación, nuestro sistema totalmente óptico ofrece un cabezal sensor no conductor y no magnético, una implementación más sencilla y funcionalidad en un amplio rango de campo magnético. Estos avances demuestran el potencial de los sistemas de de bajo coste de magnetometría portátiles adecuados para aplicaciones prácticas donde los métodos tradicionales enfrentan desafíos debido

a los componentes metálicos o de microondas. La integración de los sensores del tiempo de vida de la fluorescencia y el análisis del dominio de frecuencia posiciona a esta tecnología como una alternativa prometedora para futuros desarrollos de detección cuántica.

Acknowledgments

This thesis was developed as part of the RaQuEl project funded by the Bundesministerium für Bildung und Forschung (13N15489). The project focuses on developing advanced current sensors for electric vehicles by leveraging quantum physical effects. These sensors aim to provide more precise and reliable measurements of current flows, which are critical for efficient battery charging and power transmission to vehicle components. The goal of RaQuEl's sensors lies in their ability to surpass existing sensor technologies in terms of accuracy, power efficiency, and ease of installation. The focus lies on the use of negatively charged nitrogen-vacancy centers, hosted in diamonds, which can be addressed all-optically. The project's research efforts are centered around several key areas:

Diamond Substrate Improvement Enhancing and improving the understanding of the material properties of diamond substrates, used for quantum sensing.

Control and Evaluation Electronics Developing electronics capable of harnessing the quantum effects for practical use.

System Design Optimization Maximizing sensitivity, dynamic range and bandwidth through an optimized system design.

One of the significant advantages of using quantum effects in these sensors is their independence of the vehicle's on-board power supply voltage, which can vary from 12 V to over 800 V in electric vehicles, through their high galvanic isolation and loss-free measurement. This makes the sensors versatile for a wide range of applications. Additionally, these sensors operate at room temperature and do not require cryogenic environments or microwave radiation coupling,

which simplifies their integration into electric vehicles. The ultimate goal of the RaQuEl project is to develop a fully functional demonstrator of these quantum current sensors and assess their applicability to other industrial uses.

This PhD thesis would not have been possible without the help and support of numerous individuals, and I would like to take this opportunity to express my deepest gratitude.

First and foremost, I would like to extend my heartfelt thanks to my supervisor, Professor Peter Glösekötter. His unwavering support, appreciation, and insightful ideas have been invaluable throughout my studies and the development of this project. His outstanding commitment has been a guiding light, and without his mentorship, this thesis would not have been possible.

I am also deeply grateful to Professor Ignacio Rojas for his recommendation to admit me onto the Doctoral programme and for his supervision and support throughout this journey. His guidance has been instrumental in shaping this work.

I would like to acknowledge the invaluable contributions and collaboration of the members of the RaQuEl project team. In particular, I want to express my thanks to the colleagues at Quantum Technologies GmbH, including Lutz Langguth, Romy Müller, Dominik Rajsp, and Robert Staacke, for welcoming me into their laboratory and for their collaborative spirit. Further, I am grateful to the team at duotec GmbH, especially Jens Raacke, and to Bernd Burchard and Miles Kuper at Elmos Semiconductor SE for their support and partnership.

I would also like to extend my thanks to all past and present colleagues in the Laboratory of Semiconductor Devices and Bus Systems of Prof. Glösekötter and in the Quantum Technology Lab of Prof. Gregor at FH Münster for their support and the many fruitful discussions we had. Their insights and encouragement have been crucial throughout this process. Jens, Ann-Sophie, Dennis, Frederik, Jonas, Marina, Jan-Ole, Felix, and Andre, thanks for the good times!

Last but certainly not least, I want to express my profound gratitude to my family. My brother William and my mother Maria have been my pillars of strength, offering endless support not only during my time as a PhD candidate but throughout my life. Their belief in me has been a source of constant motivation, and for that, I am forever grateful.

Thank you all.

Published Thesis Content

The contents of this thesis draw significantly from the following publications, which were published prior to the completion of this work:

- Horsthemke, L.; Pogorzelski, J.; Stiegekötter, D.; Hoffmann, F.; Langguth, L.; Staacke, R.; Laube, C.; Knolle, W.; Gregor, M.; Glösekötter, P. Excited-State Lifetime of NV Centers for All-Optical Magnetic Field Sensing. *Sensors* **2024**, *24*, 2093. https://doi.org/10.3390/s24072093

- Horsthemke, L.; Pogorzelski, J.; Stiegekötter, D.; Hoffmann, F.; Bülter, A.S.; Trinschek, S.; Gregor, M.; Glösekötter, P. Towards Resolving the Ambiguity in Low-Field, All-Optical Magnetic Field Sensing with High NV-Density Diamonds. In Proceedings of the ITISE 2024. MDPI, 2024, ITISE 2024. https://doi.org/10.3390/engproc2024068008

- Horsthemke, L.; Pogorzelski, J.; Stiegekoetter, D.; Hoffmann, F.; Bülter, A.S.; Langguth, L.; Staacke, R.; Trinschek, S.; Gregor, M.; Gloesekoetter, P. Fluorescence Lifetime of NV Centers for Temperature-Insensitive All-Optical Magnetic Field Sensing. EasyChair Preprint 15104, 2024

- L. Horsthemke.; C. Bischoff.; P. Glösekötter.; B. Burchard.; R. Staacke.; J. Meijer. A1.4 Highly Sensitive Compact Room Temperature Quantum Scalar Magnetometer **2020**. https://doi.org/10.5162/SMSI2020/A1.4

- Horsthemke, L.; Bischoff, C.; Glosekotter, P.; Burchard, B.; Staacke, R.; Meijer, J. All optical readout scheme for photoluminescence based magnetic field sensors. In Proceedings of the 2020 IEEE SENSORS.

IEEE, 2020, pp. 1–3. https://doi.org/10.1109/sensors47125.2020.9278923

- Pogorzelski, J.; Horsthemke, L.; Homrighausen, J.; Stiegekötter, D.; Gregor, M.; Glösekötter, P. Compact and Fully Integrated LED Quantum Sensor Based on NV Centers in Diamond. *Sensors* **2024**, *24*, 743. https://doi.org/10.3390/s24030743

- Stiegekötter, D.; Pogorzelski, J.; Horsthemke, L.; Hoffmann, F.; Gregor, M.; Glösekötter, P. Microcontroller-Optimized Measurement Electronics for Coherent Control Applications of NV Centers. *Sensors* **2024**, *24*, 3138. https://doi.org/10.3390/s24103138

- Pogorzelski, J.; Horsthemke, L.; Homrighausen, J.; Stiegekötter, D.; Hoffmann, F.; Bülter, A.S.; Gregor, M.; Glösekötter, P. Calibration-Free Current Measurement with Integrated Quantum Sensor. *Engineering Proceedings* **2024**, *68*. https://doi.org/10.3390/engproc2024068058

- Homrighausen, J.; Horsthemke, L.; Pogorzelski, J.; Trinschek, S.; Glösekötter, P.; Gregor, M. Edge-Machine-Learning-Assisted Robust Magnetometer Based on Randomly Oriented NV-Ensembles in Diamond. *Sensors* **2023**, *23*, 1119. https://doi.org/10.3390/s23031119

- Stegemann, J.; Peters, M.; Horsthemke, L.; Langels, N.; Glösekötter, P.; Heusler, S.; Gregor, M. Modular low-cost 3D printed setup for experiments with NV centers in diamond. *European Journal of Physics* **2023**, *44*, 035402. https://doi.org/10.1088/1361-6404/acbe7c

- Pogorzelski, J.; Homrighausen, J.; Horsthemke, L.; Stiegekötter, D.; Lindloge, L.; Teuber, J.; Gregor, M.; Glösekötter, P. A7.4 - Bias-Tee quantum current sensor with temperature tracking based on modulated cw-ODMR with NV centers. In Proceedings of the Lectures. AMA Service GmbH, Von-Münchhausen-Str. 49, 31515 Wunstorf, Germany, 2023. https://doi.org/10.5162/smsi2023/a7.4

- Staacke, R.; John, R.; Wunderlich, R.; Horsthemke, L.; Knolle, W.; Laube, C.; Glösekötter, P.; Burchard, B.; Abel, B.; Meijer, J. Isotropic Scalar

Quantum Sensing of Magnetic Fields for Industrial Application. *Advanced Quantum Technologies* **2020**, *n/a*, 2000037. https://doi.org/10.1002/qute.202000037

Contents

List of Figures

List of Tables

1 Introduction

Nitrogen vacancy (NV) centers in diamond attracted considerable attention as quantum sensors for magnetic field sensing. Approaches using microwave (MW) excitation for spin manipulation achieve high sensitivities [20, 21] and spatial resolutions [22, 23] while operating at room temperature. They are, however, limited in their application due to the necessity of MW delivery, which typically requires a galvanic connection, by e.g. a conductive wire or a resonator in close proximity to the sensing volume. Additionally, the MW delivery adds complexity and may have adverse effects, like local heating [24] or the creation of eddy currents [25]. In contrast, all-optical approaches simplify the sensor design as a step towards industrial application. They rely on the fluorescence change caused by spin mixing for magnetic fields up to $B \approx 50\,\mathrm{mT}$, achieving sensitivities of 14–50 $\mu\mathrm{T}/\sqrt{\mathrm{Hz}}$ [26, 12, 27, 28, 29]. Other all-optical setups utilize the ground-state level-anticrossing, reporting noise floors of 0.45 $\mathrm{nT}/\sqrt{\mathrm{Hz}}$, but requiring high precision in angular alignment and a bias magnetic field [30, 14, 31]. Furthermore, the cross-relaxation features near zero magnetic field in high-NV-density samples have been investigated in MW-free setups [32, 33, 34], reporting estimated photon shot-noise-limited sensitivities of 4.5 $\mathrm{nT}/\sqrt{\mathrm{Hz}}$ [33]. All-optical schemes can be implemented using fiber optics [27, 35, 36, 32, 37] to construct a non-magnetic and high-insulation resistance probe which enables their use in harsh environments.

This work is driven by the application of current sensing through the magnetic fields which are associated with a current carrying conductor. We specifically concentrate on the all-optical approach to magnetic field sensing, using ensembles of NV centers in diamonds. The dissertation not only explores unprecedented improvements in all-optical magnetometers but also introduces

methodologies from which future developments in microwave-based quantum sensors can benefit. The methodologies introduced are designed to mitigate the vulnerabilities associated with environmental noise and thermal variations, challenges that have persistently limited the application scope of magnetic field sensors. By integrating these advancements, this research paves the way for more robust and reliable quantum sensors, extending their usability in fields where precision under varying environmental conditions is crucial.

This chapter gives a brief overview of current sensing, magnetic field sensing and NV centers and their use in magnetic field sensing, in particular, allowing the comparison of the sensing technologies in this work to other established methods.

1.1 Current Sensing

The measurement of current flow is a fundamental requirement across a broad spectrum of electrical and electronic applications, each of which imposes distinct performance demands in terms of precision, accuracy, bandwidth, dynamic range, isolation, size, and cost. To address these diverse needs, various current measurement techniques have been developed. In today's systems, the increasing demand for digital control and monitoring necessitates the availability of current data in digital form, thereby requiring the output signal from current sensing techniques to be digitized.

Shunt resistors, for example, have been widely utilized in power electronics due to their low cost, compact form factor, and relative simplicity, while offering reasonable measurement accuracy. However, as the trend toward digital sensing and control replaces conventional analog systems, driven by the need for higher system integration, improved efficiency, and more advanced control strategies, the requirement for digitized current information has grown. The voltage drop across a shunt resistor, though small, necessitates amplification, which in turn affects bandwidth, increases the overall size of the device, and raises costs. Additionally, with power converters achieving higher power densities, the inherent power losses within shunt resistors have become increasingly problematic. As a result, engineers in the field of power electronics are actively seeking alternative current sensing solutions that can offer similar levels of accuracy with reduced power losses, while also providing galvanic isolation and

an output signal that can be directly interfaced with digital systems.

Current measurement techniques can be broadly classified by the following physical principles [38]

Ohm's law of resistance The current density vector $\boldsymbol{J}$ in a conductor of resistivity σ is given by

$$\boldsymbol{J} = \sigma(\boldsymbol{E} + \boldsymbol{v} \times \boldsymbol{B}) \tag{1.1}$$

with the applied electric field $\boldsymbol{E}$. In a rest frame of the conductor, the product of conductor velocity $\boldsymbol{v}$ and magnetic flux density $\boldsymbol{B}$ is zero. When $\boldsymbol{E}$ is a time varying function, we have to account for the reactance in addition to the conductor's resistivity. On a macroscopic scale and assuming a uniform electric field is applied, we can then observe a voltage $V = ZI$, with complex impedance Z and current I. With a known impedance and measured voltage we can thus determine the current, which is a simple method of current measurement, applied in many instances, ranging from from minuscule currents arising in photodetection processes, up to the kA range in power transmission systems.

Different construction methods have been established, including surface mounted devices, coaxial tubes, squirrel cages and disc types. These aim to optimize a selection of several parameters, like maximum current, bandwidth, temperature dependency, and size [39]. In any case, the resistive element has to be inserted into the circuit, interfering with the rest of the circuitry in some way, dissipating power, and potentially requiring a downstream galvanic isolation.

Induction Current sensors based on Faraday's law of induction are a notable example of sensors that inherently provide electrical isolation between the current to be measured and the output signal. This isolation is achieved due to the non-contact nature of the measurement process, where the sensor detects the magnetic field generated by the current without physically interacting with the conductor itself. Faraday's law states that a voltage is induced in a conductor when it experiences a change in the magnetic flux, making sensors that exploit this phenomenon unable to detect static (DC) currents. Still, many applications can make use of induction for current sensing, ranging from power distribution to motor

drives and renewable energy systems, benefiting from the inherent safety by galvanic isolation.

One classical implementation is the Rogowski coil. In this setup a helical coil with no magnetic core is wound around a conductor that carries the primary current to be measured. A change in the primary current leads to a varying magnetic flux in the coil and consequently an induced voltage. This induced voltage exhibits a direct proportionality to the rate of change of the primary current, which can be subsequently integrated to yield a voltage signal proportional to the instantaneous current magnitude. These transducers demonstrate a high degree of linearity and, owing to the absence of a magnetic core, are not susceptible to magnetic saturation effects. This characteristic makes them particularly suitable as cost-effective, high-bandwidth current sensors, especially in clamp-on applications where non-contact measurement is advantageous. However, Rogowski coils also have certain inherent limitations. Next to the inability of DC current measurement, the integration process necessary for signal conditioning can potentially introduce measurement errors, such as baseline drift, and may impose constraints on the overall system bandwidth and response time.

Another notable implementation of the induction principle is the current transformer. The setup is comparable to that of a Rogowski coil, except the secondary winding is placed on a core material with high relative permeability. The transformer steps down the current proportional to the number of turns of the secondary winding, which is connect to a shunt resistor instead of an integrator. The voltage over the shunt resistor can then be easily amplified and further processed.

Magnetic fields Instead of using the induction by a changing magnetic flux, current sensing can also be based on the direct measurement of the magnetic field in the vicinity of a current carrying conductor. The Biot-Savart law states that at any point P, the magnetic field $d\boldsymbol{B}$ evoked by an element $d\boldsymbol{l}$ of a wire, carrying a current I is given by

$$d\boldsymbol{B} = \frac{\mu_0}{4\pi} \frac{I d\boldsymbol{l} \times \boldsymbol{r}}{|\boldsymbol{r}|^3} \ , \tag{1.2}$$

where $\boldsymbol{r}$ is the the distance vector from the wire element to the point at

which the magnetic field acts and $\mu_0 \approx 4\pi 10^{-7}\,\mathrm{Tm/A}$ is the permeability of free space.

Several different techniques for magnetic field sensing have been devised, which we will present in the following section. Most of these sensors can be incorporated into a current sensing setup in different ways [40]. First, the sensor may just be placed above a conductor, which can be formed in a way to increase the flux density, e.g. by a U-shape [41]. Such a simple setup allows easy integration into an application [42]. Next, the current carrying conductor may be passed through a core material with high relative permeability. The magnetic field sensor is then placed in a gap in the core material. The core effectively acts as a flux concentrator, increasing the flux density for a given current and additionally shielding the setup from external interferences [19]. This concept can lastly be extended by a secondary winding on the core. A feedback-loop then controls the current in the secondary winding, keeping the flux density at the sensing element at a constant value, typically at zero-field, making the controller output the measurement value.

Faraday Effect The Faraday Effect describes the phenomenon where the polarization plane of linearly polarized light is rotated when the light propagates through a medium exposed to a magnetic field.

A material that alters the state of polarization is referred to as birefringent. Birefringent media come in different types: circular birefringence, in which the polarization of linearly polarized light is affected, while circularly polarized light remains unchanged; and linear birefringence, where the reverse occurs, i.e. linear polarization is unaffected, but circular polarization is modified. Faraday discovered that circular birefringence could be induced in a material by applying a magnetic field parallel to the direction of light propagation. In cases where the intrinsic circular birefringence of a medium is negligible, the rotation of the polarization plane of linearly polarized light becomes proportional to the integral of the applied magnetic field, B/μ, along the propagation path. This relationship is characterized by a proportionality constant known as the Verdet constant V, a material-specific parameter that defines the strength of the Faraday Effect.

Linearly polarized light can be understood as the superposition of two orthogonal circularly polarized light waves: a right-hand circularly polarized (RHCP) wave and a left-hand circularly polarized (LHCP) wave. When the Faraday Effect occurs, the velocities of these two components are altered. Specifically, the velocity of RHCP waves decreases if the magnetic field is aligned with the propagation direction of the light, while LHCP waves experience an increase in velocity. Conversely, when the magnetic field is applied in the opposite direction, the RHCP wave velocity increases, and the LHCP wave velocity decreases. This differential velocity causes a phase difference between the RHCP and LHCP components of the light. As a result, the superposition of the two circularly polarized waves leads to a rotation of the polarization plane of the original linearly polarized light. The magnitude of this rotation is directly influenced by the strength of the magnetic field and the length of the path through the birefringent medium.

Practical implementations of this effect use optical fibers, wound N times around the conductor, carrying the current I to be measured. They launch linearly polarized light into the fiber, which is then rotated by $\theta = VNI$. The light exiting the fiber is then passed through a polarizing beam splitter, set to 45°. The ratio of the intensities of the two beams is then used to determine θ and thereby B. More complex schemes have been devised, using sending and receiving channels on both ends of the fiber to increase stability and linearity.

Such fiber optic current sensors achieve excellent isolation and can accurately measure in the kA to MA range [38]. They are however costly and require bulky infrastructure.

Magnetic field sensing is often favored for current sensing applications due to its simplicity and the inherent advantage of galvanic isolation, which allows for accurate measurement of electrical currents without direct contact with the current-carrying conductor. This isolation reduces the risk of electrical shock and interference, enhancing both safety and signal integrity in the measurement process. Additionally, magnetic field sensors are non-invasive, minimizing the impact on the system being monitored, and are capable of measuring both AC and DC currents. In the following, we will explore various magnetic field

sensing techniques in more detail, examining their principles, advantages, and specific use cases.

1.2 Magnetic Field Sensing

A large variety of magnetic field sensing techniques has been developed in the past. Here, want to give a brief overview of these techniques and point out the strengths and weaknesses. We will shortly introduce each sensing technology and summarize some figures of merit (FoM) in Table 1.1.

Hall effect sensors were first described in 1880 by Edwin Hall [43] and have since become one of the most prominent magnetic field sensor technologies. The Hall effect arises from the magnetic Lorentz force, which deflects moving charge carriers when exposed to a magnetic field, leading to a transverse voltage, directly proportional to the magnetic flux density $\boldsymbol{B}$.

In a solid metal or semiconductor, subjected to a magnetic field $\boldsymbol{B}$, the magnetic Lorentz force acting on a single charge carrier can be described by

$$\boldsymbol{F} = q(\boldsymbol{E} + \boldsymbol{v} \times \boldsymbol{B}) \,, \tag{1.3}$$

with the charge of the carrier q. The electric force $q\boldsymbol{E}$ is zero in this consideration. The instantaneous drift velocity of the moving carrier v is given by

$$v = \frac{I}{n_\mathrm{c} q w t} \,, \tag{1.4}$$

where w, t are the width and thickness of the conductor with carrier density n_c, and the current I in the conductor. The Hall voltage can then be approximated as

$$V_\mathrm{H} = \frac{BI}{n_\mathrm{c} q t} = BI\frac{R_\mathrm{H}}{t} \,, \tag{1.5}$$

where the material is characterized by the Hall resistance R_H.

Hall sensors benefit from the sophisticated CMOS technology, allowing the cheap integration in mass production. They can work at high magnetic field ranges, however come with a low sensitivity, compared to the following technologies.

Anisotropic magnetoresistance (AMR) was discovered by W. Thomson in 1857 [44]. He described a material's change in resistivity when the orientation between a current through the material, usually a permalloy, and its magnetization is varied. The resistivity R in that case can be described by

$$R = R_{\parallel} - \Delta R \cos^2 \theta \,, \tag{1.6}$$

$$\Delta R = R_{\parallel} - R_{\perp} \,, \tag{1.7}$$

where $R_{\parallel}$ is the resistivity when the current flow is parallel to the magnetization $\boldsymbol{M}$, i.e. $\theta = 0$. $R_{\perp}$ then corresponds to an orientation between current flow and $\boldsymbol{M}$ of $\theta = 90°$. The change in R can then be used to determine the magnetization which is a function of the external magnetic field. Commonly the flow of current is rotated by 45° with respect to the magnetization [45], using a metalization on the permalloy, commonly referred to as *barber pole* structure. The effect is a linearization of the sensor response and an increased sensor sensitivity [46].

AMR sensors can be manufactured on a large scale in integrated circuits, making them robust and easily mass producible, while being more sensitive than e.g. Hall sensors. They however suffer from non-linearity at the end of their comparatively low full range on the order of 1 mT.

Giant Magnetoresistance (GMR) and **tunneling magnetoresistance (TMR)** are related by their operation relying on magnetoresistance properties arising in stacks of magnetic materials.

GMR sensors are part of the family of spintronic devices, since they use the spin dependent scattering of electrons in a metal layer, sandwiched between two magnetic layers. When the magnetization of both layers is aligned, electrons with one spin polarization experience low scattering as they pass through the structure. This low scattering results in lower resistance. When the magnetizations are not parallel, electrons of both spin polarizations (up and down) experience increasing scattering, leading to higher resistance in the structure. Therefore, one layer is usually pinned into a magnetization through a a large coercivity, and the other is allowed to be magnetized by an external magnetic field.

TMR sensors have a similar structure. An insulating layer between two ferromagnetic layers can be passed by electrons through the tunneling effect. The probability of this tunneling depends on the spin orientation of the electrons relative to the magnetization direction of the layers. The TMR effect is then observed as a change in resistance depending on the relative magnetization of the two ferromagnetic layers.

Both technologies can be integrated well in CMOS processes and feature good sensitivities. They are limited to fields up to 1-10 mT above which they saturate. GMR and TMR are both also prone to 1/f noise, a noise component which rises with decreasing frequencies.

Optically Pumped Magnetometers (OPM) use alkali atoms, such as rubidium or cesium, which are spin-polarized by resonant light. When these atoms are placed in a magnetic field, their electron spins begin to precess, which affects the amount of light transmitted through the atomic vapor. As a result, changes in the transmitted light can be detected, allowing for the measurement of magnetic fields.

OPMs offer a high sensitivity, compared to the previous sensor types, enabling them to detect extremely weak magnetic fields down to the femto-Tesla range, and making them ideal for applications like magnetoencephalography and geomagnetic field measurements. They however have limited dynamic range, often requiring magnetic shielding in practice. This adds complexity and cost to their use, since even slight variations in external magnetic fields can interfere with their operation. OPMs can be miniaturized into small, portable devices [47]. In addition, OPMs do not require cryogenics like other high-sensitivity system, making them suitable for mobile applications, and environments where space is limited, such as compact medical devices. Though, their use still requires precise laser systems and optical components to polarize and detect spin states. Calibration and tuning can be technically demanding, which may limit their applicability in some settings.

Magnetoelectric (ME) sensors rely on the coupling between polarization $\boldsymbol{P}$ and magnetization $\boldsymbol{M}$, i.e., the control of $\boldsymbol{P}$ by applying a magnetic field (direct ME effect) or the manipulation of $\boldsymbol{M}$ through an electric field (converse ME effect). The direct ME effect is of great interest in

multiferroic materials, which exhibit both ferroelectric and ferromagnetic properties. These materials are extensively studied for applications like magnetic sensors due to their ability to couple electric and magnetic responses.

In addition to using multiferroic materials, magnetoelectric sensors can operate on the strain, induced by magnetostriction. In this approach, a piezoelectric material, such as Lead Zirconate Titanate, is strongly coupled to a soft magnetic material. When a voltage is applied to the material, it generates mechanical strain, which can modify the direction or amplitude of the magnetization in the magnetic material. Conversely, if a magnetic field is applied to the magnetic material, it undergoes magnetostriction, creating a strain in the piezoelectric material that induces a voltage.

This coupling enables a direct conversion between magnetic fields and electrical signals, making such sensors appealing, since they require no external voltage supply. They are limited by their dynamic response, with bandwidths of usually up to 1 kHz, though.

Coils or induction coil sensors are some of the oldest and well-known sensor types. They rely on Faraday's induction law, describing a conductor loop's output voltage

$$V = -n\frac{\delta\Phi}{\delta t} = -nA\frac{\delta B}{\delta t} \ , \tag{1.8}$$

where Φ is the magnetic flux through a coil with n windings of area A, assuming A is time-invariant. Since a change in flux is necessary to induce a voltage, coil sensors can only detect AC magnetic fields. They still find wide application, since they are easy to construct and offer low noise. A coil sensors intrinsic noise is given by the thermal noise of the windings parasitic resistance, which can be comparatively low. In addition, the sensitivity is directly proportional to the frequency, making coil sensors highly sensitive at high frequencies.

For the detection in low frequency ranges, a ferromagnetic core is placed inside the coil, acting as a flux concentrator. This sensor is usually referred to as search coil. The output voltage is then increased by the

cores relative permeability μ_r, which can be on the order of 10^5. The effective relative permeability is however significantly lower, due to the demagnetizing field effect [48].

Fluxgates consist of a soft magnetic material core surrounded by a primary excitation coil, which generates an alternating magnetic field in the kHz range to periodically saturate the core. In the absence of an external magnetic field, the core's magnetic response is symmetrical, producing no net voltage in the secondary sensing coil. However, when an external magnetic field is present, the core's response becomes asymmetrical, resulting in a detectable signal at twice the frequency of the applied current in the excitation coil.

Unlike traditional coils, fluxgates are sensitive to static (DC) magnetic fields, allowing them to detect weak fields ranging from picoteslas to nanoteslas. They can be designed in various sizes, from micrometer to centimeter scales, depending on the application. Additionally, fluxgates exhibit a flat frequency response up to several kilohertz, and their low 1/f noise characteristic make them ideal for low-noise applications.

The primary applications of fluxgates include earth's magnetic field measurements, navigation systems, and laboratory instrumentation for precision magnetic field detection. They are however limited by their magnetic bandwidth, usually in the kHz range.

Superconducting quantum interferences devices (SQUIDs) are extremely sensitive magnetometers. They make use of two properties of superconductivity, the quantization of magnetic flux and the tunneling of Cooper pairs through a weak link known as a Josephson junction. A Josephson junction is formed when two superconducting materials are separated by a very thin insulating barrier.

A SQUID consists of a superconducting loop with one Josephson junction in a RF-SQUID, or two Josephson junctions in a DC-SQUID. In a DC-SQUID, current is split between two paths around a loop, each containing a Josephson junction. These paths interfere with each other, and the amount of interference depends on the magnetic flux through the loop. When a magnetic field is applied, the output voltage of the SQUID exhibits a modulation with a period corresponding to one flux quantum

	B range	Bandwidth	Size	Sensitivity
Hall	10 T	DC - 1 MHz	1 µm-1 mm	$1\,\mu T/\sqrt{Hz}$
AMR	1 mT	DC - 10 MHz	1 µm-1 mm	$10\,nT/\sqrt{Hz}$
GMR / TMR	10 mT	DC - 1 GHz	1 µm-1 mm	$100\,pT/\sqrt{Hz}$
OPM	1 µT	DC - 1 GHz	1 mm-10 mm	$10\,fT/\sqrt{Hz}$
Magnetoelectric	1 mT	DC - 1 kHz	100 µm-10 mm	$1\,nT/\sqrt{Hz}$
Coil	10 T	AC	100 µm-1 m	$1\,fT/\sqrt{Hz}$
Search coil	1 µT	AC	100 µm-1 m	
Fluxgate	100 µT	DC - 5 kHz	100 µm-50 mm	$5\,nT/\sqrt{Hz}$
SQUID	10 µT	DC - 100 kHz	100 µm-10 mm	$10\,fT/\sqrt{Hz}$
NV Center	> 4 T	DC - 1 GHz	1 mm-100 mm	$10\,nT/\sqrt{Hz}$

Table 1.1: Comparison of magnetic field sensing technologies. Data are based on [15, 16, 17, 18, 19]. The sensitivities are typical values and can be surpassed by certain implementations in research.

$\Phi_0 = 2.08 \times 10^{-15}$ Wb. This allows the sensor to realize sensitivities on the order of $10\,fT/\sqrt{Hz}$. SQUIDs also have drawbacks, most significantly the necessity of cryogenic cooling.

We will present the physics and different modes of operation of NV centers for magnetic field sensing in the following section. The data in Table 1.1 on sensors that utilize NV centers are based on [49, 50, 51, 52]. For all sensing technologies in Table 1.1, specific implementations may trade off between the given characteristics. For instance, a specific Hall sensor that achieves a sensitivity of $1\,\mu T/\sqrt{Hz}$ may not simultaneously deliver a magnetic field range of 10 T.

1.3 Nitrogen-Vacancy Centers in Diamond

Diamond is an extraordinary material, renowned for its exceptional hardness and high thermal conductivity [53]. It is optically transparent and can contain hundreds of different point defect centers, known as color centers, which are optically active and were identified by their photon emission behavior via optical spectroscopy [54, 55]. Among these, the negatively charged nitrogen-vacancy center (NV) is one of the most extensively studied, being active in the visible spectrum [56, 57]. Its unique spin properties enable it to function as

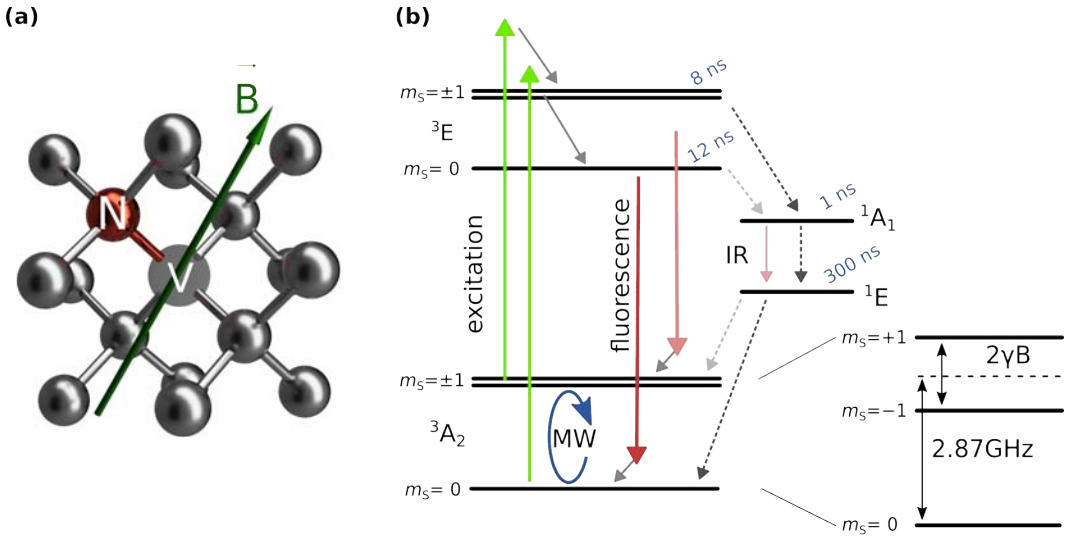

Figure 1.1: (**a**) Diamond lattice with a single NV center in one of four possible orientations in the lattice. A green arrow symbolizes a magnetic field $\boldsymbol{B}$ of arbitrary direction. (**b**) Energy level structure of the NV center. Green arrows symbolize non-resonant, spin-conserving excitations into the phonon sideband and red arrows show spin-conserving relaxations. Dashed arrows symbolize non-radiative transitions.

a solid-state *artificial atom*. NV centers have attracted significant interest for their potential applications in quantum information [58], magnetic field sensing, nanoscale nuclear magnetic resonance (NMR) spectroscopy [59, 60, 61], biosensing and marking [62, 63, 64], and thermometry [65].

The NV center is a stable color defect consisting of a substitutional nitrogen atom and an adjacent vacancy in the diamond crystal lattice, as illustrated in Figure 1.1a. In the tetrahedral arrangement of the lattice points in the crystal, with a bonding angle of 109.5°, the sp^3 hybridized orbitals of the nitrogen atom and the three neighboring carbon atoms dangling in the vacancy form a C_{3v} symmetry. The bonding line between the nitrogen atom and the vacancy acts as the rotation axis of the color center, maintaining rotation invariance for the three carbon atoms around 120°. We refer to this line as the NV axis. Due to the rotation invariance, the NV center can adopt four equivalent orientations along the ⟨111⟩ crystallographic axes: [111], $[1\bar{1}\bar{1}]$, $[\bar{1}11]$, and $[\bar{1}\bar{1}1]$.

The NV center can exist in two charge states. The neutral charge state NV^0 has five unpaired electrons, four from the neighboring carbon atoms and one from the nitrogen atom. For the negatively charged NV^- center, electron

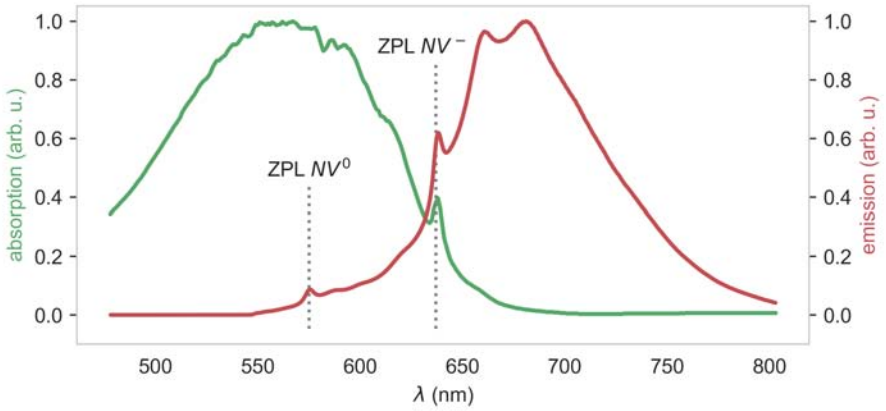

Figure 1.2: Absorption and emission spectra of the NV center. The absorption spectrum is adapted from [13]. The emission spectrum is acquired from NV-rich microdiamonds in glue, attached to an optical fiber.

spin resonance measurements have shown that it has an electron paramagnetic ground state with an electron spin angular momentum of S=1 [66]. It is therefore assumed to have six electrons, with two of them being unpaired. Both NV^- and NV^0 are optically active and can be distinguished by their Zero Phonon Lines (ZPLs) at 637 nm (1.945 eV) and 575 nm (2.156 eV), respectively and their related vibronic phonon side band with photon emission at lower energies [67, 68]. Since this work is mostly concerned with the NV^- center, we commonly refer to it by only NV center.

In Figure 1.2, we show an emission spectrum acquired from NV-rich microdiamonds in glue, attached to an optical fiber, at standard ambient conditions. We observe the ZPLs of both charge states since both may be present in NV rich diamonds. Additionally, under sufficiently high excitation powers, NV^- centers can be photo-ionized to NV^0 [69]. We also show the absorption spectrum (adapted from [13]), which is partially overlapping the emission spectrum.

In Figure 1.1b, we show the energy level structure of the NV center, consisting of a spin triplet in the ground state $^3A_2$, a spin triplet in the excited state ^3E, and additionally, two intermediate singlets states $^1A_1$ and ^1E. Due to the NV center's electron spin (S=1), three electron spin sublevels exist. They are denoted by the spin quantum numbers $m_S = 0$ and $m_S = \pm 1$. In the ground state, the degeneracy of the sublevels is lifted by spin-spin interaction of the two electrons at a zero-field splitting (ZFS) with $D_{gs} = 2.87$ GHz [70]. A ZFS is also observed for the excited state with a value of $D_{es} = 1.42$ GHz [71]. The $m_S = \pm 1$ sublevels are degenerate at zero external magnetic field

and no internal strain. Off-resonant green excitation brings the system to the excited triplet state by a usually spin conservative transition. When starting from the $m_S = 0$ sublevel, the system is excited to the $m_S = 0$ sublevel of the excited state, and decays back to the ground state, emitting red fluorescence. When promoted from the ground state to the excited state $m_S = \pm 1$ sublevels, there is a higher probability for a non-radiative decay via an intersystem crossing (ISC) through the singlet states. The $m_S = 0$ and $m_S = \pm 1$ sublevels are associated with different radiative lifetimes. For single NV centers in bulk diamonds values in the range of 12 ns and 8 ns, respectively, are commonly reported [72, 73, 74, 75, 76]. They can be explained by the differing non-radiative ISC rates to the intermediate singlet states [56, 72, 74, 77]. This decay does not emit visible fluorescence, and is thereby commonly referred to as dark state. The transition via the dark state has a high probability to end in the $m_S = 0$ triplet groundstate, enabling the spin polarization of the NV center into the $m_S = 0$ ground state by optical pumping [56, 78]. The dark state is associated with an optical transition in the infrared (IR) at a ZPL of 1042 nm, which is about four orders of magnitude weaker than that of the visible emission [79, 80]. The singlet states are associated with lifetimes of < 1 ns for $^1A_1$ and on the order of 300 ns for ^1E [81, 74, 82]. The different lifetimes of the two decay paths lead to a difference in fluorescence intensity of up to 30% in single NV centers [79, 83, 82]. This value is usually lower in ensembles [84, 85, 12].

In quantum mechanics, the Hamiltonian is a fundamental operator that represents the total energy of a system, including both kinetic and potential energy. When applying a magnetic field $\boldsymbol{B}$, the ground state spin Hamiltonian of the NV center reads [22, 12]

$$\mathcal{H}_{\mathrm{gs}} = hD_{\mathrm{gs}}S_{\parallel}^2 + g\mu_{\mathrm{B}}\boldsymbol{B}\cdot\boldsymbol{S} = \underbrace{\mathcal{H}_{\mathrm{gs}}^{\parallel}}_{hD_{\mathrm{gs}}S_{\parallel}^2 + g\mu_{\mathrm{B}}B_{\parallel}S_{\parallel}} + \underbrace{\mathcal{H}_{\mathrm{gs}}^{\perp}}_{g\mu_{\mathrm{B}}(B_xS_x + B_y + S_y)} \tag{1.9}$$

with Planck's constant h, the Bohr magneton μ_{B}, and the electron g-factor $g \approx 2$. Here, $B^{\parallel}$ is parallel to the NV axis and we neglect hyperfine interactions with nuclear spins, strain-induced splitting, and electric interaction. The excited state is also a spin triplet, and the Hamiltonian $\mathcal{H}_{\mathrm{es}}$ is given by Equation 1.9, only exchanging D_{gs} for D_{es}. The magnetic field dependent ground and excited states of the NV center and the transition rates of all states can then

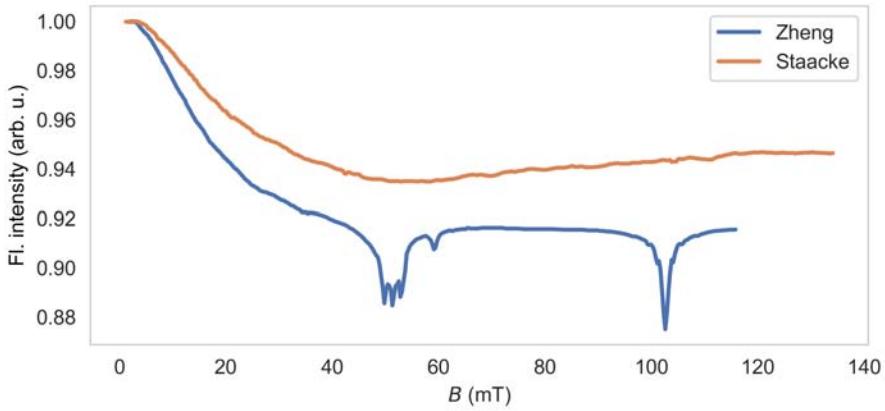

Figure 1.3: Fluorescence intensity as a function of applied magnetic field for high-NV-density bulk diamonds. The trace *Staacke* is a representative measurement for $\boldsymbol{B}$ being unaligned to all NV-axes [12]. The example *Zheng* shows a well aligned case, revealing the ESLAC and GSLAC [14].

be calculated [22]. By summing over all light emitting transitions at the steady state population, the magnetic field dependent fluorescence intensity can be simulated [12]. We do not repeat these simulations here, but qualitatively explain the results. At the application of a magnetic field, the transitions between the ground and excited state cease to be strictly spin conserving. Although optical pumping polarizes most of the spin population in an NV ensemble to the $m_S = 0$ ground state, this spin mixing allows the transition of increasing amounts of the population at rising magnetic fields to the excited $m_S = \pm 1$ states [86, 87, 32, 88]. These show a higher probability to transition via the dark state, decreasing the overall fluorescence intensity. This is the basic principle of all-optical magnetic field sensing. After initial calibration, the fluorescence intensity can be used to deduce the applied magnetic field. An example for such a magnetic field dependent fluorescence intensity is shown in Figure 1.3. Sensitivities in the range of down to $14\,\mu\mathrm{T}/\sqrt{\mathrm{Hz}}$ have been reported previously for laboratory setups that make use of this effect [12, 28, 29]. These are valid for the region of highest gradient, which in the given example is the range of $10\,\mathrm{mT} < B < 30\,\mathrm{mT}$.

In a low transverse field regime, the fluorescence intensity exhibits sharp declines at $B_\parallel \approx 51\,\mathrm{mT}$ and $B_\parallel \approx 102\,\mathrm{mT}$, corresponding to spin mixing induced by a level anti-crossing within the excited state (ESLAC) and ground state (GSLAC), respectively [30, 14, 31, 89]. These setups achieve noise floors of down to $0.45\,\mathrm{nT}/\sqrt{\mathrm{Hz}}$, but require high precision in angular alignment and

a stable and well aligned bias magnetic field of either 51 or 102 mT. We show an example measurement in Figure 1.3. The difference in sensitivity in these and the following methods generally result from the higher magnetic-field dependent change in fluorescence intensity, given that noise sources, e.g. by the photodetection process, are equal.

The Zeeman interaction term $g\mu_\mathrm{B}\boldsymbol{B}\cdot\boldsymbol{S}$ shows the $m_\mathrm{S}=\pm1$ spin states are sensitive to external magnetic fields, resulting in a split of the energy levels for an increasing magnetic field. This is the basis for optically detected magnetic resonance (ODMR). We show this behavior in the energy level structure in Figure 1.1b. The resonant frequencies are then given by

$$\nu_\pm = D_\mathrm{gs} \pm \sqrt{E^2 + (\gamma B^\parallel)^2}\,, \tag{1.10}$$

where $\gamma = g\mu_B/h \approx 28\,\mathrm{GHz\ T^{-1}}$ denotes the linear change in the splitting due to the magnetic field for $E \ll \gamma B^\parallel$. Here, we include the off-axial ZFS parameter E, which depends on the strain condition of the used diamond sample. It already lifts the degeneracy of the $m_\mathrm{S}=\pm1$ states at zero-field. In such a simplified linear model for small magnetic fields, only the magnetic field component $B^\parallel$ along the orientation of the NV center axis affects the splitting. A more complex model can be applied when non-axial magnetic field components may not be neglected. Commonly an additional dimensionless correction factor is then introduced [90, 91]. A simple way of detecting these resonances is the technique of continuous-wave optically detected magnetic resonance (CW-ODMR). Under continuous optical excitation, an oscillating microwave (MW) field is applied and its frequency is tuned in a specific frequency range. When the MW field matches the frequency of the spin transition between $m_\mathrm{S}=0$ and $m_\mathrm{S}=1$ or -1, spins can flip, and consequently a reduction in fluorescence intensity can be observed [92, 78].

The structure of the diamond lattice allows, in principle, four different orientations of the NV-axis. In a diamond sample with more than one NV center, the occurrence of the four directions is randomly distributed. For such an ensemble the external magnetic field $\boldsymbol{B}$ is projected onto each of the axes NV_i with $i \in \{1,2,3,4\}$ and a maximum of eight resonances can be observed. In a magnetometry application with a bulk diamond such a measurement may then be fitted by a sum of Gaussian functions to determine the center frequencies

ν_i [8, 93]. These can in turn be employed for determination of the vector magnetic field [91]. This scheme may also account for the temperature of diamonds, hosting the NV centers. At room temperature, the zero-field splitting D displays a temperature dependence of $\frac{dD}{dT} = -74.2\,\mathrm{kHz/K}$ [94]. This effectively shifts the complete ODMR spectrum, enabling the simultaneous detection of temperature and magnetic fields [95, 96]. Current state-of-the-art NV-based sensors, utilizing MW, realize sensitivities, reaching 0.9 $\mathrm{pT}/\sqrt{\mathrm{Hz}}$ for NV ensembles [97] and 170 $\mathrm{pT}/\sqrt{\mathrm{Hz}}$ for single NV centers [51]. While for single NV centers a lack of ensemble averaging results in worse sensitivities their appeal lie in high spatial resolutions on the nanometer scale.

Another MW-free method has been reported which utilizes the cross-relaxation features near zero magnetic field in high-NV-density samples [33, 34]. Consider a bulk diamond in which NV centers in all four possible orientations are present. When a transverse bias field is applied, so that in two of the four directions the projection of the magnetic field onto the NV-axes is non-zero, transition energies of the respective NVs are split by Zeeman interaction. With an additional magnetic field B_z, applied in parallel to one NV-axis, several crossings of transition energies occur with rising B_z. At these crossings, dips in fluorescence intensity can be observed. These are attributed to dipolar interaction between differently oriented NVs providing depolarization channels [98]. For this method a photon shot-noise-limited sensitivity of 4.5 $\mathrm{nT}/\sqrt{\mathrm{Hz}}$ has been estimated [33].

Beyond the presented MW-free methods and CW-ODMR, more sophisticated methods of magnetometry have been developed. These include coherent control e.g. via pulsed ODMR, lock-in detection and tracking of single resonances, or dynamic decoupling [78, 99]. Since this works focuses on all-optical detection, we do not explain such methods here.

2 Fluorescence Intensity Based Sensing

In this chapter, we focus on the all-optical addressing and readout of NV centers for magnetic field sensing. Therefore, we first present and analyze the optical and electrical components of an optical interrogator, which include optical excitation, photodetection, and noise suppression by lock-in amplification. Building upon this, a compact and low-cost approach to the evaluation circuitry is developed and analyzed. Lastly, we will examine the temperature dependent behavior of our sensing material.

2.1 Optical and Electrical Setup

2.1.1 Optical Setup

The excitation and fluorescence readout of NV centers requires an optical setup. In Figure 2.1, we show the schematic of such a setup, meant for the readout of fiber-coupled sensors. While we may use variations of this setup in later parts of this work, the principle will stay the same. A laser diode's beam is collimated to a beam diameter of 2.1 mm and coupled through a short dichroic mirror (DMSP567R, Thorlabs) and an achromatic collimator for multimode fibers (F950SMA-A, Thorlabs, $f_1 = 9.9\,\mathrm{mm}$) to an optical fiber. The dichroic mirror (DCM) has a cut-off wavelength of 567 nm, allowing the transmission of the excitation light, commonly in the range of 520 nm to 532 nm. At the same time, returning fluorescence from the same optical fiber is reflected from the DCM. A reflectance of the DCM below the cut-off wavelength of a few per-

cent necessitates a long-pass filter (FELH0600, Thorlabs, cut-on wavelength 600 nm), featuring an optical density (OD) of 6 below cut-on. The fluorescence beam is focused onto the active detector area of a photodiode (PD) (S5973, Hamamatsu Photonics K.K.) using a plano-convex lens (LA1951-AB, Thorlabs, $f_2 = 25.4\,\text{mm}$). The magnification of the beam from the optical fiber's end facet is given by $f_2/f_1 = 2.56$, leading to a coverage of the photodiode's detector area of 5%. This enables a robustness against positional inaccuracies by drift or thermal influence without impact on the incident power to the PD.

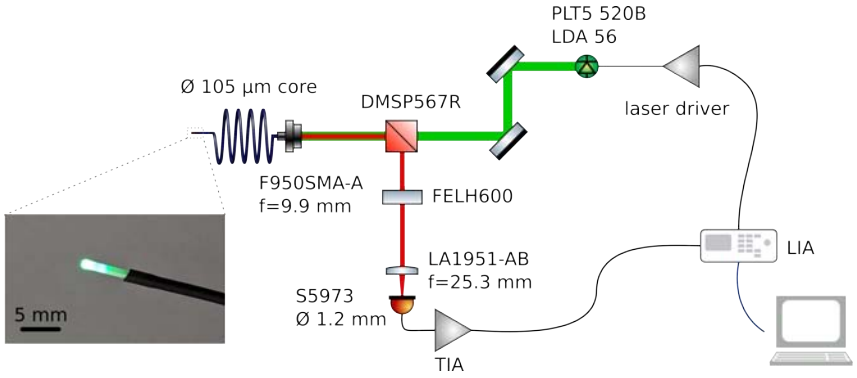

Figure 2.1: Schematic of the optical setup used for the excitation and fluorescence readout of fiber-coupled, NV-based sensor heads. The lower left panel shows a photo of the sensor head of an optical fiber-based sensor which is used in this work.

2.1.2 Sensing Material

Fiber sensors can be composed of a single bulk diamond or a collection of microdiamonds which are attached to the end facets of optical fibers by an optical grade adhesive. In Figure 2.2, we show fluorescence intensities as a function of magnetic fields at varying optical excitation powers for both configurations. We commonly refer to them as calibration curves. The curves are normalized to the intensity at zero magnetic field. For Figure 2.2a, a high-pressure, high-temperature (HPHT) bulk diamond was attached to an optical fiber and the magnetic field was aligned to one of the NV axes ($\theta < 5°$). We find an initial increase of the fluorescence with rising magnetic fields up to $\approx 6\,\text{mT}$, after which it declines towards a saturation for high magnetic fields. The decline can be explained by spin mixing (see Section 1.3). For the initial increase, dipolar coupling between neighboring NV centers leading to mixing of spin states was proposed as an explanation [29, 100, 32]. Additional dips in

fluorescence around 51 mT and 102 mT can be explained by the ESLAC and GSLAC, respectively. For a better alignment between $\boldsymbol{B}$ and one NV axis, we would expect sharper, more well defined features [30, 32]. For the misaligned case, these features are no longer visible. We also find a positive correlation of the magnetic contrast on the optical excitation power. These observations are in line with previous results, which also revealed a saturation behavior of the magnetic contrast towards higher excitation powers [12].

We define the contrast C of a measurement, specifically of calibration curves, as

$$C = 1 - \frac{\min F(B)}{F(B=0)} \tag{2.1}$$

with the fluorescence intensity F as a function of the magnetic field B.

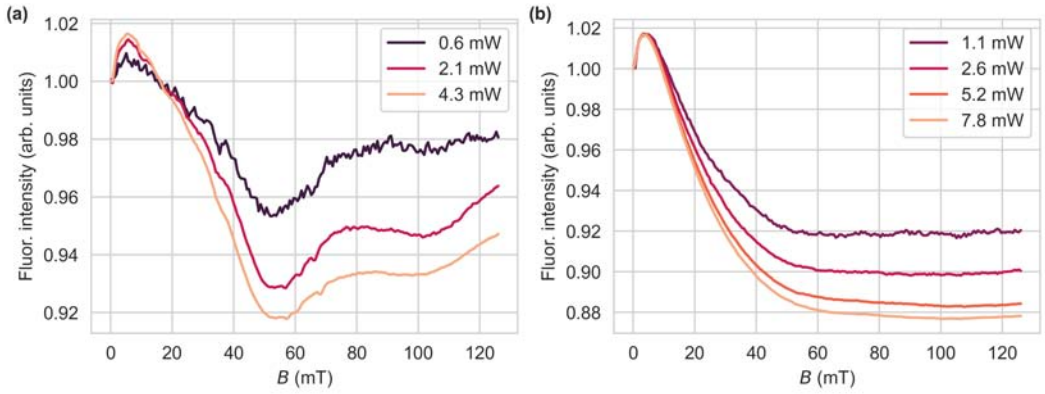

Figure 2.2: Fluorescence intensities as a function of magnetic field, at varying optical excitation powers, normalized to the intensity at $B = 0$. (**a**) Bulk diamond, attached to an optical fiber. (**b**) Micro diamonds in glue, attached to an optical fiber.

While the use of narrow-band features like the GSLAC or ESLAC has been demonstrated for MW-free magnetometry [30], in this work we rather aim for a high magnetic bandwidth and isotropic sensor. Therefore, a fiber sensor was manufactured by Quantum Technologies GmbH in collaboration with the Leibniz Institute of Surface Engineering. The end facet of the fiber is coated with NV-rich diamond powder in glue, with crystal sizes in the range of one micrometer. This is significantly smaller than the diameter of the 125 µm fiber's end facet. This allows the simultaneous addressing of a high number of individual

diamonds and consequently, a statistical averaging over all spatial directions. We show similar measurements for this fiber sensor in Figure 2.2b. Again, we observe an initial rise and subsequent decline of fluorescence intensity at rising magnetic fields, but without any additional features. The intensity decline saturates at $\approx 50\,\mathrm{mT}$.

A picture of the sensor head is shown in the lower left panel of Figure 2.1. The optical fiber with the diamond covered end facet is positioned inside a protective ferrule of 1.3 mm diameter and held in place with optical grade adhesive. This constitutes a small, high-insulation resistance, and non-magnetic probe with many potential use cases in magnetic field sensing. These may include current sensing in electric vehicles and high-voltage power grids, commutation of electric motors, or sensing in aqueous solutions, like electrolytes of metal-air batteries.

2.1.3 Optical Excitation

In this work we off-resonantly excite NV centers in diamonds, using green semiconductor lasers at typically $\lambda_E = 520\,\mathrm{nm}$. We also refer to them as laser diodes, since they operate like a diode with the current flow in the forward direction of a p-n junction. When charge carriers are introduced into the region defined by the junction, recombination radiation occurs. If the current injection is sufficiently strong, a population inversion can be established, leading to stimulated emission. The difference in refractive index between the semiconductor material and the surrounding air allows the surface of the semiconductor material to have enough reflectivity to function as a resonator cavity. Laser diodes offer high optical power densities and can be coupled well to optical fibers due to their highly directional emission. Additionally, laser diodes are low-cost, compared to other laser systems, compact, and compatible to standard electronics. A low-cost contender would be light emitting diodes (LEDs). LEDs however not only come at typical lower power densities, but also emit incoherent light from a larger emitting area, following Lambert's law. When a LED is directly coupled to an optical fiber of identical diameter, the coupling efficiency is given by

$$\eta = \frac{P_{\mathrm{fiber}}}{P_{\mathrm{LED}}} = NA^2 \tag{2.2}$$

with the fiber's numerical aperture $NA = \sin\alpha$ and acceptance angle α [101]. For the 125 µm core fiber with $NA = 0.22$, we would get a coupling efficiency of 4.84%. Usually, LEDs come in higher diameters, further reducing the coupling efficiency. It is noteworthy, that this result can not be improved by any optical system [101]. This is the main driver for the choice of laser diodes in this work. In addition, LEDs emit at a broader wavelength spectrum, overlapping the emission spectrum of NV centers, requiring an additional short-pass filter for the excitation light [6]. However, laser diodes also come with drawbacks like higher intensity noise.

Optical sources exhibit relative intensity noise (RIN), which is defined as the mean squared spectral density of laser intensity fluctuations, relative to the average DC optical intensity [102, 103]. It can be written as

$$RIN(\omega) = \frac{\Delta P_\mathrm{n}(\omega)}{\langle P_\mathrm{o}\rangle^2} \tag{2.3}$$

with the power spectral density ΔP_n as a function of frequency ω and the average optical intensity $\langle P_\mathrm{o}\rangle$. At the output of a photodetector, illuminated by such a source, we then observe intensity fluctuations, given by

$$\Delta P_\mathrm{n} = 2qi_\mathrm{ph} + i_\mathrm{ph}^2 RIN(\omega) \tag{2.4}$$

with the elementary charge q and the average photocurrent i_ph. The first term is shot noise, which is the result of the discontinuous nature of electrons and photons, and the second term is the additional laser RIN.

In Figure 2.3, we show the higher frequency noise spectrum at equal DC indications of a TIA, which we compare for a green light emitting diode and a laser diode. If the measurement was purely shot noise limited, we would expect a noise spectrum close to the dashed indicated line. Light emitting diodes are thermal Gaussian sources with short coherence times, giving rise to nearly pure shot noise at the detector [103]. On the other hand, laser diodes exhibit RIN, due to e.g. near threshold operation or optical feedback. Reflections can lead to instabilities, mode hopping, and excessive intensity noise, all of which contribute to an increase in RIN [102]. We will later find fluorescence measurements to be shot noise limited, indicating the laser diode's intensity noise does not transfer to the fluorescence at these higher frequencies.

Additionally, the long term behavior of the laser's output power is of im-

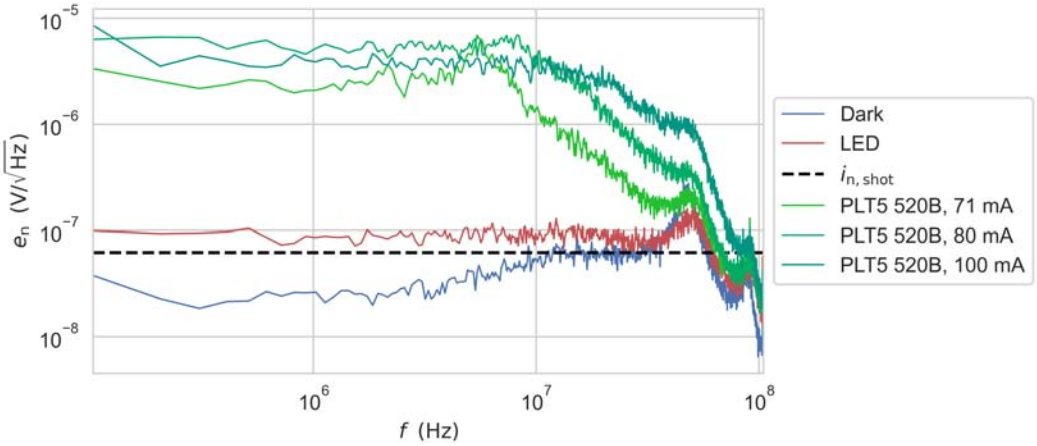

Figure 2.3: Comparison of noise spectral density from TIA (12 kΩ, f_{-3dB} = 50 MHz) at same output DC levels of ≈ 1 V for different light sources. The black line shows the expected shot noise density at the given DC level.

portance, because of its impact on the DC accuracy and drift behavior in a measurement setup. In a simple experiment we monitored the mean optical power of a collimated 520 nm laser diode (PLT5 520B, ams-OSRAM AG) by a power meter (PM120D, Thorlabs) in two different laser driver configurations. In the first configuration, shown in Figure 2.4a, a constant voltage is applied to the gate of a metal–oxide–semiconductor field-effect transistor (MOSFET) in saturation, limiting the current through the laser diode. A switching transistor in series is used to pulse the laser at 100 kHz, which is a typical mode of operation in later sections. The functionality is implemented by an integrated circuit (IC) specific to this application (iC-HKB, iC-Haus GmbH), where the current limiting gate voltage is supplied by a reference voltage IC (REF3030, Texas Instruments). We compare this circuit to one, implementing a control loop for the emitted optical power, using the laser integrated photodiode. The photodiode monitors the rear facet output beam of the laser diode, generating a photocurrent, developing a voltage across a shunt resistance R_S. The control loop and the switch is implemented by a dedicated IC (iC-NZN, iC-Haus GmbH).

We captured the mean optical power during 63 h for both setups, shown in Figures 2.4b,e. The time domain representation already shows a non-stationary mean in the time series. Additionally, in the current controlled laser intensity, we find a daily seasonality which correlates with the ambient temperature (not

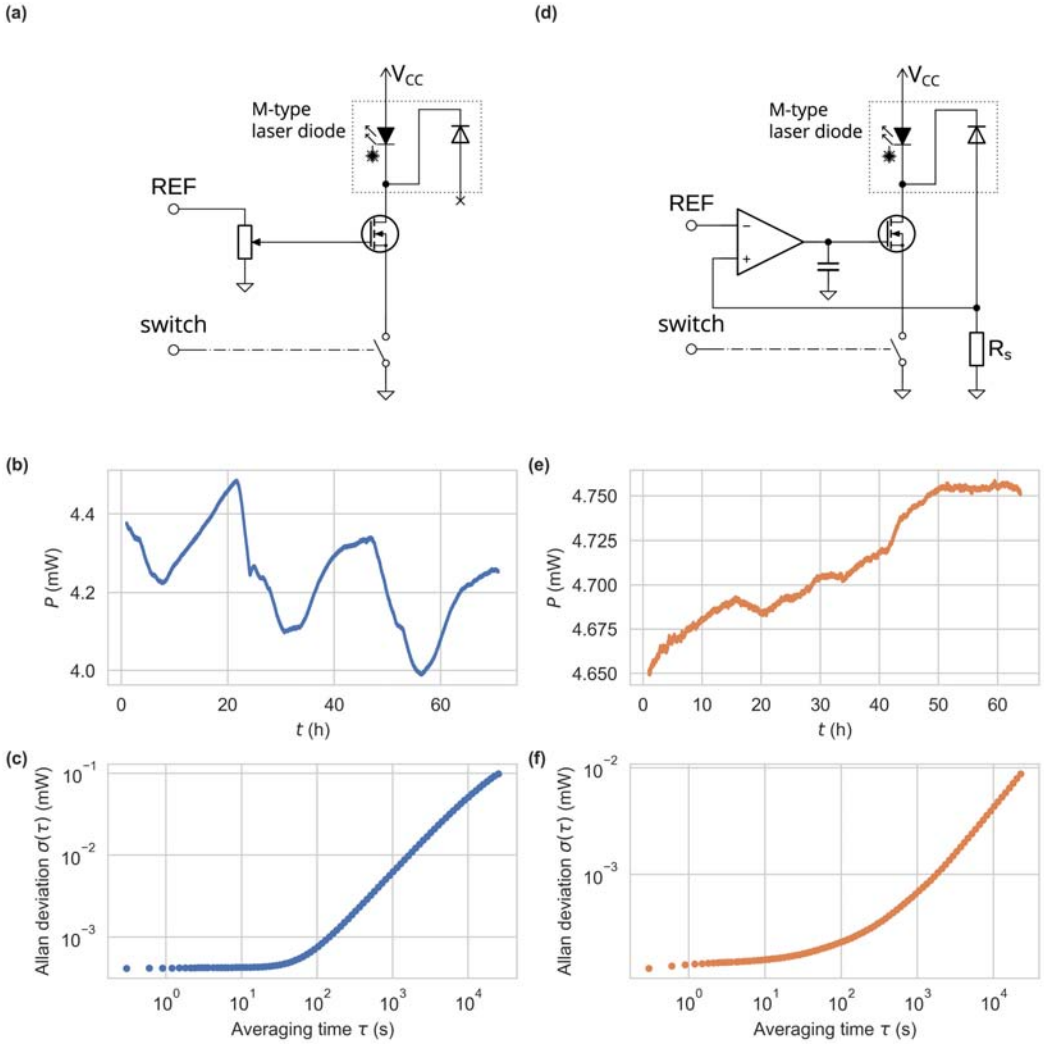

Figure 2.4: Comparison of current controlled laser driver and optical feedback laser driver. (**a**) Simplified schematic of the current controlled laser driver. A constant voltage is applied to an internal MOSFET in saturation, limiting the current through the laser diode. (**b**) Time trace of optical output power in 7 h and (**c**) the respective Allan deviation of the current controlled laser driver. (**d**) Simplified schematic of the optical feedback laser driver. The photodiode integrated into the laser diode housing is used in a control loop to stabilize the mean optical output power of the laser. (**e**) Time trace of optical output power in 65 h and (**f**) the respective Allan deviation of the current controlled laser driver.

shown). More insight can be gained by the Allan deviation of both records, which we show in Figures 2.4c,f. In both cases, we find a plateau at low integration times, since the power meter's sampling frequency of $f_S = 3\,\mathrm{Hz}$ is low compared to the time scale of drift in the system that lead to a bias instability. We find no negative slope then, which would result from averaging of white noise. In the range of $\tau = 10\,\mathrm{s}$ to $100\,\mathrm{s}$ an additional drift component leads to a slope, proportional to 0.9τ, in both scenarios. In the feedback configuration, we find an approximately three times lower bias instability. While from this data the feedback implementation seems favorable, it introduces added complexity, since back-reflections from the optical system may not only interfere with the laser itself, but also the monitor photodiode and thereby the control loop. In the following chapters we employ the current controlled laser driver for its simplicity. One may of course build upon these findings and integrate a stabilized laser driver. Next to the presented solution, we suggest balanced photodetection to reduce the impact of laser intensity noise on the measurement [104].

Not all drift components in the laser excitation can be eliminated by optical feedback. These originate e.g. in the temperature change of the laser diode, accompanied by a shift in the emitted wavelength. These again lead to a different ratio of transmission to reflection of the dichroic mirror. Also the absorption of NV centers is wavelength-dependent (see Figure 1.2). Another source of drift is given by the reference voltages that are part of the laser drivers, each contributing their own drift components. Furthermore, the monitor photodiode's sensitivity is temperature dependent, which disturbs the control loop.

Allan deviation is a statistical tool, commonly used to evaluate the deviation of measurement data grouped in intervals with observation period τ. Unlike the standard deviation, Allan deviation systematically examines data sets with respect to the averaging time τ providing valuable insight into the noise characteristics of the system and the low-frequency drift behavior of the sensor. The Allan variance is calculated by [105]

$$\sigma_A^2(\tau) = \frac{1}{2}\langle(\bar{y}_{n+1} - \bar{y}_n)^2\rangle, \tag{2.5}$$

where $\bar{y}_{n+1}$ and $\bar{y}_n$ are mean values of samples from adjacent intervals. Here, $\langle\cdot\rangle$ denotes the expectation value, which we approximate in our measurement by the average of all n available intervals [106]. Just as with standard deviation and variance, the Allan deviation is defined as the square root of the Allan variance.

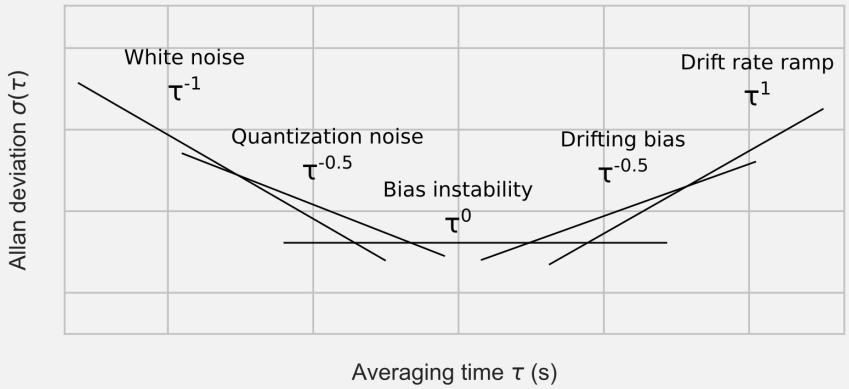

The figure above shows the different slopes in an Allan deviation plot. At high frequencies, where white noise dominates, rising integration intervals lead to a reduction in the deviation with a slope of -1. Towards higher integration times other effects like quantization noise, drift or random walk each contribute their own noise with characteristic slope. The plateau at the lowest deviation is commonly referred to as bias instability.

2.1.4 Photodetection

The most basic limit to the sensitivity of an optical measurement is set by the shot noise of the signal photons. Once other noise sources have been reduced below this level, further SNR improvements can come only from increasing the signal strength or narrowing the bandwidth [107].

Shot noise arises from the discrete nature of light and electric charge. The concept was first introduced by Schottky in 1918 [108]. Incident photons and emitted charge carriers, at an average rate proportional to the diode current i_d, are statistically independent, leading to a fluctuation in the

current around i_d, which is given by

$$i_\mathrm{n,shot} = \sqrt{\langle (i_\mathrm{d}(t) - \langle i_\mathrm{d} \rangle)^2 \rangle} = \frac{q}{\Delta t} \sqrt{\langle (n(t) - \langle n \rangle)^2 \rangle}\,, \tag{2.6}$$

with $i_\mathrm{d}(t) = \frac{qn(t)}{\Delta t}$ and $\langle i_\mathrm{d} \rangle = \frac{q\langle n \rangle}{\Delta t}$ with the elementary charge q, integration time Δt and the number of emitted charge carriers n. $\langle \cdot \rangle$ denotes the infinite time average. The fluctuation is described by a Poisson distribution, where the variance is equal to the mean value $\sigma^2 = \langle n \rangle$. For high number of counts n, which we are usually dealing with, the probability density function approaches that of a normal distribution $\mathcal{N}(\mu = \langle n \rangle, \sigma^2 = \langle n \rangle)$, yielding a root-mean-square (RMS) value of $\langle (n(t) - \langle n \rangle)^2 \rangle = 2\langle n \rangle$. Substituting into Equation 2.6 gives us

$$i_\mathrm{n,shot} = \frac{q}{\Delta t} \sqrt{2\langle n \rangle} = \sqrt{\frac{2qi_\mathrm{d}}{\Delta t}} = \sqrt{2qi_\mathrm{d}B}, \tag{2.7}$$

where the bandwidth is given by $B = \frac{1}{\Delta t}$. This is the commonly known equation for the determination of shot noise.

Detector choice

A photodetector is necessary to capture the fluorescence of the NV diamonds and enable the further electronic processing. The photoluminescence of the NV^- center has a spectrum in the range of 600 to 850 nm. When choosing a solid state detector, a Si-based detector is preferential because it has the highest quantum efficiency at these wavelengths among the common semiconductor materials [109]. Solid state detectors like phototransistors or light dependent resistors are unsatisfactory for use in measurement applications with regard to bandwidth, linearity, and temperature dependence [101]. This leaves us with photodiodes, which, operated in photoconductive mode, feature a high linearity and a fast response. In comparison to other detectors like photomultiplier tubes, photodiodes are rugged and easy to integrate, operate at a low bias voltages, and feature a high mean time to failure.

In photodiodes, incident photons give rise to charge carrier pairs due to the internal photoelectric effect, if the photoelectric threshold condition $h\nu \geq E$ is met. Here, ν is the frequency of the electromagnetic wave, h is the Planck

constant, and E is the energy which is needed to excite electrons from the valence band to the conduction band. The threshold wavelength λ_s for this effect to occur can be determined from

$$\frac{hc}{E} = \frac{1.2398\,\mu\text{m eV}}{E} \tag{2.8}$$

with $c = \nu\lambda$ and the speed of light c. For the bandgap of silicon, we find a threshold of $\lambda_s \approx 1117\,\text{nm}$ at 300 K. For the photodetection process, an electric field is further required, leading to a drift of charge carriers, enabling their collection at ohmic contacts. In photodiodes, the electric field is built-in by the depletion layer between p- and n-doped regions of the semiconductor.

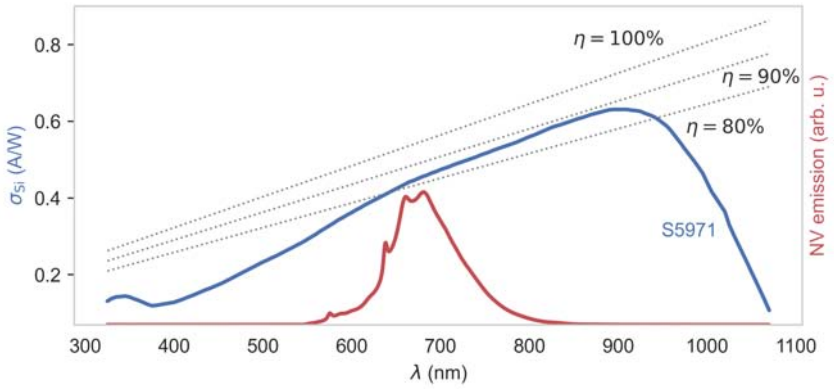

Figure 2.5: Spectral sensitivity σ_{Si} of the example Si-PD (S5971, Hamamatsu) in comparison to different quantum efficiencies and the typical emission spectrum of NV centers at room temperature.

A photodiode's spectral sensitivity is the ratio of photocurrent i_d per incident radiant power P

$$\sigma_{Si} = \frac{i_d}{P} = \frac{\eta q \lambda}{hc} \tag{2.9}$$

where a quantum efficiency η of 100% means, every incident photon gives rise to one electron hole pair. Modern photodiodes offer low reflection losses through anti-reflection coatings. Furthermore, they have been constructed in a way that most of the incident photons are absorbed within the depletion layer, among others by introducing an intrinsic undoped layer between the p and n regions. They are referred to as PIN diodes. These devices offer high quantum efficiencies, usually $\eta > 80\%$ at the wavelengths of interest, which we show for an example device (S5971, Hamamatsu) in Figure 2.5. The spectral sensitivity as a function of wavelength shows the photocurrent rises linearly

with the wavelength. This behavior stems from the fact that lower wavelength photons are associated with higher energy and thereby less current per radiant power can be generated.

PIN photodiodes may be chosen in contrast to other photodiode types, like avalanche photodiodes (APDs) or other detectors with internal gain, when the amount of incident photons per time is expected to be high enough to yield a higher signal-to-noise ratio (SNR). The dominant noise sources in solid state detectors are shot noise from the signal current i_d and the dark current i_dark as well as thermal noise from the load resistance R_L. The SNR for an APD as a function of the diode current is then given by

$$SNR_\mathrm{APD} = \frac{i_\mathrm{d}^2 M^2}{2q(i_\mathrm{d} + i_\mathrm{dark})BM^2F + \frac{4kTB}{R_\mathrm{L}}} \tag{2.10}$$

with bandwidth B, Boltzmann's constant k, and temperature T [101]. M is the internal amplification in APDs which is usually in the range of 20–200. It is accompanied by an excess noise factor F which describes the additional noise generated by the multiplication process, leading to above full shot noise contribution. The internal amplification of APDs eases requirements on the read-out electronics with regard to the load resistance R_L, which makes APDs favorable at low incident light powers and high bandwidth requirements. However, the amplification and excess noise is not present in simple photodiodes. The SNR for photodiodes is then given by equation 2.10 with $M = F = 0$. Consequently, at higher light powers the SNR rises above the one of APDs. We plot an example for the SNRs achievable with similar APDs and PDs as a function of incident light power in Figure 2.6.

APDs need additional circuitry to generate a high-voltage bias, usually around $V_\mathrm{bias} \approx 100\,\mathrm{V}$. Furthermore, the APD gain is a function of temperature. To use an APD over a wide temperature range, some kind of temperature compensation has to be implemented. This circumstance further supports the use of simple photodiodes in a cost-effective solution.

Photodiode datasheets of reputable manufacturers offer a range of specifications, of which we describe some in the following:

Spectral response is the photosensitivity as a function of the wavelength. We have shown this before in Figure 2.5 and compared it to the theoretical maximum values. We operate photodiodes with reverse bias in

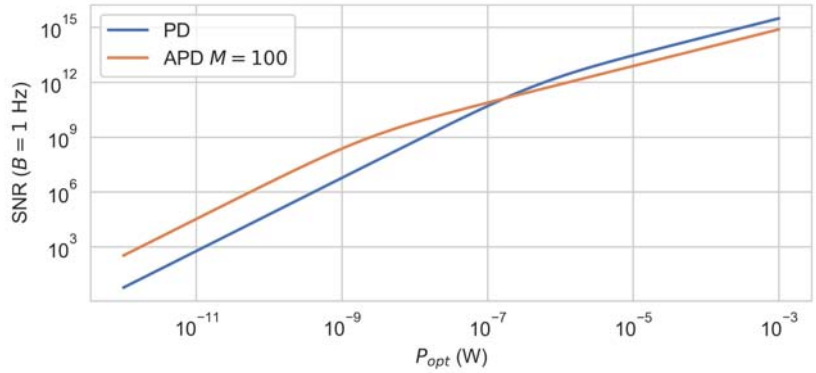

Figure 2.6: Comparison of SNR per unity bandwidth of photodiode and avalanche photodiode as a function of incident light power ($\lambda = 800\,\mathrm{nm}$). Same device characteristics for APD and PD have been assumed ($i_{\mathrm{dark}} = 1\,\mathrm{nA}$, $T = 298\,\mathrm{K}$, $R_{\mathrm{L}} = 100\,\mathrm{k\Omega}$, for the APD $M = 100$ and $F = 4$).

the third quadrant of the diode's I-V curve. This enables the spectral response to be highly linear for many decades of optical power.

Frequency response of the photodiode is usually that of a low-pass behavior. The cut-off frequency depends on the external circuitry. The highest bandwidths can be realized with a low load resistance R_{L}. The cut-off frequency is then generally given by

$$f_{\mathrm{c}} = \frac{1}{2\pi\sqrt{C_{\mathrm{p}} C_{\mathrm{j}} R_{\mathrm{l}} R_{\mathrm{s}}}}\,, \tag{2.11}$$

with the junction capacitance C_{j}, the parasitic capacitance C_{p} of all external leads and traces, and the shunt resistance R_{s} of the undepleted semiconductor. To maximize this extrinsic cut-off frequency, R_{s} and C_{j} can be reduced by reducing the detector area. Additionally, a reverse voltage can be applied to increase the depletion region, and thereby reducing C_{j} which is part of the terminal capacitance.

Terminal capacitance is the overall capacitance, measured at the leads of the device. It reduces by increasing the reverse voltage. The absolute maximum ratings set a limit, however.

Detector area next to other geometry parameters is important in the mechanical design of an opto-electrical system. Larger detector areas ease

the requirements on positional accuracy and stability, but competes with the terminal capacitance.

Noise Equivalent Power (NEP) is the minimum detectable power per square root bandwidth for a given detector [110]. It is a measure of the weakest optical signal that can be detected, below which shot noise from dark current and thermal noise of resistive components dominate over the signal power. We typically operate the photodiode in bright field, well above the NEP. Thereby, in our application this specification is of low importance.

Dark current is a function of reverse voltage and temperature, and contributes shot noise. For the same reasons as the NEP, we can usually neglect the dark current in the system design.

Temperature dependent photosensitivity as a function of wavelength has to be considered at varying ambient temperatures. Photodiodes typically show a positive temperature coefficient of the generated photocurrent, which is low for shorter wavelengths ($< 0.1\,\%/\mathrm{K}$ at 800 nm) and rises with increasing wavelengths.

Transimpedance amplifier

To convert a photodiode's output current to a usable voltage, the easiest method would be to feed the current into a resistor R. While this is straight forward, it severely limits the usable bandwidth. A voltage develops across the diode's capacitance $C_\mathrm{d} = C_\mathrm{p}||C_\mathrm{j}$ and we get a low-pass behavior with a pole at $s = -\frac{1}{RC_\mathrm{d}}$. To achieve a higher bandwidth, we can decrease the diode's capacitance by choosing a smaller diode and applying a reverse bias voltage. This only works up to a point where optical alignment, mechanical stability and the ability to focus the fluorescence set boundaries. The other approach consists in decreasing the load resistance R_L which comes with a degradation of the SNR at a certain point, as we will see later. These considerations lead us to the transimpedance amplifier (TIA), allowing us to convert the photodiode current to a voltage while reducing the voltage swing across C_d. The following analysis of the TIA is based on [111] and [107].

In Figure 2.7 we show the schematic of a simple TIA, which we model in

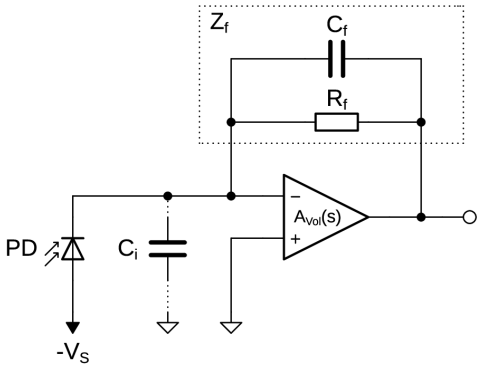

Figure 2.7: Schematic of a simple TIA. The feedback resistor R_f sets the DC gain. We use the negative bias $-V_\mathrm{S}$ to reduce the diode's capacitance. The capacitance C_i includes all parasitic capacitances from PD, traces and OP input stage.

the following. The open loop voltage gain of an inverting amplifier is given by

$$\frac{u_0}{u_\mathrm{i}} = -A_\mathrm{Vol}(s) = -A_0 \frac{\omega_0}{s+\omega_0} \tag{2.12}$$

with the DC open loop gain A_0, input and output voltages $u_\mathrm{i}, u_\mathrm{o}$, and cut off frequency of the dominant pole ω_0. The sum of currents at the inverting input of the TIA is

$$i_\mathrm{i} = \frac{u_\mathrm{i}}{Z_\mathrm{i}(s)} + \frac{u_\mathrm{i}-u_\mathrm{o}}{Z_\mathrm{f}(s)} = \frac{u_\mathrm{i}}{\frac{1}{sC_\mathrm{i}}} + \frac{u_\mathrm{i}-u_\mathrm{o}}{\frac{1}{\frac{1}{R_\mathrm{f}}+sC_\mathrm{f}}}. \tag{2.13}$$

Here C_i includes all capacitances at the input of the operational amplifier (OP), contributed by the OP's input C_in, the diode's junction, and all parasitic capacitances. Replacing u_i according to Equation 2.12 and reordering results in the transimpedance transfer function

$$\begin{aligned} Z_\mathrm{T}(s) &= \frac{u_\mathrm{o}}{i_\mathrm{i}} \\ &= \frac{A_0\omega_0 R_\mathrm{f}}{s^2 R_\mathrm{f}(C_\mathrm{i}+C_\mathrm{f}) + s(1+\omega_0 R_\mathrm{f} C_\mathrm{f}(1+A_0)+\omega_0 R_\mathrm{f} C_\mathrm{i}) + \omega_0(1+A_0)} \\ &= A_\mathrm{Vol}(s)\frac{Z_\mathrm{f}}{1+A_\mathrm{Vol}(s)+sC_\mathrm{i}Z_\mathrm{f}}. \end{aligned} \tag{2.14}$$

We plot Z_T in Figure 2.8 for an example configuration which is a common configuration in later parts of this work. It consists of an Analog Devices

ADA4627 OP ($f_\mathrm{T} = 19\,\mathrm{MHz}, C_\mathrm{in} = 8\,\mathrm{pF}$) and a Hamamatsu S5971 photodiode ($C_\mathrm{d} = 3\,\mathrm{pF}$ at $-V_\mathrm{S} = 10\,\mathrm{V}$) with $Z_\mathrm{f} = 200\,\mathrm{k\Omega}||1\,\mathrm{pF}$. We further assume the diode current to equal $i_\mathrm{d} = 1\,\mu\mathrm{A}$, which is on the same order of magnitude as all photocurrents that this work deals with. The transimpedance transfer function Z_T shows a second-order low-pass characteristic with a corner frequency at $f_{-3\mathrm{dB}} = 1318\,\mathrm{kHz}$. When the bias voltage V_S can not be further reduced, to lower C_i, we can only raise the corner frequency by lowering R_f. There is a tradeoff with the thermal noise of R_f, though, as we will see later. When dealing with large capacitances, e.g. by large area PDs or cables between TIA and PD, additional circuitry can help to reduce the voltage swing across C_i and retain a high bandwidth [107].

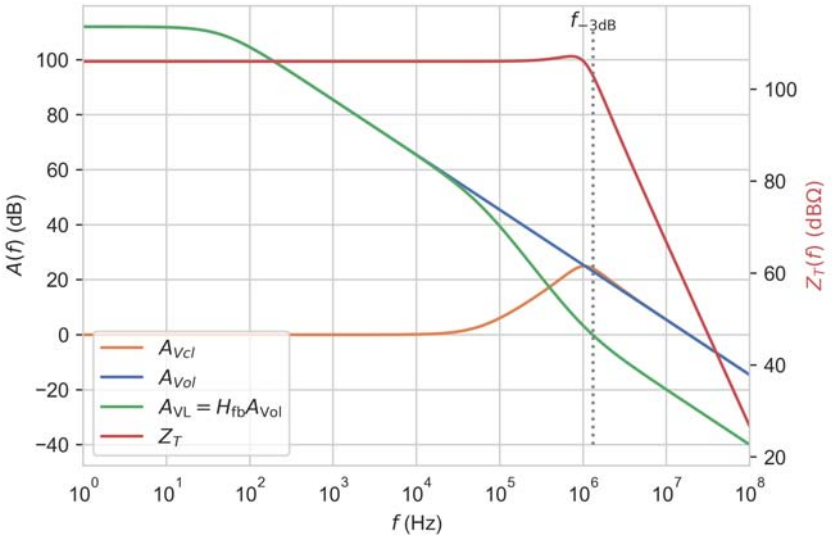

Figure 2.8: Transfer functions of transimpedance Z_T, open A_Vol and closed loop voltage A_Vcl gains, and feedback of the system A_VL. Here the OP is an ADA4627 and the PD is a Hamamatsu S5971 photodiode with $Z_\mathrm{f} = 200\,\mathrm{k\Omega}||1\,\mathrm{pF}$.

To assess the stability of the system we approach the circuit from a control systems perspective and take a look at the system's closed loop voltage gain $A_\mathrm{Vcl}(s)$. It is given by

$$A_\mathrm{Vcl}(s) = \frac{A_\mathrm{Vol}(s)}{1 + A_\mathrm{Vol}(s)H_\mathrm{fb}(s)}. \tag{2.15}$$

$H_\mathrm{fb}(s)$ denotes the feedback network's transfer function. It is given by the voltage divider, formed by Z_f and C_i. The system is stable when $A_\mathrm{VL} = A_\mathrm{Vol}H_\mathrm{fb}$

has less than 180° phase shift when it crosses unity-gain. The difference of the phase of A_{VL} to 180° is called phase margin. We aim to retain a phase margin of around 45° to prevent instability while not limiting the bandwidth. In the time domain this behavior leads to a step response with a slight overshoot. Therefore we usually need to add a zero in the transfer function. We can achieve this by using a feedback capacitor C_{f} in parallel to R_{f} which we approximate to

$$C_{\mathrm{f}} = \frac{1}{2\pi R_{\mathrm{f}} \sqrt{f_{\mathrm{T}} f_{\mathrm{RC}}}} \tag{2.16}$$

with the transition frequency f_{T} of the operational amplifier and the corner frequency of the network of the feedback resistor and the input capacitance $f_{RC} = 1/(2\pi R_{\mathrm{f}} C_{\mathrm{i}})$. We plot the magnitude and the phase margin of A_{VL} for the given example in Figure 2.9.

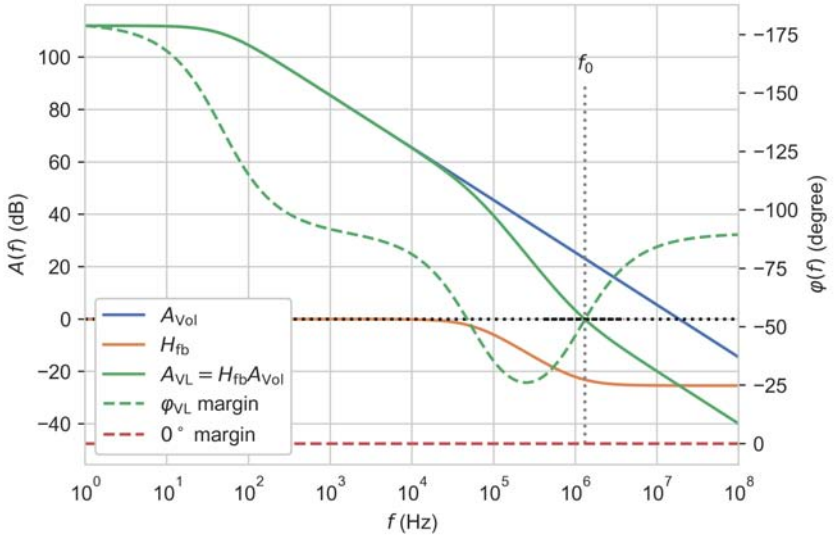

Figure 2.9: Transfer functions of open and closed loop gain. Here $C_{\mathrm{f}} = 1\,\mathrm{pF}$ for the input capacitance of $C_{\mathrm{i}} = 13\,\mathrm{pF}$. The phase margin is 52°. The secondary y-axis shows the phase margin of A_{VL}.

The SNR in this approach is fundamentally limited by the shot noise of the current from the photodiode. For a mean diode current i_{d}, the shot noise density normalized to $\sqrt{B}$ is given by $i_{\mathrm{n,shot}} = \sqrt{2qi_{\mathrm{d}}}$. A model for the noise analysis that includes $i_{\mathrm{n,shot}}$ and all following sources is shown in Figure 2.10. We calculate the optimum SNR by

$$20\log_{10}\left(\frac{i_{\mathrm{d}}}{i_{\mathrm{n,shot}}}\right) = 20\log_{10}\left(\sqrt{\frac{i_{\mathrm{d}}}{2q}}\right). \tag{2.17}$$

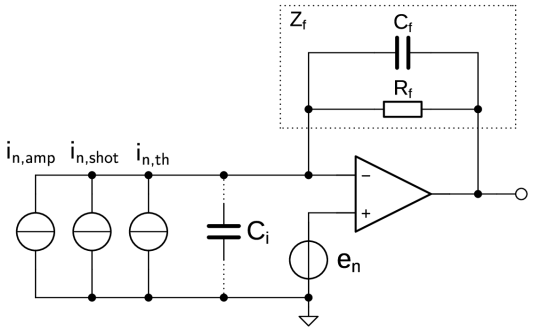

Figure 2.10: Schematic of noise sources in a simple TIA. $i_{\mathrm{n,th}}$ is the thermal noise of R_{f}. It arises in series to the resistor, but for noise analysis purposes can be modeled in parallel to the others, because of the low-impedance output of the OP.

The feedback resistor has a thermal noise density $e_{\mathrm{n,th}} = \sqrt{4kTR_{\mathrm{f}}}$ with Boltzmann's constant k and temperature T. It contributes to the input current noise density with

$$i_{\mathrm{n,th}} = \frac{e_{\mathrm{n,th}}}{R_{\mathrm{f}}} = \sqrt{\frac{4kT}{R_{\mathrm{f}}}}. \tag{2.18}$$

Setting the shot noise and the thermal noise of R_{f} equal results in

$$\begin{aligned} & i_{\mathrm{n,th}} = i_{\mathrm{n,shot}} \\ \iff & \sqrt{\frac{4kT}{R_{\mathrm{f}}}} = \sqrt{2qi_{\mathrm{d}}} \\ \iff & i_{\mathrm{d}}R_{\mathrm{f}} = \frac{2kT}{q} \approx 51\,\mathrm{mV} \end{aligned} \tag{2.19}$$

at $T = 298\,\mathrm{K}$. This means the output voltage and thereby R_{f} at a given i_{d} should be higher than 51 mV to not be limited by thermal noise. We usually aim for 0.2 to 1 V. However, the tradeoff for a higher R_{f} is the reduction in bandwidth. In the given example, R_{f} has been chosen strategically to not degrade the SNR through thermal noise by more than 0.5 dB at $u_{\mathrm{o}} = 0.2\,\mathrm{V}$.

Thermal noise, or Johnson-Nyquist noise arises in any resistance R by spontaneous voltage or current fluctuations according to

$$e_{\mathrm{n,th}} = \sqrt{4kTBR} \tag{2.20}$$

in a Thévenin equivalent circuit (noise voltage in series to ideal resistor) and

$$i_{\mathrm{n,th}} = \frac{e_{\mathrm{n,th}}}{R} = \sqrt{\frac{4kTB}{R}} \tag{2.21}$$

in the Norton equivalent circuit (noise current in parallel to ideal resistor) with Boltzmann's constant k and temperature T in a bandwidth B [112, 113]. Thermal noise is white, i.e. has a constant spectral density, for the frequencies of our interest.

The last noise source in parallel to the input signal is the amplifier input current noise $i_{\mathrm{n,amp}}$, which we add to the other current noise sources. The amplifiers input voltage noise $e_{\mathrm{n,amp}}$ is special in that it is placed across the input capacitance and therefore contributes a current $i_{\mathrm{n,e}} = sC_{\mathrm{i}}e_{\mathrm{n,amp}}$. This current density rises linearly with the frequency and is only limited by the overall gain of the system. In many implementations this leads to a noise peaking near the transimpedance's corner frequency $f_{-3\mathrm{dB}}$. We plot all noise sources, including the resulting overall noise for the given example configuration and for $i_{\mathrm{d}} = 1\,\mu\mathrm{A}$ in Figure 2.11.[1] We see $i_{\mathrm{n,e}}$ rising with f and dominating above $f_{-3\mathrm{dB}}$. Implementing a consecutive low-pass filter is generally recommended to mitigate the effects of noise peaking. In the pass-band shot noise dominates, down to low frequencies, when 1/f noise components of the OP rise above the shot noise level. This is one of the reasons for using lock-in amplification (see the following Section 2.2).

All these considerations lead to criteria for the selection of the OP. First, we want to stay shot noise-limited, i.e. the OP's input-referred voltage and current noise densities should be well below the thermal noise of R_{f}. At low diode currents, which we are dealing with here, this usually limits the choice to field-effect-transistor (FET) based OPs. Their inputs typically feature high input impedances, which in consequence have low input currents. Since input current noise originates from shot noise of the input current, this noise contribution is usually lower in FET-based OPs.[2] Additionally, $e_{\mathrm{n,amp}}$ should be low enough, so $i_{\mathrm{n,e}} = sC_{\mathrm{i}}e_{\mathrm{n,amp}}$ does not rise above shot noise within the desired bandwidth.

[1] All noise sources here are uncorrelated and thereby add in a root-mean-square sense.
[2] Beware of high GBW FET-based OPs, like the OPA858, in high bandwidth applications. The transistors parasitic capacitances to drain, source, and substrate reduce the impedance towards higher frequencies. i_{n} rises above that of comparable bipolar OPs in the range of 10–100 MHz.

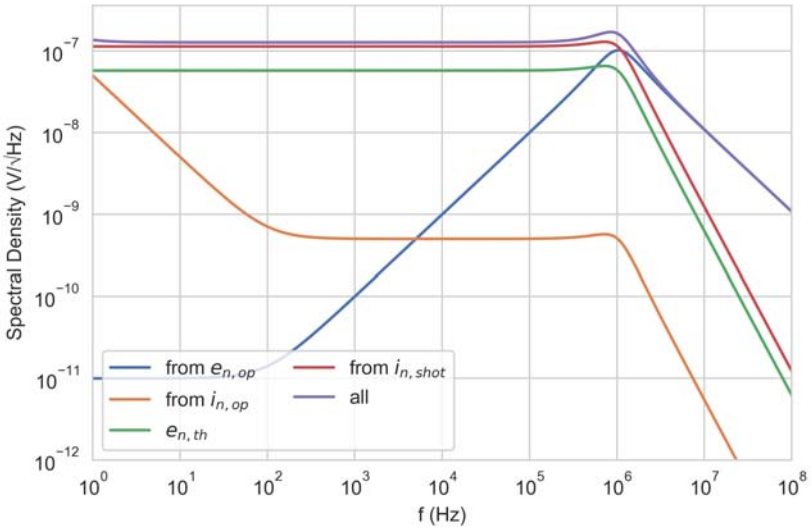

Figure 2.11: Noise at the output of the transimpedance amplifier. The OP is an ADA4627 and the PD is a Hamamatsu S5971 with $Z_\mathrm{f} = 200\,\mathrm{k\Omega}||1\,\mathrm{pF}$, operated at $i_\mathrm{d} = 1\,\mu\mathrm{A}$.

In Figure 2.12, we show the output noise spectral density of an implementation of the TIA we analyzed so far. We compare the simulation to a measurement for the dark case and a photocurrent at which shot noise dominates. We find a good agreement of the simulation to the data. A rising noise floor towards lower frequencies in the case with illumination can be attributed to the current source, used to drive the LED, we used for illumination. We can use these two measurements to estimate the bandwidth of the transimpedance Z_T. The power spectral density at illumination e_n^2 is given by

$$e_\mathrm{n}^2 = e_0^2 + 2qi_\mathrm{d}Z_\mathrm{T}^2, \tag{2.22}$$

with the spectral density in dark e_0^2. The second term is the additional shot noise, which is spectrally white and can thereby be used to estimate the transimpedance at high frequencies.[3] We denote the estimation of the transimpedance from the measurements by $\tilde{Z}_\mathrm{T}$, which we determine by a fit to the data, after calculating Equation 2.22. $\tilde{Z}_\mathrm{T}$ is shown in the lower panel of Figure 2.12, where we find a 3 dB corner frequency of 500 kHz.

In the example in Figure 2.11, 1/f noise of the input current dominates at

[3] Other methods, like a test adapter which feeds a test current into the TIA's summing junction have to compensate for parasitic capacitances [114]. This makes the measurement potentially unreliable at high frequencies. A high DC accuracy is, however, easier to achieve.

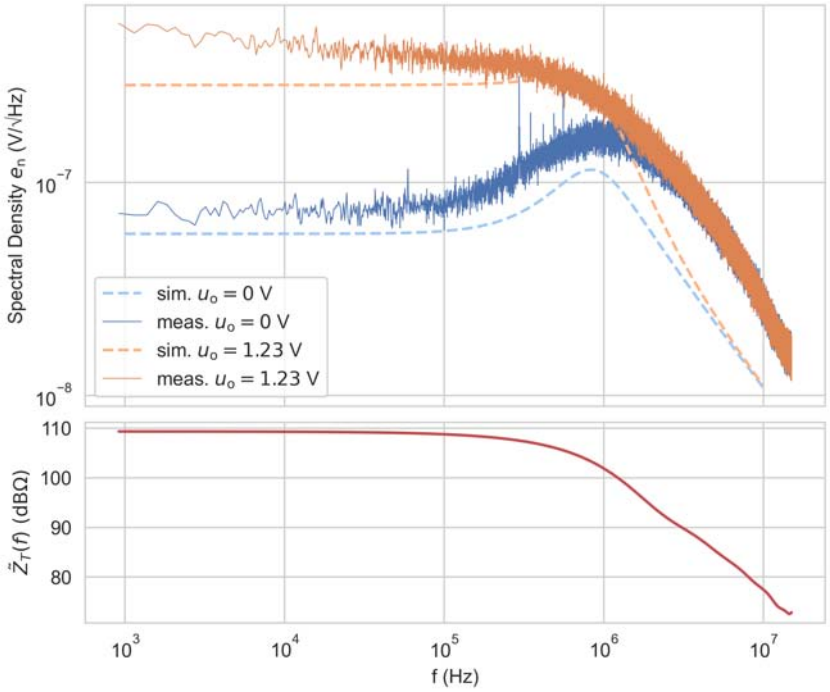

Figure 2.12: Comparison of TIA output noise spectral densities at $u_0 = 0\,\mathrm{V}$ and $u_0 = 1.23\,\mathrm{V}$.

frequencies below 1 Hz. Other electronic components in the signal chain may also introduce their own 1/f noise or show drift behavior through variation in temperature, supply voltage, and by ageing. In the following section we will introduce a concept to counteract the influence of these noise components.

2.2 Lock-In Amplifiers

We have seen in the previous chapter that the noise components of an optical detector usually include 1/f components. These components include drift and instabilities on long time-scales. In fact, all electrical components in the excitation and detection signal processing may be prone to 1/f noise. As they are usually uncorrelated, these contributions add up in quadrature and may seriously degrade the SNR of the measurement. A solution to this is the use of homodyne detection with lock-in amplifiers (LIA). The concept is simple: Shift the measurement from DC to a frequency band which lies in the white noise region. Being able to freely choose the frequency range has the added benefit of being able to avoid technical noise sources that may be present anyway, like the mains frequency at 50 or 60 Hz, switch mode power supplies, or

mobile communication systems. In Figure 2.13 we show a qualitative noise spectrum where the lock-in frequency at which the experiment is excited is chosen to lie within the white noise region. The transmission window, which we explain later, avoids any narrow-band distortions. It is obvious that the lock-in frequency can be chosen freely within the white noise region without impact on the SNR, except for any additional interferences.

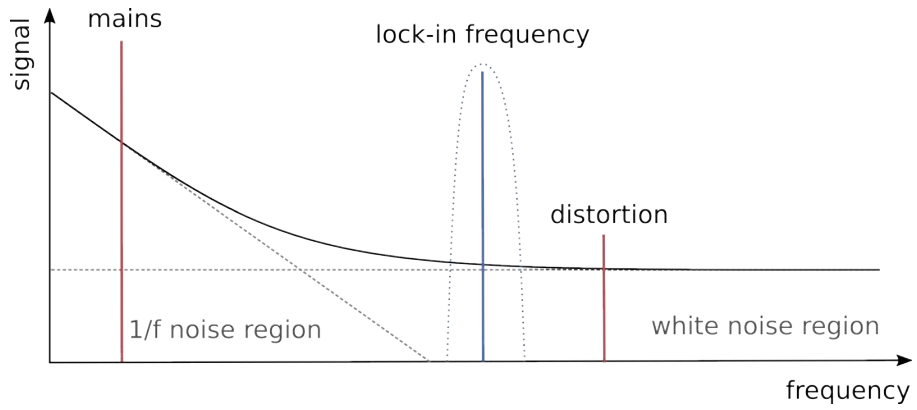

Figure 2.13: Qualitative noise spectrum. The lock-in or excitation frequency of the experiment is chosen to lie within the white noise region and avoid distortions.

Another possible solution is the use of chopper- or auto-zero-amplifiers. They are built upon the same principles as lock-in amplifiers and thereby come with their own set of limitations, like lower bandwidth than comparable OPs. This also means they are prone to intermodulation products and harmonic components at the output. Also, drift in optical alignment and gain of electrical components can not be avoided by these fixed-function integrated circuits.

2.2.1 Theory of Operation

In Figure 2.14 we show the general concept of a dual-phase LIA. In this case an internal oscillator drives the internal mixers as well as the externally connected experiment. Usually, the internal oscillator has to be locked-in to an external oscillator, e.g. via the measurement signal itself and a phase-locked loop (PLL). This gives the LIA its name. In the experiments we are concerned with here, this is not necessary. We are only interested in the LIAs ability to shift the measurement away from baseband.

In general a LIA features two phase-sensitive detectors (PSDs), each composed of a mixer and a low-pass filter. They are driven by the reference signal,

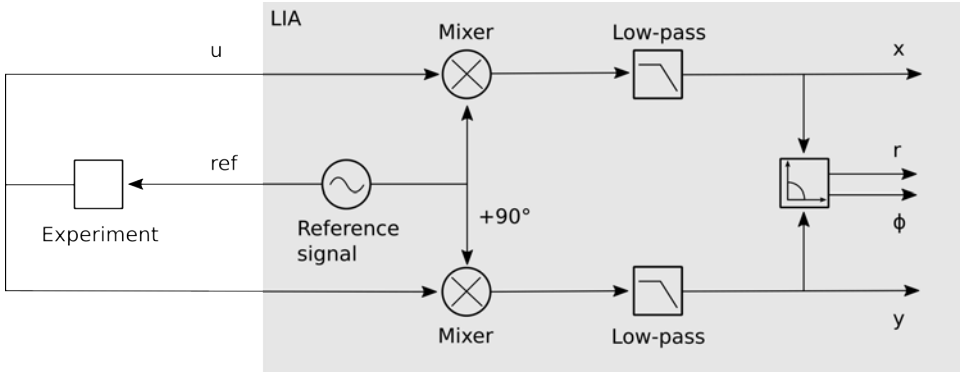

Figure 2.14: Schematic of a dual-phase LIA. The internal oscillator drives the mixers, as well as the connected experiment. Mixer and low-pass filter in series constitute a phase-sensitive detector. Two PSDs, where one is driven by the reference, shifted by 90°, allow the vector representation of the input signal as in-phase x and quadrature y.

shifted by either 0° or 90°. This is equal to homodyne detection, demodulating the signal in a bandwidth, set by the low-pass filter, around the reference frequency $\omega_\mathrm{r} = 2\pi f_\mathrm{r}$. The resulting signals are denoted as in-phase $x(t)$ and quadrature $y(t)$, given by

$$\begin{aligned} x(t) &= \langle u(t)\cos(\omega_\mathrm{r} t)\rangle \\ y(t) &= \langle u(t)\sin(\omega_\mathrm{r} t)\rangle \end{aligned} \tag{2.23}$$

with the input signal $u(t)$, which is the experiments output. Here $\langle\cdot\rangle$ denotes the averaging by the low-pass filter. With $u(t) = a\cos(\omega_\mathrm{r} t + \phi)$ and a and ϕ being functions of the experiment we can write

$$\begin{aligned} x &= \langle a\cos(\omega_\mathrm{r} t + \phi)\cos(\omega_\mathrm{r} t)\rangle \\ &= \langle \frac{a}{2}\Big(\cos(\phi) + \cos(2\omega_\mathrm{r} t + \phi)\Big)\rangle \\ &= \langle \frac{a}{2}\cos(\phi)\rangle. \end{aligned} \tag{2.24}$$

The low-pass filter effectively removes the component at twice the reference frequency f_r. This is usually the case, because we choose the bandwidth of the low-pass filter lower than f_r. Analogous we can write $y = \langle \frac{a}{2}\sin(-\phi)\rangle$. More importantly, the low-pass filter sets the bandwidth of the measurement itself. There is always the tradeoff between bandwidth and noise, and we can tune the filter to the requirements of the measurement. This is a special case, where the experiment's output is a time-invariant scaled and shifted copy of

the reference signal. More generally $a(t)$ and $\phi(t)$ are functions of time, making $u(t)$ a potentially wider bandwidth signal. The phase-sensitive detection then acts like a transmission window, i.e. a band-pass filter with high Q-factor, around the reference frequency f_r. We show this in Figure 2.13 as an equivalent band-pass filter about f_r. Mixing with orthogonal functions also enables us to represent the input signal as a vector $l(t) = x(t) + jy(t) = r(t)e^{j\phi(t)}$ with

$$r = \sqrt{x^2 + y^2}, \quad \phi = \tan^{-1}\Big(\frac{y}{x}\Big). \tag{2.25}$$

The inverse tangent is usually implemented by the two-argument arctangent, which maps to the value range $\phi \in]-\pi, +\pi]$.

In the frequency domain, this process of mixing and subsequent low-pass filtering can be written as

$$\begin{aligned} L(f) &= \mathcal{F}\{u(t)\cos(2\pi f_\mathrm{r} t)\} H_\mathrm{lpf}(j2\pi f) \\ &= U(f) * \frac{1}{2}\Big(\delta(f - f_\mathrm{r}) + \delta(f + f_\mathrm{r})\Big) H_\mathrm{lpf}(j2\pi f) \end{aligned} \tag{2.26}$$

where $*$ denotes the convolution and $H_\mathrm{lpf}(j\omega)$ is the transfer function of the low-pass filter.[4] Again, the low-pass filter not only suppresses the higher frequency component, but also acts like a transmission window, centered around f_r. For the simple example of $u(t) = a\cos(2\pi f_\mathrm{r} t + \phi)$, the result is

$$\begin{aligned} L(f) &= \mathcal{F}\{\cos(2\pi f_\mathrm{r} t) a\cos(2\pi f_\mathrm{r} t + \phi)\} H_\mathrm{lpf}(j2\pi f) \\ &= a\mathcal{F}\{\cos(2\pi f_\mathrm{r} t)\} * \mathcal{F}\{\cos(2\pi f_\mathrm{r} t + \phi)\} H_\mathrm{lpf}(j2\pi f) \\ &= \frac{a}{4}\Big(\underbrace{\delta(f - 2f_\mathrm{r})}_{=0 \text{ by } H_\mathrm{lpf}} + 2\delta(f) + \underbrace{\delta(f + 2f_\mathrm{r})}_{=0 \text{ by } H_\mathrm{lpf}}\Big) e^{j\phi} H_\mathrm{lpf}(j2\pi f) \\ &= \frac{a}{2}\delta(f) e^{j\phi} \ , \end{aligned} \tag{2.27}$$

assuming $H_\mathrm{lpf}(0) = 1$, which evaluated at $f = 0$ gives

$$L(f) = \frac{a}{2}\cos(\phi) + j\frac{a}{2}\sin(\phi) \ . \tag{2.28}$$

We find the same in-phase and quadrature representation for the single cosine wave input signal as in the time domain approach. In real world applications, where $a(t)$ and $\phi(t)$ are functions of time, the base band signal is bandwidth

[4] We define the Fourier transform $\mathcal{F}\{\cdot\}$ as $\mathcal{F}\{x\} = \int_{-\infty}^{\infty} x(t) e^{-j2\pi f t}\, dt$, where f is the frequency and t is the time.

limited by $H_{\mathrm{lpf}}(j2\pi f)$. In our application, a magnetic field causes a change in fluorescence intensity, resulting in an amplitude modulation of the reference signal. The measurement quantity $a(t)$ is directly proportional to the value of the calibration curve (see Figure 2.2) which is a function of the magnetic field. We will find a use of $\phi(t)$ in a later chapter.

For $H_{\mathrm{lpf}}(j2\pi f)$, we commonly use a cascade of n equal first-order low-pass filters

$$H_{\mathrm{lpf}}(j\omega) = \left(\frac{1}{1+j\omega\tau}\right)^n, \tag{2.29}$$

where the time constant τ relates to the cut-off frequency by $f_{\mathrm{c}} = \frac{1}{2\pi\tau}$. Each order introduces a 20 dB per decade roll-off above f_{c}, approaching a brick-wall filter behavior with rising n. Care has to be taken when the phase shift is of importance, because each order introduces an additional $-90°$ towards high frequencies. When the phase is used as a measurement quantity, the absolute value might need to be corrected for the shift $\arg\Big(H_{\mathrm{lpf}}(j\omega)\Big)$. If the signal was used as a part of a control loop, higher orders can introduce instability in the feedback loop and necessitate a slower feedback response, meaning a lower f_{c}. In the time domain we may be interested in the settling time of the filter, which directly relates to it's order and phase shift. A system's settling time is the time elapsed from an instantaneous step input to the time at which the output has settled to within a specified error band around the steady-state condition. It can be calculated, using the step response $g(t)$ of the system. For a cascade of n first order filters, we start with the impulse response, given by the inverse Laplace-transform $\mathcal{L}^{-1}\{\cdot\}$ of the transfer function

$$h(t) = \mathcal{L}^{-1}\left\{\left(\frac{\omega_{\mathrm{c}}}{(\omega_{\mathrm{c}}+s)}\right)^n\right\} = \frac{(\omega_{\mathrm{c}}t)^{n-1}}{(n-1)!}\omega_c e^{-\omega_{\mathrm{c}}t}u(t), \tag{2.30}$$

with the Heaviside step function $u(t)$ and the corner frequency $\omega_{\mathrm{c}} = 2\pi f_{\mathrm{c}}$ [115]. The step response is given by the integration of $h(t)$ with respect to time

$$g(t) = \int_{-\infty}^{t} h(\tau)d\tau = \left(1 - e^{-\omega_{\mathrm{c}}t}\sum_{k=0}^{n-1}\frac{(\omega_{\mathrm{c}}t)^k}{k!}\right)u(t)\ . \tag{2.31}$$

Knowing the step response of such a filter approaches it's steady-state output asymptotically, we can use the step response to compute the settling times to within certain percentages of the final value. We show some example values

Order	Settling times				Bandwidths		
n	50%	90%	99%	99.9%	$f_{-3\,\mathrm{dB}}$	$ENBW$	$\frac{ENBW}{f_{-3\,\mathrm{dB}}}$
1	0.69	2.30	4.61	6.91	0.159	0.248	1.56
2	1.68	3.89	6.64	9.23	0.102	0.125	1.22
3	2.67	5.32	8.41	11.23	0.081	0.094	1.16
4	3.67	6.68	10.05	13.06	0.069	0.078	1.13
5	4.67	7.99	11.60	14.79	0.061	0.068	1.12
6	5.67	9.27	13.11	16.45	0.056	0.062	1.11
7	6.67	10.53	14.57	18.06	0.051	0.056	1.10
8	7.67	11.77	16.00	19.63	0.048	0.052	1.10
9	8.67	12.99	17.40	21.16	0.045	0.049	1.09
10	9.67	14.21	18.78	22.66	0.043	0.046	1.09

Table 2.1: Settling times and bandwidths as function of filter order. We show values for a cascade of first order low-pass filters, which may differ from those of a single nth order filter. Settling times are given in multiples of the filter's time constant τ. Bandwidths are multiples of $2\pi f_c$, except for the ratio $ENBW/f_{-3\,\mathrm{dB}}$.

for different filter orders in Table 2.1. Higher filter orders are associated with larger settling times, which is a natural consequence of the attenuation of higher frequency signal content and has to be accounted for when aiming for accurate measurements.

Another important application for lock-in techniques is spectrally resolved noise measurement [116]. For accurate results, we have to be aware of the low-pass filter's noise transmission behavior, which is characterized by the equivalent noise bandwidth ($ENBW$). From a given frequency response $H(j\omega)$, we can determine the $ENBW$, which is the bandwidth of an ideal brick-wall filter that transmits the same white noise power by [117]

$$ENBW = \frac{1}{2\pi}\int_0^\infty \left|\frac{H(j\omega)}{\max H(j\omega)}\right|^2 d\omega \,. \tag{2.32}$$

In Table 2.1, we show the corresponding equivalent noise bandwidths and their relation to the filter bandwidths $f_{-3\,\mathrm{dB}}$. We find the noise transmission behavior approaches that of the brick-wall filter with rising order, since the

ratio of $ENBW/f_{-3\,\mathrm{dB}}$ approaches 1.[5]

More complex filter topologies are possible, for which comparable considerations apply. We may be interested in a steeper roll-off and use a Chebyshev or elliptic filter, in tradeoff for higher passband or stopband ripple. In all cases the bandwidth has to be chosen high enough to transmit the desired signal content, with acceptable phase shift and settling time, while limiting the transmitted noise power.

2.2.2 Noise and Sensitivity

An important figure of merit for any magnetic field sensor is the sensitivity

$$s = \delta B_{\mathrm{min}} \sqrt{\tau} \,, \tag{2.33}$$

which describes the minimum magnetic field strength δB_{min} which can still be resolved in a measurement time τ, resulting in an output SNR of 1. Usually, s is a function of signal frequency, when the signal response or noise sources are not constant in the frequency domain, meaning they are not white noise components. Additionally, in our case of all-optical magnetometry with NV centers, s depends on the absolute magnetic field, since the sensitivity is directly proportional to the derivative of the calibration curve (see Figure 2.2).

Shot noise sets a lower bound to the achievable sensitivities in the presented setup. It arises in optical devices due to fluctuations in the number of photons detected per time because they occur independently of each other. In the following we will determine the resulting shot noise limited sensitivity (SNLS) for all-optical setups. Shot noise is white, showing a spectral density of $S(f) = 2q|i_{\mathrm{d}}|$, so we will only focus on the absolute magnetic field dependency. In later measurements, we will also investigate frequency dependency. To determine the impact of shot noise on intensity- or phase-based all-optical systems, first, the influence of noise on amplitude and phase in general has to be determined. The following considerations are based on [119, 120, 121]. We include the phase as a measurement quantity for reasons that will become clear in a later chapter.

[5] The same considerations apply to window functions (tapers), which are applied for estimation of a signal's power spectral density. Calculating the density from the power spectrum needs to account for the window's ENBW. See [118] for more details.

A lock-in amplifier output signal can be considered to be

$$l(t) = x(t) + jy(t) = r(t)e^{j\phi(t)} \tag{2.34}$$

with in-phase $x(t)$ and quadrature $y(t)$ components or amplitude $r(t)$ and phase $\phi(t)$. For each component, the mean and standard deviation are given by μ and σ, subscripted by the component name. The output is considered to be the response of a homodyne detector to a sinusoidal signal with additional noise. It can be assumed that the noise components of in-phase and quadrature are

1. Gaussian random processes with zero-mean, normal distributions,
2. statistically independent, and
3. contain identical energy, i.e. $\sigma_x = \sigma_y = \sigma$.

with the parameter $\mu = \sqrt{\mu_x^2 + \mu_y^2}$, the amplitude is then described by the Rician distribution

$$f(r) = \frac{r}{\sigma^2} e^{-\frac{r^2+\mu^2}{2\sigma^2}} I_0\left(\frac{r\mu}{\sigma^2}\right), \qquad r \geq 0 \tag{2.35}$$

with the modified Bessel function of the first kind with order zero I_0. The phase distribution is given by

$$f(\phi) = \frac{e^{-\frac{\mu^2}{2\sigma^2}}}{2\pi}\left(1 + \frac{\mu}{\sigma}\sqrt{\frac{\pi}{2}}\operatorname{erfcx}\left(-\frac{\mu}{\sigma}\sqrt{2}\cos(\phi-\theta)\right)\right), \qquad -\pi \leq \phi \leq \pi \tag{2.36}$$

with $\theta = \tan^{-1}(\mu_y/\mu_x)$ and the scaled complementary error function erfcx. While for the amplitude distribution the mean μ_r and standard deviation σ_r are well defined, there are no closed-form formulas for the phase distribution. Hence, in this work, they are obtained computationally by $\mu_\phi = \int_{-\infty}^{\infty} \phi f(\phi) d\phi$ and $\sigma_\phi^2 = \int_{-\infty}^{\infty} \phi^2 f(\phi) d\phi - \mu_\phi^2$. When numerically evaluating Equation 2.36 the nature of the erfcx function necessitates an arbitrary-precision floating-point arithmetic library, like mpmath [122].

In the given application, the photodiode's output current i_{rms} is rectangular with a DC offset $i_{\text{DC}} = i_{\text{rms}}/\sqrt{2}$ and an AC component $i_{\text{AC}} = i_{\text{rms}}/\sqrt{2}$. We define μ as the mean of the lock-in DC indication, so $\mu = i_{\text{AC}}$, if the PSD responds to the whole AC component. This may occur when the input signal

is demodulated by another waveform than a single harmonic sine wave, which is true for the square wave PSD in a later section. Later, we will also see applications in which the signal is composed of a DC offset i_{DC} and sine wave AC component of amplitude i_{AC}, resulting in a root-mean-square current $i_{\mathrm{rms}} = \sqrt{i_{\mathrm{DC}}^2 + \frac{i_{\mathrm{AC}}^2}{2}}$. In that case, we would get a mean of $\mu = i_{\mathrm{AC}}/\sqrt{2}$. In general, the shot noise density is then given by $i_{\mathrm{sn}} = \sqrt{2qi_{\mathrm{rms}}}$ with the elementary charge q. With $\sigma = i_{\mathrm{sn}}$, the shot noise limited sensitivity for the magnitude can then be defined as

$$s_{r,\mathrm{snl}} = \left| \frac{\delta r(B)}{\delta B} i_{\mathrm{AC}} \right|^{-1} \sigma_r \tag{2.37}$$

in units of $\mathrm{T}/\sqrt{\mathrm{Hz}}$. Here $r(B) = |H_r(s = j\omega, B)|$ is the calibration curve, which is the change in magnitude relative to the case of $B = 0$ at a fixed excitation frequency $\omega = 2\pi f$. Similarly the SNLS for the phase as a measurement quantity is given by

$$s_{\phi,\mathrm{snl}} = \left| \frac{\delta \phi(B)}{\delta B} \right|^{-1} \sigma_\phi \tag{2.38}$$

with $\phi(B) = \angle H_r(s = j\omega, B)$. Please note that in the last steps σ_r and σ_ϕ are spectral densities instead of RMS values. The argument stays valid because the shot noise is white, i.e. constant over frequency.

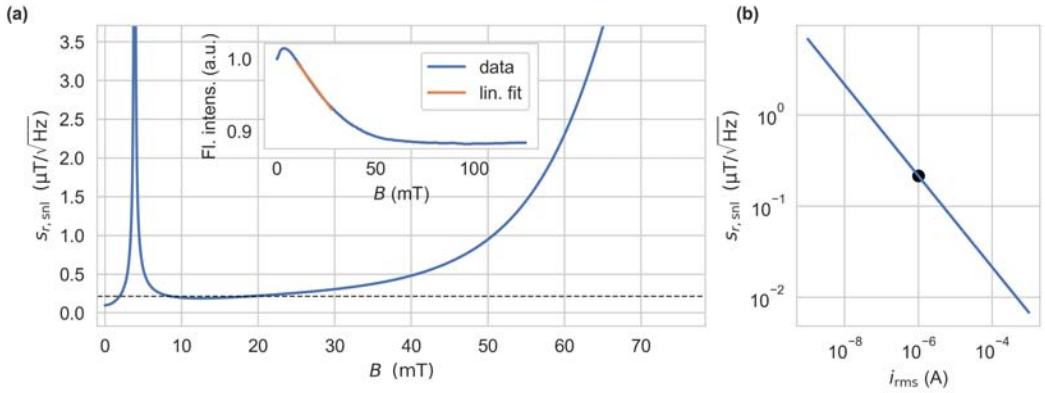

Figure 2.15: (**a**) Shot noise limited sensitivity $s_{r,\mathrm{snl}}$, using the vector length component of a LIA r, as a function of the magnetic field ($i_{\mathrm{rms}} = 1\,\mu\mathrm{A}$). The inset shows the relative fluorescence intensity in the same magnetic field range. (**b**) Shot noise limited sensitivity $s_{r,\mathrm{snl}}$ with the linear fit from the inset in (a) as a function of the photocurrent.

In Figure 2.15a, we show the shot noise limited sensitivity, when using the fluorescence intensity as measurement quantity. We chose $i_{\mathrm{rms}} = 1\,\mu\mathrm{A}$ for this

example. From Equation 2.37, we know the sensitivity is directly proportional to the derivative of the calibration curve, that is shown in the figure's inset. We often use the linear fit to the calibration curve in the range of 10 to 20 mT, where a low sensitivity, coupled with a high magnetic bandwidth is given. Note that a lower sensitivity means the measurement is less noisy, which is of course preferred. For this case, the dashed line in Figure 2.15a indicates the resulting sensitivity of $0.215\,\mu\mathrm{T}/\sqrt{\mathrm{Hz}}$. We show the same value in the dot in Figure 2.15b, where we sweep the photodiode current and plot the resulting SNLS. We neglect the change in magnetic contrast with varying optical excitation powers, necessary for varying photocurrents. A 10-fold decrease in $s_{r,\mathrm{snl}}$ needs a 100-fold increase in photodiode current, which conforms to the consideration that the SNR improves with $\sqrt{N}$ when getting N more photons per time.

2.3 Square Wave Phase-Sensitive Detection

While commercial solutions for lock-in amplification are widely available, they usually come as laboratory test and measurement equipment. For many applications a less cost prohibitive and easier to integrate solution is required. This motivates the following section, in which we develop an evaluation circuitry that is tailored towards the application of all-optical NV-based magnetometry. In this section, we focus on the evaluation electronics, where the laser driver input and the TIA output form the all-electric interface.

The major simplification of our circuitry compared to commercial LIAs is the use of a single phase phase sensitive detector (PSD), combined with a square wave excitation and synchronous-rectification. A single phase is sufficient, because we expect no change of the phase difference between excitation and fluorescence emission. As becomes evident in a later chapter this holds true only for low reference frequencies, meaning $f_\mathrm{r} \ll 1\,\mathrm{MHz}$, which we base our design on. We are only interested in the magnetic field dependent change of the fluorescence intensity. With a single phase PSD, we have to adjust the phase offset ϕ_r to bring the signal $u(t)$ and reference $ref(t)$ in phase at the multiplier and thereby the DC indication of the PSD to a maximum. This compensates for the signal runtime in the connected experiment. The PSD output will then follow signal amplitude variations, given that the PSD's low-pass filter has a high enough bandwidth to transmit these variations.

Square wave excitation and synchronous-rectification allow for a simpler implementation, compared to a single harmonic frequency. In this case the multiplication process can be done by a simple phase-reversal switch, followed by a difference amplifier. We have to be aware of the additional transmission windows at odd harmonics. The reference signal

$$ref(t) = \begin{cases} 1 & \text{if } 0 < t < \frac{T_\mathrm{r}}{2} \\ -1 & \text{if } -\frac{T_\mathrm{r}}{2} < t < 0 \end{cases} \tag{2.39}$$

with period T_r can be described by the fourier series

$$ref(t) = \sum_{n=1,3,5,\ldots}^{\infty} \frac{4}{\pi n} \sin(n\omega_\mathrm{r} t) \tag{2.40}$$

with $\omega_\mathrm{r} = 2\pi f_\mathrm{r} = 2\pi/T_\mathrm{r}$. The PSD then effectively demodulates the signal components at the odd harmonics, scaled by the inverse of the harmonic order. Assuming that the input signal has only signal content at ω_r and has otherwise additive white Gaussian noise, we get only additional noise contributions from the odd harmonic transmission windows. The noise contributions from these windows are uncorrelated and thereby add as the sum of powers, increasing the RMS noise by $\sqrt{1 + \frac{1}{3^2} + \frac{1}{5^2} + \ldots} = \sqrt{\frac{\pi^2}{8}}$ [123]. For this case of white noise and no additive disturbances in the transmission windows, the noise effectively increases by $\approx 11\%$, decreasing the SNR by 0.91 dB. In our case, the TIA's output signal may also contain higher order signal components next to the fundamental frequency when the TIA's bandwidth is able to pass them. The higher order harmonics add coherently, making this SNR penalty a worst case scenario.

2.3.1 First Implementation

In contrast to the common approach of digitizing the response signal and post processing it digitally, a pure analog implementation is presented. This decision is driven by a lower cost, a smaller footprint and a lower power consumption compared to a system with a Field Programmable Gate Array or Digital Signal Processor, found in recent commercial implementations.

We set a few requirements, this implementation has to comply with. A usable bandwidth for the detection of magnetic field changes around 10 kHz is

required. This bandwidth originates in the application of current sensing in electric vehicles (EV). For a precise estimation of the battery's state of charge, high-frequency ripple in an EVs power electronics has to be captured [124]. Furthermore, we want to be able to change the reference frequency at which the measurement is done in the range of 25 to 500 kHz. We want to position a 20 kHz wide window in this frequency range, which enables us not only to avoid 1/f noise, but also other noise sources. These might vary in bandwidth and intensity, depending on the application. For example, current sensing in an automotive application might have to deal with the switching frequency of the power electronics and its harmonics, which can vary between models and manufacturers. With the ability to change the reference frequency in the given range, there is enough flexibility to react to the environment of the application.

Circuit decription

In Figure 2.16a, we show the schematic of the first generation square wave PSD. A STM32G031 microcontroller unit (MCU) controls the externally connected laser driver via pulse width modulation (PWM), using a first timer peripheral *Timer 1*. The timer's frequency can be varied within the required bandwidth and the duty cycle is usually set to 50%. A second timer peripheral *Timer 2* runs at the same frequency and a variable phase offset to *Timer 1*, driving the synchronous rectifier. They are also referred to as excitation and demodulation timers. The phase offset enables us to compensate any delays introduced by the electrical and optical components to maximize the output of the phase sensitive detector (PSD). The timers run at a base clock frequency of 128 MHz which leads to a resolution in the time difference of 7.8125 ns. At the maximum reference frequency $f_\mathrm{r} = 500\,\mathrm{kHz}$ we use here, this leads to effectively 8 bits of resolution in phase. In our setups we usually deal with delays of around $\tau = 100\,\mathrm{ns}$ to $300\,\mathrm{ns}$ between the excitation and the received fluorescence signal. We measure the delays between the respective rising edges. The exact delay values depend on the configuration of the electronics and the length of the optical fiber.

The synchronous-rectifier (SR) consists of an ADA4000 operational amplifier in a difference amplifier configuration. It switches between gains $G_\mathrm{PSD} = 1$ and $G_\mathrm{PSD} = -1$ using monolithic analog single-pole/double-throw (SPDT) switches (DG419, Analog Devices), which are driven by opposite polarity sig-

nals (see Figure 2.16b). The PSD is made of the SR and a following 4th-order Butterworth low-pass filter. The input signal from the experiment is high-pass filtered, to remove the DC offset and increase the out-of-phase-rejection at lower frequencies. All filters and the SR are implemented using the same quad operational amplifier. The signal is then fed to the PSD and digitized by a 12-bit analog-to-digital converter (ADC) at a sampling rate of up to $f_\mathrm{S} = 144\,\mathrm{kHz}$ including 8 times oversampling. The ADC adds not cost since it is an integrated peripheral of the MCU. Data is streamed to a personal computer via a CP2102N USB to UART bridge.

Out-of-phase-rejection characterizes the ability of a phase-sensitive detector to deliver accurate results at the presence of signals, outside the transmission window. While asynchronous signal content is not demodulated and thereby rejected, it can lead to non-linearity, e.g. by distortion and clipping in the input stage [123].

To utilize the ADC's full scale range (FSR), we need to introduce gain at some point. We do this as early as possible in a stage between the TIA and our circuitry, commonly in a cable driver OP. This minimizes the impact of the following stages on the SNR. When aiming for a 3 V DC signal at the ADC, leaving some head room to the FSR of 3.3 V, and knowing that the SR produces the average rectified value (ARV), the input before the high-pass has to be at $U_\mathrm{i} = 6\,\mathrm{V_{pp}}$. This assumes the signals to be rectangular, i.e. a duty cycle of 50%. This signal's RMS voltage is then $\frac{U_\mathrm{i}}{\sqrt{2}} = 4.24\,\mathrm{V_{rms}}$. We aim to not degrade the performance by choosing a feedback resistance in the TIA of R_f, that leads to a dominant thermal noise. We have shown before, that to be shot-noise-limited we want an RMS output voltage of at least $U_\mathrm{out} = i_\mathrm{d} R_\mathrm{f} = 0.2\,\mathrm{V}$. So, we implement a gain of $G = 20$ at the TIA output. If this amplification was not given, the gain could be optionally implemented in the high-pass filter.

Characterization

First, we take a look at the individual building blocks of the circuit. At the input we use a second order Butterworth high-pass filter (hpf), composed of one OP in a Sallen-Key topology. We set the cut-off frequency to $f_{-3\mathrm{dB}} = 16\,\mathrm{kHz}$. This conforms to the set requirements because we need to be able

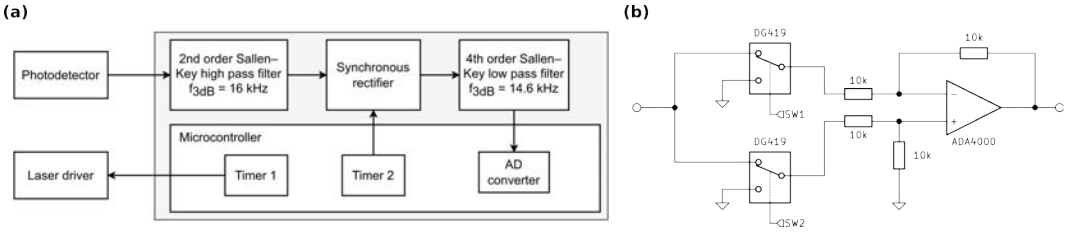

Figure 2.16: (**a**) Schematic of a first generation square wave PSD. (**b**) Detailed schematic of the synchronous-rectifier implementation.

to pass the lower sideband around the reference frequency f_r at the lowest value of f_r. Towards higher frequencies the bandwidth is limited by the OP with its Gain Bandwidth Product $GBP = 5\,\mathrm{MHz}$. The Bode-plot of this configuration is shown in Figure 2.17a. In Figure 2.17b, we show the output-referred intrinsic noise of this filter as well as an exemplary noise density from a TIA, as we analyzed it in 2.1.4, multiplied with the gain of this stage. The TIA is the dominant noise contributor in the frequency range of 0.5 kHz to 30 MHz. Alternatively, we could configure this stage as a band-pass filter. This would be advisable when the TIA showed significant noise peaking at its upper frequency end or if there were other high frequency noise sources, which should be attenuated.

When we want to estimate the range of photocurrents i_d, for which the TIA stays the dominant factor, we have to take a few assumptions. First we aim to be shot-noise-limited, i.e. the only noise contribution we need to worry about is the shot noise $i_\mathrm{n,shot} = \sqrt{2qi_\mathrm{d}}$. We also saw that we need to add a gain of $G \approx 20$ for our example, to ensure minimal noise contribution of the following stages and utilize the ADC's FSR. The gain is accounted for, but expected to be implemented at the TIA buffer in front of the high-pass filter. We also aim to use the TIA in a frequency range, low enough, so that the transimpedance is given by the feedback resistance. The output voltage noise of the TIA, which is the input noise of the high-pass, can then be written as $e_\mathrm{n,TIA} = \sqrt{2qi_\mathrm{d}}R_\mathrm{f}G$. We set it equal to the output noise of the high-pass $e_\mathrm{n,hpf}$ to find the point at which the SNR is down by 3 dB. We can then write

$$i_\mathrm{d} = 2q\frac{(U_\mathrm{out}G)^2}{e_\mathrm{n,hpf}^2}, \tag{2.41}$$

which is approximately 5.3 mA for our case at frequencies up to 100 kHz. Above

100 kHz, the permissible photocurrent rises to 20 mA, because the noise contribution of the hpf goes down. For any photocurrent higher than this we could not make use of the higher SNR in the TIA signal, because the high-pass filter would be the limiting factor. The additional gain in the TIA also helps to increase these values. At $G = 1$ and consequential $U_{\text{out}} = 0.2\,\text{V}$, the currents would be 13.3 µA and 50 µA, respectively.

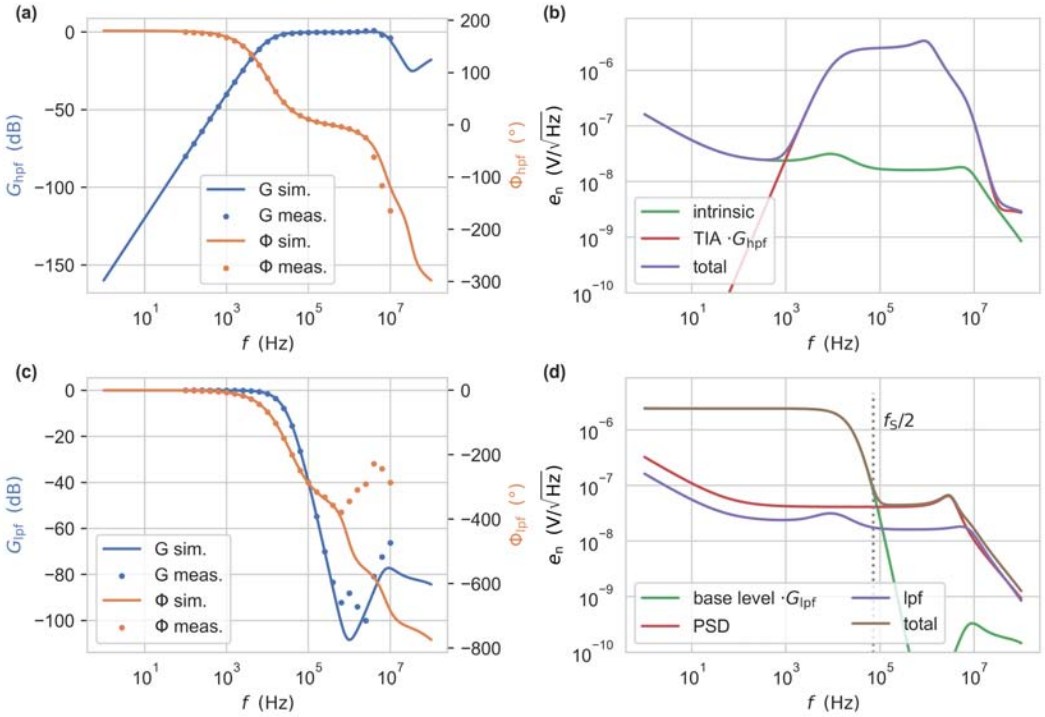

Figure 2.17: (**a**) Gain and phase of the high-pass filter at the input of the PSD. (**b**) Noise of a TIA in a typical scenario and additional noise from the hpf. (**c**) Gain and phase of the low-pass filter, following the SR. (**d**) Individual noise components of the SR, lpf, and signal. The first Nyquist zone at the chosen sampling frequency of $f_S = 144\,\text{kHz}$ is indicated by a dashed line.

For the SR itself, we can evaluate the static condition at $G = 1$ or $G = -1$. In this case each of the 10 kΩ resistors contribute thermal noise of $\sqrt{4kTR} = 12.9\,\text{nV}/\sqrt{\text{Hz}}$ at $T = 300\,\text{K}$, in addition to the input voltage noise of the OP, summing up to $41\,\text{nV}/\sqrt{\text{Hz}}$. The contribution by the input current noise density of this JFET input OP is negligible in this case. With the same reasoning as for the high-pass filter, this noise does not contribute significantly in our application. The value of 10 kΩ for the resistors in the difference amplifier is a tradeoff between the input impedance of the SR and the noise contribu-

tion. With 10 kΩ we do not significantly increase the noise above the OPs contribution. The input impedance is not critical because it is driven by a low-impedance source. From this stage on, we need to worry about additional 1/f noise, because the measurement is shifted back to base band. They originate in the PSD, the low-pass filter (see Figure 2.17d), as well as the ADC and the accompanying reference voltage.[6]

Lastly, the low-pass filter is composed of two OPs in a 4th-order Sallen-Key topology. A simple Butterworth configuration is chosen for its monotonic amplitude response in both passband and stopband, with corner frequency of $f_{-3\mathrm{dB}} = 14.6\,\mathrm{kHz}$. The corresponding Bode-plot is shown Figure 2.17c. We can see the expected $-80\,\mathrm{dB/decade}$, which attenuates signals above the first Nyquist-zone of the ADC ($> f_\mathrm{S}/2$) more than 30 dB. The resulting noise spectrum at the low-pass filter output is shown in Figure 2.17d. The output spectrum contains contributions from the low-pass OPs, the SR, and the demodulated noise. We call this demodulated noise the base level. It is the sum of the noise in the harmonic windows, scaled by the respective amplitudes, which results in our example almost exclusively from the first harmonic window. The noise up to the frequency of 100 MHz then integrates to $e_\mathrm{RMS} = \sqrt{\int_{1\,\mathrm{Hz}}^{100\,\mathrm{MHz}} e_\mathrm{n}^2(f)df} = 338\,\mu\mathrm{V}$. The noise in the first Nyquist-zone integrates to 309 µV, showing the low-pass filter's attenuation is sufficient to avoid aliasing of noise.

With the RMS noise at the input, the noise-free code resolution of the ADC can be calculated. Therefore, the noise at the input to the ADC can be assumed as normal distributed. In a normal distribution 99.9% of the values lie within 3.3 times the standard deviation and the peak-to-peak value follows as $e_\mathrm{pp} = 6.6 e_\mathrm{RMS} = 2.23\,\mathrm{mV}$. The noise-free resolution *NFR* is then the base-2 logarithm of FSR/e_pp, resulting in 10.5 bits in our case. Equivalently, the effective resolution can be calculated as the base-2 logarithm of $FSR/e_\mathrm{rms} = NFR + 2.7\,\mathrm{bits} = 13.2\,\mathrm{bits}$. This shows, the MCU's 12 bit ADC does not, in principle, pose a limit to a noise-free resolution measurement. Ideally, the ADC would not limit the effective resolution either, which is not given here.

[6] It may be tempting to use Auto-Zero or Chopper Amplifiers at this stage for their ability to effectively cancel 1/f noise and drift. They rely on the same principle as lock-in amplifiers. Therefore they employ switching electronics, though. This may lead to interference with the high-frequency components of the PSD's output and higher noise in the output signal of the low-pass filter. In our application we found this to be true for a OPA4187 in the LPF.

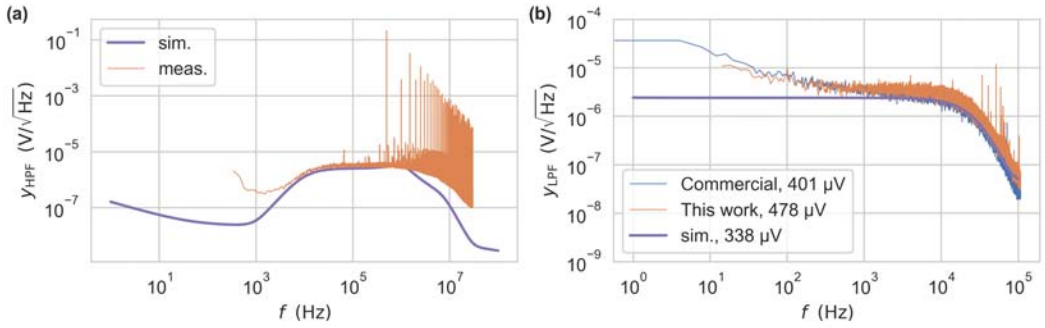

Figure 2.18: (**a**) Comparison of the simulated noise spectrum from the high-pass filter in comparison to the measured spectrum. The input signal by the optical interrogator with a fiber sensor had a peak-peak amplitude of $U_\mathrm{i} = 6\,\mathrm{V_{pp}}$. We used a Hann window at a resolution bandwidth of 7.153 Hz. (**b**) Linear spectral density of the PSD in comparison to a commercial LIA output at equal reference frequencies and low-pass filter configurations ($f_\mathrm{r} = 500\,\mathrm{kHz}$ and 4th-order, $f_{-3\mathrm{dB}} = 14.6\,\mathrm{kHz}$ LPF).

In Figure 2.18a, we again show the simulation of the signal entering the PSD and compare it to a measurement at the given operating point. In the simulation we used a DC signal, while in the measurement we create the actual case of a rectangular excitation of the experiment. In both cases the RMS output current from the photodiode in the TIA was equal, leading to the same shot noise and thereby good agreement of the noise floors. The spectrum contains narrow-band noise components next to the actual signal, which are caused by components in the circuit, like the MCU and the ADC, but also originate from the environment. Only those which are within the bandwidth of the low-pass filter around multiples of f_r will be transmitted to the output. We show the resulting output spectrum in Figure 2.18b. The narrow-band components only appear at frequencies above the cut-off frequency of the LPF. The output spectrum agrees well to the simulation, except for an increased noise floor towards lower frequencies. From the simulations we expect no significant contributions to the output 1/f noise above $\approx 0.1\,\mathrm{Hz}$. We also compare our circuit to a commercial LIA, operated at the same configuration, which shows the same low frequency noise. At this point we suspect the signal chain from the laser driver to the TIA to be the driving low-frequency noise source.

Now, we test the actual functionality of the PSD, which is the response to

an input signal at the reference frequency and varying phase shift θ with a proportional DC indication. We therefore use a sine wave at a reference frequency $f_\mathrm{r} = 500\,\mathrm{kHz}$ given by the timer in the MCU, sweep θ, and record the DC indication. We implement this measurement by using a separate commercial LIA, which locks-in to the laser driver output of our circuit. It allows us to feed a sine wave of same frequency and varying θ to the evaluation circuit's input. In Figure 2.19a, we show the DC indication $y(\theta)$ for three different input voltages. With this measurement we effectively trace the convolution of the rectangular reference waveform with the input signal. It is no surprise that we get a $\cos(\theta)$ waveform, because we use a sine wave at the input. When the input signal is in-phase ($\theta = 0$), we get a maximum DC indication. In an ideal PSD we would expect the DC indication value to equal the average rectified value (ARV) of the sine wave, which is $\frac{2}{\pi}\,\hat{x}$ with the amplitude $\hat{x}$. The measurements show 7% to 10% lower values. The DG419 switches feature a Break-Before-Make action with an interval of typically $t_\mathrm{D} = 13\,\mathrm{ns}$. This accounts for at least 1.3% drop in DC indication at the chosen f_r. The remainder can be explained by the inaccuracies in the amplification of the involved stages.

The circuit has a symmetric power supply, enabling the PSD to deliver the expected negative output at a phase mismatch between 90° and 180°. In the actual application, care should be taken to avoid this point of operation and stay within the permissible limits of the ADC. Additionally in practice, higher harmonics will be part of the input signal, so the convolution would approach a triangular waveform. As a consequence, the change in the output voltage from a change in the phase alignment would be $\delta y/\delta\theta \approx -\frac{4}{\pi^2}\hat{x}$. With the aforementioned resolution in phase we can then expect to maximize the DC indication within $\delta y \approx 1.6\,\mathrm{mV}$ of the theoretical maximum. In our measurement in Figure 2.19a, the output is less sensitive to phase deviations with $\delta y/\delta\theta \approx 0$ for small $\delta\theta$ because of the cosine waveform. In an application that suppresses higher harmonics to achieve this behavior, we would trade this insensitivity to phase deviations off for a lower SNR, as previously described.

Next, we test the linearity of the PSD's output with respect to the input amplitude. We recorded the DC indication, resulting from an in-phase sine wave input signal with a varying amplitude in the range of 0 V to 2 V. Figure 2.19b shows the difference of the measurement to a linear fit to the data. The range of 3 mV non-linearity corresponds to 0.15% of the full range. This

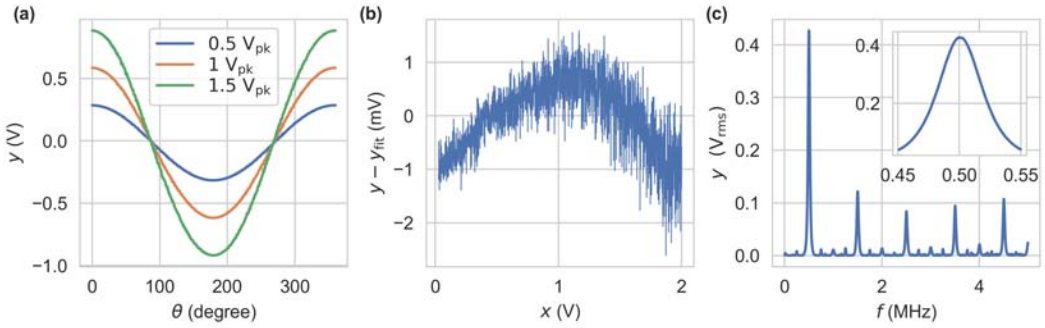

Figure 2.19: (**a**) Phase response of the PSD to a sine wave of same frequency as the excitation signal and varying phase difference θ. (**b**) Deviation from a least-squares fit to the DC output voltage as function the amplitude of an in-phase input sine wave. The response of the PSD to a sine wave of same frequency as the excitation signal and varying amplitude x was recorded. A linear regression yields the relation $y_{\text{fit}} = 0.598x - 0.014\,\text{V}$. (**c**) Frequency response $y(f)$ of PSD to an out-of-phase input sine wave.

value is not critical with respect to the application, because the dependency of the fluorescence intensity to magnetic fields is non-linear. A post-processing system would have to account for this non-linearity anyway.

To assess the frequency response of the PSD, we keep the reference signal at a constant frequency $f_{\text{r}} = 500\,\text{kHz}$ and sweep an independent input sine wave in the range of 0 to 5 MHz. We expect the PSD's output to be composed of sine waves at frequencies of $f_{\text{r},n} + f_{\text{t}}$ and $|f_{\text{r},n} - f_{\text{t}}|$ with the harmonics of the reference signal $f_{\text{r},n}, n \in [1, 3, 5, \dots]$ and the frequency of the input test signal f_{t}. Consequently, the PSD's output RMS voltage is recorded with a voltmeter in AC mode, depicted in Figure 2.19c. We observe a response at the respective harmonics $f_{\text{r},n}$, scaled by their amplitudes $1, \frac{1}{3}, \frac{1}{5}, \dots$. They can be described by a convolution of δ-pulses at the harmonics with the frequency response of the PSD's low-pass filter. We show the transmission window in detail for $n = 1$ in the inset in Figure 2.19c. The PSD also responds to signals at even harmonics with up to $-28\,\text{dB}$, relative to the output voltage at f_{r}. We attribute this behavior to jitter in the reference signal, which is different from the one in the input test signal. Jitter leads to deviations of the square wave duty cycle from 50%. In this case the Fourier series coefficients at even harmonics do not vanish anymore. In a later application we expect the response at these even harmonics to be lower, because we use the same timing source

for the excitation of the experiment and the PSD.

While the presented circuit accomplishes the set task of phase-sensitive detection, several points of improvement have been identified. First, the ADC and the reference voltage source integrated to the microcontroller lack a characterization by the manufacturer. For example, it is not known at this point to what extend 1/f noise of the reference voltage deteriorates long-term measurements. Also, a higher resolution was necessary to reach the effective resolution, set by the shot-noise-limited sensitivity. Next, the two analog switches inevitably introduce voltage spikes at their outputs in switching moments due to charge injection. While the low-pass filter attenuates these components, they may still have an effect on the measurement by stray coupling and intermodulation products. The two separate switches may not be well matched in their charge-injection either, leading to a DC shift at the low-pass filter's output. Lastly, we used the USB supplied voltage, which is not well defined in it's noise properties, possibly adding interferences.

2.3.2 Second Implementation

In a second implementation we want to address some of the previously found shortcomings of the PSD circuit. Therefore, we only highlight the circuitry changes. Also, we will not show all the previous measurements again, but focus on the performance in the actual application. The hardware design and firmware for the MCU in this revision was developed in cooperation with duotec GmbH, especially Jens Raacke.

New Circuit

The previous implementation was powered from the USB 5 V rail. It delivered the bus voltage itself and a -5 V rail from a charge pump to the components. While this is a simple and cost-effective solution, it may subject the components to high amounts of ripple and noise on the bus rail. Also, there is a new requirement of the ability to power the circuit from a 12 V supply, targeting the application in an automotive environment. A new supply was thus implemented, delivering ± 5 V needed for operation of the circuitry through a synchronous step-down converter, based on the Texas Instruments LMR50410. The converter's output is followed by ultralow-noise positive/negative linear

regulators (TPS7A30/TPS7A49, Texas Instruments). We found the output spectral noise densities to match the expectations from the data sheet with $4\,\mu V/\sqrt{Hz}$ at 1 Hz and lower than $0.1\,\mu V/\sqrt{Hz}$ above 1 kHz.

The effective resolution was previously found to be limited by the MCU integrated ADC. For this revision, we switch to a dedicated 24-Bit Delta-Sigma ADC (MCP3562, Microchip), which can achieve an effective resolution of at least $ER = 15.7$ bits at a sampling rate of 153.6 kHz. Usually, we are dealing with lower necessary bandwidths, allowing us to increase the oversampling ratio (OSR) and thereby increasing the effective resolution. The use of a dedicated ADC then results in a higher dynamic range for shot noise limited measurements. At $ER = 15.7$ bits, the amplification following the TIA in our previous example could be reduced 5 fold, before being limited by the ADC.

The SPDT switches have been replaced by a phase reversal switch (MAX4526, Maxim Integrated). The phase reversal switch offers a low absolute charge injection (10 pC), with well matched charge injection (2 pC match), lower transition time (max. $t_{\mathrm{TRANS}} = 100$ ns), and well matched on-resistances ($8\,\Omega$).

The high-pass filter and the SR are now built from dedicated OPs (THS4031, Texas Instruments), surpassing the performance of the previous OPs in their place. The low-pass filter, following the SR, has been extended to an 8th order Butterworth configuration, utilizing a quad OP (TLV9154IPWR, Texas Instruments) at a cut-off frequency of $f_{-3\mathrm{dB}} = 10$ kHz. This achieves a higher rejection of aliasing, realizing an attenuation of 67 dB at 75 kHz.

Characterization

For the following measurements, the evaluation circuit is connected to the same optical interrogator with an NV fiber sensor, which we used in the previous sections. First, we will find the best point of operation with regard to the phase offset of the excitation and the demodulation timers. Therefore, we sweep the phase offset t_{delay} between the timers in a range of 10 ns to 500 ns and record the mean value μ_y of 1024 ADC samples. In Figure 2.20a, we show the result for different reference frequencies f_{r} in the range of 50 kHz to 500 kHz. We observe a maximum in μ_y at $t_{\mathrm{delay}} = 200$ ns for lower reference frequencies, shifting to $t_{\mathrm{delay}} = 250$ ns with rising f_{r}. We attribute this behavior to frequency-dependent phase shifts in the signal processing chain, especially by the input high-pass filter. The rectangular excitation waveform is distorted, because

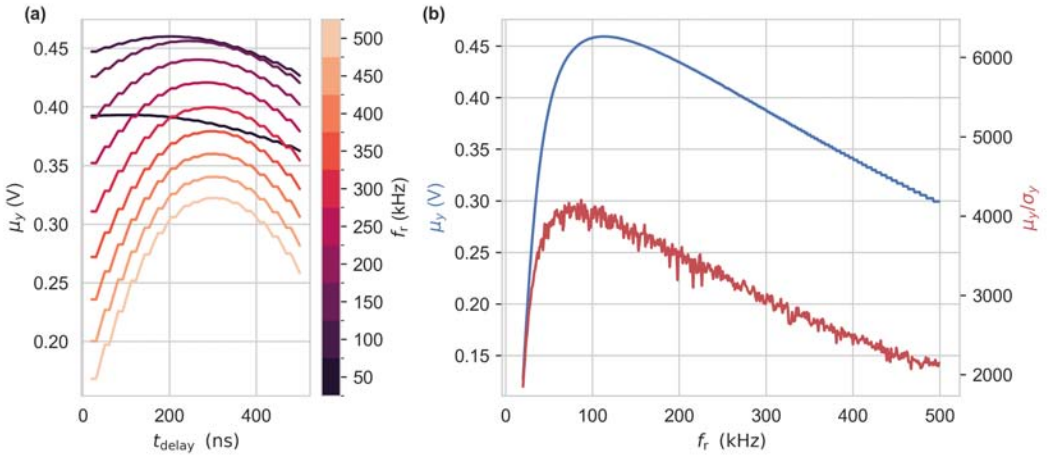

Figure 2.20: Influence of timer delays and reference frequency while connected to the presented NV-fiber based setup. (**a**) Mean values μ_y of 1024 samples ($f_\mathrm{s} = 15.625\,\mathrm{kHz}$) as a function of time delay between excitation and demodulation timers t_delay and varying reference frequencies f_r. (**b**) Mean values μ_y and ratio of mean to standard deviation μ_y/σ_y from 8192 samples ($f_\mathrm{s} = 15.625\,\mathrm{kHz}$) as a function of the reference frequency f_r.

the fundamental frequency and the higher harmonics are subjected to different amounts of phase shift. This changes t_delay, which maximizes the DC indication from a synchronous rectifier. At frequencies below it's pass-band, a high-pass filter introduces a positive phase shift, meaning a negative phase delay. When the fundamental frequency of the rectangular waveform falls within this range, it's phase is shifted so that a smaller phase shift compensation of the SR is necessary to maximize the DC indication for the complete fluorescence waveform.

Next, we sweep the reference frequency f_r in the range of 20 to 500 kHz, with t_delay fixed to 200 ns, recording blocks of 8192 ADC samples at a sampling rate of $f_\mathrm{s} = 15.625\,\mathrm{kHz}$. In Figure 2.20b, we show the mean μ_y and the ratio of mean to standard deviation μ_y/σ_y for each block as a function of f_r. Initially, μ_y rises sharply up to around $f_\mathrm{r} = 120\,\mathrm{kHz}$, after which it gradually declines. We attribute this shape to the combination of two effects. Firstly, the incline with rising f_r can be explained by the input high pass filter. It is configured to have a $f_{-3\mathrm{dB}} = 25\,\mathrm{kHz}$ corner frequency, meaning the attenuation drops below 1% above 130 kHz. Secondly, the TIA's bandwidth of 0.5 MHz attenuates higher harmonics of the input signal, lowering the DC indication with rising f_r. While at $f_\mathrm{r} = 100\,\mathrm{kHz}$ up to the 5th harmonic is within the passband, this

gradually decreases to only the fundamental frequency within the range of f_r in Figure 2.20b. This results in a decrease by 1/3, which is in good agreement to the observation.

The ratio of mean to standard deviation μ_y/σ_y shows a qualitatively equal waveform, indicating that in a controlled laboratory environment the complete range of f_r can be utilized without a SNR penalty, except for the lower DC indication towards higher f_r. In a different environment, this measurement might show frequencies with higher variance due to interference, e.g. by switching power electronics in an automotive current sensing application. In that case we were able to position f_r in a potentially lower noise region, which we can choose from the whole specified range of f_r.

Now, we investigate the dynamic behavior of the complete system using an AC magnetic field, which we sweep in the frequency range of 10 Hz to 100 kHz. Therefore, the sensor head is placed in an electromagnet (see Appendix A.1) and a bias magnetic field of $\approx$ 20 mT is applied by a permanent magnet. An AC current of constant amplitude is then applied using a four quadrant voltage controlled current source (TOE7621, Töllner), leading to an AC magnetic field of 1.17 mT at low frequencies. First, we measure the magnetic field amplitude as a function of the frequency with a reference Hall-effect sensor (A1366LKTTN-10-T, Allegro, B = 120 kHz). The magnitude of the transfer function normalized to the value at low frequencies $\hat{y} = y/y(f = 10\,\mathrm{Hz})$ is shown in Figure 2.21. We find a 3 dB corner frequency for the complete measurement system of 13 kHz. This is just enough to test the here presented configuration of the evaluation circuitry with a target bandwidth of 10 kHz.

Next, we replace the Hall sensor with the NV fiber sensor head and record the transfer function, also shown in Figure 2.21. The system is set to f_r = 120 kHz and t_delay = 200 ns. We find a good agreement to the reference sensor up to 1 kHz. At further increasing frequencies the amplitude declines, leading to a 3 dB corner frequency of 5 kHz and an attenuation of 7 dB at 10 kHz. Above 10 kHz the amplitude declines as expected, following the reference transfer function, which is limited by the test setup. We attribute the lower bandwidth to the evaluation circuitry, especially the low-pass filter. The theoretical bandwidth limit, set by the intrinsic parameters of NV centers, is expected to be higher. The lowest transition rates are found for the intersystem crossing from the dark to the ground state of 0.4 to 3.3 MHz, reported

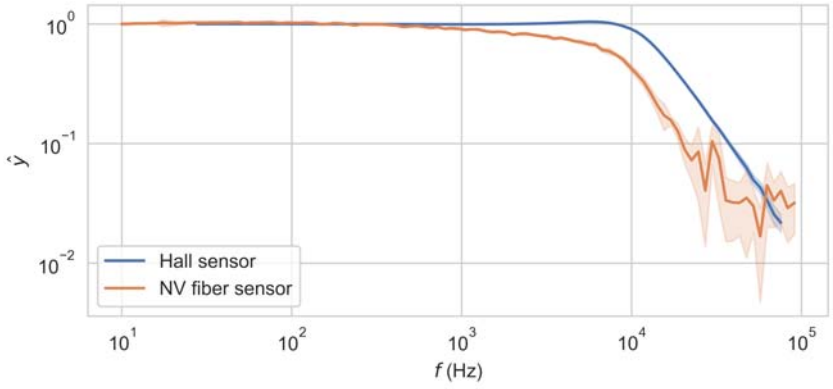

Figure 2.21: Magnitude of transfer functions, normalized to $y(f = 10\,\mathrm{Hz}) = 1.17\,\mathrm{mT}$ for the reference Hall effect sensor and the NV fiber sensor. A bias of 20 mT was applied in both cases. The shaded areas show the standard deviation.

for single NV centers and ensembles [125, 81, 22, 126]. Further studies are necessary to find the bandwidth limitation of the all-optical readout of NV centers. In comparison, other broadband DC sensing methods, using pulsed or continuous wave ODMR, are typically limited to bandwidths of 10 kHz in CW operation and up to 100 kHz otherwise [99, 20].

Lastly, we want to find the sensitivity and minimum detectable magnetic field of the sensor system as a function of the frequency. Therefore the noise spectral density is employed, which is estimated by Welch's method [127]. We have shown spectral densities before, but introduce the method for their determination now formally here.

Welch's method computes a modified periodogram for each segment and averages these estimates to produce the power spectral density (PSD) estimate. Given that the process is wide-sense stationary and Welch's method utilizes PSD estimates from different segments of the time series, the modified periodograms are approximately uncorrelated estimates of the true PSD, and averaging them reduces variability.
Segments of a recorded time series y are multiplied by a window function $w(n)$, such as a Hann window [128]. The mth window is given by

$$y_m(n) = y(n + mR)w(n), \quad n = 0, 1, \ldots, M-1, \; m = 0, 1, \ldots, K-1, \tag{2.42}$$

with the length of segment and window M, the number of segments K, and the segment hop size R. Segments may be overlapping, increasing the number of periodograms available for averaging. The squared discrete Fourier-transform of each segment is then computed by [129]

$$P_{y_{m,M}}(\omega_k) = \left|\mathrm{DFT}_{N,k}(y_m)\right|^2 = \left|\sum_{n=0}^{N-1} y_m(n) e^{-j2\pi nk/N}\right|^2 . \tag{2.43}$$

Next, the result has to be scaled appropriately. The power spectrum (PS) can be determined by correcting for the squared sum of the window function

$$P^{PS}_{y_{m,M}}(\omega_k) = \frac{P_{y_{m,M}}(\omega_k)}{S_1^2}, \tag{2.44}$$

with

$$S_1 = \sum_{n=1}^{M-1} w(n). \tag{2.45}$$

The PS is used when the power or amplitude of a narrow band signal is to be estimated. Alternatively, the power spectral density (PSD) may be determined, which is usually employed for estimation of the noise floor. This requires scaling $P_{y_{m,M}}(\omega_k)$

$$P^{PSD}_{y_{m,M}}(\omega_k) = \frac{P_{y_{m,M}}(\omega_k)}{f_\mathrm{S} S_2}, \tag{2.46}$$

with

$$S_2 = \sum_{n=1}^{M-1} w^2(n) \tag{2.47}$$

and the sampling frequency f_S. For a given window function we can define the *ENBW*, like we did for low-pass filters before, by

$$ENBW = f_\mathrm{S} \frac{S_2}{S_1^2} , \tag{2.48}$$

which relates the PS to the PSD by

$$P^{PSD}_{y_{m,M}}(\omega_k) = \frac{P^{PS}_{y_{m,M}}(\omega_k)}{ENBW} . \tag{2.49}$$

Since the width of the window in the frequency domain results in the

collection of noise from adjacent windows in the PS, the normalization to the *ENBW* has to be applied, correcting for this phenomenon.
The final estimate of the PS is then the average of all periodograms

$$S_y(\omega_k) = \frac{1}{K}\sum_{m=0}^{K-1} P^{PS}_{y_{m,M}}(\omega_k) \tag{2.50}$$

and analogous for the PSD. Since we are dealing with real-valued signals, their spectrum is conjugate symmetric. Hence, we commonly use the single sided spectrum

$$S_y^+(\omega_k) = \begin{cases} 2S_y(\omega_k) & \text{if } \omega_k > 0 \\ 0 & \text{if } \omega_k < 0 \end{cases} \tag{2.51}$$

Window functions are applied to remove discontinuities that result from the segmentation, leading to spurious ringing artifacts in the time domain, which translate to spectral leakage in the frequency domain. For the RMS value estimation of narrow band signals in the PS, we commonly apply flattop windows, delivering higher accuracy. When estimating noise spectral densities, narrow band windows like Hann are preferred for their higher side-lobe suppression.

For these measurements we used an aged fiber sensor with lower total fluorescence output at same optical excitation power than before, delivering a photocurrent of $i_\mathrm{d} = 0.2\,\mu\mathrm{A}$. In conjunction with the common setup, we used up to this point, that contains a TIA with $R_\mathrm{fb} = 200\,\mathrm{k}\Omega$ and $G = 20$, the measurements are not shot-noise-limited and we expect a deviation from the SNLS through thermal noise by 3.7 dB. Following the calculations from Section 2.2.2, the SNLS is at $s_\mathrm{snl} = 0.634\,\mu\mathrm{T}/\sqrt{\mathrm{Hz}}$. At a 3.7 dB lower SNR, we expect the measurement to yield a sensitivity of $s \approx 1\,\mu\mathrm{T}/\sqrt{\mathrm{Hz}}$. We show the noise spectral density in Figure 2.22a for two recordings at different lengths and sampling rates.[7] We observe a white noise region at signal frequencies above 250 Hz up to the corner frequency of the low-pass filter at $S_y \approx 1\,\mu\mathrm{T}/\sqrt{\mathrm{Hz}}$, in good agreement with the expectation. Towards higher frequencies, signal and

[7] This division is only done to lower the memory and computational requirements during evaluation. For a wide sense stationary process, which we assume here, both recordings approximate the actual statistics well.

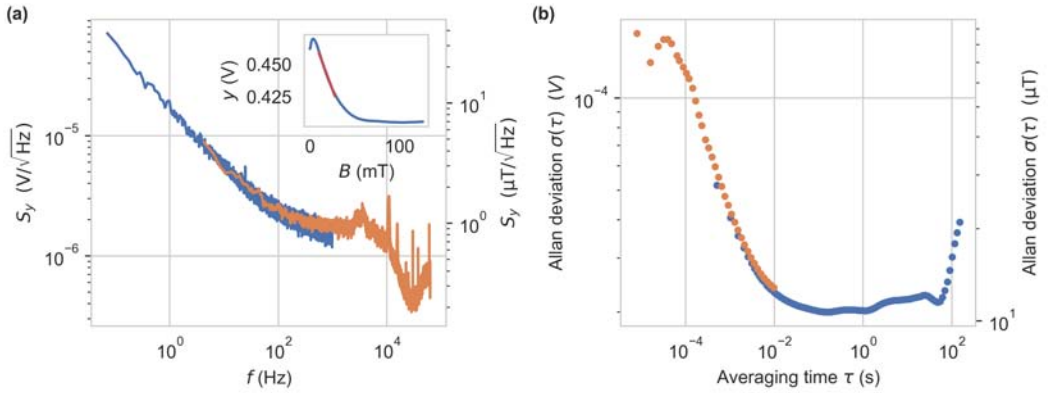

Figure 2.22: Noise characteristics of second phase sensitive detector implementation with microdiamonds attached to an optical fiber (see Figure 2.2b) (**a**) Noise spectral density at zero bias field, computed by Welch's method with a Hann window. Data were recorded at $f_s = 1953.125\,\text{Hz}$ in 15 min (blue trace, window length 28.11 s) and at $f_s = 125\,\text{kHz}$ in 15 s (orange trace, window length 0.47 s). A linear fit to the calibration curve, shown in the inset, was used to generate a second y-axis with the magnetic field values. (**b**) Allan deviation of the same data as in (a) with the same color correspondence. A second y-axis with magnetic field values uses the same fit to the calibration curve from the inset.

noise components are equally attenuated. As a consequence the measurement is not representative of the actual sensitivity at higher frequencies. At lower frequencies, we observe additional 1/f noise.

The minimum detectable magnetic field and the sensitivity can alternatively be determined as a function of the integration time using the Allan deviation. We show the Allan deviation for the previous data sets in Figure 2.22b. With increasing averaging time, $\sigma(\tau)$ initially decreases, up to $\tau \approx 10\,\text{ms}$, reaching a plateau of 10 µT. This behavior is to be expected from a white noise region at the corresponding signal frequencies. At higher averaging times, we observe a plateau, where 1/f noise introduces additional noise power. From $\tau \approx 60\,\text{s}$ upwards, the deviation increases again, hinting to an additional instability. For completeness, we also measured the circuit in a direct feedback configuration, shown in Appendix A.3. Since the trigger output is further binarized by the laser driver input, any interferers or drift are of low importance in an application.

Example Application: Power Grid

One of the possible applications of this system is the measurement of currents in the power grid. For demonstration we conceived a simple setup in which we place the optical fiber sensor directly next to an insulated conductor of type H07Z-K with a cross section of 2.5 mm^2, shown schematically in Figure 2.23a. A permanent magnet is placed in vicinity of the fiber head, applying an offset magnetic field of $B_\mathrm{b} \approx 15\,\mathrm{mT}$, and thereby biasing the system to a state of high sensitivity. We apply a 50 Hz line frequency AC current of $I_\mathrm{m} = 0.707\,\mathrm{A}$ to the conductor, expecting a resulting magnetic field at the center of the fiber sensor head of

$$B_\mathrm{m} = \frac{\mu_0}{2\pi}\frac{I_\mathrm{m}}{r} = 58.9\,\mu\mathrm{T}, \tag{2.52}$$

where $r = (d_\mathrm{w} + d_\mathrm{f})/2 = 2.4\,\mathrm{mm}$ is the distance between centers of the conductor and the fiber sensor head, and μ_0 is the magnetic permeability of free space. The variables d_w and d_f are the diameters of the wire and the fiber tip, respectively. The equation follows the application of the Biot-Savart law to a thin straight wire.

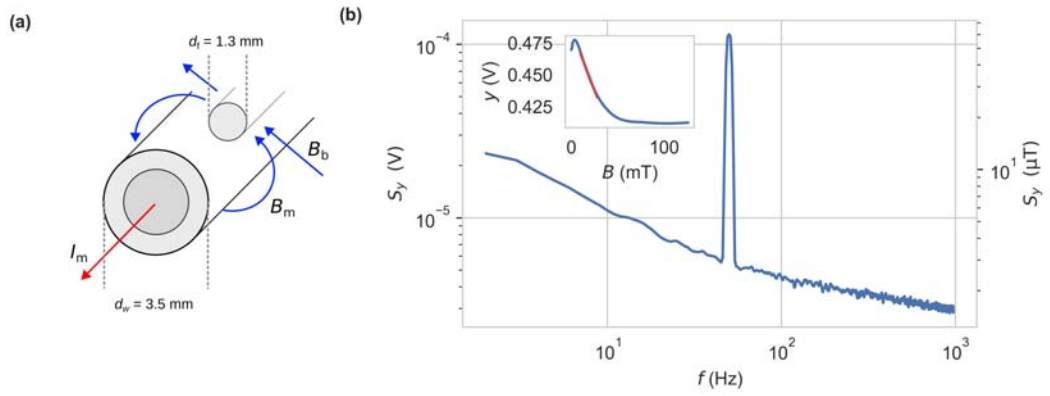

Figure 2.23: (**a**) Schematic of the current sensing setup. The optical fiber is placed parallel to the current carrying conductor. A bias field of $B_\mathrm{b} \approx 15\,\mathrm{mT}$ is applied. (**b**) Linear spectrum of the signal by Welch's method (flattop window, window length 1 s) at an ADC sampling rate of $f_\mathrm{s} = 1953.125\,\mathrm{Hz}$. A linear fit to the calibration curve, shown in the inset, was used to generate a second y-axis with magnetic field values.

In Figure 2.23b, we show the linear spectrum of the example power grid measurement with 1 s windows at a $f_\mathrm{s}/2 \approx 1\,\mathrm{kHz}$ bandwidth. The peak at the line frequency has a value of 60.14 µT, which is in good agreement to the

expectation. We attribute the error of 2.1% to an inaccuracy of the positioning of the sensing volume to the conductor, as well as a local deviation of $\delta y/\delta B$ from the linear fit to the range of 10 mT to 30 mT, which we used for the calculations. We estimate the SNR for long term measurements in this setup by

$$SNR_{\mathrm{A}} = 20\log_{10}\left(\frac{B_{\mathrm{m}}}{\sigma(\tau)}\right) = 14.4\,\mathrm{dB}, \tag{2.53}$$

using the Allan deviation $\sigma(\tau = 20\,\mathrm{ms}) = 11.5\,\mu\mathrm{T}$. These considerations can apply to wires of different cross sectional areas, allowing for higher maximum currents. We show the resulting maximum SNR_{A} for example values in Table 2.2, accounting for the respective diameters d_{w}. The current carrying capacity rises more quickly than the wire's diameter with increasing cross sectional area, which results in a rising signal B_{m} and SNR.

Cross section (mm^2)	max. current (A)	max. B_{m} (mT)	max. SNR_{A} (dB)
2.5	20	1.67	43.22
10.0	50	1.65	43.15
35.0	115	2.71	47.43
120.0	250	3.76	50.29
300.0	460	4.80	52.42

Table 2.2: Cross section and resulting maximum SNR at the given current through a H07RN-F wire. Maximum currents are taken from DIN VDE 0298 Part 4 for an ambient temperature of 35 °C, a max. wire temperature of 70 °C, and operation in a closed cabinet. Wires are a assumed to be spaced apart by at least their diameter.

While this setup is simple and effective, it could be enhanced by a magnetic flux concentrator to increase the flux density at the sensing volume and shield from stray fields, thereby improving the sensitivity. Of course, such a setup could also be extended by a secondary winding on the magnetic core to realize a control loop that keeps the flux density at the sensing head at a point of maximum sensitivity. These technologies are commonly found for other setups, like Hall-effect sensors, and have also been proposed for NV center-based sensors, although using MW for ODMR [130, 131].

2.3.3 Comparison to DC

In this section, we want to show the advantage over a base band measurement in the given application. With a commercial LIA connected to the experiment we used up to this point, we operate the system either pulsed at a reference frequency of $f_\mathrm{r} = 120\,\mathrm{kHz}$ and demodulate the fundamental frequency, or operate the system in base band. In both cases the low-pass filter is set to $f_{-3\mathrm{dB}} = 10\,\mathrm{kHz}$ and the mean optical excitation power was equal. We use a commercial LIA (MFLI, Zurich Instruments) for its ability to support both operating modes and good comparability of the measurements. We recorded data and analyze them, like we did before, with the power spectral density and the Allan deviation, shown in Figure 2.24.

In the spectrum in Figure 2.24a, we find a shift of the 1/f noise corner frequency from 100 Hz up to 1 kHz and a consequential rise of the noise floor by 7 dB at lower frequencies when operating the system at base band instead of AC. This shows, that components which are part of the AC signal chain in lock-in operation, notably the photodetector and the following amplifier, contribute 1/f noise. Their noise adds to the signal in base band operation, lowering the SNR. We can also observe this effect in the Allan deviation plot, showing a higher plateau and a drift component in the range of $\tau = 3\,\mathrm{s}$ to 30 s. However, we see that not all low frequency noise components can be avoided. These originate at all electrical components, involved outside the AC signal chain. Next to the low-pass filter and ADC, including reference voltage in the reception path, we mostly attribute it to optical power fluctuations in the excitation light. We found lower frequency noise and drift in the laser diode's optical power, which we detail in Appendix A.2. When pulsing or otherwise AC modulating the intensity, lower frequency noise is mixed with the AC waveform resulting in an amplitude modulation (AM) of the carrier. Such AM directly reflects in the demodulated fluorescence signal. We did not investigate the long term gain and phase stability of components in the AC signal chain, which might also have an effect on the measurement.

At higher frequencies the noise spectral densities are nearly equal, which is to be expected when the dominant noise sources in this region are shot noise and thermal noise from the photodetector, which are spectrally white above the 1/f corner frequency up to the bandwidth limits of the TIA. Care

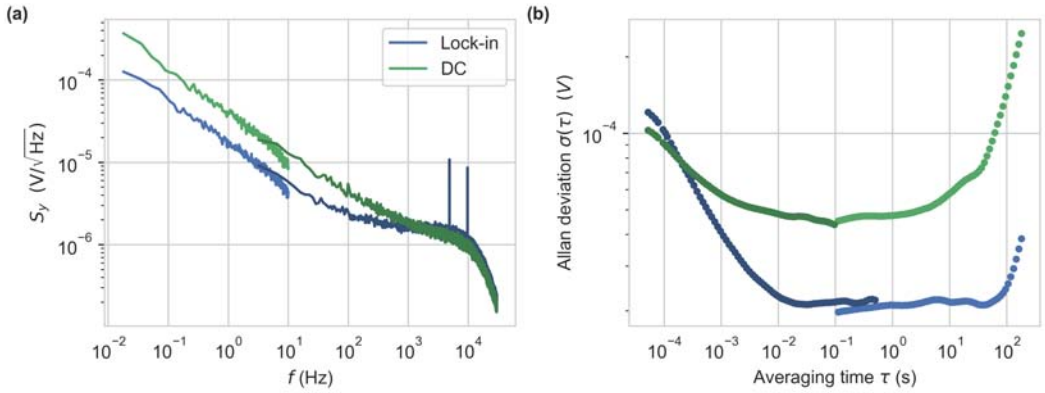

Figure 2.24: Comparison of noise characteristics between lock-in amplifier (blue trace) and base band (green trace) evaluation, while connected to an NV-sensor experiment. (**a**) Noise spectral density at zero bias field by Welch's method (Hann window). Data were recorded at $f_s = 224.8\,\mathrm{Hz}$ in 30 min (lighter traces, window length 56.25 s) and $f_s = 115.131\,\mathrm{kHz}$ in 10 s (darker traces, window length 0.31 s). (**b**) Allan deviation of the same data as in (a) with the same color correspondence.

has to be taken when choosing a reference frequency for LIA operation. We purposefully chose a point of operation in Figure 2.24, where two narrow band interferences fall into the transmission bandwidth. This may be avoided with correct placement of f_r in the spectrum. Larger required bandwidths make this task more difficult, especially in noisy environments like for example electric vehicles.

These measurements additionally allow us to compare a commercial laboratory solution to the presented circuit in the same application (compare Figure 2.22). We find nearly identical power spectral densities up to the low-pass filters bandwidth, showing the evaluation circuit is not limiting the performance in the given point of operation. Additional small bandwidth interferers in our circuit can be observed, which do not originate in the connected experiment, but in the evaluation circuit itself.

2.3.4 Conclusion

In this section we developed an evaluation circuitry for all-optical NV-based sensing, using phase-sensitive detection by square wave synchronous rectification in the analog domain. This implementation allows the shift of the measurement away from base band to a frequency up to 500 kHz, which enables

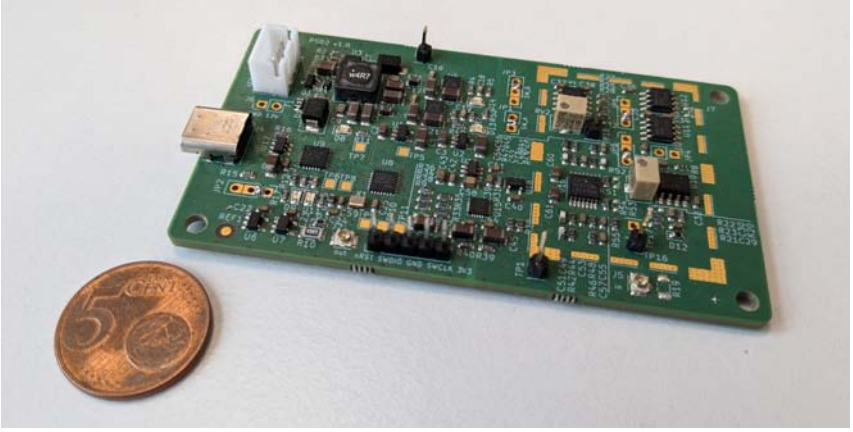

Figure 2.25: Picture of the second PSD evaluation circuit, containing the power supply, the analog phase-sensitive detection, the digitization and the data transmission. A metal cap can be installed above the analog section to suppress electromagnetic interference.

us to avoid application specific interferers and reduces the impact of 1/f noise on the output signal to some extend. The setup allows the capture of magnetic fields at a 5 kHz bandwidth with a shot-noise-limited sensitivity down to $s \approx 1\,\mu\mathrm{T}/\sqrt{\mathrm{Hz}}$. In the given point of operation, our implementation has similar performance, compared to a commercial laboratory lock-in amplifier. We show a picture of the second implementation in Figure 2.25. The small size and low cost of less than 90€ in small quantities paves the way for industrial application of all-optical NV-based magnetic field and current sensing. The system may be combined with a compact and portable duplex module, containing a laser diode, a photodiode, a dichroic mirror, and a fiber port, making the system easily integrable. Alternatively, other sensor designs, like LED-based sensors may benefit from this circuitry [132, 6]. The square wave PSD approach may also be used with duty cycles lower than 50%, e.g. in boxcar averager operation, improving the SNR in pulsed experiments [7].

2.4 Temperature Effects

Thermal dependency is an important factor in the prospective application of all-optical magnetic field sensing with NV centers. In this section we take a look at previous studies and compare them to our own findings.

2.4.1 Background

Thermometry with NV centers is a topic of active research. One common way of temperature sensing is the detection of the shift of the zero-field splitting (ZFS) in an ODMR experiment. The ZFS frequency at approximately $D = 2.87\,\mathrm{GHz}$ is temperature dependent because of the thermal lattice expansion and temperature dependence of the electron–phonon interaction [133, 65]. Values of $\frac{dD}{dT}$ on the order of $-74.2\,\mathrm{kHz/K}$ are commonly reported [94]. However, the exact values vary from one sample to another and with the temperature range [134, 135, 136]. Sensitivities down to $2.3\,\mathrm{mK}/\sqrt{\mathrm{Hz}}$ for bulk diamond sensors with sensors sizes in the range of 1 mm to 3 mm have been demonstrated [135]. Alternatively nanodiamonds (ND) with sizes of approximately 100 nm have been employed, realizing high spatial resolutions. Their sensitivities are on the order of $1\,\mathrm{K}/\sqrt{\mathrm{Hz}}$, however [135, 137].

All-optical approaches for NV-based thermometry are also feasible and usually based on the change of the spectral shape [138, 139]. They rely on the observation of shift in wavelength of intensity of the zero-phonon line (ZPL). Also, the ratio of the ZPL to the entire spectrum, i.e. the Debye–Waller factor has been used [140]. This ratiometric approach is a robust solution for temperature measurements because the overall fluorescence intensity can be affected by many other factors. Sensitivities of $0.3\,\mathrm{K}/\sqrt{\mathrm{Hz}}$ were reported for this approach using NDs [138].

A rise in temperature is accompanied by an overall reduction of the fluorescence intensity [141, 135, 142]. In time-resolved fluorescence spectroscopy a reduction of the fluorescence lifetime with rising temperature has been shown [141, 143]. Increasing temperatures can enhance non-radiative decay channels, effectively decreasing the excited-state lifetime. This is associated with a drop in quantum efficiency, leading to a reduced steady-state intensity. Toyli et al. studied the spin and orbital dynamics of single NV centers in diamond between room temperature and 700 K, finding a temperature-invariant $m_\mathrm{S} = 0$ excited-state up to $\approx 550\,\mathrm{K}$ and a temperature dependence at higher temperatures, which are well described by the Mott-Seitz formula for nonradiative relaxation via multiphonon emission [144]. Plakhotnik and Gruber on the other hand investigated an ensemble of NDs, finding a temperature-dependence of the excited-state lifetime in the range of 300 K to 700 K [141]. Bommidi and

Pickel also found a decrease of the average lifetime for single NDs in the range 300 K to 500 K. The behavior however did not fit well to the Mott-Seitz model and was therefore described by a linear relationship [143].

In all-optical, as well as MW-based measurements, NV centers show temperature dependent effects, which have to be considered during a magnetometry application. NV centers may also be used for temperature sensing, even simultaneously to magnetic field sensing [145]. We show example values from literature for the just discussed temperature dependent measurands in Table 2.3.

Ref.	Samples	$\frac{dD}{dT}$ (kHz/K)	$\frac{dI_{\mathrm{fl.}}}{dT}$ (%/K)	$\frac{d\tau}{dT}$ (ns/K)
[94]	Bulk	-74.2		
[141]	NDs		-0.2	$\tau_{\mathrm{short}} : -0.0067$, $\tau_{\mathrm{long}} : -0.0486$
[135]	NDs	-65.4 ± 5.5	-3.9 ± 0.7	
[143]	NDs on silicon and glass			$\tau_{\mathrm{avg.}} : -0.04$ (silicon), $\tau_{\mathrm{avg.}} : -0.059$ (glass)
[134]	Bulk	-100 (at 500 K)	-0.2	
[142]	NDs		$-0.58(\mathrm{NV}^-)$ $-0.46(\mathrm{NV}^0)$	

Table 2.3: Reported temperature dependencies of the ZFS D, the overall fluorescence intensity $I_{\mathrm{fl.}}$, and the fluorescence lifetime τ.

In the following, we will use the sensor design from the previous sections, subject it to temperature variations, and compare it to expectations from literature.

2.4.2 Measurement Setup

For temperature dependent fluorescence intensity measurements, we use the optical and electrical setup, previously described in Section 2.1. We set an average optical excitation power of 5 mW, measured before coupling into the fiber and pulse the laser at 100 kHz and 50 % duty cycle. The returning fluorescence is detected by a TIA (Hamamatsu S5971, 200 kΩ) and passed to a

LIA (MFLI, Zurich Instruments), demodulating the fundamental oscillation using a 3rd order, 11 Hz low-pass filter. The fiber tip was placed into a climate chamber (MK115, Binder) and the ambient temperature was simultaneously tracked using a PT100 sensor. We set the oven to cycle between 0 °C and 100 °C with each up- or down-ramp taking 1 hour and 10 minute wait times in between. No magnetic fields were applied during this measurement.

In a second step, the experiment is extended by a varying magnetic field to investigate the simultaneous temperature and magnetic field dependence. We placed the sensor tip in the center of a Fanselau electromagnet (see Appendix A.1) and monitored the magnetic field by a Hall effect-based sensor (TL493D, Infineon Technologies AG). The fiber sensor was replaced by a dry fiber, in which the end facet is placed directly next to the microdiamonds in a glass cuvette without applying any glue. We set the climate chamber to a temperature sweep from 0 °C to 100 °C and simultaneously swept the magnetic field from 0 mT to 80 mT, repeating every eight minutes.

2.4.3 Results and Discussion

During the first 40 hours to 60 hours of exposing the fiber tip to temperature cycles, we observed a changing behavior. The fluorescence at first showed a positive temperature coefficient in the lower temperature range of 0 °C to 20 °C and an otherwise approximately constant intensity. This characteristic shifted towards a negative temperature coefficient over the whole temperature range, which after approximately 60 hours stayed consistent. In Figure 2.26a, we show the first ten hours of a longer run, illustrating the profile of the temperature cycles and the fluorescence intensity in the same time span. A more practical visualization is shown in Figure 2.26b, where the fluorescence intensity is plotted against the temperature and the time is encoded by color. We determine a mean slope of $dI_{\mathrm{fl.}}/dT = -0.091\,\%/\mathrm{K}$ ($\pm -0.011\,\%/\mathrm{K}$) during 43 temperature ramps. In the literature, a range of $dI_{\mathrm{fl.}}/dT = -3.9\,\%/\mathrm{K}$ to $-0.2\,\%/\mathrm{K}$ has been reported for different samples and temperature ranges (see Table 2.3). Our findings are in a similar range, where the difference may be explained by differences in the sample itself, specifically the size of the diamonds and the NV concentration, and the addressing via the optical fiber, which is, in part, also subjected to the temperature variations.

In addition to the temperature dependency, the fluorescence intensity showed

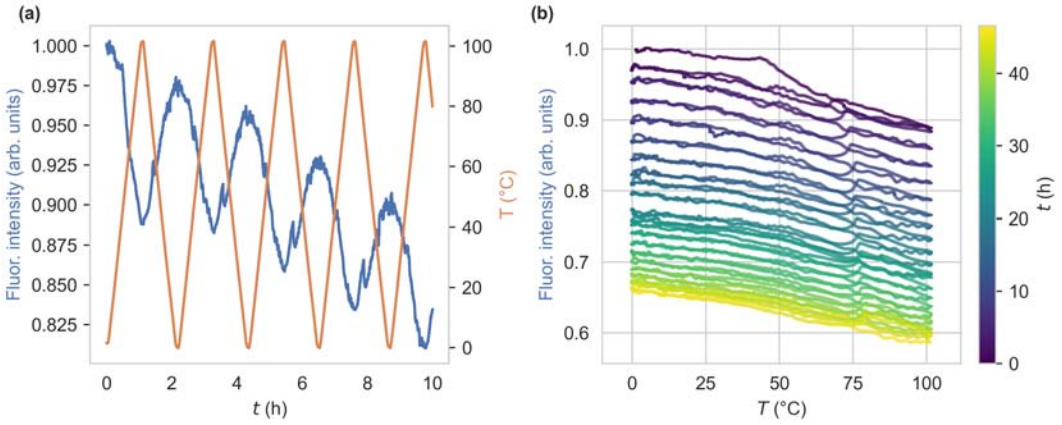

Figure 2.26: (**a**) Ten hours of temperature cycling, showing the fluorescence intensity and the temperature during four full temperature cycles in the range of $T = 0\,°\mathrm{C} - 100\,°\mathrm{C}$. The fluorescence intensity has been normalized to the value at $t = 0$. (**b**) Fluorescence intensity as a function of the temperature T. The first ten hours correspond to the data in (a).

an overall decreasing trend. After an initial 2 %/hour of intensity reduction, this value reduced to 0.3 %/hour after 200 hours of temperature cycling without reaching a saturation. We hypothesize the decreasing trend to originate from a degradation of the optical adhesive, with which the microdiamonds are attached to the fiber's end facet. To test this hypothesis, we replaced the fiber with a dry fiber, without the application of glue. We repeated the measurements[8] with the dry fiber, finding a mean slope of $dI_{\mathrm{fl.}}/dT = -0.105\,\%/\mathrm{K}$ ($\pm -0.005\,\%/\mathrm{K}$) during 18 temperature ramps. The fluorescence intensity showed good repeatability during the temperature cycles, with the variation at a fixed temperature $T = 3\,°\mathrm{C}$ spanning a range of 0.7%. This drift can be well explained by the drift inherent to all components involved in the excitation and detection process during the experiment's duration of 21 hours. The lack of a non-reversible effect indicates the optical adhesive to be the main influence in the previously found long-term decline.

Lastly, we want to find the influence of temperature variation on the fiber sensor's magnetic field sensing ability by repeatedly acquiring the calibration curve during a temperature sweep. In Figure 2.27a, we show the calibration curves for a temperature range of 2 °C to 94 °C, normalized to the intensity

[8] The measurements were conducted at Quantum Technologies GmbH, using a continuous-wave setup at 2.33 mW optical excitation power. For the temperature studies, we expect no significant difference in results to the previous setup with pulsed excitation at low reference frequencies and lock-in amplification.

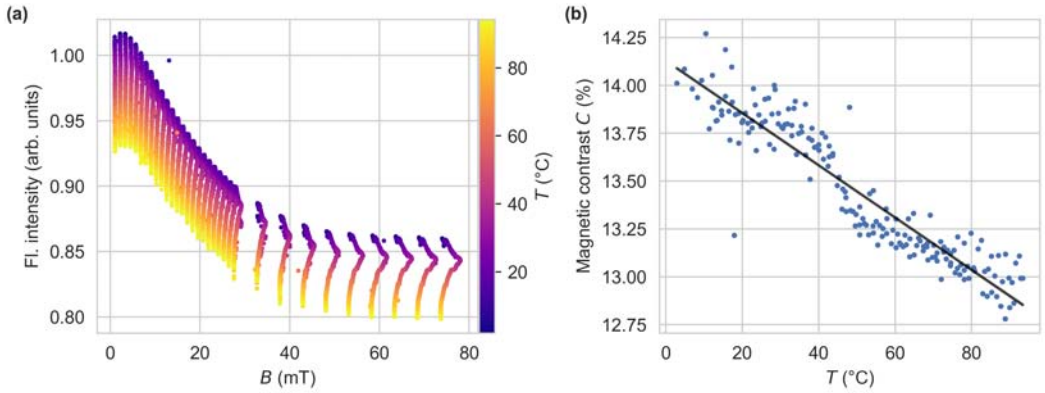

Figure 2.27: (**a**) Calibration curves in a temperature range of 2 °C to 94 °C from a 14 hours temperature sweep. (**b**) Magnetic contrast C as a function of temperature T. The linear fit has a slope of $-0.013\,65\,\%/\mathrm{K}$.

at $T = 2.0\,^{\circ}\mathrm{C}$ and zero field. We find a qualitatively similar calibration curve for all temperatures, with the exception of a varying offset, which can be explained by the previously found temperature induced fluorescence intensity reduction. These measurements however show that magnetic fields can be sensed, even at elevated temperatures. We applied equal current steps to the electromagnet during each magnetic field sweep, from which we expect equal magnetic fields. The variation of magnetic fields in Figure 2.27a can be explained by the temperature dependent behavior of the Hall-based sensor. From the calibration curves we can determine the respective contrasts, shown in Figure 2.27b. The contrast $C \approx 14\%$ at $T = 2.0\,^{\circ}\mathrm{C}$ shows a temperature induced reduction by 1.25% in the shown temperature range.

While this temperature dependent behavior has to be accounted for in an application, we have shown the ability of magnetic field sensing over a wide temperature range, with only a small reduction in contrast and thereby small impact on sensitivity. If the temperature can be measured additionally in an application, the repeatable behavior would even allow to determine and apply a correction factor. Temperature correction is a common practice in other magnetic field sensor technologies like Hall sensors [146, 147].

3 Fluorescence Lifetime Based Sensing

Fluorescence intensity-based designs are subject to challenges like movement in the optical fiber or laser power fluctuations. Furthermore, in the previous chapter, we found drift components in the measurements, which can not be avoided by lock-in amplification and likely result from the intensity noise of the laser excitation. These fluctuations would be misinterpreted as magnetic field changes. In this chapter we investigate the use of the fluorescence lifetime as a non-intensity quantity for magnetic field sensing. In the literature the fluorescence lifetime was reported to show a relative change, similar to the fluorescence intensity, upon application of a magnetic field [148, 22]. We aim to utilize the fluorescence lifetime as a measurement quantity that is insensitive to the aforementioned fluctuations.

In this chapter, a sample composed of an ensemble of microdiamonds is characterized in a time-correlated single-photon counting (TCSPC) setup with regard to the magnetic field-dependent fluorescence lifetime. Therefore, first the concept of TCSPC is introduced, the specific setup for our case is described, and the findings are presented. Afterward, a setup is proposed in which the material is fixed to the tip of an optical fiber, where the same fiber is used for excitation and fluorescence collection. The magnitude and the phase of the fluorescence upon excitation with a varying frequency in the range up to 100 MHz is recorded and its dependence on magnetic fields is analyzed. Building upon the findings, the phase at one specific excitation frequency is used for magnetic field sensing and analyzed, concerning its immunity to disturbances and noise characteristics.

Lastly, we employ machine learning methods to utilize the information contained in the frequency domain data. We will address the ambiguity in the fluorescence intensity at low magnetic fields, as well as the temperature dependence we previously found.

3.1 Time-Correlated Single-Photon Counting

For the time-resolved measurement of the decay dynamics of fluorophores, time-correlated single-photon counting is a common tool in several branches of science. In the following sections we describe its principles and apply it to the material, used in this work.

3.1.1 TCSPC Theory

Consider the simplified model of a fluorophore with only one excited state and one ground state. Upon optical transition to the excited state, the fluorophore relaxes back to the ground state. This process is associated with an emissive rate Γ and a non-radiative decay k_{nr}. Here, all non-radiative processes have been combined to one rate constant k_{nr}. Both depopulate the excited state and we can define the quantum yield [149]

$$q = \frac{\Gamma}{\Gamma + k_{\mathrm{nr}}} \,, \tag{3.1}$$

that is the number of emitted photons per previously absorbed photons. The lifetime of the excited state is the average time the fluorophore stays in the excited state, given by

$$\tau = \frac{1}{\Gamma + k_{\mathrm{nr}}} \,. \tag{3.2}$$

In the concept of TCSPC, an infinitely short pulse of light excites the fluorophores, which results in an initial population n_0 to be transferred to the excited state. The excited state population then decays according to

$$\frac{\delta n(t)}{\delta t} = (\Gamma + k_{\mathrm{nr}}) n(t) \,, \tag{3.3}$$

where $n(t)$ is the time-dependent number of fluorophores, in our case NV centers, in the excited state. The individual fluorophores emit randomly throughout the decay. The solution to Equation 3.3 is an exponentially decaying

population. Since the fluorescence intensity is proportional to the excited state population, an experiment would observe the fluorescence intensity decay, given by

$$F(t) = F_0 e^{-\frac{t}{\tau}} \ . \tag{3.4}$$

F_0 is the initial intensity, which depends on the fluorophore concentration and several instrumental parameters, like excitation intensity or detection efficiency. In a more complex scenario, the decay may follow a multi-exponential function with different lifetimes and respective amplitudes. For NV centers in microdiamonds we can expect a multi-exponential decay, since the spin-sublevels of the excited state are associated with different lifetimes [72, 74, 77]. Additionally, short decay time components may be caused by surface or bulk impurities [150, 151] and we expect contributions from the neutral charge state NV^0, which differs in its lifetime from NV^- [151, 152, 153].

TCSPC is unique, in that it does not record the whole time trace from a single excitation. Rather, conditions are adjusted, that only one in many excitation pulses leads to a photon detection event (PDE) on a single photon detector, which observes the fluorescence. The time between excitation and PDE is measured for each detection event and stored in a histogram. The excitation is repeatedly done by a short pulse laser, with times between the repetitions much higher than the decay time of the fluorophore. Under these conditions, the histogram represents the waveform of the decay [149].

Some instrumental parameters need to be set for a TCSPC measurement:

Repetition rate A re-excitation of the sample before the decay of the fluorescence should be avoided. The repetition interval T_r between two excitations is usually chosen in the range of 10 to 20 times the observed lifetime. At an expected lifetime on the order of $\tau = 12\,\mathrm{ns}$, a repetition rate $\frac{1}{T_\mathrm{r}} = 8\,\mathrm{MHz}$ is reasonable.

Detector count rate The count rate at the detector observing the fluorescence is chosen so that, on average, one in 100 excitation pulses results in a PDE at the detector. Higher detection rates can lead to biasing towards the detection of photons arriving at shorter times, a phenomenon known as pulse pile-up. Consequently, we aim for a count rate of $\frac{1}{100T_\mathrm{r}} = 80\,\mathrm{kHz}$ at the detector in our application.

Timing resolution In practice the excitation light source does not emit an

infinitely short pulse of light. In the application, a short pulse diode laser with pulse lengths of full width at half maximum (FWHM) in the range of 30 ps to 200 ps is employed. For a Gaussian pulse, the RMS error e_{exc} is then approximated by the FWHM divided by 2.36.[1] Additional timing errors are introduced by jitter of the photodetector e_{det} and the time tagging module e_{tt}. These errors add up to

$$e_{\mathrm{tot}} = \sqrt{e_{\mathrm{exc}}^2 + e_{\mathrm{det}}^2 + e_{\mathrm{tt}}^2} \,. \tag{3.5}$$

We can compare the expected timing error to the actual error through the instrument response function (IRF), which depends on the shape of the excitation pulse and how the pulse is detected by the instrument. We usually capture the IRF by directly observing scattered excitation light.

The timing resolution is determined by the time quantization step width, i.e. the bin width in the histogram. It is chosen smaller than the analog error distribution, usually 1/10 of e_{tot}, to prevent additional errors. In the setup we present later, the expected error equals $e_{\mathrm{tot}} = 95\,\mathrm{ps}$. This error is determined using the values taken from the datasheets of the individual instruments. Thus, we choose a bin width of 10 ps. From e_{tot}, we expect a FWHM of the IRF of 218 ps.

Capture time The process of excitation and detection is repeated many times, commonly until greater than 10^3 counts have been collected in the histogram's peak channel. Depending on the bin width and the detector count rate, capturing a full histogram may take many seconds. Since the count rate is limited by the lifetime τ, the duration for capturing a full histogram can not be improved by faster detection electronics.

The acquired histogram contains the time differences between excitation and fluorescence photon detection events. It is further processed by subtracting the background count rate and subsequently fitting a model function to the data via a non-linear least-squares fitting (NLLS). We fit single- ($k = 1$) or multi-exponential ($k > 1$) functions

$$I_{\mathrm{fit}}^k(t) = \sum_{i=1}^{k} a_{k,i}\, \mathrm{e}^{-t/\tau_{k,i}} \tag{3.6}$$

[1] For a Gaussian waveform, the FWHM relates to the standard deviation σ by $FWHM = 2\sqrt{2\ln 2} \approx 2.36\sigma$.

to extract the lifetimes $\tau_{k,i}$ and their respective amplitudes $a_{k,i}$. The intention of NLLS fitting is to test whether a certain model is consistent with the data and to find the parameters of the model that are most likely to be correct. We aim to find the least-complex model that describes the data well. To judge the fit, we first examine the residuals, i.e. the difference between data and model. In the absence of systematic errors, the residuals are randomly distributed around zero and the model is likely to be correct. Additionally, we determine the goodness-of-fit parameter χ^2, given by the squared residuals, scaled by the variance for each observation

$$\chi^2 = \sum_{n=1}^{m} \frac{1}{\sigma_m^2} \Big(I_{\text{fit}}^k(t_n) - F(t_n) \Big)^2 \tag{3.7}$$

$$= \sum_{n=1}^{m} \frac{\Big(I_{\text{fit}}^k(t_n) - F(t_n) \Big)^2}{F(t_n)} \tag{3.8}$$

with m bins in the histogram [149]. The standard deviation σ_m for each bin is found through the Poisson statistics of the photon detection process as the square root of the number of photons recorded in the bin. χ^2 scales with the number of observations, which makes comparisons inconvenient. Therefore, we use the reduced χ^2_{R}, which is given by

$$\chi^2_{\text{R}} = \frac{\chi^2}{m - p} \,, \tag{3.9}$$

with the number of data points m and the number of free parameters p. Good fits are then given for χ^2_{R} close to unity.

3.1.2 TCSPC Setup

Here, we describe the optical and electrical setup for the time-based measurement of fluorescence lifetimes. A schematic of the TCSPC setup is shown in Figure 3.1a. A picosecond diode laser (BDS-SM-515, Becker & Hickl GmbH) is used to excite a sample via a dichroic mirror (DMLP550R, Thorlabs) and a microscope objective lens (CFI Plan Apo Lambda 60XC, Nikon). The beam is widened to $\approx 5.3\,\text{mm}$ (ACN127-030-A and LA1708-AB, Thorlabs) and focused by the objective to a beam spot size of $0.42\,\mu\text{m}$. The fluorescence is collected through the same objective and passed through the dichroic mirror and a 550 nm long-pass filter (FEL0550, Thorlabs). It is focused (LA1433-AB,

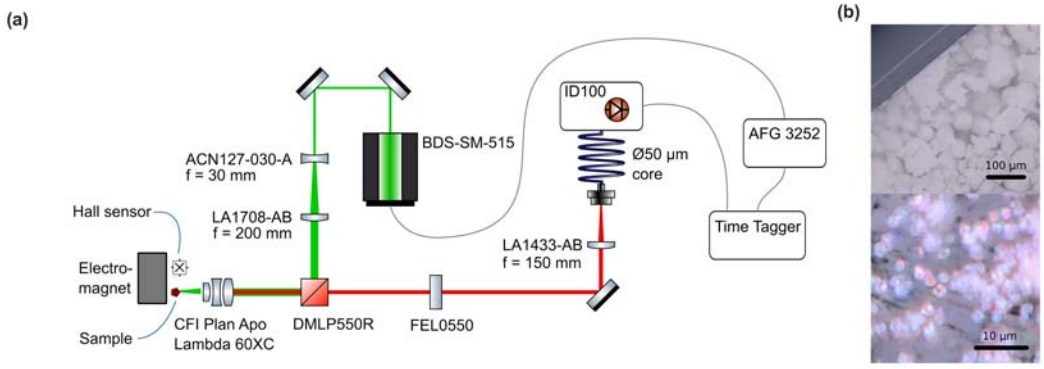

Figure 3.1: (**a**) Schematic of the optical setup used for lifetime measurements. (**b**) Photograph of the ensemble of microdiamonds in a glass cuvette. The lower panel shows a close-up that reveals individual crystals. A red hue appears due to contrast enhancement.

Thorlabs) onto the end facet of a multimode fiber, connected to an avalanche photodiode (APD) detector module (ID100, ID Quantique SA). Since we use no spatial filtering, a larger volume than the beam spot size is effectively excited and contributes to the collected fluorescence. The laser is triggered by a function generator (AFG3252, Tektronix Inc.), and histograms are acquired by a time-tagging module (Time Tagger 20, Swabian Instruments GmbH). A sample is mounted in front of an electromagnet connected to a laboratory power supply. A Hall effect-based sensor (TL493D, Infineon Technologies AG) next to the sample is used to measure the applied magnetic field. We measure the IRF by placing a cover slip in the sample location and acquiring the histogram without the long-pass filter in the beam path via reflection of the excitation light. The sample, shown in Figure 3.1b, is a powder composed of µm-sized diamonds with a high concentration of NV centers, which for the measurements was contained in a glass cuvette. For this material, we expect an isotropic response to magnetic fields, which has already been demonstrated for the use of fluorescence intensity [12].

The recorded fluorescence histograms are background-corrected by the average count in the first 20 ns and fit using a single- ($k = 1$) or double-exponential ($k = 2$) function by Equation 3.6 using NLLS analysis, implemented by LMFIT [154]. Normalized amplitudes of the multi-exponential components are denoted by $\hat{a}_{k,i} = a_{k,i} / \sum_{j=1}^{k} a_{k,j}$.

3.1.3 Results and Discussion

We captured histograms of the microdiamond powder sample, which are now further analyzed. In Figure 3.2a, a single histogram at zero magnetic field is shown. The histogram can be fit well using a double-exponential function resulting in $\chi^2_{\mathrm{R}} = 1.081$ with $\hat{a}_{2,1} = 0.675$, $\tau_{2,1} = 6.13\,\mathrm{ns}$, $\hat{a}_{2,2} = 0.325$, and $\tau_{2,2} = 14.54\,\mathrm{ns}$. A single exponential function would give a worse fit, with the residuals showing a systematic error instead of a normal distribution around zero. Next, the magnetic field was varied. We recorded the magnetic field-dependent fluorescence histograms, shown in Figure 3.2b, and analyzed them using either single- or bi-exponential fits, as shown in Figure 3.2c. We still see an overall better agreement of the data to a bi-exponential fit and B-field-dependent changes in the decay times, which correlate with the fluorescence intensity. The resolution of two decay time components is challenging if the decay times are of the same order of magnitude [149]. While the data support the acceptance of two decay components, the values of $a_{k,i}$ and $\tau_{k,i}$ are not well determined. To increase the quality of the fit for the application of magnetic field sensing, the fit parameters $\hat{a}_{2,1} = 0.65$ and $\hat{a}_{2,1} = 0.35$ are fixed. However, similar fits could also be obtained by a positive shift of $\hat{a}_{2,1}$ towards higher magnetic fields and a constant short decay time $\tau_{2,1}$, as well as intermediate values. To characterize the influence of B on a measurement quantity x, we define the magnetic contrast of the quantity as $1 - x(B)/x(B = 0)$ with the saturation value $x(B)$ towards high magnetic fields and its value at $B = 0$. The reduction in fluorescence count rate shows a magnetic contrast of 13.9% while the larger decay time displays a contrast of 15.2%.

The use of single-exponential fits can be found in the literature, where fluorescence lifetimes of 10.0 ns–12.9 ns for ensembles of NV centers [155, 156, 81, 148] and a range of 10 ns–30 ns for single centers [157, 144, 158, 153] are reported. However, even in single NV centers, the existence of a bi-exponential decay has been shown and is attributed to spin sub-levels of the excited-state ^{3}E with different lifetimes due to differing non-radiative decay rates to the intermediate singlet states [72, 74, 77]. Lifetimes of the sub-levels of 6.3 ns–9.0 ns for $\mathrm{m_S} = \pm 1$ and 12.0 ns–17.8 ns for $\mathrm{m_S} = 0$ have been found [72, 73, 74, 75, 76]. When an off-NV-axis magnetic field is present, a mixing of spin states arises [159]. This magnetic coupling leads to a lifetime of mixed states showing

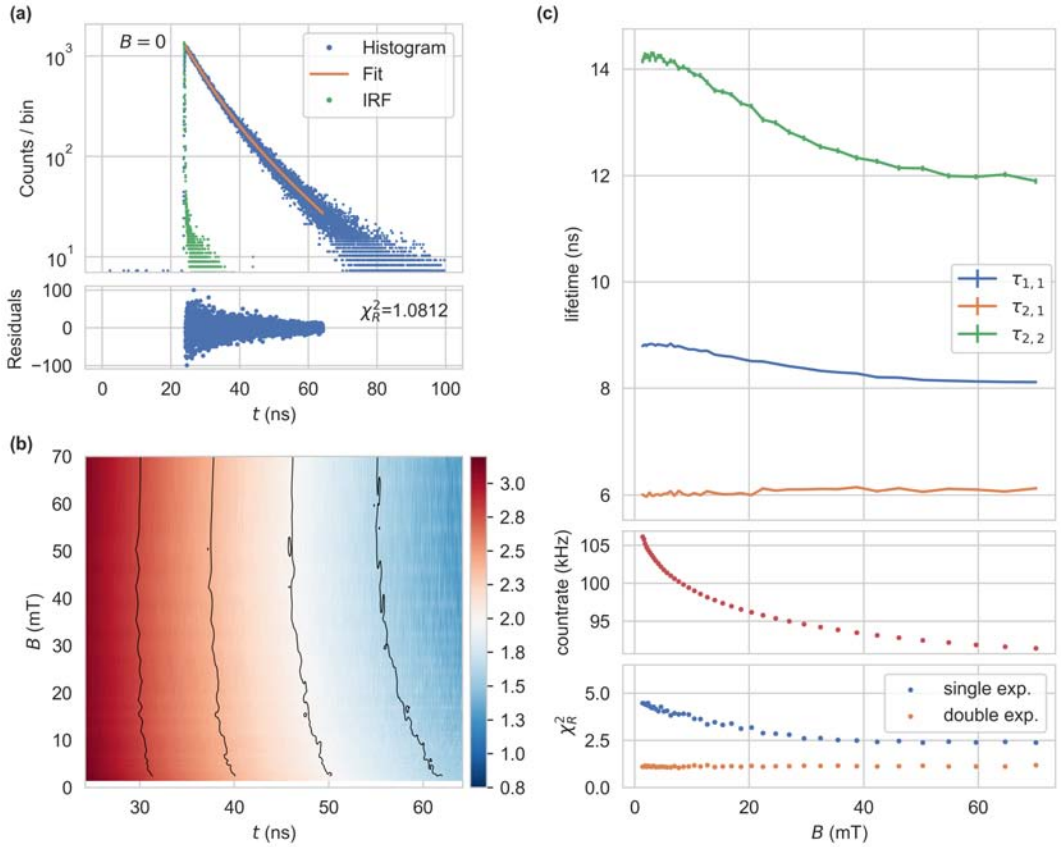

Figure 3.2: (**a**) Single- histogram of a sample composed of NV-rich diamond powder, captured at $B = 0$ (Bin width 10 ps, 15 s capture time, 8 MHz repetition rate, 240 µW average power, APD count rate 81 kHz). The average count in the first 20 ns of 5.7 counts has been subtracted. The lower panel shows the residuals of a double-exponential fit ($a_{2,1} = 848, \tau_{2,1} = 6.13$ ns, $a_{2,2} = 408, \tau_{2,2} = 14.54$ ns, $\chi^2_{\mathrm{R}} = 1.0812$). For the fit, we use a time span of 40 ns, following the maximum. The IRF was captured at the same count rate at the APD (FWHM = 0.2 ns). (**b**) Histograms of the sample at varying magnetic flux densities B, shown in the time range used for the fit. A logarithmic color scale is chosen. (**c**) Single and double-exponential fits for the data in (b) with fixed $\hat{a}_{2,1} = 1 - \hat{a}_{2,2} = 0.65$. The three panels show the extracted lifetimes, the count rate at the APD, and χ^2_{R} for the respective fits as functions of B.

an intermediate value, which has been observed for ensembles of NV centers in bulk diamond [148]. The reduction of the larger decay time by magnetic fields may be explained similarly in our measurements. In nanodiamonds, a short decay time component is usually attributed to surface or bulk impurities and the larger decay time component to the fluorescence of NV centers [150, 151, 160, 161]. Such effects may also explain the observation of a short-lived component in our measurement. Control or even tuning of these parameters can be achieved by radiation treatment, annealing, and surface termination [151]. Additionally, the crystal size has an influence on the observed lifetimes [161, 162] and we expect fluorescence contributions from the neutral charge state NV^0, which differs in its lifetime from NV^- [151, 152, 153]. Although further investigation is needed, the sample used in this work shows a magnetic field-dependent behavior that can be utilized in a sensing application.

	$\tau_{2,2}$ (ns)		C (%)	$\tau_{2,1}$ (ns)	
	$B = 0$	$B = 70\,\mathrm{mT}$		$B = 0$	$B = 70\,\mathrm{mT}$
Sample					
this work	14.1	11.90	15.60	6.01	6.13
15um-Hi	12.04	10.5	12.79	6.1	5.91
150um-Hi	8.96	8.39	6.36	4.26	3.85
Bulk	8.12			3.36	
DNV-B1	0			16.23	

Table 3.1: Magnetic field dependent changes in bi-exponential fits to fluorescence decays for three different samples. We include the magnetic contrast C for the larger time component. Additionally, the zero field fluorescence lifetimes for two bulk samples were measured.

We measured the magnetic field dependent fluorescence lifetime of further high NV-density microdiamond samples, namely 15um-Hi and 150um-Hi by Adámas Nanotechnologies, Inc. with mean sizes of 15 µm and 150 µm, respectively. The samples are specified to have NV concentrations of 3 ppm, measured by electron paramagnetic resonance. The results are shown in Appendix A.4. In both samples the fluorescence intensity decreases with increasing magnetic field, which is to be expected. The measurements can again be fit well with bi-exponential functions, showing a behavior which is qualitatively equal to the measurements in Figure 3.2. We summarize the fit parameters in Table 3.1, finding a decreasing larger time component $\tau_{2,2}$ and a decline in magnetic contrast with increasing crystal size. For comparison, we also acquired TCSPC

histograms of bulk diamonds at zero magnetic field. The sample denoted by *Bulk* is a 2 mm HPHT diamond with similar high NV concentration as the microdiamonds we used up to this point. Like the previous samples, the *Bulk* histograms can be fit well by a bi-exponential function. The correlation of decreasing lifetime with increasing crystal size is in line with previous samples. For the last sample, a CVD diamond with a typical 0.3 ppm NV-concentration (DNV-B1, Element Six (UK) Ltd.), the histograms can be fit well by a single-exponential function with a significantly higher lifetime than previous samples.

3.2 Frequency Domain Lifetime Measurements

While TCSPC measurements deliver complete histograms, their implementation is technically demanding. Additionally, the acquisition is slow when considering the application of magnetic field sensing. A setup based on the frequency domain measurement is proposed to make use of the change in the excited-state fluorescence lifetime of NV centers for magnetometry. The fluorescence response can be understood as a convolution of the excitation signal with the decay dynamics, acting as a low-pass filter. Instead of monitoring the time-domain decay from a short excitation pulse, we employ a harmonic oscillation with a variable frequency. With an increasing frequency, the low-pass characteristic will lead to a reduction of the fluorescence amplitude, commonly referred to as demodulation. This is accompanied by a phase shift of the fluorescence signal from 0° to 90° [149]. In our setup, we intensity modulate the excitation light, sweep the frequency of the modulation up to 100 MHz, and record the system response in both amplitude and phase. This frequency response not only contains the effects of the NV diamond powder, but additionally the effects of all electronic and optical components involved in the excitation and recording of the fluorescence. Examples for such effects are a frequency-dependent excitation power or the transition time of the signal through the system, leading to a frequency-dependent phase shift. Therefore, we record a reference frequency response at $B = 0$, which is used to calibrate subsequent measurements. The resulting measurements then directly reflect the change in the fluorescence decay dynamics at the application of a magnetic field.

3.2.1 Frequency Domain Concept

In Figure 3.3, we show the concept of frequency domain lifetime measurements with the example of a single lifetime component of $\tau = 12\,\text{ns}$. The excitation is continuously modulated in its intensity at a specific modulation frequency, shown in the time domain representation in the left panel. The emission follows the excitation at a reduced amplitude, due to the demodulation, given by

$$m = \frac{B/A}{b/a}\,, \tag{3.10}$$

with the intensity offsets a, A and amplitudes b, B. The emission is also shifted in phase with regard to the excitation. With increasing frequency, the low-pass behavior of the decay dynamics results in a phase ϕ of up to 90°, shown in Figure 3.3b.

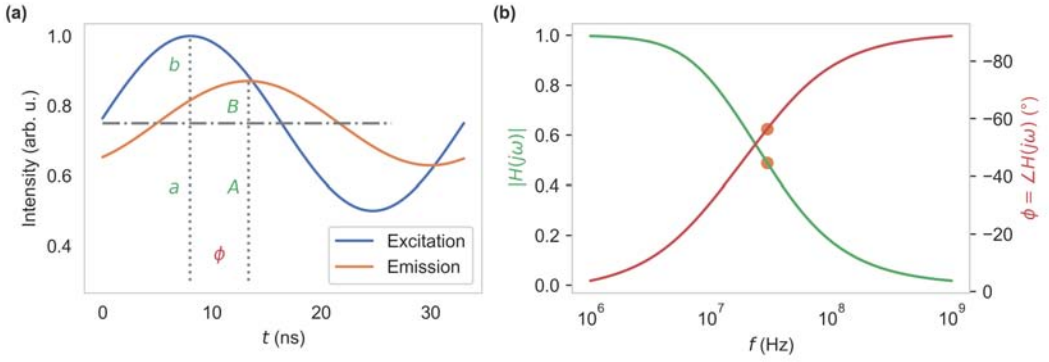

Figure 3.3: Concept of the frequency domain lifetime measurement. (**a**) Time domain representation of the excitation and the emission at one excitation frequency. (**b**) Frequency domain plot of the demodulation $|H(j\omega)|$ and the phase $\phi = \angle H(j\omega)$. The orange dots indicate the magnitude and phase of the emission in the example in (a).

Different lifetimes now change the frequency-dependent modulation and phase relationship. While a single lifetime component τ can be determined from either magnitude or phase at a single frequency [149], one can also measure the response at numerous frequencies and use NLLS fitting of the frequency response. This process becomes mandatory for a multi-exponential decay. From the transfer function in the Laplace domain of Equation 3.6,

given by

$$H(s) = \sum_{n=1}^{k} H_n(s) = \sum_{n=1}^{k} \frac{a_n \tau_{k,n}}{1 + s\tau_{k,n}} \tag{3.11}$$

with $s = \sigma + j\omega$, we can determine magnitude and phase of the frequency response $H(j\omega)$:

$$|H(j\omega)| = \sum_{n=1}^{k} |H_n(j\omega)| = \sum_{n=1}^{k} \frac{a_n \tau_{k,n}}{\sqrt{1 + (\omega\tau_{k,n})^2}} \,, \tag{3.12}$$

$$\angle H(j\omega) = \frac{1}{|H(j\omega)|} \sum_{n=1}^{k} -|H_n(j\omega)| \arctan(\omega\tau_{k,n}) \,. \tag{3.13}$$

Frequency domain setups typically have to correct for the instrument response function, introduced by the electrical and optical components, such as a non-constant modulation of the excitation light with frequency variation, or the lengths of cables and optical paths, introducing phase shifts. They therefore record a reference frequency response to which further measurements can be compared, typically by alternatively observing the sample and scattered light. Response data in the form of those in Figure 3.3b can then be obtained by correction of measurements with the reference response, enabling a fit of equations 3.12 and 3.13. Since in our application we are only interested in the effect of magnetic fields on the sensing material, we do not aim to recover the different lifetime components from the measurements. Rather, we record a reference response at zero-field, which we then compare further measurements to, simplifying the application of the frequency domain concept.

3.2.2 Frequency Domain Setup

The optical setup for the described measurement method is comparable to the time-domain setup. The main difference lies in the need for a continuous excitation with a varying frequency intensity modulation and a continuous fluorescence detection. The specific optical and electrical setup we use here is depicted in Figure 3.4a. A 520 nm laser diode (PLT5 520B, ams-OSRAM AG) is driven by a constant current source based on a laser driver integrated circuit (NZN, iC-Haus GmbH). Additionally, it is modulated by an AC-coupled radio frequency (RF) amplifier (35 dB, 1–700 MHz, 3.2 W) at an input power of −9 dBm. The collimated excitation light propagates through a dichroic beam

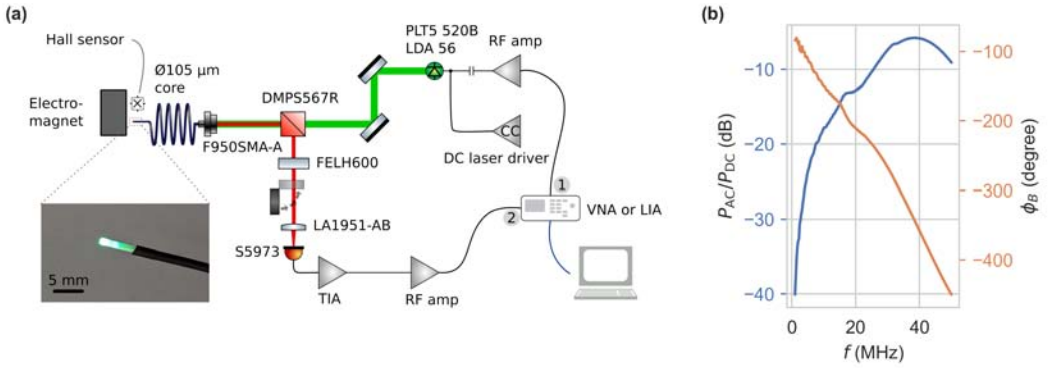

Figure 3.4: (**a**) Schematic of the optical and electrical setup used for frequency domain measurements. (**b**) Excitation light modulation $P_{\mathrm{AC}}/P_{\mathrm{DC}}$ measured via reflections with the long-pass filter removed and the phase difference ϕ_B between the excitation and the reception signal.

splitter (DMPS567R, Thorlabs) and is coupled to a 105 µm core diameter fiber. The end facet of the fiber is coated with NV-rich diamond powder in glue, with crystal sizes much smaller than the facet diameter.

The material is comparable in NV density to the material used in [12]. The fiber sensor was manufactured by Quantum Technologies GmbH in collaboration with the Leibniz Institute of Surface Engineering. The fluorescence is collected through the same fiber, passing through a long-pass filter and focused (FELH600 & LA1951-AB, Thorlabs) onto a Si-photodiode (S5973, Hamamatsu Photonics K.K.). The photodiode is part of a transimpedance amplifier based on an OPA847 operational amplifier (300 MHz, 1.2 kΩ). Its output is passed through a low-noise RF amplifier (20 dB, 0.1–2000 MHz) to a PicoVNA 106 vector network analyzer (VNA) (Pico Technology) or a HF2LI lock-in amplifier (Zurich Instruments AG), which also drives the laser diode modulation. An electromagnet, connected to a PC-controlled power supply, is being monitored by a Hall effect sensor and enables the application of magnetic flux densities from 0 mT to 120 mT.

The modulation of the excitation light can be described by an offset P_{DC} and an amplitude of the AC component P_{AC}. To assess the modulation, we measured these via reflection of the pump beam after removing the long-pass filter at the DC-coupled TIA output. Their ratio $P_{\mathrm{AC}}/P_{\mathrm{DC}}$ is depicted in Figure 3.4b. It shows a high pass characteristic and an overall non-constant ratio originating from the RF amplifier for the laser modulation. The laser diode

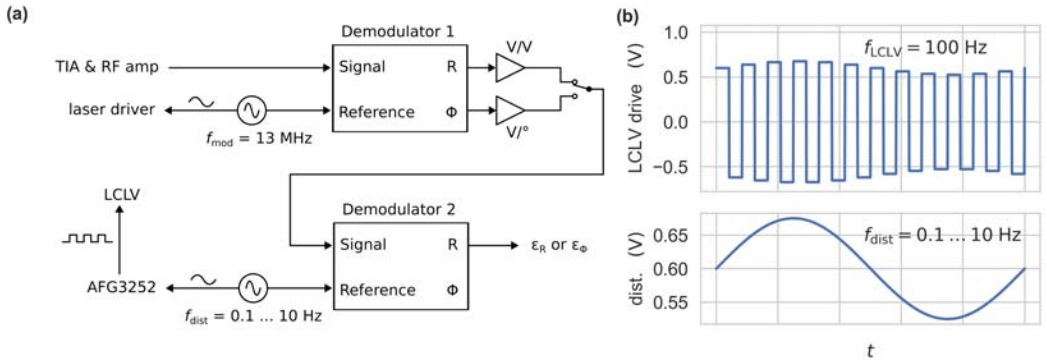

Figure 3.5: (**a**) Schematic of the electrical setup for disturbance measurements with a LCLV. A first LIA channel monitors magnitude and phase at a reference frequency $f_{\mathrm{mod}} = 13\,\mathrm{MHz}$. A second LIA channel demodulates either R or Φ from the first channel at the disturbance frequency. (**b**) Qualitative drive signal for the LCLV in the upper panel, which is amplitude modulated by the disturbance signal, shown in the lower panel.

output power was measured before the dichroic mirror, and varied between 33 and 37 mW, depending on the modulation frequency. The use of a VNA, in particular, requires the calibration of the scattering parameter S_{21}, i.e. the magnitude and phase relationship of the signals of ports one and two. Therefore, *isolation* and *through* was calibrated by either blocking the fluorescence path or passing it unrestricted to the photodetector, ensuring no magnetic field was applied to the sensor head. Thus, the VNA automatically corrects for the reference frequency response.

Later, we use the LIA at a fixed excitation frequency and observe the magnitude and phase, while adding an artificial disturbance in the excitation light intensity. We investigate the impact of excitation intensity changes on the two measurement quantities, which can be caused e.g. by bending of the optical fiber, laser intensity drift, or instabilities in the optical path. The artificial intensity modulation is implemented through a Liquid Crystal Light Valve (LCLV) by Liquid Crystal Technologies Inc., placed in the beam path of the collimated laser. In Figure 3.5a, we show the schematic of the respective electrical setup. The first LIA channel monitors magnitude and phase at a reference frequency $f_{\mathrm{mod}} = 13\,\mathrm{MHz}$. A second LIA channel demodulates either the magnitude R or the phase Φ from the first channel at the disturbance frequency f_{dist}. We apply a 100 Hz mean-free rectangular waveform to drive

the LCLV, employing a function generator (AFG3252, Tektronix Inc.). The disturbance modulation is then used to amplitude modulate this LCLV drive signal, continuously changing the transmission of the LCLV, which we show in the lower panel of Figure 3.5b. The transmission modulation response of the shutter drops off at 1 Hz, which is the reason why we sweep f_{dist} only in a range of 0.1 to 10 Hz. This is sufficient to investigate the disturbance behavior of the two measurement quantities.

3.2.3 Results and Discussion

Figures 3.6a,b show the magnitude and the phase of the fluorescence signal as a function of modulation frequency and the applied magnetic field relative to $B = 0$. They were acquired acquired with the VNA. The horizontal and vertical lines correspond to the other measurements shown in the figure. On the left edge at near zero frequency, we see a relative magnetic contrast of 16% in magnitude, which has already been observed and used for all-optical magnetometry [12, 4]. These observations shows this approach to be a generalized form of intensity-based read-out, used in Chapter 2. The magnetic field dependent intensity modulation can thus be attributed to the change in the lifetime components. At higher modulation frequencies, this behavior changes significantly. The magnitude for all $B > 0$ declines, and a response of the phase to magnetic fields emerges. The phase displays a maximum in the magnetic contrast of 5.8° at 13 MHz. Towards higher modulation frequencies, both quantities decrease in magnetic contrast, and the magnitude rises above one at an inflection point around 30 MHz. At this frequency, the magnitude is nearly independent of the magnetic field (see pink trace in Figure 3.6e) while the phase still shows a magnetic contrast of 3.6°. This could potentially be used to calibrate the optical path. At lower optical excitation powers, we observe a similar behavior with the difference of a lower signal-to-noise ratio and a decrease in magnetic contrast of both measurement quantities. Many fiber sensors were produced and show good reproducibility in fluorescence intensity and response to static magnetic fields, but lifetime measurements were only performed for one fiber. We also expect lifetime measurement results to be similar for different fiber sensors.

We operate the system at optical excitation powers for which we expect no saturation behavior [163, 164]. In this linear regime, the fluorescence can be

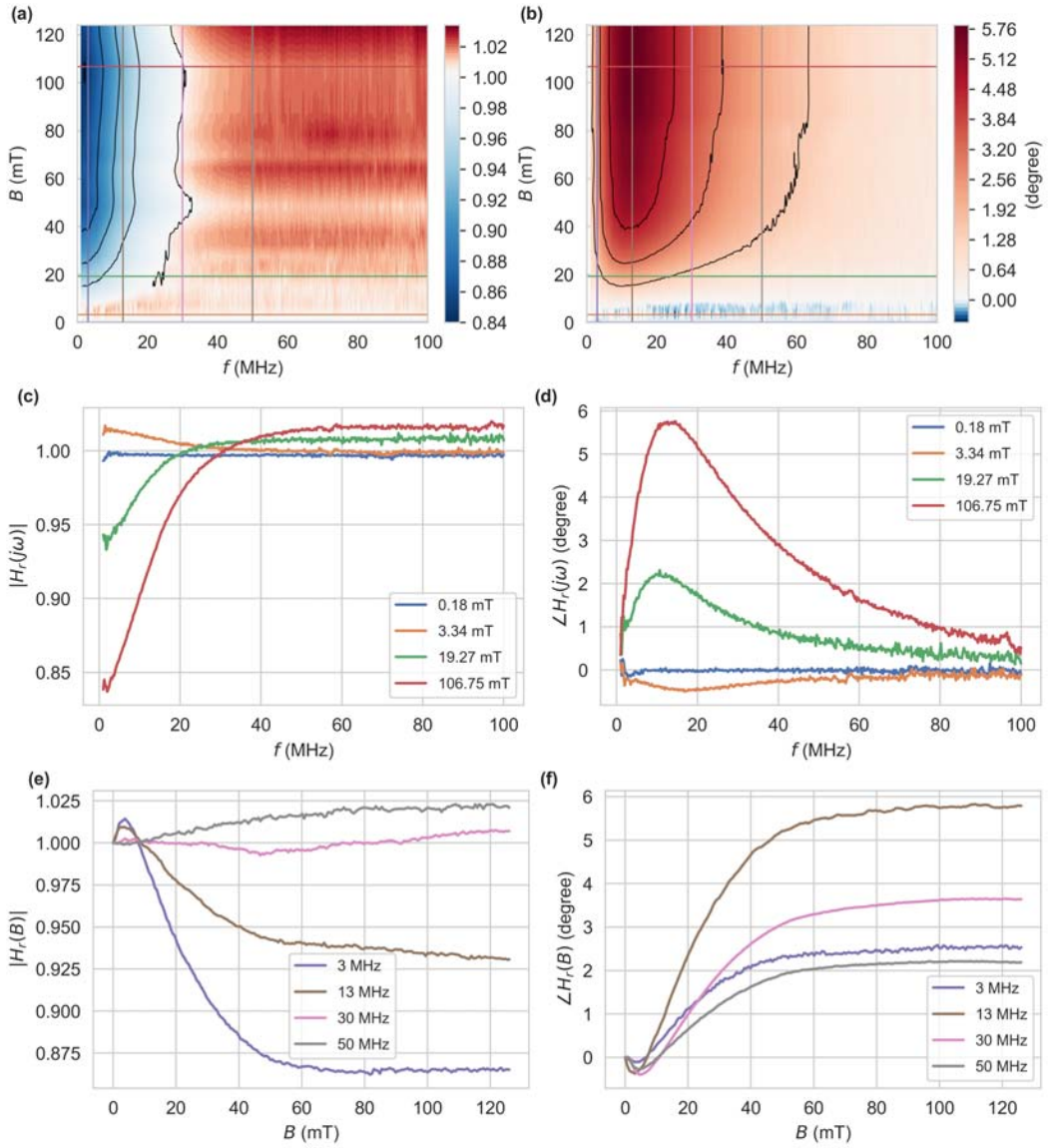

Figure 3.6: Measurements of the complex transfer function $H_r = |H_r|e^{j\angle H_r}$. The left and right columns show the magnitude $|H_r|$ and phase $\angle H_r$, respectively. H_r is the transfer function $H(j\omega, B)$, relative to $H(j\omega, B = 0)$. (**a**–**d**) were obtained directly by sweeping the modulation frequency using a VNA, which was calibrated at $B = 0$. For (**e**,**f**), a LIA at the respective modulation frequencies was used to capture magnitude and phase. The data were subsequently normalized to the value at $B = 0$.

understood as a convolution of the excitation signal with the decay dynamics, acting as linear time-invariant (LTI) system, specifically a low-pass filter. Considering single- and bi-exponential fluorescence decays, their respective transfer functions $H(s)$ can be written as

$$H(s) = \frac{a_{2,1}}{s + \frac{1}{\tau_{2,1}}} + \frac{a_{2,2}}{s + \frac{1}{\tau_{2,2}}} \tag{3.14}$$

by the Laplace-transform of Equation (3.6), where for a single-exponential approach $a_{2,2} = 0$. To model the measurements in Figure 3.6, the normalization to $H(s; B = 0)$ is considered, resulting in $H_r(s) = \frac{H(s;B)}{H(s;B=0)}$. The magnitude $|H_r(j\omega)|$ and the phase $\angle H_r(j\omega)$ can then be obtained from this $H_r(s)$. To reproduce the inflection point around 30 MHz and a magnitude greater one at high modulation frequencies, at least a bi-exponential approach is needed. This necessity becomes apparent when considering

$$H_r(s) = \left(1 + \frac{\Delta a}{a_{1,1}}\right) \frac{s(\tau_{1,1} + \Delta\tau) + 1 + \frac{\Delta\tau}{\tau_{1,1}}}{s(\tau_{1,1} + \Delta\tau) + 1} \tag{3.15}$$

for a single-exponential approach, with

$$\begin{aligned} \tau_{1,1}(B) &= \tau_{1,1}(B = 0) + \Delta\tau(B) \ , \\ a_{1,1}(B) &= a_{1,1}(B = 0) + \Delta a(B) \ , \end{aligned} \tag{3.16}$$

and $\Delta\tau$, Δa being functions of B. $|H_r(s = j\omega)|$ can then only be strictly greater or less than one for $\Delta\tau > 0$ or $\Delta\tau < 0$, respectively. Therefore, a single-exponential approach is insufficient to model this behavior. The data can, however, be fit by $H_r(s)$ with constant factors $\hat{a}_{2,1} = 1 - \hat{a}_{2,2} = 0.65$ resulting in $\Delta\tau_{2,1} = -2.52\,\text{ns}$ and $\Delta\tau_{2,2} = 0.19\,\text{ns}$ at $B > 100\,\text{mT}$. These findings agree well with the fits to the time-domain histograms from Figure 3.2. Analogous to the time domain fits, similar fitting transfer functions could be obtained from a constant $\tau_{2,2}$ and a shift in $\hat{a}_{k,i}$, or intermediate values. The exact dynamics do not need to be deduced from these measurements, as the behavior, especially the reduction in the larger decay time, allows the utilization in a sensing application. This may be done by capturing the complete frequency response to calculate the applied magnetic field. Alternatively, we record the magnitude and the phase at one excitation frequency with a LIA, yielding a

higher acquisition speed.

The key advantage of using the phase instead of the magnitude lies in its immunity to disturbances that affect the intensity of the signal. These disturbances include laser intensity noise and thermal drifts in the optical alignment, as well as motion in the fiber, causing fluctuations in the excitation and the returning fluorescence. We use a LIA to monitor and compare the magnitude and the phase. Hence, we set the excitation frequency to $f = 13\,\mathrm{MHz}$, where the phase shows the maximum contrast. Now, we test the disturbance immunity. We add a small modulation of the laser intensity in a frequency range up to 10 Hz. This translates to an excitation intensity modulation, which can be expected in an application through attenuation by, e.g. bending of the fiber. This artificial disturbance is achieved by a LCLV placed between the adjustment mirrors and the dichroic beam splitter, which can be continuously modulated in its transmission. Figure 3.7a shows magnitude $|H_r|$ and phase $\angle H_r$ in a time range of 20 s. The additional disturbance modulation with frequency $f_{\mathrm{dist}} = 1\,\mathrm{Hz}$ is switched on at $t = 5\,\mathrm{s}$, which leads to an excitation intensity of 8.88 mW fluctuating with $\pm 0.17\%$. Additionally, at $t = 12\,\mathrm{s}$, a magnetic field of $> 100\,\mathrm{mT}$ was applied for an easy comparison of both measurement quantities to their magnetic contrast. A lower impact on $\angle H_r$ relative to its contrast is obvious.

To measure these errors in a wider frequency range and at a higher precision, the LIA's 13 MHz demodulator outputs R or ϕ were fed back into a second demodulator, running at f_{dist} and therefore measuring the root-mean-square (RMS) value of the disturbance modulation components. We set the first demodulator low-pass filter to 1 kHz, making sure the additional disturbance component passes to the second one without attenuation. Additionally, a bias magnetic field corresponding to half of the magnetic contrast was applied to bring the system to a point of operation that is realistic during an application. We then swept f_{dist} in a frequency range of 0.1 Hz to 10 Hz and recorded the second demodulator output. This second output is a measure for the low-frequency disturbances in magnitude or phase, which we denote by ϵ_R or ϵ_ϕ, respectively. They are shown in Figure 3.7b. For lower frequencies $\epsilon_R \approx 1.1 \times 10^{-3}$, which is 2.3% of the magnetic contrast of $|H_r|$. In comparison $\epsilon_\phi \approx 0.35 \times 10^{-3}$ degree, a disturbance of only 0.02%, relative to the magnetic contrast of $\angle H_r$. Above $f_{\mathrm{dist}} = 1\,\mathrm{Hz}$, the LCLV drops off in its modulation

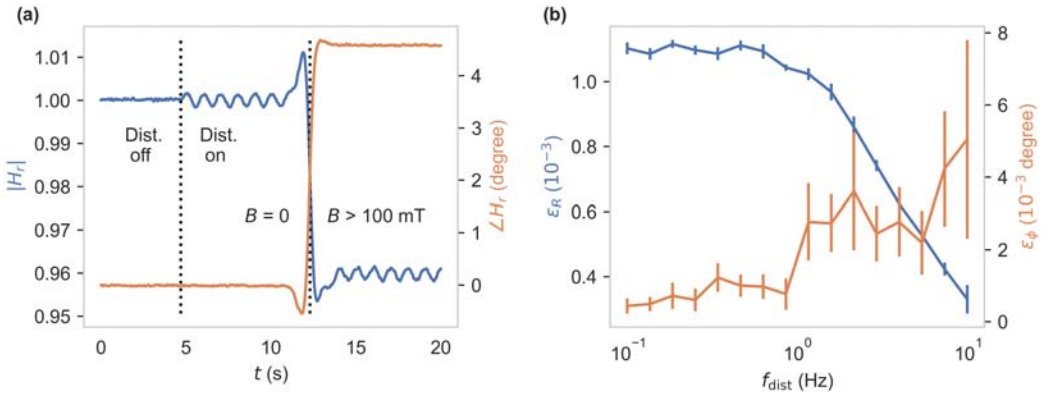

Figure 3.7: (**a**) Measurement quantities $|H_r|$ and $\angle H_r$ at $f = 13\,\mathrm{MHz}$ (4th order, 3.89 Hz low-pass demodulator). The excitation disturbance modulation with frequency $f_{\mathrm{dist}} = 1\,\mathrm{Hz}$ was switched on at $t = 5\,\mathrm{s}$. For comparison to the magnetic contrasts of both quantities, a magnetic field of > 100 mT has been applied at $t = 12\,\mathrm{s}$. (**b**) Root-mean-square values of the AC components of the magnitude and the phase at the disturbance frequency f_{dist} in a range of 0.1–10 Hz. Here, a bias magnetic field corresponding to half of the magnetic contrast was applied.

amplitude, leading to a reduction in ϵ_R and a higher error in the measurement of ϵ_ϕ. This is caused by the slow response of the LCLV, and we expect the immunity to persist at higher frequency disturbances.

The sensitivity achievable by both approaches, i.e. the magnitude or the phase as a measurement quantity, was further investigated. Therefore, a bias magnetic field of $B = 20\,\mathrm{mT}$ was applied, and data were recorded with the LIA set to $f = 13\,\mathrm{MHz}$ and subsequently converted to magnetic field values using linear fits to $|H_r(B)|$ and $\angle H_r(B)$, depicted in the insets of Figure 3.8. The respective noise spectral densities shown in Figures 3.8a,c reveal a white noise region above 1 Hz with sensitivities of $s_r = 35\ \mu\mathrm{T}/\sqrt{\mathrm{Hz}}$ and $s_\phi = 20\ \mu\mathrm{T}/\sqrt{\mathrm{Hz}}$. The excitation light source was operated at 11.5 mW. In this case, the fluorescence signal leads to a photodiode current with DC component $i_{\mathrm{DC}} = 0.213\,\mu\mathrm{A}$ and amplitude of the AC component of $i_{\mathrm{AC}} = 0.171\,\mu\mathrm{A}$ at $f = 13\,\mathrm{MHz}$. This results in shot-noise-limited sensitivities (SNLS) of $s_{r,snl} = 1.13\ \mu\mathrm{T}/\sqrt{\mathrm{Hz}}$ and $s_{\phi,snl} = 0.95\ \mu\mathrm{T}/\sqrt{\mathrm{Hz}}$. See Section 2.2.2 for the derivation of the SNLS in LIA-based setups. The difference in the achieved sensitivities is largely based on the TIA's output noise spectral density, being limited by the feedback resistor's thermal noise of $4.4\ \mathrm{nV}/\sqrt{\mathrm{Hz}}$ and the operational amplifier's input current

noise contributing 3.24 nV/$\sqrt{\text{Hz}}$. These dominate the shot noise, contributing only 0.336 nV/$\sqrt{\text{Hz}}$ at the given photocurrent. The same measurement at $f = 3\,\text{MHz}$ leads to sensitivities of $s_r = 12\ \mu\text{T}/\sqrt{\text{Hz}}$ and $s_\phi = 43\ \mu\text{T}/\sqrt{\text{Hz}}$, which are caused by different magnetic contrasts at this frequency (see Figure A.8 in the appendix). Additional 1/f components dominate the spectrum below 1 Hz in both approaches. These are attributed largely to the excitation and detection electronics.

For the data from the two approaches, using magnitude and phase as measurement quantities, we show the respective Allan deviations in Figures 3.8b,d. In both cases, an increasing averaging time τ initially leads to a reduction in standard deviation up to $\tau \approx 1\,\text{s}$, which we expect from white noise at the corresponding frequencies in the noise spectral densities. Since the magnitude data shows a higher 1/f noise corner frequency, the minimum in the Allan deviation occurs at a lower averaging time, compared to the phase data. Also, this bias instability is lower than for the phase data at $\sigma_{\phi,\text{Allan}} = 11.5\,\mu\text{T}$, compared to the magnitude data at $\sigma_{r,\text{Allan}} = 41\,\mu\text{T}$. Even at 3 MHz excitation, the magnitude still shows a higher bias instability with $\sigma_{r,\text{Allan}} = 22.4\,\mu\text{T}$ at $\tau = 0.26\,\text{s}$. In the whole range of investigated averaging times, the phase-based approach shows a lower standard deviation, compared to the magnitude.

Lastly, we investigate the combination of magnitude- and phase-data to a single measurement quantity. We therefore use inverse-variance weighting of the estimated magnetic fields B_r and B_ϕ from magnitude- and phase-approach, respectively. A combined estimate of the magnetic field is given by

$$B_{\text{ivw}} = \frac{B_r/\sigma_r^2 + B_\phi/\sigma_\phi^2}{1/\sigma_r^2 + 1/\sigma_\phi^2} = \left(B_r/\sigma_r^2 + B_\phi/\sigma_\phi^2\right)\sigma_{\text{ivw}}\ , \tag{3.17}$$

which has the lowest variance among all weighted averages of magnitude- and phase-derived magnetic fields [165]. The variance of the resulting quantity is then given by $\sigma_{\text{ivw}} = 1/\sigma_r^2 + 1/\sigma_\phi^2$. For weighting, we used the Allan deviations at $\tau = 1 \times 10^{-1}\,\text{s}$ which correspond to white noise regions in the spectral densities, i.e. $\sigma_r^2 = 6492\,\mu\text{T}^2$ and $\sigma_\phi^2 = 2309\,\mu\text{T}^2$. For the given data, the spectral density and Allan deviation are shown in Figures 3.8e,f. In the white noise frequency range we can achieve a sensitivity of $15.7\,\mu\text{T}/\sqrt{\text{Hz}}$ which is lower than in magnitude- or phase-approach alone. Towards lower frequencies, i.e. longer integration times however, both measurement quantities can no

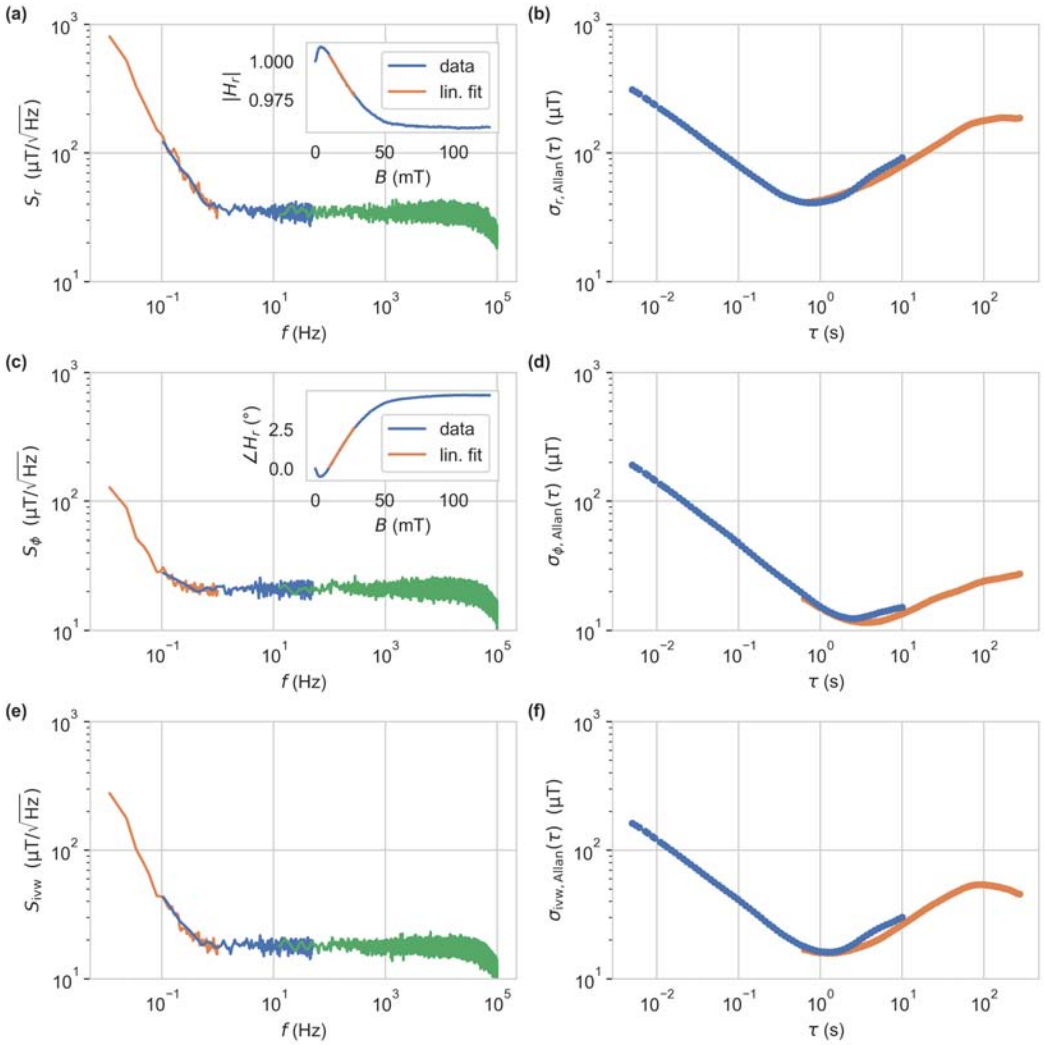

Figure 3.8: Noise spectral densities based on magnitude S_r (**a**) and phase S_ϕ (**c**). The excitation frequency was set to $f = 13\,\mathrm{MHz}$, and a bias field of $B = 20\,\mathrm{mT}$ was applied. Data were recorded by the LIA with the low-pass filter set to fourth order at corner frequencies of 88 kHz, 200 Hz and 2 Hz, corresponding to the green, blue and orange traces. They have been subsequently converted to magnetic field values using the linear fits drawn in the respective insets and converted to spectral densities by Welch's method (Hann windows of lengths 0.31 s, 9.38 s, 85.31 s). Allan deviations of magnitude (**b**) and phase (**d**) from the data in (a) and (b). Spectral density (**e**) and Allan deviation (**f**) of inverse-variance weighted average of magnitude and phase data from (a) and (c).

longer be assumed to be unbiased estimators of the underlying true magnetic field. Therefore, we find a higher bias instability and higher random walk in B_{ivw} than in the phase data alone. Thus at higher observation times, in this case $\tau > 1\,\mathrm{s}$, the use of a weighted average of both measurement quantities is not recommended.

3.3 Resolving the Ambiguity

In NV rich diamonds, we observe a dip in the fluorescence intensity at zero magnetic field [32]. Current research relates this dip to dipolar coupling between neighboring NV centers, leading to a mixing of spin states [29, 100]. The same feature can also be observed when using the phase as a measurement quantity [1]. This leads to an ambiguity, i.e. a non-injective function, for magnetic fields below $\approx 8\,\mathrm{mT}$. We plot the fluorescence intensity as a function of magnetic fields in the left panel of Figure 3.9, qualitatively, showing this behavior.

The measurement of the phase or the intensity at a fixed excitation frequency can be realized with a lock-in amplifier, yielding a high acquisition speed and a potentially simpler implementation, compared to using a whole frequency sweep. The complete response of the magnitude and the phase in a frequency range of 1–100 MHz on the other hand holds more information. In this section we utilize the complete response to resolve the ambiguity in all-optical magnetic field sensing. First we prove this ability of resolving the ambiguity by fitting the data with a model function and use the fit parameters for regression. Afterwards, we explore the use of neural networks with the raw spectra as inputs, omitting the fitting process, which is less computationally expensive. These two approaches are shown schematically in Figure 3.9.

In principle, the use of a bias field greater than 3 mT is also possible to overcome this ambiguity problem. However, we would lose the ability of isotropic sensing, which is an important feature for the implementation in a measurement application [12]. Additionally, a bias field, e.g. by a permanent magnet in the fiber head, would drop the properties of a non-magnetic and non-conductive sensor head. This would restrict the universal applicability of the sensor head.

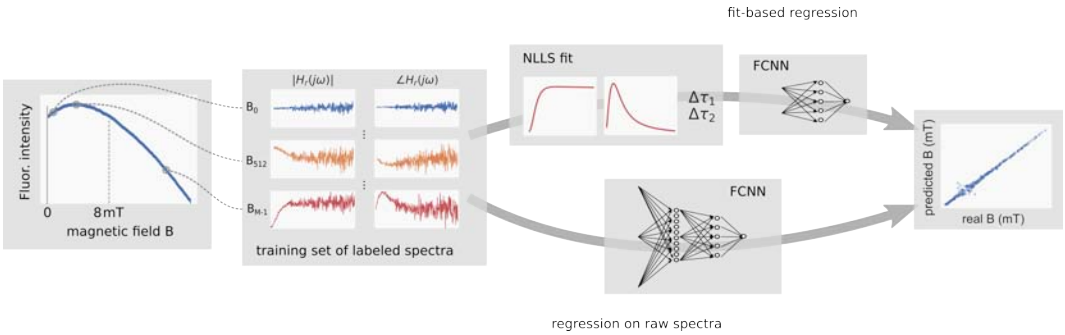

Figure 3.9: Schematic of the machine learning approach. A dataset of labeled spectra at different magnetic fields up to 15 mT is captured and processed in two ways. The spectra consist of the magnitude and the phase of the fluorescence from a frequency sweep of the optical excitation up to 100 MHz. The spectra are processed by either fitting a model function with two degrees of freedom and a subsequent simple regression neural network or a more complex neural network which is trained on the raw spectra.

3.3.1 Measurement Setup

Here we use the setup shown in Figure 3.4a, except for a different laser driver. Instead of an AC-coupled, sinusoidal current modulation, we use a square wave excitation. The modulation is implemented by a comparator (LTC6752, Analog Devices Inc.), digitizing the incoming sinusoidal signal from the VNA and controlling a laser switch integrated circuit (iC-HKB, iC-Haus GmbH). The VNA is sensitive only to the fundamental frequency, making the results comparable to previous studies. We not only simplify the setup with this step, but also make it more immune to distortions and reduce dependency of the modulation $P_{\mathrm{AC}}/P_{\mathrm{DC}}$ on the frequency (previously shown in Figure 3.4b).

Fit-based Regression

For the following section we accept that the fluorescence decay can be described by a bi-exponential function. The respective transfer function can then be written as the sum of two first-order low-pass filters

$$H(s) = \frac{a_1}{s + \frac{1}{\tau_1}} + \frac{a_2}{s + \frac{1}{\tau_2}} \tag{3.18}$$

with $s = \sigma + j\omega$, following the Laplace-transform of the sum of two exponential functions. Compared to Equation 3.14 we just dropped the index, which

indicated a bi-exponential fit. The VNA corrects for the system response $H(s; B = 0)$. This system response results from all electrical and optical components necessary for the measurement, as well as the low-pass characteristic of the fluorescence itself. The resulting measurement can be described by the ratio $H_r(s) = H(s; B)/H(s; B = 0)$.

We fit the recordings of the system response at different B-fields with $H_r(s)$, using non-linear least squares fitting. Therefore we write the independent components as their values at $B = 0$ and additional B-field dependent terms Δa_1, Δa_2, $\Delta\tau_1$, and $\Delta\tau_2$. To increase the quality of the fit for the application of magnetic field sensing, the fit parameters $a_1 = 0.65$ and $a_2 = 0.35$ are fixed, i.e. $\Delta a_1 = \Delta a_2 = 0$. These values stem from the previously described TCSPC measurements. Additionally, the decay times at zero field $\tau_{1,B=0}$ and $\tau_{2,B=0}$ were constrained to be the same for all data sets. The fitting process was done in two steps. First we recorded a set of 30 measurements at different magnetic fields up to 80 mT to fit $\tau_{1,B=0}$ and $\tau_{2,B=0}$. This small set was chosen due to the large necessary computation time. It is still sufficient to reliably estimate $\tau_{1,B=0}$ and $\tau_{2,B=0}$. In the second step, we collected 1000 system responses up to 15 mT with a distribution favoring low magnetic fields and in a random order. All data sets were fit individually with the previously found parameters for $\tau_{1,B=0}$ and $\tau_{2,B=0}$ set constant, yielding $\Delta\tau_1(B)$ and $\Delta\tau_2(B)$. In Figure 3.10 we show a subset of measured frequency responses at different B-fields with their corresponding fits.

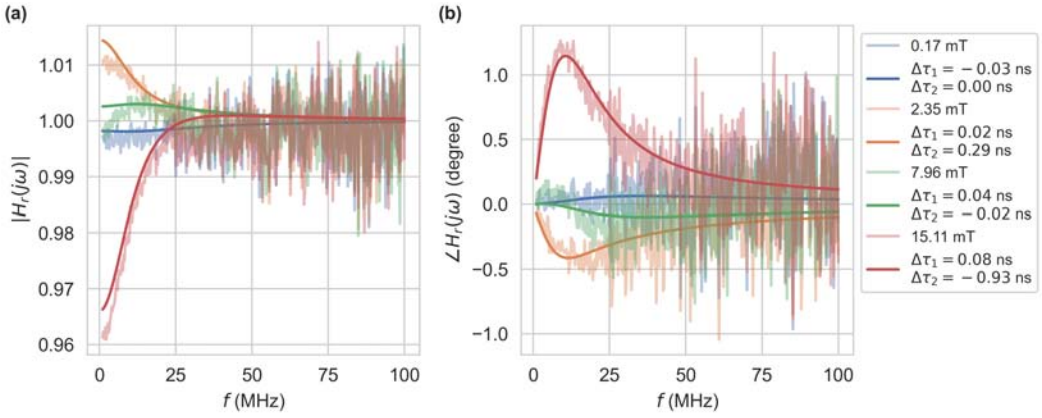

Figure 3.10: Subset of the measured frequency responses with the magnitude $|H_r|$ (**a**) and the phase $\angle H_r$ (**b**) at different B-fields, and the corresponding fits of H_r with the constants $\tau_{1,B=0} = 6.04$ ns and $\tau_{2,B=0} = 11.89$ ns.

To determine the B field via regression from $\Delta\tau_1$ and $\Delta\tau_2$, obtained by the fit, we use a small fully connected neural network (FCNN). The network consists of two nodes in the input layer, one hidden layer and one output layer with a single node and a linear activation function. The hidden layer is composed of a variable number of neurons with rectified linear unit (ReLU) activation functions. Using a grid search, we determine an optimum for the number of neurons in the hidden layer up to a maximum of 60 nodes. We split the observations by ratios of 55%, 15%, and 30% into training-, validation- and test-sets, respectively. During the hyperparameter study, the network's performance is validated on the validation set. The best network is later trained on the combination of training- and validation-set, and the performance is assessed on the test-set.

A FCNN is the simplest form of an artificial neural network (ANN), which consists of multiple interconnected layers of varying number of nodes. Each node is inspired by the behavior of biological neurons. The preactivation z_i of a node is given by the sum of incoming signals x_j where each signal is weighted by w_{ij} and biased by b_i [166]

$$z_i = b_i + \sum_{j=1}^{n_{\text{in}}} w_{ij} x_j \quad \text{for} \quad i = 1, \ldots, n_{\text{out}} \,, \tag{3.19}$$

with the number of inputs of the layer n_{in} and number of outputs of the layer n_{out}. The preactivation is passed through an activation function ϕ, yielding the output, i.e. if the neuron *fires* or not, given by

$$h_i = \phi(z_i) \,. \tag{3.20}$$

The first layer takes the observations as input data and has consequently the same dimensionality as the input data. The output is passed to a variable number of interconnected hidden layers and lastly to an output layer. The output layer yields the classification or regression of a number of labels, given the weights have been adjusted accordingly. In this work, we only deal with supervised learning, meaning we have training data sets with labelled observations. A simple example configuration of a FCNN is shown in the figure beneath.

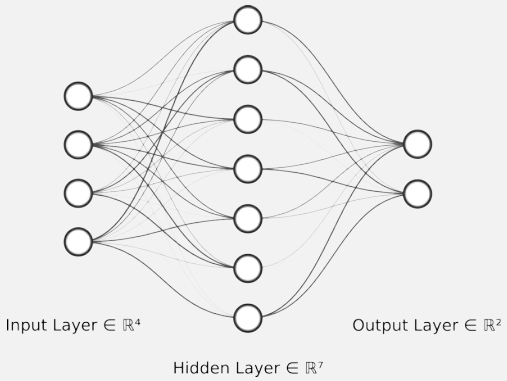

While the number of input and output nodes are determined by the dimensionality of the observations and labels, many parameters like number and sizes of hidden layers and the respective activation functions are so called hyperparameters.

For many years, researchers encountered significant challenges in developing an effective method to train the weights of ANNs. However, in 1986, David Rumelhart, Geoffrey Hinton, and Ronald Williams published a pioneering paper introducing the backpropagation algorithm [167], a method that remains foundational in neural network training today. The algorithm can be understood as an efficient implementation of Gradient Descent, enabling automatic computation of gradients. Through a two-pass process—one forward pass and one backward pass—the backpropagation algorithm calculates the gradient of the network's error with respect to each model parameter. This allows for precise adjustments to each connection weight and bias term, facilitating error minimization. With these computed gradients, a standard Gradient Descent step is applied, and this iterative process continues until the network converges to an optimal solution.

Regression on Raw Spectra

For the practical application in magnetometry, NLLS fitting may require too many resources. Therefore, we explore neural networks for the regression on the raw system response measurements as the input and compare their performance to the fit-based method. Additionally, we focus on the use of FCNNs, which in previous studies have shown a good performance in similar problems [9]. We have further shown the ability of such networks to perform inference

in edge-machine learning based setups, enabling the integration of the solution in a practical application [9].

Here, we use a FCNN with three hidden layers, using ReLU activation functions, and vary their sizes to find the network with the lowest complexity which still shows an acceptable performance. Observations are labeled by the magnetic field B and consist of the concatenations of the magnitude $|H_r|$ and the phase $\angle H_r$, which were measured at 401 different frequencies. Consequently, the input layer consists of 802 nodes. For the regression, the output layer has a single node with a linear activation function, like before in the fit-based regression. Again, we split the observations by ratios of 55%, 15%, and 30% into training-, validation- and test-sets, respectively. The observations are scaled per feature to lie within the interval [0,1] by fitting a *MinMaxScaler* to the training data and applying the scaler to all data. We use TensorFlow for the implementation and training of the networks [168].

3.3.2 Results and Discussion

Fit-based Regression

In the two-step fitting process, we first found the zero-field components $\tau_{1,B=0} = 6.04\,\text{ns}$ and $\tau_{2,B=0} = 11.89\,\text{ns}$ from 30 measurements up to 80 mT. In the second step, we determined $\Delta\tau_1$ and $\Delta\tau_2$ as functions of the magnetic field for all datasets, which we show in Figure 3.11a. These fits are in good agreement to the TCSPC data, except for $\tau_{2,B=0}$ which shows an approximately 2 ns lower value. This difference may be explained by the different optical excitation power, which may also lead to a different temperature of the sensing material, as well as the differing environments, i.e. air or optical adhesive.

The value $\Delta\tau_2$ shows a high responsivity to magnetic fields but displays the same ambiguity that can be observed in the fluorescence intensity. The monotonically increasing component $\Delta\tau_1$, however, aids in resolving this ambiguity. We use these two components as inputs to a simple previously described FCNN to test this hypothesis. In Figure 3.11b, we show the root-mean-square (RMS) error on the validation-set as a function of the number of nodes in the single hidden layer n_h. The RMS error declines to a value of around $\epsilon_\text{rms} = 0.4$ mT at 45 nodes and shows no improvement at a higher node count. Consequently, the FCNN was finally trained with $n_\text{h} = 45$ on the combined training- and

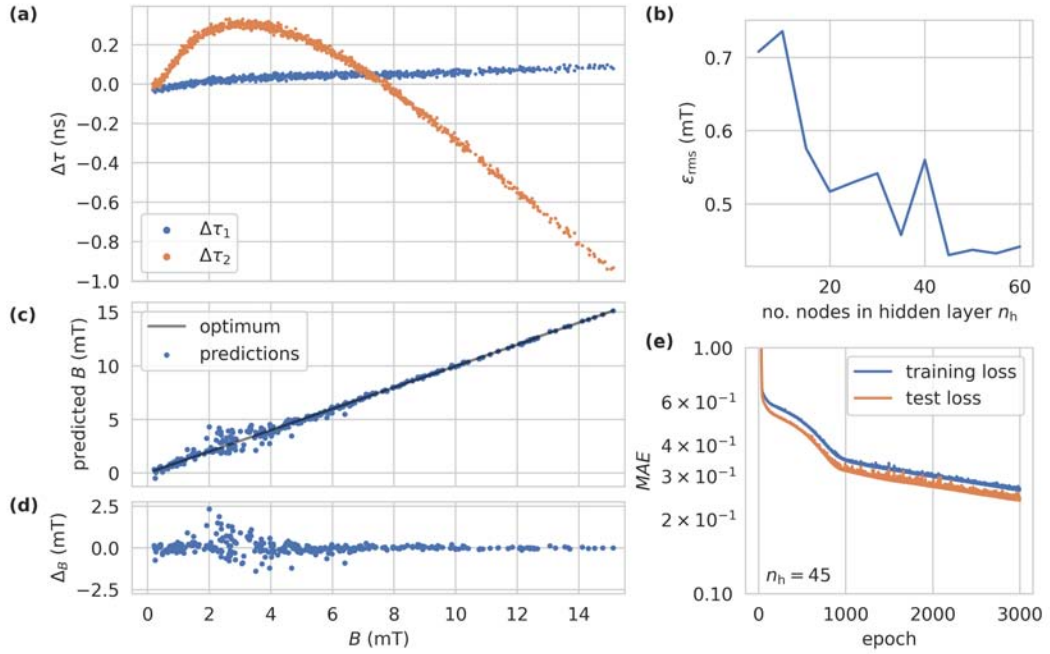

Figure 3.11: (**a**) Magnetic field dependent changes in the lifetimes from fits to the frequency responses at $\tau_{1,B=0} = 6.04\,\text{ns}$ and $\tau_{2,B=0} = 11.89\,\text{ns}$. (**b**) Root-mean-square error of predictions of the simple FCNN on the validation set as a function of the number of hidden nodes n_h. (**c**) Overlay of the predictions of the FCNN ($n_\text{h} = 45$) on the test set in comparison to the optimum linear relationship. (**d**) Differences of the predictions in (c) to the linear function. (**e**) Mean average error on the training and test set during training of the FCNN.

validation-set. We chose the mean average error (*MAE*) as the loss function $L(\cdot)$ on the training- and test-sets, shown in Figure 3.11e. During the training process we observed no significant improvement above 800 epochs and the test loss closely followed the training loss, showing no signs of over-fitting. Deeper networks showed no improvements in the performance in this task, except for a quicker convergence of the loss function during the training.

In Figures 3.11c,d, we show the predictions of the FCNN as a function of the real magnetic field values on a validation set and the differences from the optimum linear relationship, respectively. Below 2 mT and above 4 mT, the predictions are in good agreement with the real values, within an error of $\pm 0.2\,\text{mT}$. In the range of 2–4 mT, the error rises up to $\pm 2.5\,\text{mT}$. We attribute this behavior to the low change in both fit parameters ($\Delta\tau_1$, $\Delta\tau_2$) compared to their local variance in this magnetic field range. We observed no outliers, showing that the measurement of the magnetic fields below and above $\approx 3\,\text{mT}$

can be distinguished.

Regression on Raw Spectra

A future implementation of a sensing application might utilize a resource constrained environment like an embedded device. On such an a device the computational requirements for a NLLS fitting are likely unpractical. Therefore, we also pursued an alternative approach using a FCNN, where the input consists of the raw system response measurements, i.e. the concatenation of $|H_r|$ and $\angle H_r$. A grid search was done to find an optimum for the number of nodes in each of the three hidden layers. The number of nodes were varied in the ranges of $n_{\mathrm{h},1} \in [50, 200]$, $n_{\mathrm{h},2} \in [20, 60]$, and $n_{\mathrm{h},3} \in [5, 25]$, where $n_{\mathrm{h},x}$ is the number of nodes in layer x. In Figures 3.12a,b, we show the predictions of the FCNN as a function of the real magnetic field values on a validation-set. Therefore, the number of nodes were set to $n_{\mathrm{h},1} = 75$, $n_{\mathrm{h},2} = 50$, and $n_{\mathrm{h},3} = 20$, where the loss showed a minimum. The network is again able to resolve the ambiguity around 3 mT. It performs slightly better than the fit-based approach with maximum deviations from the real magnetic field of ± 1.2 mT and an RMS error on the test set of $\epsilon_{\mathrm{rms}} = 0.27$ mT. During training, the MAE on the test set converges quickly and we see signs of over-fitting from 30 epochs onward (cf. Figure 3.12c).

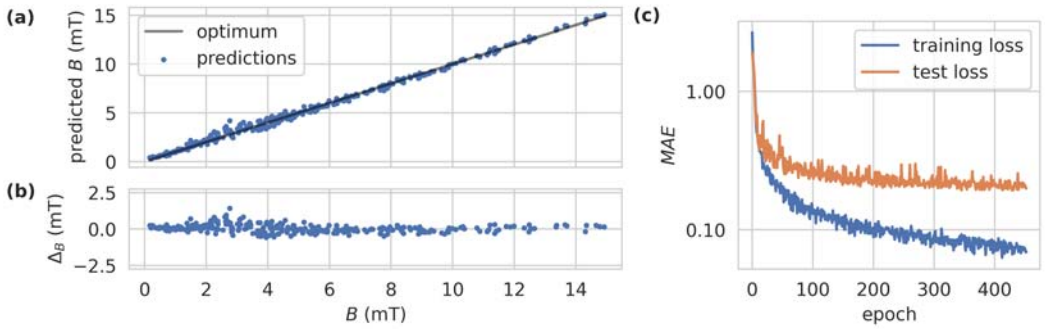

Figure 3.12: (**a**) Overlay of the predictions of the FCNN ($n_{\mathrm{h},1} = 75$, $n_{\mathrm{h},2} = 50$, $n_{\mathrm{h},3} = 20$) on the test-set in comparison to the optimum linear relationship. (**b**) Differences of predictions in (a) to the linear function in which the prediction equals the label. (**c**) Mean average error on the training- and the test-set during the training of the FCNN.

On a workstation PC, we found an about 170 times faster execution of this approach compared to the fit-based regression. This improvement does

not account for the previous training, which can be done in advance in an application.

Feature Selection

Until now, we used raw spectra consisting of measurements at 401 discrete frequencies. The question arises if we can get the same results, or at least retain the ability to resolve the ambiguity, using fewer frequencies. At a reasonably low number of discrete frequencies, a lock-in amplifier approach with multiple simultaneous channels becomes feasible. The optical excitation could be implemented by the combination of the discrete frequencies by the setup we used in Section 3.2.2, i.e. the modulation of a CW-driven laser by an AC coupled signal. Alternatively, we previously employed a setup with square wave excitation. In this setup the excitation and fluorescence signals consist of the fundamental and additional odd harmonics which could be evaluated simultaneously.

We will now explore if such a set of excitation frequencies exists, how the associated error behaves, and if we can even implement it with the constrains set by a square wave excitation. Therefore, we first apply a feature ranking with recursive feature elimination (RFE) to the analysis, based on raw spectra as inputs [169]. The goal of the RFE is the selection of features by recursively considering progressively smaller sets of features. In our case the features are the distinct frequencies at which the measurement of magnitude and phase are carried out. First, the model $\hat{f}$ is trained on the initial set of features. Next, the features are ranked by their importance and the least important ones are pruned from the feature matrix X. The procedure is recursively repeated until a minimum number of features is reached. This produces a feature subset ranking of nested subsets $X_1 \subset X_2 \subset \dots X$.

To obtain feature importances (FIs) we employ the permutation feature importance algorithm [170, 171]. It is based on the permutation of one feature in X, to estimate that feature's importance. The permutation breaks the association of the feature and the true outcome y. The ratio of the new prediction error and the original error is then a measure for the importance of that feature. We summarize the algorithm here:

1. Estimate the original model error $e_{\text{orig}} = L(y, \hat{f}(X))$.

2. For each feature j:

   - Generate the permutation feature matrix X_p where $X_p = X$, except for feature j which is randomly permutated.
   - Estimate the new model error $e_{\text{perm}} = L(y, \hat{f}(X_p))$.
   - Determine the feature importance by $FI_j = e_{\text{perm}}/e_{\text{orig}}$.

3. Sort the features by their FI.

We applied this procedure to the previously shown data and FCNN structure. In Figure 3.13, we show the RMS error on the test set as a function of the number of features. We start at 198 features, which contain all frequencies from the previous sets below 50 MHz and the number of features is reduced by the RFE one by one. We can see a constant error down to about 75 features. Below this point, the error gradually increases and peaks at 2.15 mT. This indicates that the waveform, i.e. magnitude and phase data over a larger frequency range is necessary to predict magnetic fields and to resolve the ambiguity.

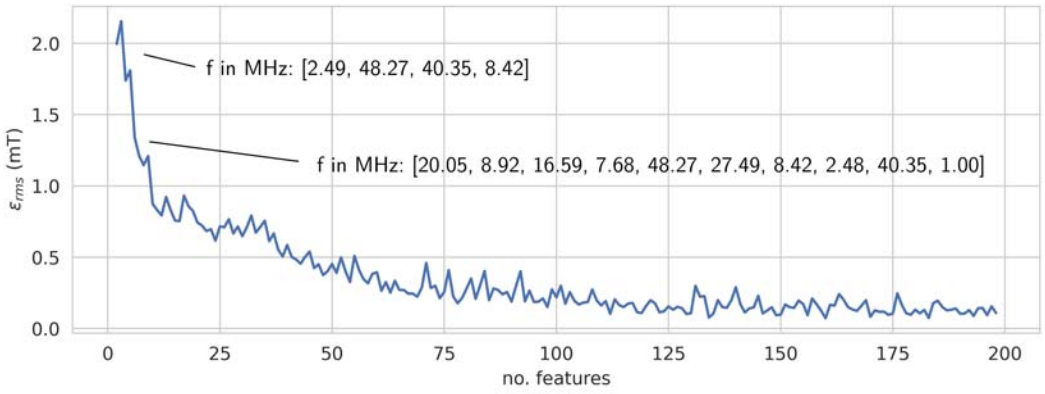

Figure 3.13: RMS error on the test-set as a function of the number of features. Starting at 198 features, which includes all frequencies below 50 MHz, the number of features is reduced by RFE one by one. We show the remaining frequencies at four and ten features in order of the descending FI.

Conclusion

The overall precision of the presented approaches is lower than in all-optical methods based on the measurement of the fluorescence magnitude or the phase at a single excitation frequency. This holds true especially in the measurement

range of 2 mT–4 mT. However, we are able to resolve the ambiguity in these setups for magnetic fields below 8 mT. Also, we have to be cautious, when comparing these results to previously shown lock-in amplifier based measurements. The frequency-domain measurements were carried out in a random order over a time span of tens of minutes. We have seen earlier, that 1/f-noise and drift dominate in this time range.

A setup combining both approaches would be possible, where the electronics switches between a VNA and a lock-in amplifier mode, depending on the applied magnetic field. Thereby existing setups could benefit from the presented work to construct a sensor system with a high magnetic bandwidth, starting at zero field.

3.4 Temperature-Insensitive Measurement

In Section 2.4, we found that a rise in the temperature is accompanied by an overall reduction of the fluorescence intensity [141, 135], and in time-resolved fluorescence spectroscopy a reduction of the fluorescence lifetime with a rising temperature has been shown [141, 143]. In an experiment, which only observes the intensity or phase at a fixed excitation frequency, this behavior leads to a temperature-dependent measurement quantity.

In this section, we investigate a sample of NV rich diamond powder in a frequency domain fluorescence lifetime measurement at varying temperatures and magnetic fields. We use the frequency domain approach to obtain more information about the sample with the aim to extract the magnetic field independent, or at least less sensitive, to temperature fluctuations.

3.4.1 Measurement Setup

The setup for these measurements is similar to the previous ones. We extended it by a climate chamber to enable the variation of the ambient temperature. In Figure 3.14, we show the optical and electrical setup for frequency domain measurements. A collimated 520 nm laser diode (PLT5 520B, ams-OSRAM) is driven by a laser switch (iC-HKB, iC-Haus GmbH) at a mean optical output power of 12 mW. The input stage of the laser driver is based on a comparator, responsible for switching the laser on or off during the positive and negative half waves of the input signal. The excitation light is passed through a dichroic

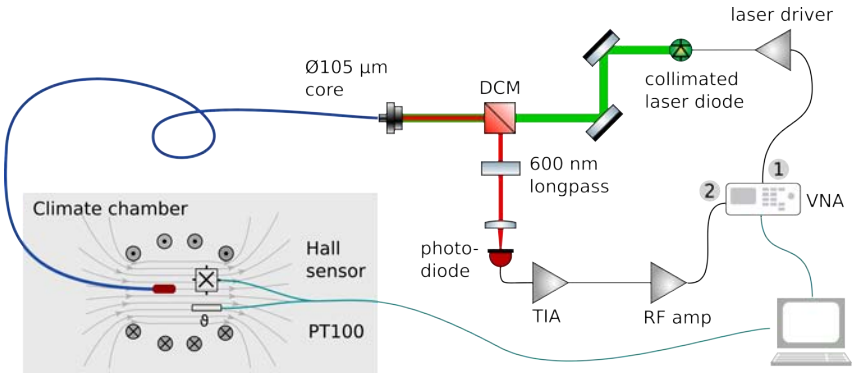

Figure 3.14: Schematic of the optical and electrical setup for the frequency domain measurements. The fiber tip with NV-rich diamond powder is placed in an electromagnet, which is monitored by a Hall effect sensor and a PT100 temperature probe.

mirror (DMPS567R, Thorlabs) and coupled to a 105 µm core diameter fiber. Another difference to previous setups is given by the NV diamond sample. The end facet of the fiber is placed next to high NV-density micro diamonds in a glass cuvette. The amount of micro diamonds is large enough to completely cover the fiber's end facet. We use no glue here, to avoid additional effects, like a drift of the intensity with temperature cycles. The fluorescence of the NV diamonds is collected via the same fiber, passed through a long-pass filter and focused (FELH600 & LA1951-AB, Thorlabs) on a photodiode. The photocurrent is amplified by a transimpedance amplifier (12 kΩ, 75 MHz bandwidth) and passed to the Vector Network Analyzer. The VNA sweeps the frequency of the output signal at port one, which is connected to the laser driver, in a range of 1–100 MHz and records the response in the magnitude and the phase at port two. In each sweep, the VNA records this response at 401 distinct frequencies with a bandwidth of 1 kHz. We record the average of five sweeps for one observation.

An electromagnet, monitored by a Hall effect sensor, is used to apply magnetic fields up to 80 mT. The design is an improved version of the Helmholtz coil and was originally developed by Fanselau et al. [172]. The detailed characterization is given in Appendix A.1. The electromagnet, containing the sample, is placed in a climate chamber. We additionally monitor the ambient temperature inside the coil with a PT100 temperature probe.

In Figure 3.15, we show example measurements of the magnitude $|H_r|$ and the phase $\angle H_r$ at different temperatures and magnetic fields. Like before, we

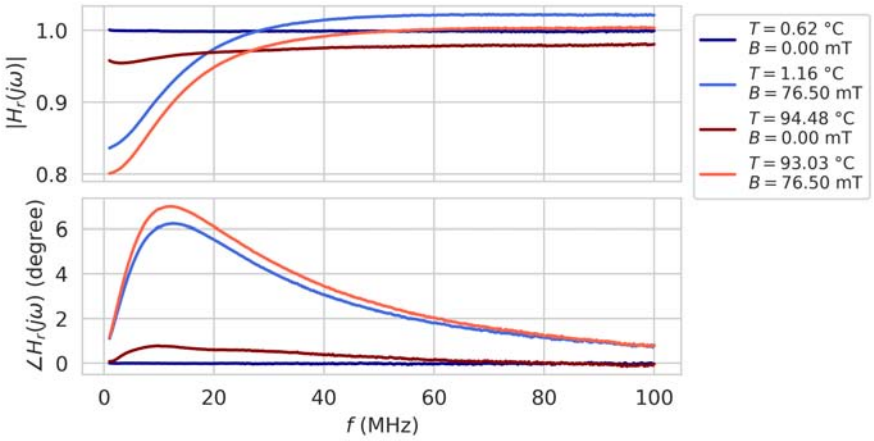

Figure 3.15: Measurements of the magnitude $|H_r|$ and the phase $\angle H_r$, as functions of the excitation frequency f at different temperatures T and magnetic fields B.

observe a high magnetic contrast of the magnitude at low frequencies, as well as a high magnetic contrast of the phase around 13 MHz. Under constant magnetic fields and increasing temperatures the magnitude decreases in the whole range of the excitation frequencies. Additionally, the phase increases with rising temperatures at low frequencies.

In previous experiments we only varied the magnetic fields and were able to fit Equation 3.18 to the measurements. With the additional variation of the temperature, we can no longer satisfactorily apply these fits. We therefore employ machine learning algorithms for the regression of these two variables. We aim to investigate if temperature independent magnetometry can be implemented with the frequency domain approach.

Temperature Dependence

At first, we swept the climate chamber's set temperature between 0 °C to 100 °C at zero magnetic field, with each ramp taking one hour. We added dwell times at the extremes of 10 minutes. During 18 sweeps, taking 22 hours, we recorded 18373 frequency responses. We use a neural network for the regression of the temperature from the measurements. Therefore, we implemented a fully connected neural network with three hidden layers of sizes 95, 65, and 35 nodes, using ReLU activation functions, and an output layer with a single node and a linear activation function. Observations are labeled by the temperature T and consist of the combination of the magnitude $|H_r|$ and the phase $\angle H_r$ at 401

different frequencies. Consequently, the input layer consists of 802 nodes. We split the observations by ratios of 55%, 15%, and 30% into training-, validation- and test-sets, respectively. The observations are scaled per feature to lie within the interval [0,1] by fitting a MinMaxScaler to the training data and applying it to all data. We use TensorFlow for the implementation and the training of the networks [168].

Temperature and Magnetic Field Dependence

Next, we swept the climate chamber's temperature from 0 °C to 96 °C in 8hours, back to 0 °C in 4hours and lastly to 96 °C in 1.5hours. During this time, we continuously swept the magnetic field from 0 mT to 30 mT in 25 steps and further to 80 mT in 15 additional steps. We reduced the number of discrete magnetic field steps at higher values to limit the additional heating by the electromagnet to 20 K above the ambient temperature. During 16 hours, we recorded 6494 frequency responses. For the combined regression of temperature and magnetic field from the measurements, we use a FCNN with the same architecture, as in the previous case. The only change lies in the output layer which now has two nodes with linear activation functions. We further used the same splits between training-, validation- and test-sets, and applied a MinMaxScaler. The observations are now labeled by T and B.

3.4.2 Results and Discussion

Temperature Dependence

In the first experiment the frequency responses were acquired at varying temperatures and zero magnetic field. A FCNN was trained in 800 epochs, after which the validation loss showed no significant improvement. The loss functions, plotted in Figure 3.16c, show no signs of overfitting. In Figure 3.16a, we show the predictions of the FCNN on the test-set. We find a mean deviation from the linear relation of 0.29 °C and a standard deviation in Δ_T of 1.24 °C. These results were consistent over multiple training runs with different randomly chosen subsets for training and test. We observed no significant outliers, with 99% of the values of Δ_T lying within ±3.8 °C, showing the temperature can be estimated at zero magnetic field.

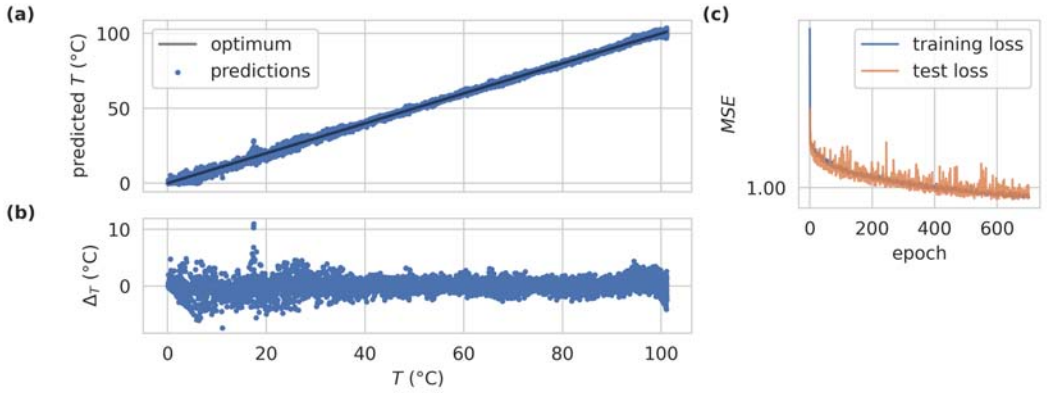

Figure 3.16: (**a**) Overlay of the predictions of the FCNN on the test set in comparison to the optimum linear relationship. (**b**) Differences of predictions in (a) to the linear relation. (**c**) Mean squared error on the training- and validation-sets during the training of the FCNN.

Temperature and Magnetic Field Dependence

In the second experiment the measurements were acquired at slowly varying temperatures, while sweeping the applied magnetic field in discrete steps up to 76 mT. The Hall effect magnetic field probe showed a temperature dependence of approximately $-620\,\mathrm{ppm/K}$, leading to a low accuracy at high temperatures. To obtain more accurate magnetic field labels, the currents at the discrete steps were used. Therefore, we recorded the magnetic field in the electromagnet at $T = 25\,^{\circ}\mathrm{C}$ with the Hall sensor as a function of the current in the electromagnet. A linear fit was then used to calculate magnetic field labels from the actual currents in the electromagnet.

The same network structure as before, except for two output nodes with linear activation functions, was used to simultaneously predict magnetic fields and temperatures from the observations. We observed no overfitting in over 600 epochs, after which the validation loss stopped to improve. In Figures 3.17a,b, we show the predictions of the temperatures and the differences to a linear relationship, respectively. In comparison to the previous study, we find a higher variance with outliers up to $\pm 22\,^{\circ}\mathrm{C}$ from the real values. We observe a mean deviation from the linear relation of $-0.15\,^{\circ}\mathrm{C}$ and a standard deviation in Δ_T of $3.63\,^{\circ}\mathrm{C}$. Additionally, the colors indicate the magnetic fields which are associated with the observations. This color coding allows us to visualize potential clusters of magnetic fields, which might lead to observations with higher error in the predictions. However, we see no such clusters.

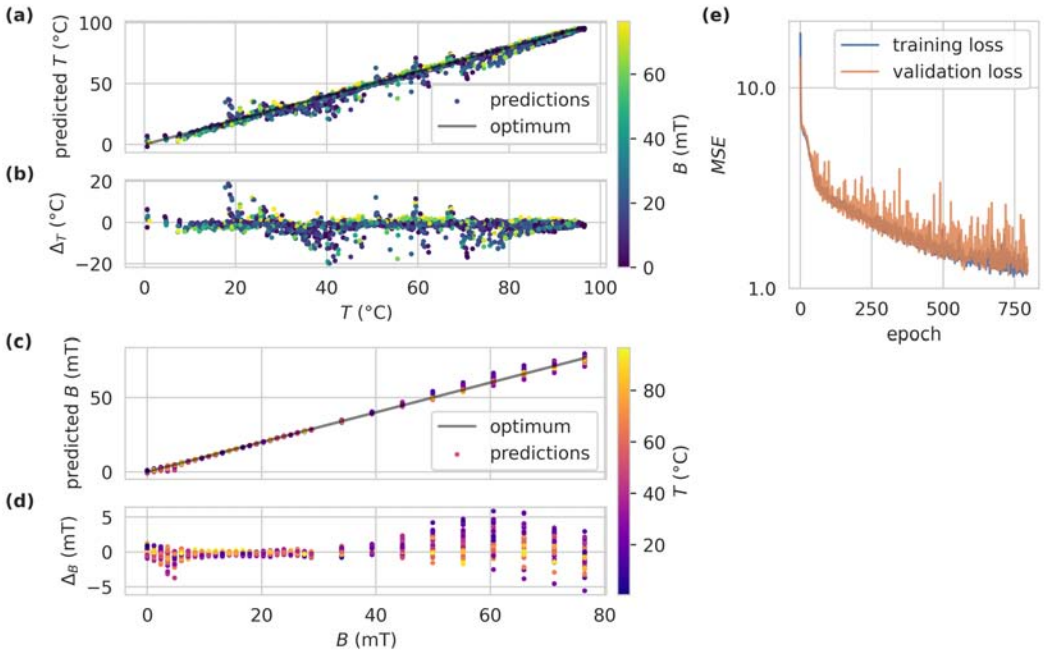

Figure 3.17: Combined regression of the temperature and the magnetic field. (**a**) Predictions of the temperature on the test-set in comparison to the optimum linear relationship. The colors show the respective magnetic field of the observation. (**b**) Differences of the predictions in (a) to the linear relation. (**c**) Predictions of magnetic fields on the test-set in comparison to the optimum linear relationship. The colors show the respective temperature of the observation. (**d**) Differences of predictions in (c) to the linear relation. (**e**) Mean squared error on the training- and validation-sets during the training of the FCNN.

Figures 3.17c,d show the same predictions with respect to the magnetic fields. We find a mean deviation from a linear behavior of $-0.13\,\mathrm{mT}$ at a standard deviation of $0.79\,\mathrm{mT}$. Additionally, 99% of the values of Δ_B lie within $\pm 3.27\,\mathrm{mT}$, showing the ability to predict magnetic fields, insensitive to varying sample temperatures. A higher variance at high magnetic fields is observed. This may be a consequence of the lower number of observations at these fields. Colors are used to show the temperatures, associated with the predictions and their underlying observations. We see no correlation of the error with certain temperature ranges.

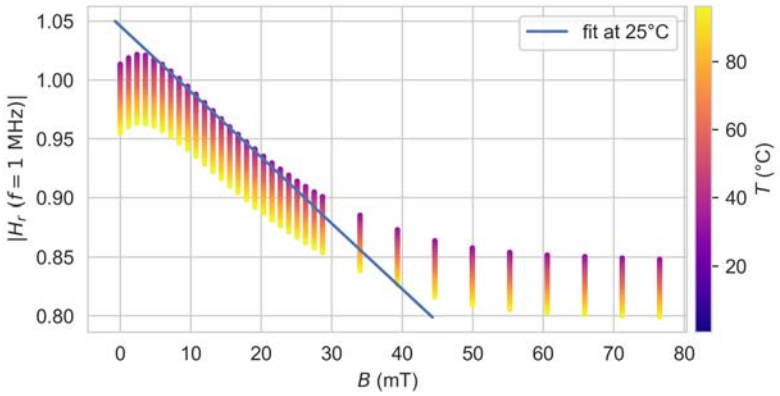

Figure 3.18: Fluorescence intensity at an excitation frequency of $f = 1\,\mathrm{MHz}$ as a function of the magnetic field and the temperature. The linear fit was applied to the data at 25 °C in the range of 10 mT to 20 mT.

For an implementation that only observes the fluorescence intensity, we can estimate the error, which is introduced by varying temperatures. In Figure 3.18, we show the fluorescence intensity $|H_r|$ at the lowest excitation frequency of $f = 1\,\mathrm{MHz}$ as a function of the magnetic field in the tested temperature range. We apply a linear fit to the data at 25 °C in the range of 10 mT to 20 mT. The fit is then used to calculate the magnetic fields from the data at nominally 15.5 mT. The resulting magnetic field values then span a range of 9 mT and show a standard deviation of 2.73 mT. The observation of the phase at a fixed excitation frequency would lead to similar values. In contrast, in our solution, the predicted magnetic field at nominally 15.5 mT spans a range of 370 µT for the recorded temperature range and shows a standard deviation of only 120 µT.

Conclusion

In this section, we investigated the combined temperature and magnetic field dependent behavior of high NV-density microdiamonds in an all-optical frequency domain based setup, utilizing the change in the fluorescence lifetime. At zero magnetic field, we have shown the ability to predict temperatures in the range of 0 °C to 100 °C, with a standard deviation of 1.24 °C. Furthermore, we have shown the ability to predict applied magnetic fields, while varying the ambient temperature, with a lower impact of temperature variations, compared to the sole observation of the fluorescence intensity at a single excitation frequency. With the recent development of low-cost VNAs [173, 174], this work shows a step towards temperature-insensitive industrial application of all-optical NV-based magnetometry.

3.5 Frequency Domain Modelling

In Section 3.3, we used fits to the frequency domain data as a way to extract features for a subsequent regression task. We, however, did not examine the quality of the fits. From the previous section, we have data at different ambient temperatures available, which do not include any possible effects of the optical adhesive like in previous measurements. In addition, the measurements offer a higher SNR since a larger fluorescence intensity could be collected in this setup. We will now examine fits of the model function, which is based on a bi-exponential decay in the time domain, to the new data. Our goal is to find a LTI model as a function of the magnetic field and the temperature for the sensing material under investigation and for a certain optical excitation power. This model would allow the integration into larger system simulations for the optimization of readout techniques.

3.5.1 Constant Temperature

Like before, we fit the ratio of transfer functions $H_r(s) = H(s;B)/H(s;B=0)$, where

$$\begin{aligned} H(s;B) &= \frac{a_1}{s+\frac{1}{\tau_1}} + \frac{a_2}{s+\frac{1}{\tau_2}} \\ &= \frac{a_1}{s+\frac{1}{\tau_{1,B=0}+\Delta\tau_1}} + \frac{a_2}{s+\frac{1}{\tau_{2,B=0}+\Delta\tau_2}} \,. \end{aligned} \tag{3.21}$$

The fitting algorithm minimizes

$$\chi^2_{\mathrm{R}} = \frac{\chi^2}{m-p} \,, \tag{3.22}$$

with the number of data points $m = 802$ and the number of free parameters p, where

$$\chi^2 = \sum_{n=1}^{m} \left(\frac{\hat{H}_{\mathrm{meas}} - \hat{H}_r}{\sigma_m} \right)^2 \,, \tag{3.23}$$

i.e. the squared sum of residuals scaled by their standard deviation. $\hat{H}_{\mathrm{meas}}$ denotes the measured frequency response. We define the symbols in Equation 3.23 as the concatenations of magnitude and phase measurements at the 401 discrete frequencies f_n, i.e.

$$\begin{aligned} \hat{H}_{\mathrm{meas}} &= |H_{\mathrm{meas}}|(f_n) \frown \angle H_{\mathrm{meas}}(f_n) \,, \\ \hat{H}_r &= |H_r|(j2\pi f_n) \frown \angle H_r(j2\pi f_n) \,, \\ \sigma_m &= \sigma_R(j2\pi f_n) \frown \sigma_\phi(j2\pi f_n) \,. \end{aligned} \tag{3.24}$$

The standard deviations in magnitude and phase were estimated from a sequence of 135 measurements at nearly constant ambient temperature $T = 0.3\,^{\circ}\mathrm{C}$ and zero-field. The standard deviations are shown in Appendix A.6. We employ the Levenberg–Marquardt algorithm, implemented by LMFIT [154].

We use the data acquired in Section 3.4 from a sweep of the magnetic field B at a constant temperature and follow a two-step approach for the NLLS fitting. First, we set $\Delta a_1 = 1 - \Delta a_2 = 0.65$, and allow $\tau_{1,B=0}$, $\tau_{2,B=0}$, $\Delta\tau_1$, $\Delta\tau_2$ to be varied. We fit all 33 frequency responses simultaneously to find sensible values for $\tau_{1,B=0}$ and $\tau_{2,B=0}$, where we set them equal for all responses. In a second step, we use these zero-field lifetimes and only allow $\Delta\tau_1$ and $\Delta\tau_2$ to be varied.

In a magnetic field sweep at a constant temperature $T = 0.7\,^{\circ}\mathrm{C}$, we found the best agreement of the model to the data at zero-field lifetimes $\tau_{1,B=0} = 4.73\,\mathrm{ns}$ and $\tau_{2,B=0} = 11.56\,\mathrm{ns}$. In Figure 3.19a, we show the subsequent individual fit values and the corresponding goodness-of-fit χ^2_{R}. We find a $\chi^2_{\mathrm{R}} \gg 1$, increasing up to 650 at larger B. This indicates the simple bi-exponential behavior with fixed amplitudes to not adequately reflect the observations. We show four example fits and the corresponding measurements in Figures 3.19b,c. The residuals show systematic errors in both, the magni-

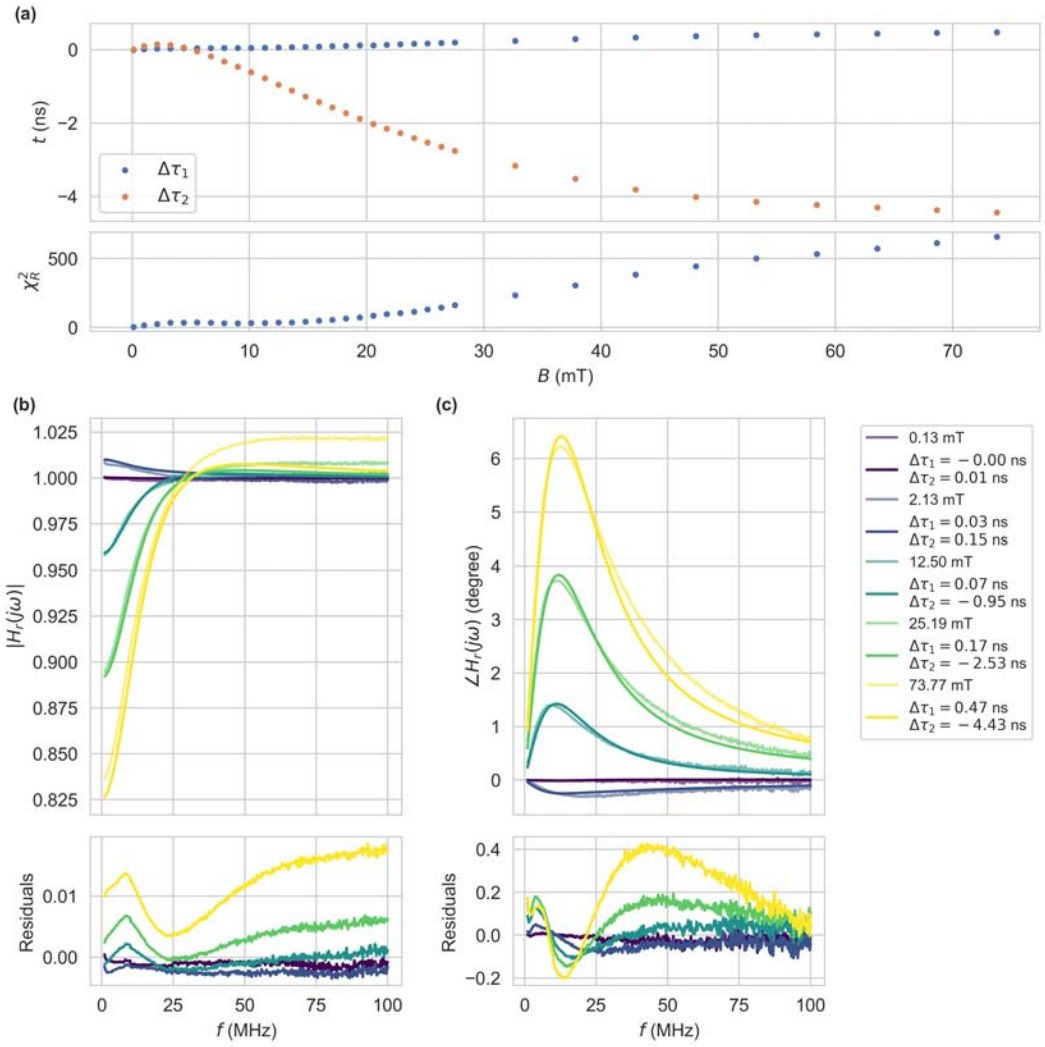

Figure 3.19: (**a**) Magnetic field dependent changes in the lifetimes from fits to the frequency responses at $T = 0.7\,^{\circ}\mathrm{C}$, with $\tau_{1,B=0} = 4.73$ ns and $\tau_{2,B=0} = 11.56$ ns. (**b**) The magnitude and (**c**) the phase for four example measurements and the corresponding fits. The bottom panels show the respective residuals.

tude and the phase. The discrepancy between the model and the data can be largely attributed to an increasing fluorescence intensity with rising magnetic fields at excitation frequencies $f \gg 30\,\mathrm{MHz}$. While we have shown in Section 3.2.3, that with a bi-exponential decay model we can achieve $|H_r| > 1$, such a model still necessitates the magnitude to approach 1 for large f.

In comparison to the TCSPC data, we find $\approx 20\%$ lower zero-field values of both lifetime components, and a higher magnetic contrast of the longer-lived component τ_2. The comparison is shown in Table 3.2. Besides the vastly different acquisition methods, these differences in lifetimes may be explained by the different optical excitation powers and the differing ambient temperatures [175].

	τ_2 (ns)		C (%)	τ_1 (ns)	
	$B = 0$	$B = 70\,\mathrm{mT}$		$B = 0$	$B = 70\,\mathrm{mT}$
Method					
TCSPC	14.1	11.90	15.6	6.01	6.13
F-Domain	11.57	7.13	38.4	4.73	5.21

Table 3.2: Magnetic field dependent changes in bi-exponential fits to TCSPC and frequency domain data.

Higher DoF Fit

When we lift the association to time-domain fits in which we found a good fit for bi-exponential behavior with fixed amplitudes, we become free in our choice of model. With more free parameters, i.e. more degrees of freedom (DoF), we can naturally find a better fit to the data. In our pursuit to find a LTI model which allows the integration into system simulations, the aim is to still use a simple model with as few independent variables as possible. Additionally, the variables shall be smooth functions of the magnetic field, so they in turn can be well approximated by simple continuous functions like polynomials of low order. Therefore, we start with the previously used model $H_r(s) = H(s;B)/H(s;B=0)$, but additionally allow $a_1 = a_{1,B=0} + \Delta a_1(B)$ and $a_2 = a_{2,B=0} + \Delta a_2(B)$ to be varied. The constraint $\Delta a_1 = 1 - \Delta a_2$ still holds true. In the two-step approach, the zero-field components were first found for a global fit to all frequency responses at varying magnetic fields and a constant ambient temperature. Then single fits to the measured transfer

	A	μ	σ	γ	c
Δa_1	-3.51×10^{-4}	-4.75×10^{-3}	2.19×10^{-2}	5.42	1.07×10^{-2}
Δa_2	3.51×10^{-4}	-4.75×10^{-3}	2.19×10^{-2}	5.42	-1.07×10^{-2}
$\Delta \tau_1$	-9.48×10^{-13}	-8.15×10^{-3}	2.80×10^{-2}	4.30	2.19×10^{-11}
$\Delta \tau_2$	4.11×10^{-10}	-1.77×10^{-2}	3.40×10^{-2}	3.06	-8.03×10^{-9}

Table 3.3: Parameters of skewed Gaussian models per Equation 3.25, describing the fit parameters. B is in units of Tesla, resulting $\Delta a_{\{1,2\}}$ are unit-less and resulting $\Delta \tau_{\{1,2\}}$ are in units of seconds. Note that since $\Delta a_2 = 1 - \Delta a_2$, the first two rows are redundant.

functions were used to find the magnetic field dependent changes in the four free parameters that minimize χ^2_{R}.

The global fit yielded $a_{1,B=0} = 0.9831$, $a_{2,B=0} = 0.01685$, $\tau_{1,B=0} = 0.7522\,\mathrm{ns}$, and $\tau_{2,B=0} = 13.31\,\mathrm{ns}$. These parameters differ from previous fits by a larger relative amplitude, and a significantly lower short-lived component $\tau_{1,B=0}$. We show the same example transfer functions with respective fits in Figures 3.20b,c as used in Figure 3.19. Systematic errors in the residuals are now mostly limited to the magnitude at low excitation frequencies. Consequently, χ^2_{R} can now be kept below 13 for all measurements, shown in Figure 3.20a. The magnetic field dependent fit variables contain no outliers and can in turn be fit well by smooth functions. We fit these values with skewed Gaussian models, inspired by a skewed normal distribution

$$f(B;(A,\mu,\sigma,\gamma,c)) = \frac{A}{\sigma\sqrt{2\pi}} e^{[-(B-\mu)^2/2\sigma^2]} \left(1 + \mathrm{erf}\Big[\frac{\gamma(B-\mu)}{\sigma\sqrt{2}}\Big]\right) + c \qquad (3.25)$$

which are functions for the magnetic field B with the five parameters amplitude (A), center (μ), sigma (σ), gamma (γ), and offset (c). We show the fits as continuous lines in the same figure. The benefit of these single peaked functions is their saturation behavior, which is expected at magnetic field values above which we took measurements for. Polynomials, for instance, would not be well behaved in that regard outside the range of investigated magnetic fields. The respective fit parameters are given in Table 3.3.

Model Validation

We could hypothesize that this more complex model also reflects the actual decay dynamics well. This conclusion is not valid, since up to this point we fit models to $H_r(B)$, which are measurements normalized to a zero-field

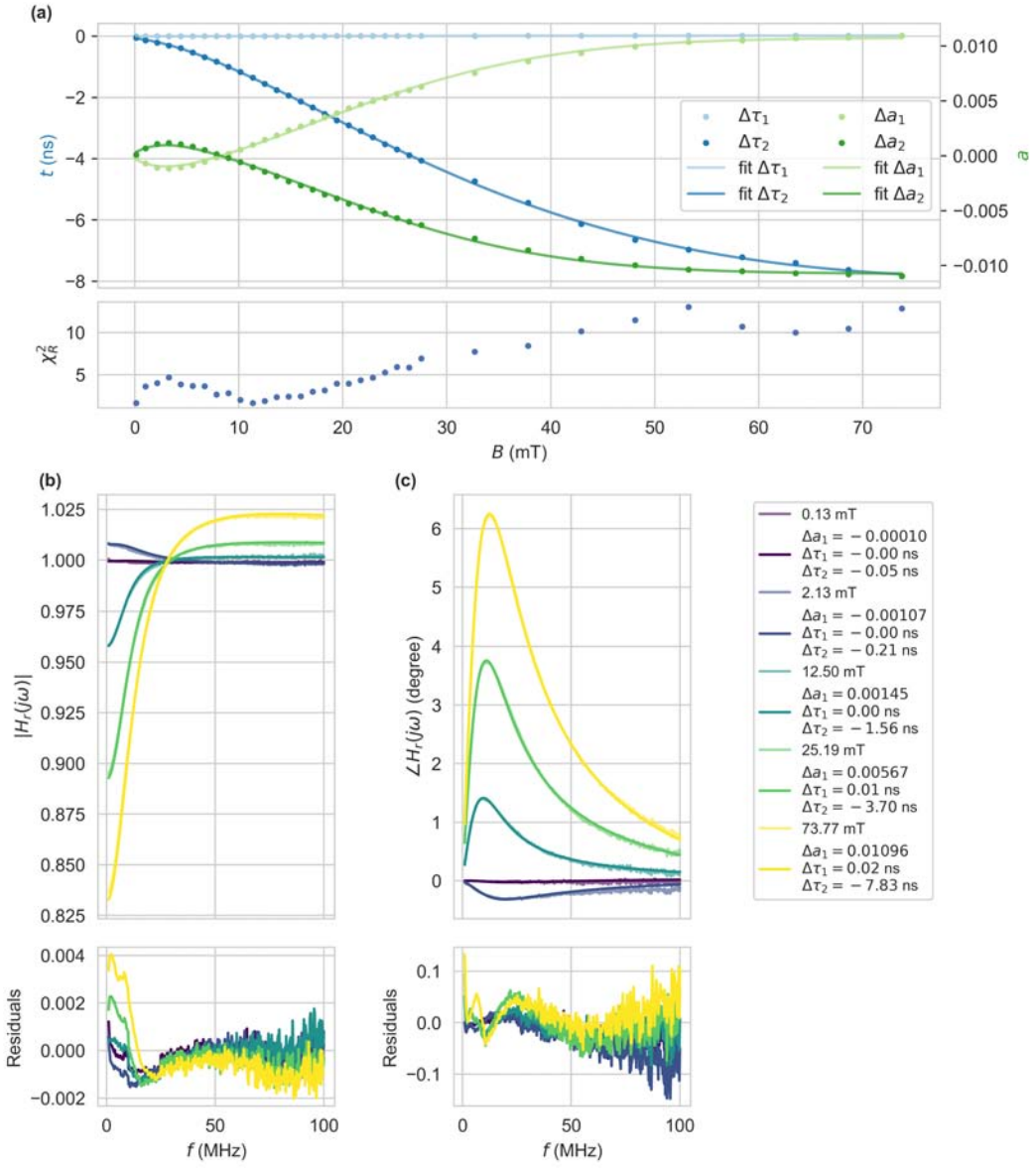

Figure 3.20: (**a**) Magnetic field dependent changes in lifetimes and respective amplitudes from fits to frequency responses at $T = 0.7\,°\mathrm{C}$ with $a_{1,B=0} = 0.9831$, $a_{2,B=0} = 0.01685$, $\tau_{1,B=0} = 0.7522\,\mathrm{ns}$, and $\tau_{2,B=0} = 13.31\,\mathrm{ns}$. The values are in turn fit by single peaked functions of B. (**b**) The magnitude and (**c**) the phase for four example measurements and corresponding fits. The bottom panels show the respective residuals.

response. Therefore, we devised a simple experiment in which we use the same measurement setup as before and do not calibrate the VNA with the zero-field response, but a fiber which is connected to a short-lifetime reference material. In this instance a red dyed plastic part is used, delivering roughly the same fluorescence intensity as a fiber with NV diamond powder. The response of such a short-lifetime reference has a nearly constant magnitude and close to 0° phase shift with regard to the excitation at frequencies up to 100 MHz. When the short-lifetime reference fiber is then exchanged for the NV diamond fiber, the VNA measurement reflects the actual low-pass behavior of the fluorescence. In Figure 3.21, we show the magnitude measurements for a zero-field and a high magnetic field of $B > 100\,\mathrm{mT}$ from this setup in red. We fit the simpler model with constant amplitudes $a_1 = 1 - a_2 = 0.65$ (const. a) as well as the new model with varying amplitudes and zero-field values of $a_{1,B=0} = 1 - a_{2,B=0} = 0.9831$ (var. a) to the measurements. The simpler model more closely matches the measurements. While for the more complex model, H_r can be reproduced well, these simulated values of the corresponding magnitude show that it can be rejected for explaining the actual fluorescence decay dynamics. The phase is not shown since a difference in the two fibers' lengths leads to a frequency-dependent phase shift, which would have to be corrected for. This is of course possible, but not necessary to show the discrepancy between the more complex model and the measurements.

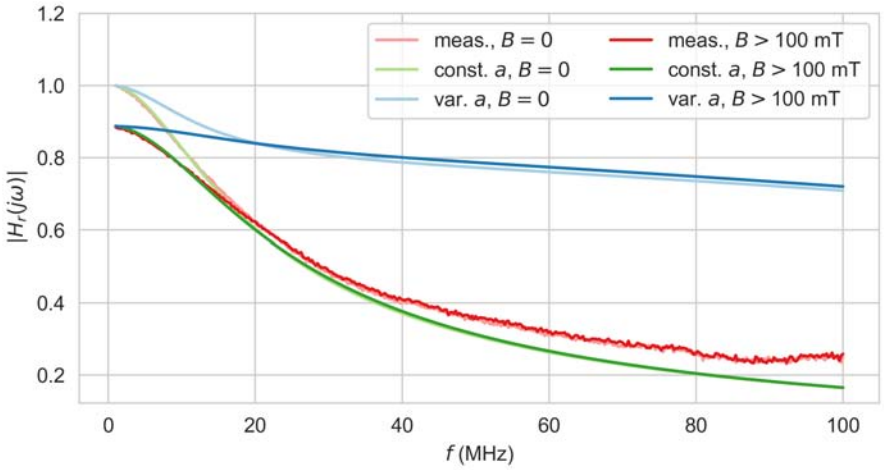

Figure 3.21: Magnitudes of the frequency responses. Comparison of the measurement of the NV diamond fluorescence to bi-exponential decay models with fixed amplitudes (const. a) and higher DoF (var. a).

In practice, the choice of model depends on the use case. If the absolute frequency response is required, the simple model with fixed amplitudes (Figure 3.19) is in good agreement to the TCSPC data and more closely reflects the response measurements, which were calibrated with a red dye reference. A complete system simulation would additionally have to account for the frequency responses of all other instruments. In comparison, the more complex model with magnetic field dependent changes in amplitude and lifetime is able to more reliably reproduce the actual decay dynamics.

In a last step, a model that accurately reflects the decay dynamics–and the magnetic field dependent behavior–can be obtained by combining the two models to

$$\begin{aligned} H(j\omega;B) &= H_{\text{const.}a}(j\omega;B=0)H_{r,\text{var.}a}(j\omega;B) \\ &= \left(\frac{0.65}{s+\frac{1}{4.73\,\text{ns}}}+\frac{0.35}{s+\frac{1}{11.57\,\text{ns}}}\right)\frac{\frac{0.9831+\Delta a_1(B)}{s+\frac{1}{0.7522\,\text{ns}+\Delta\tau_1(B)}}+\frac{0.01685+\Delta a_2(B)}{s+\frac{1}{13.31\,\text{ns}+\Delta\tau_2(B)}}}{\frac{0.9831}{s+\frac{1}{0.7522\,\text{ns}}}+\frac{0.01685}{s+\frac{1}{13.31\,\text{ns}}}} \end{aligned} \tag{3.26}$$

with the simple model $H_{\text{const.}a}$ and the varying amplitudes model $H_{r,\text{var.}a}$, respectively. The magnetic field components are determined via Equation 3.25 and Table 3.3.

To model the measurements in a setup, the instrument response would have to be determined and accounted for. This response includes the responsed of e.g. the TIA, the laser driver, and the optical path lengths. The absolute intensity is also influenced by the optical excitation power and the coupling efficiency to the fluorescent material. Furthermore, this model from Equation 3.26 is valid for one specific optical excitation power. Since the fluorescence intensity shows an increasing contrast with rising excitation power and a saturation behavior, we expect a similar behavior for the complete frequency response [12]. Lastly, the model can be applied to data taken at other temperatures, and the results will be qualitatively similar. The values given in Equation 3.26 are however valid for the measurements at $T = 0.7\,^{\circ}\text{C}$. We expect decreasing magnetic contrasts of the magnitude and the phase with rising temperatures, which were observed before in the intensity based measurements in Section 2.4.

3.5.2 Varying Temperature

Next, we additionally varied the temperature in addition to the magnetic field. We swept the ambient temperature from 0 °C to 96 °C in 8hours, and back to 0 °C in 4hours. During this time, we continuously swept the magnetic field with the profile presented in the previous section (compare Figure 3.19a). See Section 3.4.1 for details on the measurement setup.

The magnitude showed a long-term drift and an additional non-linear temperature dependency in this test. We show this behavior with the mean magnitude as a function of the temperature at $B = 0$ in Figure A.10 in the appendix. To be able to still include the magnitude information in our analysis, we define the mean-free magnitude

$$|\widetilde{H_r}|(f_m) = |H_r|(f_m) - \frac{1}{401}\sum_{n=1}^{401}|H_r|(f_n) \tag{3.27}$$

with the discrete frequencies f_m at which the VNA recorded the magnitude and the phase. Assuming the drift acts independently of the excitation frequency, a comparability between the measurements of varying magnetic fields and temperatures is thereby reobtained. The phase showed no such fluctuations. In Figure 3.22, we show the modified magnitude and the phase at zero-field. We find a decline in the fluorescence intensity at low frequencies with an increasing temperature. This observation is in agreement with the findings in Section 2.4, where we only observed the DC fluorescence intensity. Comparable to the magnetic field variation, the temperature induced intensity reduction has a lower contrast towards higher excitation frequencies. By the nature of the modified magnitude we can however not deduce if the intensity rises above unity at higher frequencies, like it did with B variation. The phase initially decreased with increasing temperatures at higher frequencies and showed a positive temperature coefficient with a maximum around $f = 13\,\mathrm{MHz}$. Since we show data from both an increasing and a decreasing temperature ramp in the same graphs, we can show the observed effects to be reversible. A remaining drift component in both magnitude and phase explains the faint horizontal lines in the graphs. In the appendix, the same measurements for two magnetic field values $B = 11.9\,\mathrm{mT}$ (see Figure A.11) and $B = 71.19\,\mathrm{mT}$ (see Figure A.12) are included. We find qualitatively equal temperature-induced deviations from

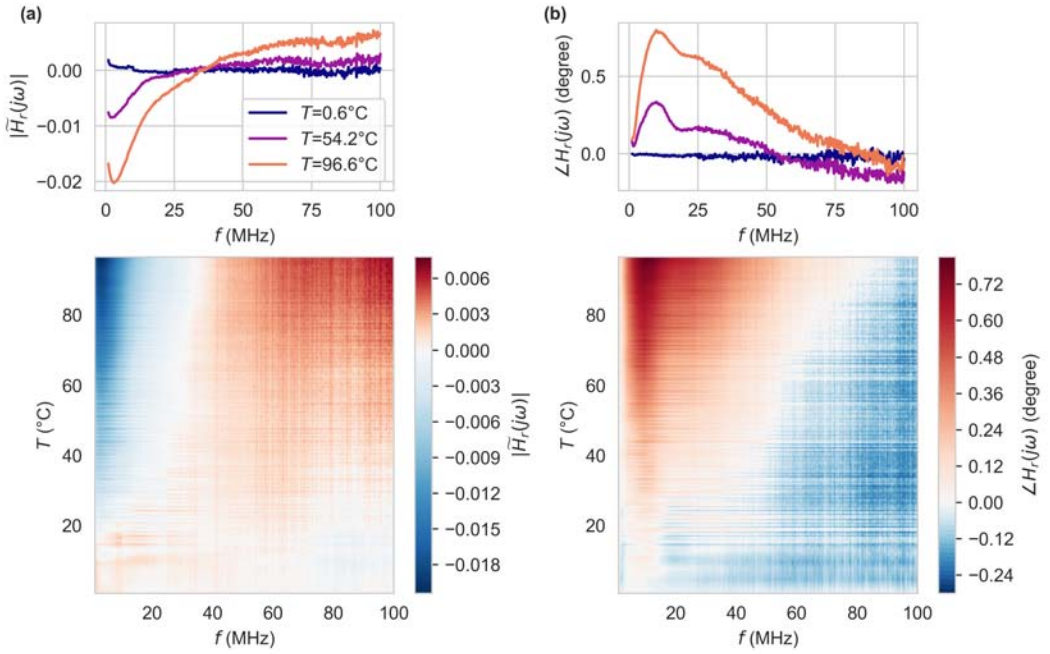

Figure 3.22: Modified relative magnitude (**a**) and phase (**b**) responses as a function of temperature at $B = 0$. The top panels show examples, from the whole set of 100 responses, plotted in the bottom panels. The modified relative magnitude does not allow any conclusions about the absolute intensity, but only comparison between different ambient temperatures.

the frequency responses we expect for the respective magnetic fields.

From these observations we may hypothesize that temperature and magnetic field act independently of each other on the frequency domain measurement, i.e. they can be represented by the linear combination of

$$H_r(j\omega;(B,T)) = H'_r(j\omega;B) + H''_r(j\omega;T)\ , \tag{3.28}$$

where H'_r and H''_r are different models for the transfer functions as functions of either the magnetic field or the temperature, respectively. H'_r would then have to equal the previously found B-dependent model. This behavior would greatly simplify the design of a LTI model suited for system simulations. To test this hypothesis, we start with the whole data set of the frequency response measurements at varying B and T. The calibration of the VNA, which sets the reference, was done at $B_0 = 0\,\mathrm{mT}$ and $T_0 = 0.7\,^\circ\mathrm{C}$. The data set contains $H_r(f_m;(B_0,T))$ as well as $H_r(f_m;(B,T_0))$, which are the measurements at these reference conditions, with the other parameter being varied. Inserting them

for H_r' and H_r'' in Equation 3.28 and rearranging results in

$$\Delta H_r = H_r(f_m;(B_0,T)) + H_r(f_m;(B,T_0)) - H_r(f_m;(B,T)) = 0\ , \tag{3.29}$$

where H_r is composed of the actual magnitude and phase measurements, additionally accounting for the drift in the magnitude via the modified magnitude

$$H_r = \Big(|\widetilde{H}_r| + 1\Big)e^{j\angle H_r}\ . \tag{3.30}$$

To check the equality to zero for the measurement-based ΔH_r, we use the mean absolute difference (MAD)[2]. If the hypothesis held true, the magnitude and the phase of ΔH_r would show mean-free distributions and the MAD would be close to zero for all B and T. To find comparison values of the MAD for the rejection of the hypothesis, we use $H_{r,0} = H_r(f_m;(B_0,T_0))$, for which we determine

$$\begin{aligned} \mathrm{MAD}(|\widetilde{H}_{r,0}|) &= 0.00034 \\ \mathrm{MAD}(\angle H_{r,0}) &= 0.013\,46^\circ\ . \end{aligned} \tag{3.31}$$

Figures 3.23a,b show the MADs of the magnitude and the phase of ΔH_r. For both quantities, the MADs are almost equal to the comparison values for low B or low T. However, at rising B and T we find for the magnitude two distinct regions which rise above $\mathrm{MAD}(|\widetilde{H}_{r,0}|)$ around

1. $T > 60\,^\circ\mathrm{C}$ and at
2. $B > 40\,\mathrm{mT}$ and $15\,^\circ\mathrm{C} > T > 40\,^\circ\mathrm{C}$.

The first region can also be found in the MAD plot of the phase. In these regions we find significant deviations in ΔH_r, from which we can conclude that the hypothesis has to be rejected. This means for the modelling of the transfer function that dependencies on B and T can not be separated.

Lastly, we apply the fit with varying lifetimes and varying amplitudes $H_{r,\mathrm{var}.a}$ to all frequency responses from a rising and a subsequent declining temperature ramp, during which the magnetic field was constantly swept. We use the same parameters for $H(s;(B_0,T_0))$ as before and let $\Delta\tau_{\{1,2\}}$, $\Delta a_1 = -\Delta a_2$ be varied. Of course, the objective function that returns the residuals for the fit procedure respects the modified magnitude by computing the residuals on the mean-free magnitude. The resulting fit parameters are shown in

[2] $\mathrm{MAD}(\boldsymbol{X}) = \frac{1}{n}\sum_{n=1}^{m}|x_n - \bar{x}|$

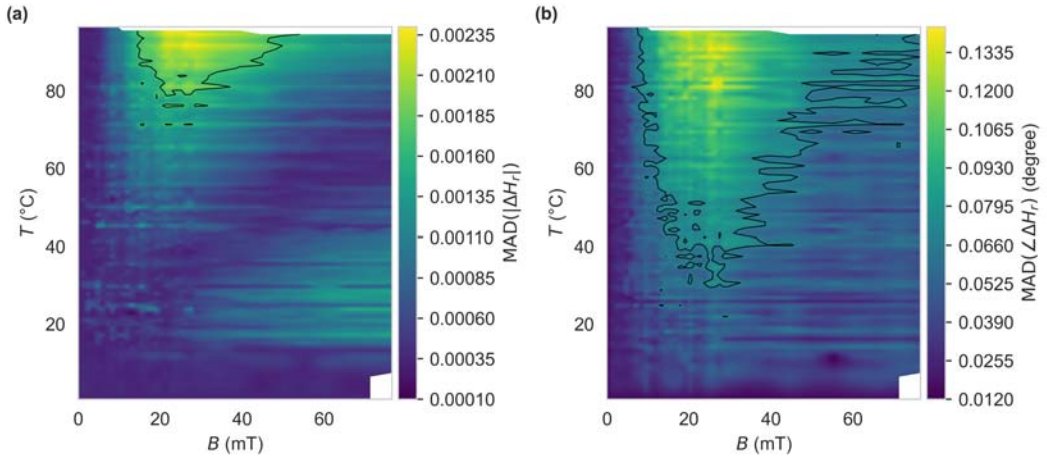

Figure 3.23: MAD of (**a**) $|\Delta H_r|$ and (**b**) $\angle \Delta H_r$ as functions of the magnetic field and the temperature. The contour lines show five times the respective MAD of $H_{r,0}$.

Figures 3.24a,b,c with the respective goodness-of-fit in Figure 3.24d. The fit parameters for low temperatures agree well with the parameters of the previous section. Towards higher frequencies, an interlacing of different value ranges for the parameters can be observed. This interlacing stems from the data that were acquired at rising and falling temperatures. Even though we use the modified magnitude, remaining drift components in both magnitude and phase lead to these deviations between frequency responses and associated fits at similar temperatures. The goodness-of-fit χ^2_R shows the same interlacing with low and high values, where the high values support the rejection of the model function for explaining the observations. The rising χ^2_R stems from the model function not accounting for these drift components. From the data we can not conclude, even for the initially rising temperature ramp, when the drift becomes too large for the fit to still deliver trustworthy values. To model and then account for this drift, we would need more closely spaced measurements at the calibration conditions T_0 and B_0. Even if they were present, the resulting higher degree of freedom for the fit would then deliver less reliable results.

We can conclude for the modelling of the frequency responses at varying magnetic fields B and temperatures T with a LTI function that the presently available data is not appropriate. Future work would have to identify the drift sources and eliminate them or vary T and B on time scales that allow drift

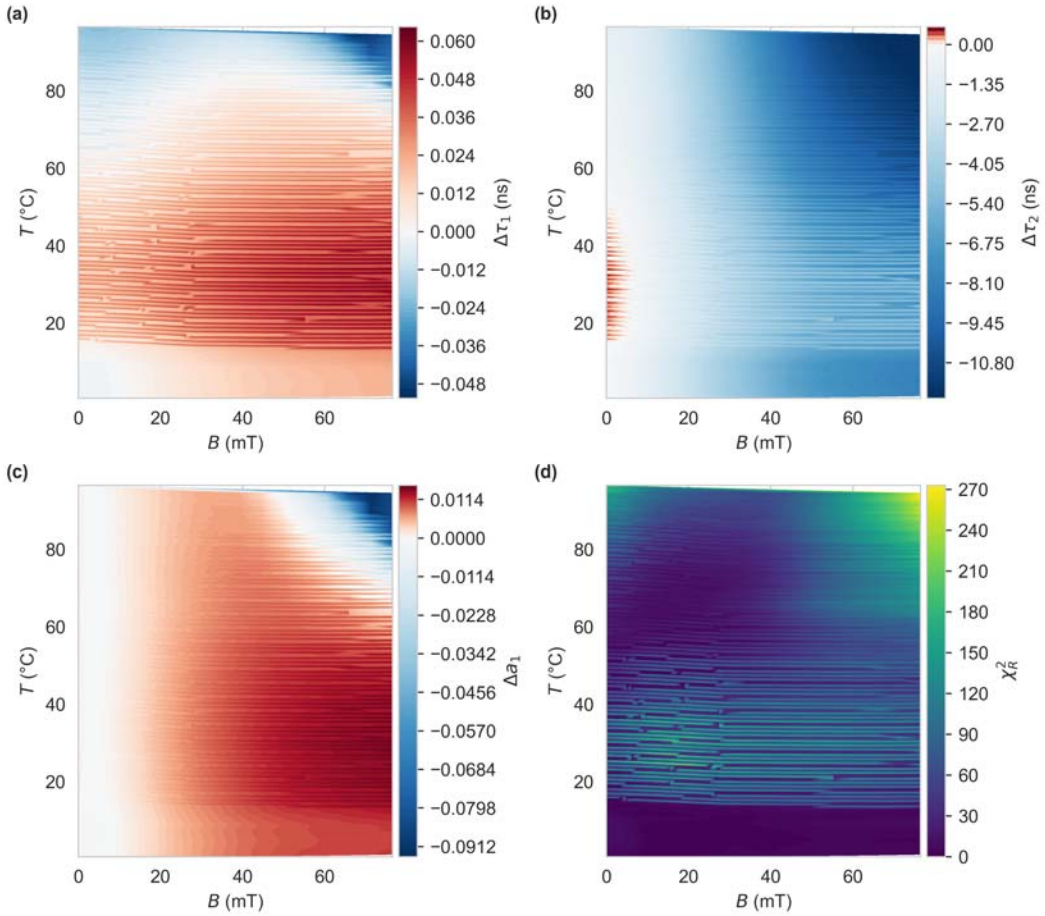

Figure 3.24: Magnetic field and temperature dependent changes in the lifetimes (**a,b**) and the respective amplitudes (**c**) from fits to frequency responses with $a_{1,B=0} = 0.9831$, $a_{2,B=0} = 0.01685$, $\tau_{1,B=0} = 0.7522$ ns, and $\tau_{2,B=0} = 13.31$ ns. (**d**) Goodness-of-fit χ^2_R for the fits.

components to be neglected. These observations match those of the previous chapter, where we acquired the magnitude and the phase with a LIA and found drift components in the Allan deviation on time scales longer than several seconds. However, this shows the strength of the approach from Section 3.4, where we used a FCNN trained on the raw spectra to infer the magnetic fields.

3.6 Square Wave PSD Revisited

With the knowledge we gained in this chapter about the decay characteristics in the time and frequency domain, it is worth revisiting the previous considerations about lock-in amplification with square wave excitation. Specifically,

we can find the DC indication of a single-phase phase square wave sensitive detector as a function of the reference frequency, assuming we are not bandwidth limited by the excitation and detection electronics. This computation of the DC indication allows us to determine an upper bound for sensible reference frequencies f_{ref}. For a single harmonic detection scheme, which is usually implemented with commercial lock-in amplifiers, the choice of f_{ref} can be directly determined from our previous studies, shown in Figure 3.6. When a square wave PSD also demodulates the odd harmonics, we have to account for the attenuation and phase shift at the respective frequencies.

In general we can write the time domain output of a lock-in amplifier as

$$l(t) = \underbrace{\Big((\mathit{ref}(t) * g(t))}_{\text{fluorescence signal}} \cdot \underbrace{\mathit{ref}(t)\Big)}_{\text{PSD}} * h_{\mathrm{lpf}}(t)\,, \tag{3.32}$$

where $g(t) = h_{\mathrm{NV}} * h_{\mathrm{irf}}$ is the combined response of the NV decay characteristics and the instrument response function. For our considerations, we set $h_{\mathrm{irf}} = \delta(t)$, since we only want to find the limitations imposed intrinsically by the diamond sensing material. This intrinsic response h_{NV} is approximated by the bi-exponential decay as per Equation 3.6. Further, $\mathit{ref}(t)$ is the square wave excitation and the demodulation signal, for which we showed the Fourier series in Equation 2.40. The respective Fourier transform is given by a sum of scaled and shifted Dirac functions

$$REF(f) = \mathcal{F}\{\mathit{ref}(t)\}(f) = \sum_{n=1,3,5,\ldots}^{\infty} \left[\frac{4}{\pi n}\frac{1}{2j}\Big(\delta(f - nf_{\mathrm{ref}}) - \delta(f + nf_{\mathrm{ref}})\Big)\right]. \tag{3.33}$$

For the frequency domain representation of $l(t)$ we can then find

$$\begin{aligned} L(f) &= \Big(\Big(REF(f)H_{\mathrm{NV}}(j2\pi f)\Big) * REF(f)\Big)H_{\mathrm{lpf}}(j2\pi f) \\ &= \sum_{n=1,3,5,\ldots}^{\infty}\left[\left(\frac{j2}{\pi n}\right)^2\Big(\delta(f + 2nf_{\mathrm{ref}}) - 2\delta(f) + \delta(f - 2nf_{\mathrm{ref}})\Big)|H_n|e^{j\phi_n}\right]H_{\mathrm{lpf}}(j2\pi f) \end{aligned} \tag{3.34}$$

where $|H_n| = |H_{\mathrm{NV}}(j2\pi n f_{\mathrm{ref}})|$ and $\phi_n = \angle H_{\mathrm{NV}}(j2\pi n f_{\mathrm{ref}})$. Furthermore, we already made use of the properties of $H_{\mathrm{lpf}}(j2\pi f)$, effectively eliminating all products of $\delta(f + mf_{\mathrm{ref}})$ and $\delta(f + nf_{\mathrm{ref}})$ with $m \neq n$. For the same reason,

the components at $f \pm 2nf_{\mathrm{ref}}$ can be canceled, leading to

$$L(f) = \frac{8}{\pi^2} \sum_{n=1,3,5,\ldots}^{\infty} \left[\frac{1}{n^2} \delta(f) |H_n| \Big(\cos\phi_n + \underbrace{j \sin\phi_n}_{=0} \Big) \right], \tag{3.35}$$

where in our case of a single-phase PSD, the $j \sin\phi_n$ component does not exist. We show the resulting DC indication of $L(f)$ for varying f_{ref} in Figure 3.25, finding a $-3\,\mathrm{dB}$ corner at 6.86 MHz. This simulation assumes H_{NV} to be the sum of two first-order low-pass filters, as per Equation 3.11, with $a_1 = 0.65, \tau_1 = 6.1\,\mathrm{ns}$, $a_2 = 0.35$, and $\tau_2 = 14.5\,\mathrm{ns}$.

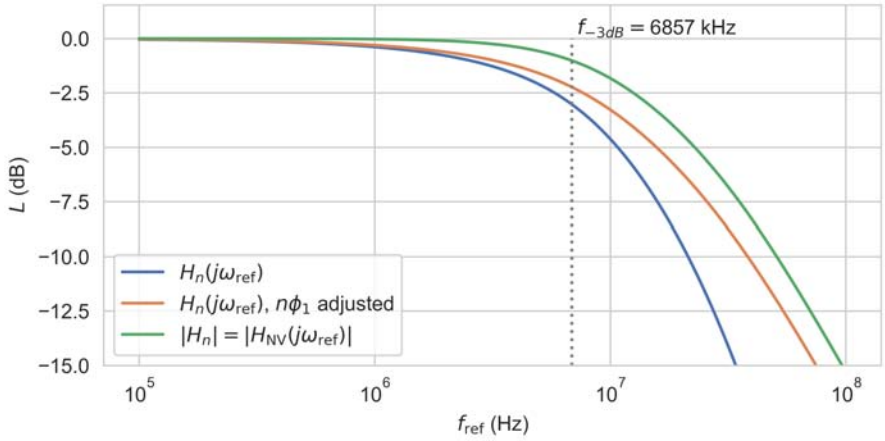

Figure 3.25: DC indication of a square wave PSD as a function of the reference frequency (blue trace), corrected for the phase shift of the fundamental frequency (orange trace), and $|H_n|$ (green trace). All $L(f)$ are normalized to $H_{\mathrm{NV}}(0)$.

In the application of a single-phase approach, we first calibrate the phase offset between excitation and detected fluorescence to maximize the DC indication. This calibration effectively cancels ϕ_1 at the fundamental frequency. In this case, we can replace $\cos\phi_n$ in Equation 3.35 by $\cos(\phi_n - n\phi_1)$. We also plot the resulting PSD output, denoted by $n\phi_1$ *adjusted*, finding an extension of the $-3\,\mathrm{dB}$ corner to 9.26 MHz. From this, we find a sensible maximum value of $f_{\mathrm{ref}} \ll 1.6\,\mathrm{MHz}$, where the DC indication is down by no more than 5%. For comparison, we also show the magnitude $|H_n|$, which would govern the response in a usual lock-in amplifier setup with a dual-phase demodulation of a single harmonic. This is just the magnitude of the frequency response from the const. a model, shown previously in Figure 3.21.

Lastly, the magnetic contrast is a function of the excitation frequency, as

we saw in previous sections. We can determine the DC indication of the single-phase square wave PSD $L(f;B)$ at a given magnetic field B. The model for the magnetic changes in magnitude and phase from Equation 3.25 is used for this task. In Figure 3.26, we show the resulting contrast $C = 1 - L(f;B)/L(f;B = 0)$ for $B = 75\,\mathrm{mT}$. We again differentiate between demodulation with a constant phase and a phase-adjustment to the fundamental components, labelled as $n\phi_1$ *adjusted* in the figure. In both cases, we find a decreasing contrast towards higher frequencies and a negative value above a threshold frequency, since the fluorescence intensity rises above that of zero-field at sufficiently high modulation frequencies (see Figures 3.6c,e). dependency of the contrast on the excitation frequency leads to a second criterion for the choice of f_{ref}. If we do not want to loose more than e.g. 0.5% magnetic contrast, f_{ref} has to be kept below 1 MHz.

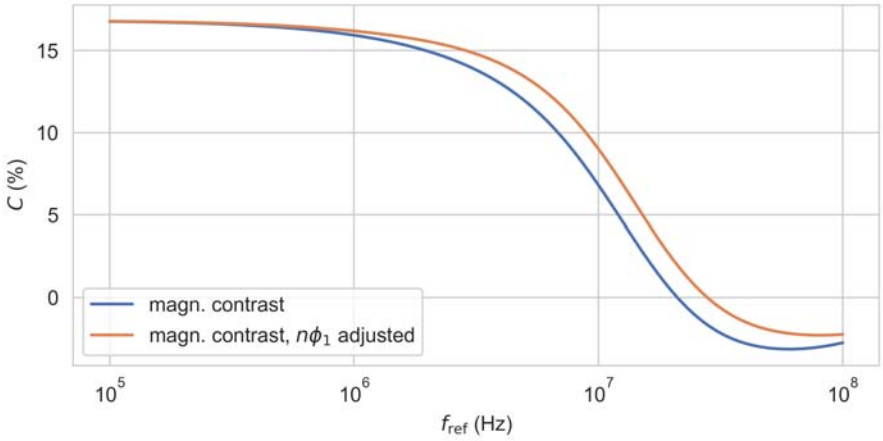

Figure 3.26: Magnetic contrast of the DC indication for $B = 75\,\mathrm{mT}$ using the var. *a* model. The orange trace accounts for the phase at the fundamental frequency of $H_{\mathrm{NV}}(f_{\mathrm{ref}})$.

4 Conclusions and Outlook

In the first chapter, we gave an introduction to current sensing and magnetic field sensing, especially quantum sensing with NV centers in diamonds. We described the physics of the NV center and common readout-methods, distinguishing between MW-based and MW-free, or even all-optical methods.

In Chapter 2, we showed and analyzed a setup for all-optical magnetometry with NV centers, with a focus on fiber-based sensors. After detailing the building blocks of such a system, we introduced the concept of phase-sensitive detection for the purpose of noise reduction. We built upon this concept in two revisions of an application specific evaluation circuitry. The circuit was analyzed in detail and the ability to capture magnetic fields at a 5 kHz bandwidth with a shot-noise limited sensitivity down to $s \approx 1\,\mu\mathrm{T}/\sqrt{\mathrm{Hz}}$ was shown. We found this setup's performance to be comparable to that of a commercial laboratory instrument at a significantly lower price point. Further, temperature dependent behavior of the fiber sensor was investigated, where a negative temperature coefficient of the fluorescence intensity was found, which is in good agreement to the literature. The dynamic response of the developed system was tested in the range up to several kHz. While in the applications we considered this performance suffices, future work may investigate the dynamic response of the NV fluorescence to magnetic field changes in isolation. The results could be incorporated into a LTI system description. In general, we can not assume the fluorescence to follow the magnetic field instantaneously.

In Chapter 3, the fluorescence lifetime of a high-NV-density microdiamond powder has been investigated, showing a bi-exponential behavior with a magnetic contrast of the larger decay time of 15.2%. The lifetime constitutes a non-intensity-based quantity for magnetic field sensing, which is used in a MW-

free fiber-based setup. The bi-exponential function is interpreted as a sum of two first-order low-pass filters, which change their gain and corner frequencies upon application of a magnetic field. This is accompanied by a change in the phase, which shows a maximum in the magnetic contrast of 5.8° at 13 MHz. We employ a LIA at this modulation frequency and use the phase as a non-intensity quantity for magnetic field sensing. A 100-times-higher immunity to intensity fluctuations was realized because we avoid the misinterpretation of changes in fluorescence intensity as changing magnetic fields. In the current state, the system shows similar realized sensitivities and expected SNLS for the magnitude and phase approaches. The construction of the TIA leaves room for improvement upon narrowing the required bandwidth to a small band around 13 MHz to realize a sensitivity closer to the SNLS, which we estimate to $s_{\phi,snl} = 950\ \mathrm{nT}/\sqrt{\mathrm{Hz}}$ at an excitation power of 11.5 mW. In shot noise limited measurements, the signal-to-noise ratio scales with the square root of the detected photons per time. However, we are limited in significant increases of the excitation power and, therefore, the fluorescence intensity by heat introduced into the fiber head. Dry fibers, which we used in later parts of this work, may not pose this limitation, but are not practical in an application. Future work may focus on sensor construction techniques which avoid adhesives, e.g. by embedding the diamond particles in glass [176]. Next to the shot noise, the achievable sensitivity in our setup is primarily determined by the gradients of the measurement quantities $\delta|H_r|/\delta B$ and $\delta\angle H_r/\delta B$, which increase with the excitation power. We expect a saturation towards higher optical pumping powers, which has been observed for the magnitude before [12].

Current state-of-the-art NV-based sensors realize impressive sensitivities, reaching 0.9 $\mathrm{pT}/\sqrt{\mathrm{Hz}}$ for NV ensembles [97] and 170 $\mathrm{pT}/\sqrt{\mathrm{Hz}}$ for single NV centers [51]. They are based on optically detected magnetic resonance, requiring MW excitation. MW-free setups also achieve high sensitivities at 0.45 $\mathrm{nT}/\sqrt{\mathrm{Hz}}$–6 $\mathrm{nT}/\sqrt{\mathrm{Hz}}$, using the GSLAC [30, 14, 31], or estimated $s \approx$ 10 $\mathrm{nT}/\sqrt{\mathrm{Hz}}$, utilizing the zero-field features [33]. Both are based on narrow-band features, requiring stable bias magnetic fields with accurate alignment. All of these setups need bulky and costly infrastructure bound to a laboratory environment. Our setup, in contrast, can potentially be realized in a more compact and less costly manner. It also shows a consistent sensitivity in a higher magnetic field range of approximately 10 mT–40 mT, making it more

universally applicable. These findings establish the basis for the application of fluorescence lifetime in all-optical, low-noise, and robust magnetometry.

We used the complete frequency response, which holds more information than either the magnitude or the phase at a single frequency alone, to resolve the ambiguity at low magnetic fields and achieve a low impact of temperature variations in a magnetometry application. Therefore, two evaluation methods of the frequency response were compared. First we fit a model function, based on the assumption of a bi-exponential decay in the time domain, which in the frequency domain is the sum of two first order low-pass filters. The fit parameters were then used in a regression algorithm to predict magnetic field values, allowing us to resolve the ambiguity. When additionally varying the temperature of the diamond material, this simple LTI model could not be fit well anymore. To capture the complexity in the data, we trained an artificial neural network on the raw response vector. This method not only allowed us to still resolve the low-field ambiguity, but the system could also predict magnetic field values insensitive to temperature variations.

Lastly, the fits of the model functions were examined in more detail, delivering a LTI model that reflects the actual frequency response and its magnetic field dependence well. This model would allow the integration into larger system simulations for the choice and optimization of readout techniques. Additionally, the temperature dependence was examined. The available data, however, do not allow the determination of reliable parameters. Future work may identify and eliminate drift and 1/f noise components in the read-out process. Eliminating these noise components is not only important for any sensing application, but would also allow capturing of reliable frequency domain data at varying temperatures with the aim of fitting a LTI model.

For the acquisition of the frequency response, other read-out methods are conceivable. These may rely e.g. on the excitation with broadband noise and the correlation between input and output signals of the system. In any case, the integration of the all-optical frequency domain approach holds promise for advancing magnetic field sensing capabilities, particularly in applications where conventional methods are limited by a galvanic connection, metallic components in the sensing volume, or the interaction with MW radiation.

In summary, this thesis showed advancements in all-optical magnetometry using NV centers in diamonds, with a focus on fiber-based sensor systems. We

explored fluorescence intensity- and fluorescence lifetime-based systems, investigating sensitivity and temperature dependencies. We showed that lifetime-based measurements can yield higher immunity to disturbances and deliver more information, allowing to resolve the low-field ambiguity and reduce temperature influences. The implications of this research are profound, extending well beyond the realm of all-optical sensing. The novel techniques developed to reduce interference and enhance temperature stability are readily adaptable to microwave-based quantum sensors, offering a pathway to overcome long-standing barriers in this technology. This work not only enriches the existing body of knowledge but also serves as a cornerstone for future advancements in quantum sensing technologies, potentially transforming industries that depend on high fidelity measurements in environmentally sensitive settings.

5 Conclusión

En el primer capítulo, presentamos una introducción a la detección de corrientes y campos magnéticos, especialmente a la detección cuántica con centros NV en diamantes. Describimos la física del centro NV y los métodos de lectura habituales, distinguiendo entre los basados en MW y los libres de MW, o incluso los métodos totalmente ópticos.

En el capítulo 2, mostramos y analizamos una configuración para la magnetometría totalmente óptica con centros NV, centrándonos en los sensores basados en fibra. Después de detallar los bloques de construcción de un sistema de este tipo, introdujimos el concepto de detección sensible a la fase con el fin de reducir el ruido.Nos basamos en este concepto en dos revisiones de un circuito de evaluación específico de la aplicación. El circuito se analizó en detalle y se demostró la capacidad de capturar campos magnéticos en un ancho de banda de 5 kHz con una sensibilidad limitada al ruido de disparo de hasta $s \approx 1\,\mu\mathrm{T}/\sqrt{\mathrm{Hz}}$. El rendimiento de esta configuración es comparable al de un instrumento comercial de laboratorio a un precio significativamente inferior. Además, se investigó el comportamiento del sensor de fibra en función de la temperatura, y se observó un coeficiente negativo de la intensidad de fluorescencia en función de la temperatura, lo que concuerda con la bibliografía. Aunque en las aplicaciones que hemos considerado este rendimiento es suficiente, en futuros trabajos se podría investigar la respuesta dinámica de la fluorescencia NV a los cambios de campo magnético de forma aislada. En general, no podemos suponer que la fluorescencia siga al campo magnético de forma instantánea.

En el capítulo 3, se ha investigado el tiempo de vida de la fluorescencia de un polvo de microdiamante de alta densidad NV, mostrando un compor-

tamiento biexponencial con un contraste magnético del tiempo de decaimiento mayor del 15,2%. El tiempo de vida constituye una cantidad no basada en la intensidad para la detección de campos magnéticos, que se utiliza en una configuración basada en fibra libre de MW. La función biexponencial se interpreta como una suma de dos filtros de paso bajo de primer orden, que cambian su ganancia y sus frecuencias de esquina al aplicar un campo magnético, lo que va acompañado de un cambio en la fase, que muestra un máximo en el contraste magnético de 5.8° a 13 MHz. Empleamos un LIA en esta frecuencia de modulación y utilizamos la fase como una cantidad de no-intensidad para la detección del campo magnético. Se obtuvo una inmunidad 100 veces mayor a las fluctuaciones de intensidad porque evitamos la interpretación errónea de los cambios en la intensidad de fluorescencia como campos magnéticos cambiantes. En el estado actual, el sistema muestra sensibilidades realizadas similares y SNLS esperados para las aproximaciones de magnitud y fase. La construcción del TIA deja margen de mejora al estrechar el ancho de banda requerido a una pequeña banda alrededor de 13 MHz para obtener una sensibilidad más cercana al SNLS, que estimamos en $s_{\phi,snl} = 950$ nT/$\sqrt{\text{Hz}}$ con una potencia de excitación de 11.5 mW. Sin embargo, estamos limitados en los aumentos significativos de la potencia de excitación y, por lo tanto, la intensidad de fluorescencia por el calor introducido en el cabezal de la fibra. Las fibras secas, que utilizamos en partes posteriores de este trabajo, pueden no plantear esta limitación, pero no son prácticas en una aplicación.El trabajo futuro puede centrarse en técnicas de construcción de sensores que eviten adhesivos, por ejemplo, mediante la incrustación de las partículas de diamante en vidrio [176]. Junto con el ruido de disparo, la sensibilidad alcanzable en nuestra configuración viene determinada principalmente por los gradientes de las magnitudes de medida $\delta|H_r|/\delta B$ y $\delta\angle H_r/\delta B$, que aumentan con la potencia de excitación. Esperamos una saturación hacia potencias de bombeo óptico mayores, lo que se ha observado para la magnitud antes [12].

Los sensores actuales basados en NV presentan sensibilidades impresionantes, que alcanzan los 0.9 pT/$\sqrt{\text{Hz}}$ para conjuntos de NV [97] y los 170 pT/$\sqrt{\text{Hz}}$ para centros de NV individuales [51]. Se basan en la resonancia magnética detectada ópticamente, que requiere excitación MW. Las configuraciones sin MW también alcanzan altas sensibilidades a 0.45 nT/$\sqrt{\text{Hz}}$–6 nT/$\sqrt{\text{Hz}}$, utilizando el GSLAC [30, 14, 31], o estimado $s \approx 10$ nT/$\sqrt{\text{Hz}}$, utilizando las características

de campo cero [33]. Ambas se basan en características de banda estrecha, que requieren campos magnéticos de polarización estables con una alineación precisa. Todas estas configuraciones necesitan una infraestructura voluminosa y costosa ligada a un entorno de laboratorio. Nuestra configuración, en cambio, puede realizarse potencialmente de una manera más compacta y menos costosa, y también muestra una sensibilidad consistente en un rango de campo magnético más alto, de aproximadamente 10 mT–40 mT, lo que la hace más universalmente aplicable. Estos resultados sientan las bases para la aplicación de la magnetometría de la vida útil de la fluorescencia en todas las ópticas, de bajo ruido y robusta.

Utilizamos la respuesta en frecuencia completa, que contiene más información que la magnitud o la fase en una sola frecuencia, para resolver la ambigüedad en campos magnéticos bajos y lograr un bajo impacto de las variaciones de temperatura en una aplicación de magnetometría. Por lo tanto, se compararon dos métodos de evaluación de la respuesta en frecuencia. Primero ajustamos una función modelo, basada en la suposición de un decaimiento bi-exponencial en el dominio del tiempo, que en el dominio de la frecuencia es la suma de dos filtros de paso bajo de primer orden. A continuación, los parámetros ajustados se utilizaron en un algoritmo de regresión para predecir los valores del campo magnético, lo que nos permitió resolver la ambigüedad. Al variar adicionalmente la temperatura del material de diamante, este modelo LTI simple ya no se podía ajustar bien. Para captar la complejidad de los datos, entrenamos una red neuronal artificial con el vector de respuesta en bruto. Este método no sólo nos permitió resolver la ambigüedad del campo bajo, sino que el sistema también pudo predecir valores de campo magnético insensibles a las variaciones de temperatura.

Por último, se examinaron con más detalle los ajustes de las funciones del modelo, obteniéndose un modelo LTI que refleja bien la respuesta en frecuencia real y su dependencia del campo magnético. Este modelo permitiría la integración en simulaciones de sistemas más amplios para la elección y optimización de técnicas de lectura. Además, se examinó la dependencia de la temperatura. Sin embargo, los datos disponibles no permiten determinar parámetros fiables. El trabajo futuro podría identificar y eliminar los componentes de deriva y ruido 1/f en el proceso de lectura. La eliminación de estos componentes de ruido no sólo es importante para cualquier aplicación de detección, sino que

también permitiría la captura de datos fiables en el dominio de la frecuencia a temperaturas variables con el objetivo de ajustar un modelo LTI.

Para la adquisición de la respuesta en frecuencia, son concebibles otros métodos de lectura. Éstos pueden basarse, por ejemplo, en la excitación con ruido de banda ancha y en la correlación entre las señales de entrada y salida del sistema. En cualquier caso, la integración del enfoque del dominio de la frecuencia totalmente óptico es prometedora para el avance de las capacidades de detección del campo magnético, especialmente en aplicaciones en las que los métodos convencionales están limitados por una conexión galvánica, componentes metálicos en el volumen de detección o la interacción con la radiación MW.

En resumen, esta tesis ha mostrado avances en la magnetometría totalmente óptica utilizando centros NV en diamantes, con especial atención a los sistemas de sensores basados en fibras. Exploramos sistemas basados en la intensidad de fluorescencia y en la vida útil de la fluorescencia, investigando la sensibilidad y las dependencias de la temperatura. Demostramos que las mediciones basadas en la vida útil pueden ofrecer una mayor inmunidad a las perturbaciones y proporcionar más información, lo que permite resolver la ambigüedad de campo bajo y reducir las influencias de la temperatura. Las implicaciones de esta investigación son profundas y van mucho más allá del ámbito de la detección totalmente óptica. Las novedosas técnicas desarrolladas para reducir las interferencias y mejorar la estabilidad térmica son fácilmente adaptables a los sensores cuánticos basados en microondas, lo que ofrece una vía para superar los antiguos obstáculos de esta tecnología. Este trabajo no sólo enriquece el acervo de conocimientos existente, sino que también sirve de piedra angular para futuros avances en las tecnologías de detección cuántica, transformando potencialmente las industrias que dependen de mediciones de alta fidelidad en entornos sensibles desde el punto de vista medioambiental.

A Supplementary Information

A.1 Electromagnet

For controlled application of magnetic fields, like required in the acquisition of calibration curves, we use a lab-built electromagnet. The design is based on Fanselau et al. [172] and was built by Timo Staudinger. It was chosen for its high homogenity and high absolute magnetic field. The high homogenity is desirable for the relaxed requirements on positional accuracy and the ability to place multiple sensors, like a reference Hall-based sensor, in the respective volume.

The schematic of the Fanselau coil geometry is shown in Figure A.1. We chose the parameters per Table A.1. The radius of the first coil R_1 dictates all other geometric parameters and was chosen just large enough to accommodate all expected types of fiber sensor heads. The coils were wound on a core, made of Acrylonitrile butadiene styrene (ABS). Such an insulating core allows us to apply AC magnetic currents, without the creation of eddy currents in the base material.

Parameter	**Value**
Radius of first coil	$R_1 = 3\,\mathrm{cm}$
Distance from center to first coil	$z_1 = 0.29759 R_1$
Distance from center to second coil	$z_2 = 0.90673 R_1$
Radius of second coil	$R_2 = 0.76324 R_1$

Table A.1: Geometry parameters of electromagnet.

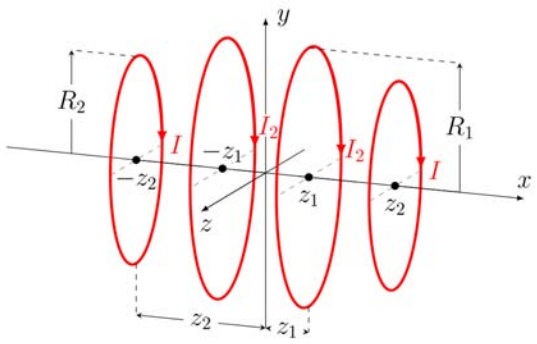

Figure A.1: Schematic of the Fanselau coil geometry.

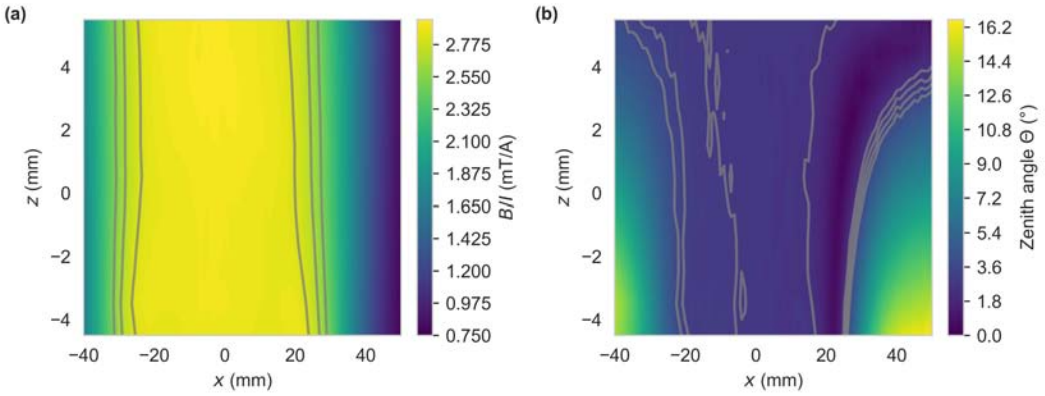

Figure A.2: (**a**) Ratio of magnetic flux density B per coil current I as a function of position x, z in the plane central in the bore of the electromagnet ($I = 7\,\mathrm{A}$). (**b**) Zenith angle Θ as a function of position x, z.

To evaluate the design, a measurement was carried out, using a Hall effect-based sensor (TL493D, Infineon Technologies AG), mounted to a $x, y, z-$stage. First, a sweep of the coil current I with the sensor placed centrally in the electromagnet showed a linear relationship with $B/I = 3\,\mathrm{mT/A}$. Next, we measured the vector magnetic field in the plane central in the bore of the electromagnet, which we show in Figure A.2a. We find a homogeneous region (B/I deviates $< 0.7\%$ from the maximum) of $\pm 20\,\mathrm{mm}$ within the bounds in z set by the Hall-sensor. In Figure A.2a, we show the zenith angle, defined by

$$\Theta = \arccos\left(\frac{|B_x|}{|\boldsymbol{B}|}\right), \tag{A.1}$$

effectively showing the deviation of the direction of $\boldsymbol{B}$ from the x-axis. We find a standard deviation in Θ of $0.3°$ within $x = \pm 20\,\mathrm{mm}$.

A.2 Laser Intensity Fluctuation

In this section we want to find the degree to which laser intensity fluctuations are the cause for noise or drift in the fluorescence signal in a pulsed LIA experiment. We therefore extend the experiment from Section 2.1 by a second TIA which monitors the laser intensity via the reflection at the dichroic mirror. We record data from both detectors for laser intensity monitoring $l(t)$ and fluorescence $f(t)$ using a LIA ($f_\mathrm{r} = 80\,\mathrm{kHz}$), and normalize the individual recordings to their RMS value. We compute the coherency spectrum for its ability to show the extent to which two signals are linearly related to one another. The coherency spectrum between two signals $l(t)$ and $f(t)$ is defined as

$$C_{lf}(f) = \frac{|S_{lf}|}{\sqrt{S_{ll}(f)S_{ff}(f)}}, \tag{A.2}$$

where S_{lf} is the cross-spectral density and S_{ll} and S_{ff} are the (auto) power spectral densities of $l(t)$ and $f(t)$ using Welch's method [177].

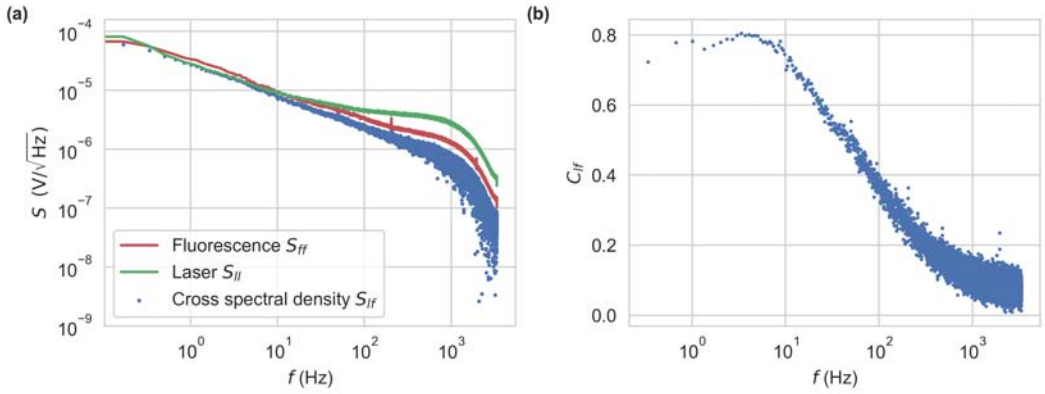

Figure A.3: (**a**) Noise spectral densities of recordings from laser and fluorescence monitor photodetectors, and their cross spectral density. (**b**) Coherence between laser and fluorescence signals.

We show the spectral densities and the resulting coherency spectrum in Figure A.3. For low frequencies $< 10\,\mathrm{Hz}$, C_{lf} is near 0.8. This shows the laser intensity has a high impact on the fluorescence, even when used in a lock-in amplifier setup. At higher frequencies, other noise components, notably thermal and shot noise from the photodetectors add non-coherently, reducing C_{lf}.

A.3 More Noise Measurements

Figure A.4 shows the noise characteristics, analogous to previous measurements in Section 2.3. The fiber sensor was exchanged to the bulk diamond tipped fiber. We find a higher bias instability and a significantly higher drift component, dominating from integration times of 1 s upwards. Since all other optical and electrical components have otherwise remained unchanged, the higher Allan deviation at high integration times can be attributed to the bulk fiber sensor.

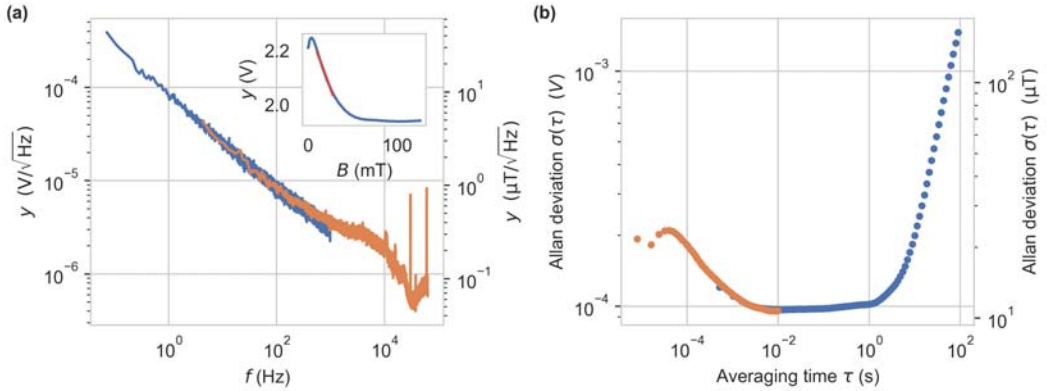

Figure A.4: Noise characteristics of second phase sensitive detector implementation with bulk diamond attached to optical fiber (see Figure 2.2a). (**a**) Noise spectral density at zero bias field by Welch's method (Hann window). Data were recorded at $f_s = 1953.125$ Hz in 15 min (blue trace, window length 28.11 s) and $f_s = 125$ kHz in 15 s (orange trace, window length 0.47 s). A linear fit to the calibration curve, shown in the inset, was used to generate a second y-axis with magnetic field values. (**b**) Allan deviation of the same data as in (a) with the same color correspondence. A second y-axis with magnetic field values uses the same fit to the calibration curve from the inset.

We measured the noise characteristics of the second phase sensitive detector implementation in a direct feedback configuration, which we show in Figure A.5. The spectral density shows numerous narrow bandwidth interferers. These were not present in previous measurements in the complete setup, indicating their origin in the trigger output. Since the trigger output is further binarized by the laser driver input, any interferers or drift in noise spectrum and Allan deviation are of low importance in an application.

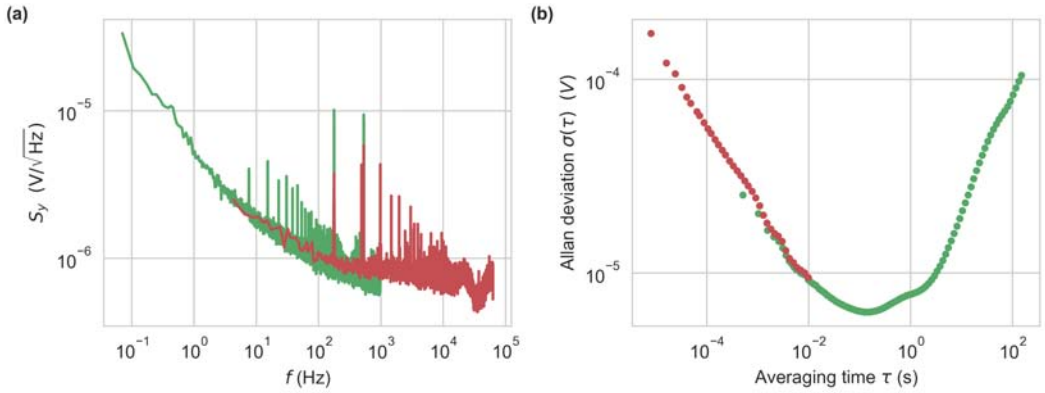

Figure A.5: Noise characteristics of second phase sensitive detector implementation in direct feedback configuration. (**a**) Noise spectral density by Welch's method (Hann window). Data were recorded at $f_s = 1953.125\,\text{Hz}$ in 15 min (green trace, window length 28.11 s) and $f_s = 125\,\text{kHz}$ in 15 s (red trace, window length 0.47 s). (**b**) Allan deviation of the same data as in (a) with the same color correspondence.

A.4 Magnetic Field Dependent Fluorescence Lifetime

To compare our material to other diamonds with high NV-density, we investigated the magnetic field dependent fluorescence lifetimes of samples by Adámas Nanotechnologies, Inc. with the same TCSPC setup, which we described in Chapter 3. We show them in Figures A.6 and A.7.

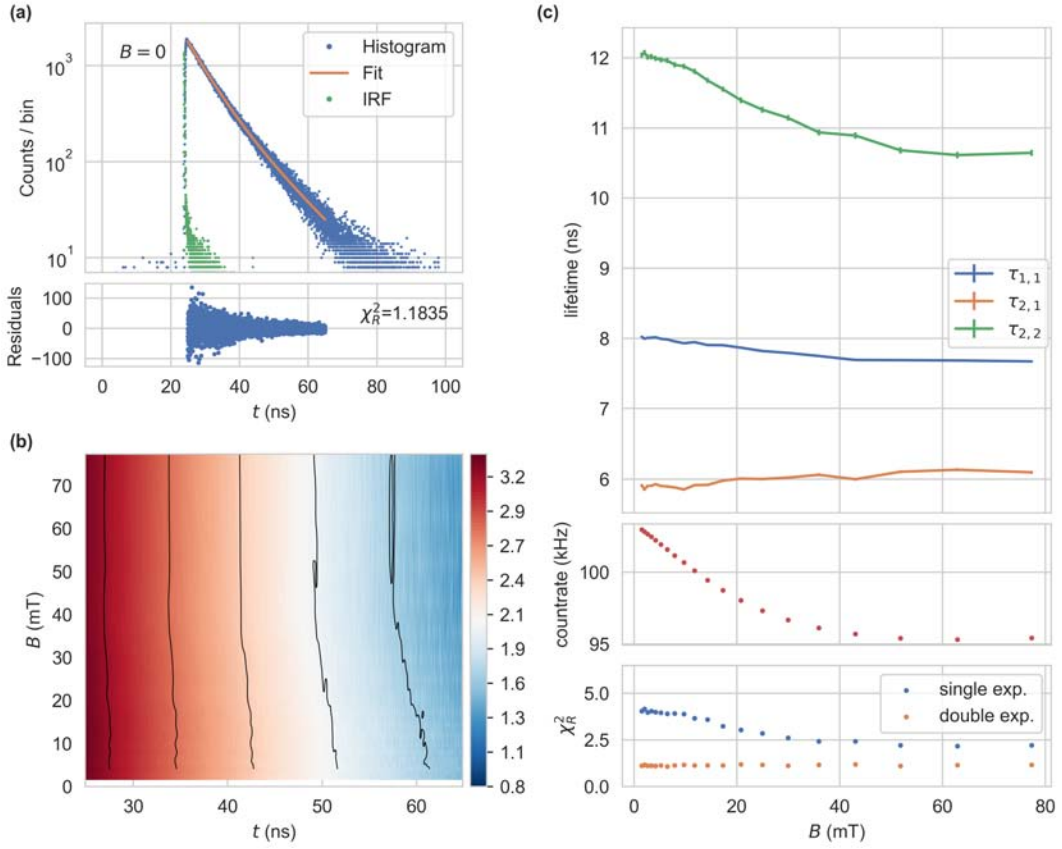

Figure A.6: TCSPC measurements of 15um-Hi by Adámas Nanotechnologies, Inc. in a glass cuvette. The diamonds are specified to have mean sizes of 15 µm and a NV concentration of 3 ppm. (**a**) Single histogram, captured at $B = 0$ (Bin width 10 ps, 20 s capture time, 8 MHz repetition rate, 37 µW average power, APD count rate 83 kHz). The average count in the first 20 ns of 7.03 counts has been subtracted. The lower panel shows the residuals of a double-exponential fit ($a_{2,1} = 1280, \tau_{2,1} = 6.14$ ns, $a_{2,2} = 504, \tau_{2,2} = 12.9$ ns, $\chi^2_\mathrm{R} = 1.1835$). For the fit, we use a time span of 40 ns, following the maximum. The IRF was captured at the same count rate at the APD (FWHM = 0.2 ns). (**b**) Histograms of the sample at varying magnetic flux densities B, shown in the time range used for the fit. A logarithmic color scale is chosen. (**c**) Single- and double-exponential fits for the data in (b) with fixed $\hat{a}_{2,1} = 1 - \hat{a}_{2,2} = 0.65$. The three panels show the extracted lifetimes, the count rate at the APD, and χ^2_R for the respective fits as functions of B.

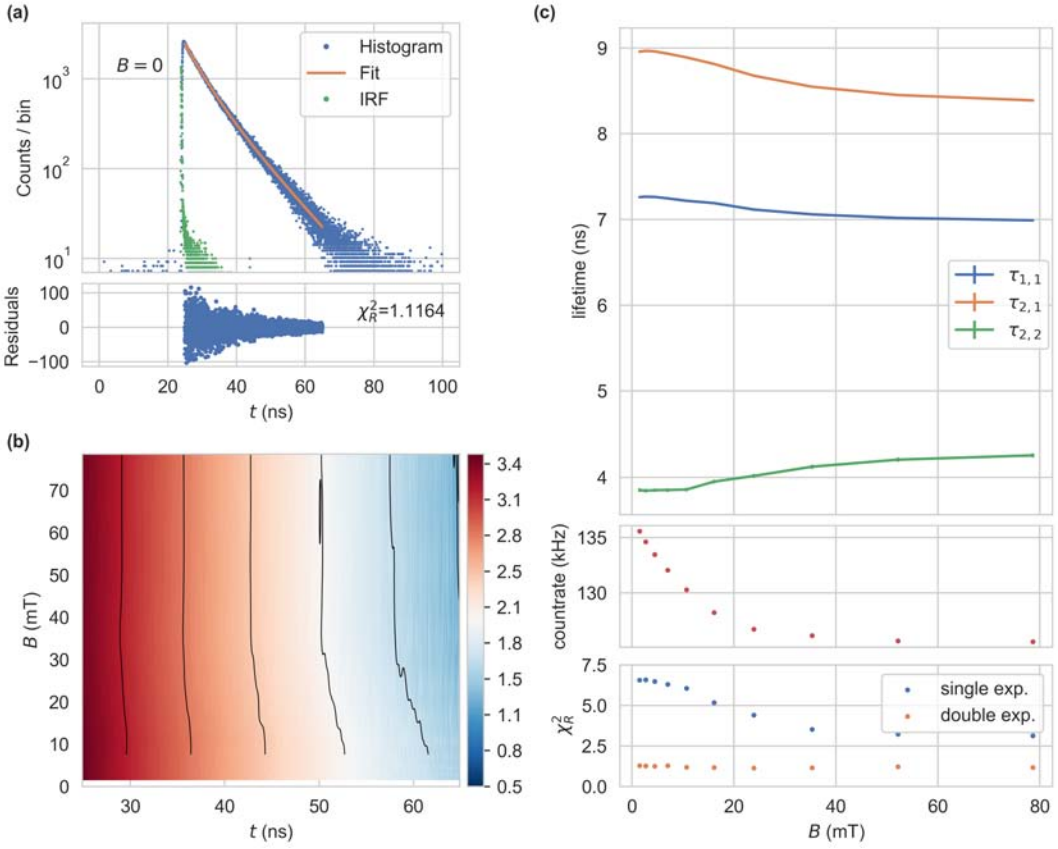

Figure A.7: TCSPC measurements of 150um-Hi by Adámas Nanotechnologies, Inc. in a glass cuvette. The diamonds are specified to have mean sizes of 150 µm and a NV concentration of 3 ppm. (**a**) Single histogram, captured at $B = 0$ (Bin width 10 ps, 20 s capture time, 8 MHz repetition rate, 116 µW average power, APD count rate 104 kHz). The average count in the first 20 ns of 10.34 counts has been subtracted. The lower panel shows the residuals of a double-exponential fit ($a_{2,1} = 1404, \tau_{2,1} = 4.90$ ns, $a_{2,2} = 1052, \tau_{2,2} = 10.3$ ns, $\chi^2_{\mathrm{R}} = 1.1164$). For the fit, we use a time span of 40 ns, following the maximum. The IRF was captured at the same count rate at the APD (FWHM = 0.2 ns). (**b**) Histograms of the sample at varying magnetic flux densities B, shown in the time range used for the fit. A logarithmic color scale is chosen. (**c**) Single- and double-exponential fits for the data in (b) with fixed $\hat{a}_{2,1} = 1 - \hat{a}_{2,2} = 0.65$. The three panels show the extracted lifetimes, the count rate at the APD, and χ^2_{R} for the respective fits as functions of B.

A.5 Magnitude and Phase in LIA Setup

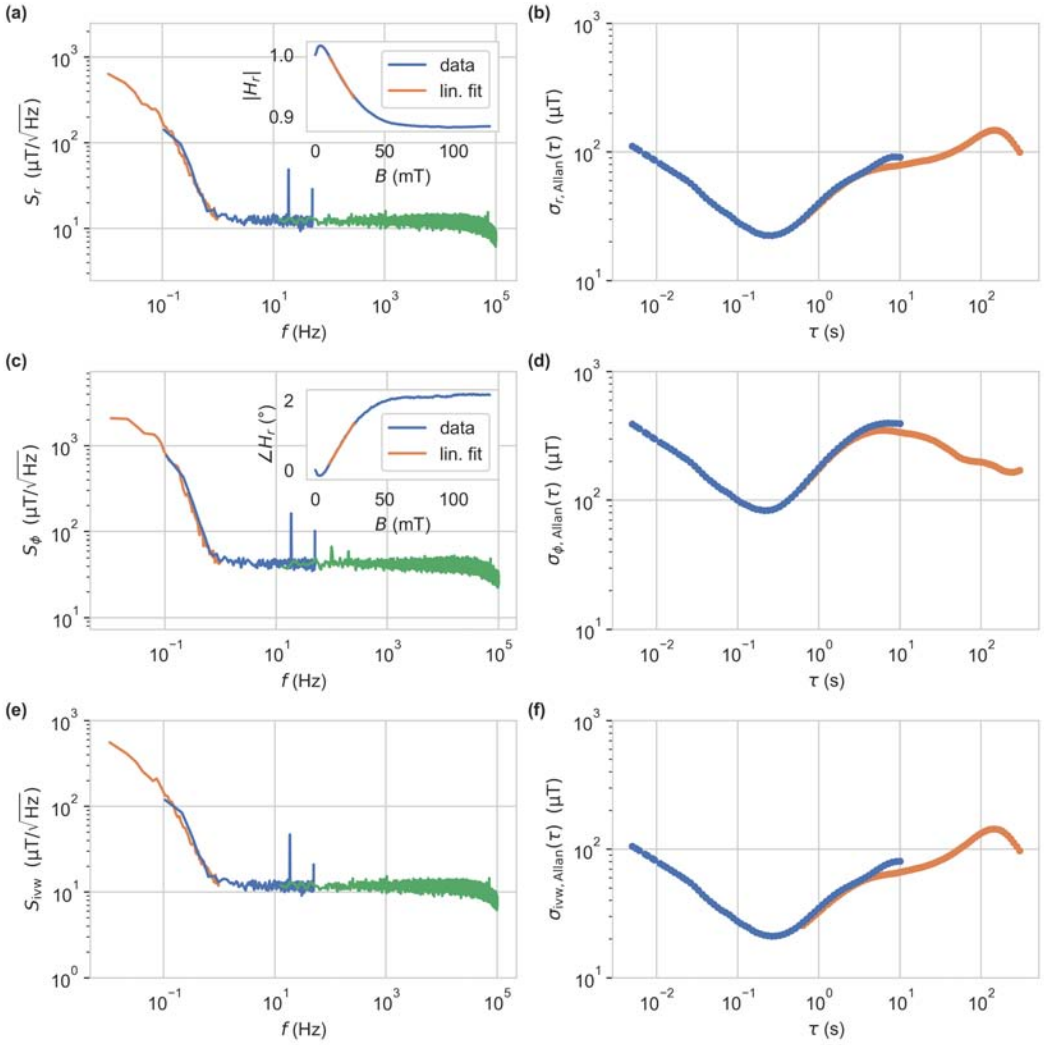

Figure A.8: Noise spectral densities based on magnitude S_r (**a**) and phase S_ϕ (**c**). The excitation frequency was set to $f = 3$ MHz, and a bias field of $B = 20$ mT was applied. The optical excitation was set to $P_{\text{opt}} = 11.57\,\text{mW}$. Data were recorded by the LIA with the low-pass filter set to fourth order at corner frequencies of 88 kHz, 200 Hz and 2 Hz, corresponding to the green, blue and orange traces. They have been subsequently converted to magnetic field values using the linear fits drawn in the respective insets and converted to spectral densities by Welch's method (Hann windows of lengths 0.31 s, 9.38 s, 85.31 s). Allan deviations of magnitude (**b**) and phase (**d**) from the data in (a) and (b). Spectral density (**e**) and Allan deviation (**f**) of inverse-variance weighted average of magnitude and phase data from (a) and (c).

A.6 Frequency Domain Fits

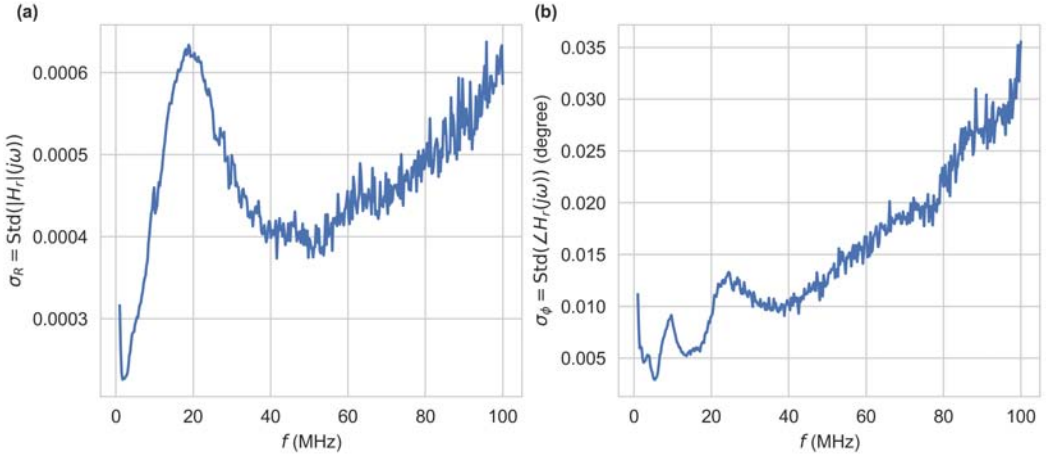

Figure A.9: The standard deviations in (**a**) magnitude and (**b**) phase, estimated from a sequence of 135 measurements at nearly constant ambient temperature $T = 0.3\,°\mathrm{C}$ and zero-field.

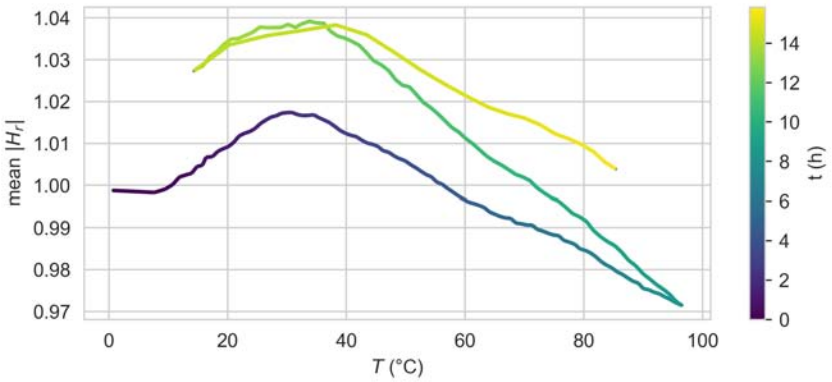

Figure A.10: Mean relative magnitude $\frac{1}{401}\sum_{n=1}^{401}|H_r|(j2\pi f_n)$ as a function of temperature at $B = 0$. We swept the ambient temperature from 0 °C to 96 °C in 8 h, back to 0 °C in 4 h and lastly to 96 °C in 1.5 h.

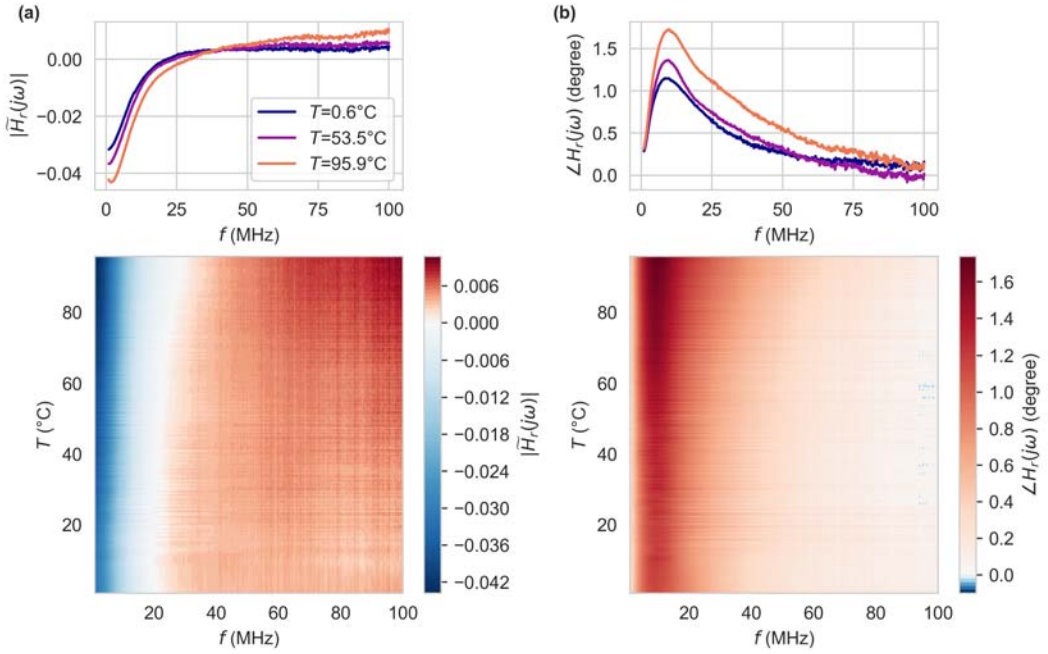

Figure A.11: Modified relative magnitude (**a**) and phase (**b**) responses as a function of temperature at $B = 11.96\,\mathrm{mT}$. The top panels show examples, from the whole set of 100 responses, plotted in the bottom panels. The modified relative magnitude does not allow any conclusions about the absolute intensity, but only comparison between different ambient temperatures.

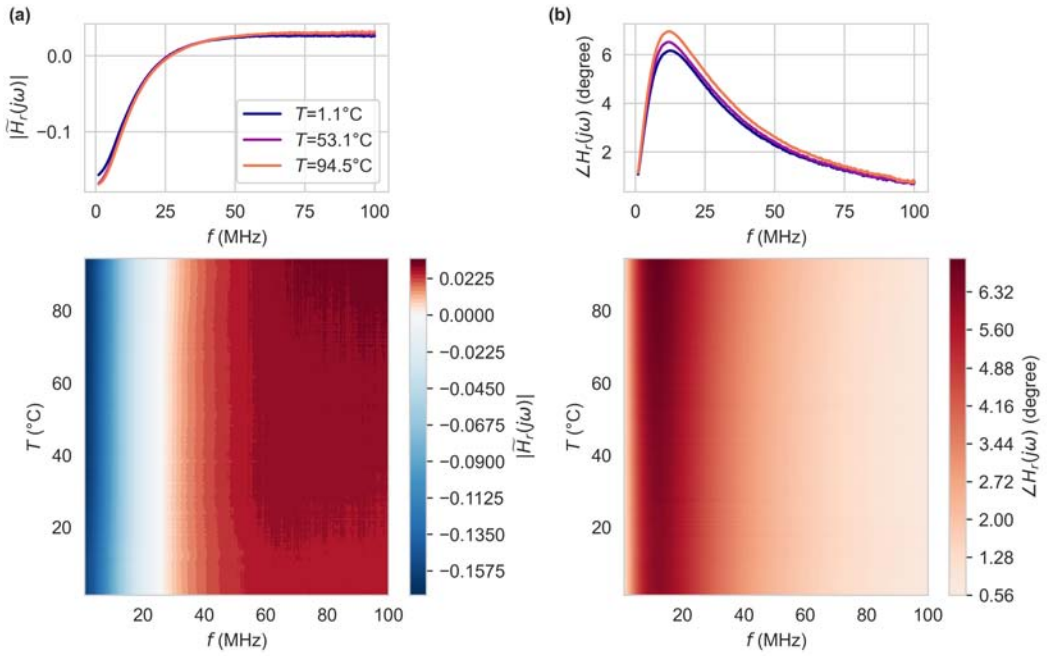

Figure A.12: Modified relative magnitude (**a**) and phase (**b**) responses as a function of temperature at $B = 71.19\,\mathrm{mT}$. The top panels show examples, from the whole set of 100 responses, plotted in the bottom panels. The modified relative magnitude does not allow any conclusions about the absolute intensity, but only comparison between different ambient temperatures.

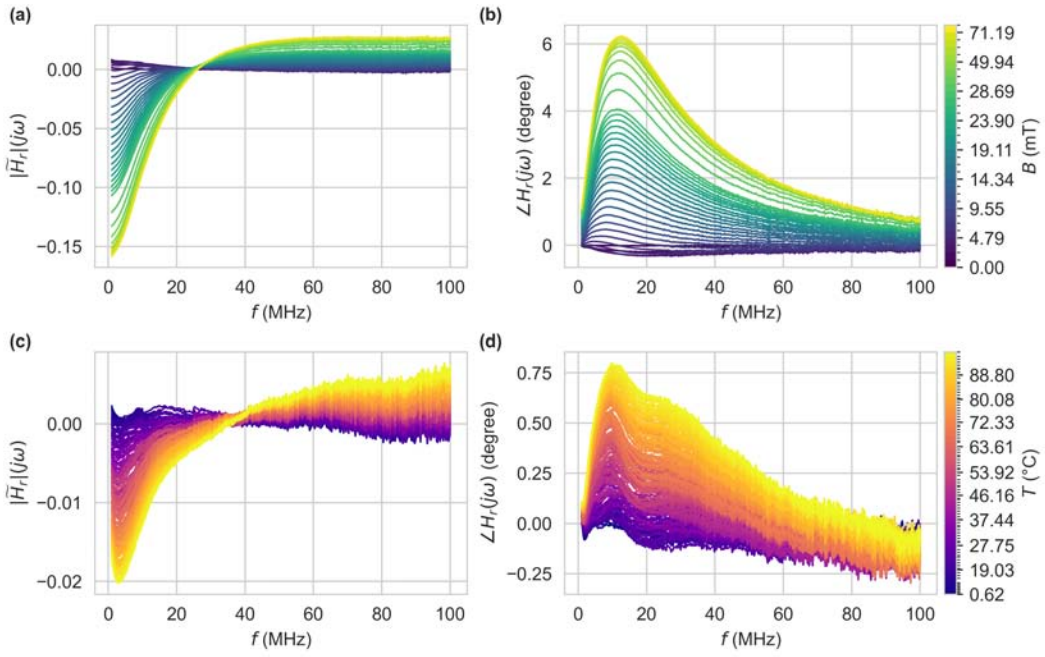

Figure A.13: Modified relative magnitude (**a**) and (**c**), and phase (**b**) and (**d**) at reference conditions $T_0 = 0.7\,^{\circ}\mathrm{C}$ with B being varied (top row) and $B_0 = 0\,\mathrm{mT}$ with T being varied (bottom row).

Bibliography

[1] Horsthemke, L.; Pogorzelski, J.; Stiegekötter, D.; Hoffmann, F.; Langguth, L.; Staacke, R.; Laube, C.; Knolle, W.; Gregor, M.; Glösekötter, P. Excited-State Lifetime of NV Centers for All-Optical Magnetic Field Sensing. *Sensors* **2024**, *24*, 2093. https://doi.org/10.3390/s24072093.

[2] Horsthemke, L.; Pogorzelski, J.; Stiegekötter, D.; Hoffmann, F.; Bülter, A.S.; Trinschek, S.; Gregor, M.; Glösekötter, P. Towards Resolving the Ambiguity in Low-Field, All-Optical Magnetic Field Sensing with High NV-Density Diamonds. In Proceedings of the ITISE 2024. MDPI, 2024, ITISE 2024. https://doi.org/10.3390/engproc2024068008.

[3] Horsthemke, L.; Pogorzelski, J.; Stiegekoetter, D.; Hoffmann, F.; Bülter, A.S.; Langguth, L.; Staacke, R.; Trinschek, S.; Gregor, M.; Gloesekoetter, P. Fluorescence Lifetime of NV Centers for Temperature-Insensitive All-Optical Magnetic Field Sensing. EasyChair Preprint 15104, 2024.

[4] L. Horsthemke.; C. Bischoff.; P. Glösekötter.; B. Burchard.; R. Staacke.; J. Meijer. A1.4 Highly Sensitive Compact Room Temperature Quantum Scalar Magnetometer **2020**. https://doi.org/10.5162/SMSI2020/A1.4.

[5] Horsthemke, L.; Bischoff, C.; Glosekotter, P.; Burchard, B.; Staacke, R.; Meijer, J. All optical readout scheme for photoluminescence based magnetic field sensors. In Proceedings of the 2020 IEEE SENSORS. IEEE, 2020, pp. 1–3. https://doi.org/10.1109/sensors47125.2020.9278923.

[6] Pogorzelski, J.; Horsthemke, L.; Homrighausen, J.; Stiegekötter, D.; Gregor, M.; Glösekötter, P. Compact and Fully Integrated LED Quantum Sensor Based on NV Centers in Diamond. *Sensors* **2024**, *24*, 743. https://doi.org/10.3390/s24030743.

[7] Stiegekötter, D.; Pogorzelski, J.; Horsthemke, L.; Hoffmann, F.; Gregor, M.; Glösekötter, P. Microcontroller-Optimized Measurement Electronics for Coherent Control Applications of NV Centers. *Sensors* **2024**, *24*, 3138. https://doi.org/10.3390/s24103138.

[8] Pogorzelski, J.; Horsthemke, L.; Homrighausen, J.; Stiegekötter, D.; Hoffmann, F.; Bülter, A.S.; Gregor, M.; Glösekötter, P. Calibration-Free Current Measurement with Integrated Quantum Sensor. *Engineering Proceedings* **2024**, *68*. https://doi.org/10.3390/engproc2024068058.

[9] Homrighausen, J.; Horsthemke, L.; Pogorzelski, J.; Trinschek, S.; Glösekötter, P.; Gregor, M. Edge-Machine-Learning-Assisted Robust Magnetometer Based on Randomly Oriented NV-Ensembles in Diamond. *Sensors* **2023**, *23*, 1119. https://doi.org/10.3390/s23031119.

[10] Stegemann, J.; Peters, M.; Horsthemke, L.; Langels, N.; Glösekötter, P.; Heusler, S.; Gregor, M. Modular low-cost 3D printed setup for experiments with NV centers in diamond. *European Journal of Physics* **2023**, *44*, 035402. https://doi.org/10.1088/1361-6404/acbe7c.

[11] Pogorzelski, J.; Homrighausen, J.; Horsthemke, L.; Stiegekötter, D.; Lindloge, L.; Teuber, J.; Gregor, M.; Glösekötter, P. A7.4 - Bias-Tee quantum current sensor with temperature tracking based on modulated cw-ODMR with NV centers. In Proceedings of the Lectures. AMA Service GmbH, Von-Münchhausen-Str. 49, 31515 Wunstorf, Germany, 2023. https://doi.org/10.5162/smsi2023/a7.4.

[12] Staacke, R.; John, R.; Wunderlich, R.; Horsthemke, L.; Knolle, W.; Laube, C.; Glösekötter, P.; Burchard, B.; Abel, B.; Meijer, J. Isotropic Scalar Quantum Sensing of Magnetic Fields for Industrial Application. *Advanced Quantum Technologies* **2020**, *n/a*, 2000037. https://doi.org/10.1002/qute.202000037.

[13] Acosta, V.M. Optical Magnetometry with Nitrogen-Vacancy Centers in Diamond, 2011.

[14] Zheng, H.; Chatzidrosos, G.; Wickenbrock, A.; Bougas, L.; Lazda, R.; Berzins, A.; Gahbauer, F.H.; Auzinsh, M.; Ferber, R.; Budker, D. Level anti-crossing magnetometry with color centers in diamond, 2017. https://doi.org/10.48550/ARXIV.1701.06838.

[15] Fermon, C. Introduction on Magnetic Sensing and Spin Electronics, 2017. https://doi.org/10.1002/9783527698509.ch1.

[16] Grosz, A.; Haji-Sheikh, M.J.; Mukhopadhyay, S.C., Eds. *High sensitivity magnetometers*; Springer eBook Collection, Springer: [Cham], 2017.

[17] Coey, J.M.D.; Parkin, S.S.P., Eds. *Handbook of magnetism and magnetic materials*; Springer Nature reference, Springer: Cham, 2021.

[18] Khan, M.A.; Sun, J.; Li, B.; Przybysz, A.; Kosel, J. Magnetic sensors-A review and recent technologies. *Engineering Research Express* **2021**, *3*, 022005. https://doi.org/10.1088/2631-8695/ac0838.

[19] Parsa Sirat, A.; Parkhideh, B. Current Sensor Integration Issues with Wide-Bandgap Power Converters. *Sensors* **2023**, *23*, 6481. https://doi.org/10.3390/s23146481.

[20] Barry, J.F.; Schloss, J.M.; Bauch, E.; Turner, M.J.; Hart, C.A.; Pham, L.M.; Walsworth, R.L. Sensitivity optimization for NV-diamond magnetometry. *Reviews of Modern Physics* **2020**, *92*, 015004. https://doi.org/10.1103/revmodphys.92.015004.

[21] Xie, Y.; Yu, H.; Zhu, Y.; Qin, X.; Rong, X.; Duan, C.K.; Du, J. A hybrid magnetometer towards femtotesla sensitivity under ambient conditions. *Science Bulletin* **2021**, *66*, 127–132. https://doi.org/10.1016/j.scib.2020.08.001.

[22] Tetienne, J.P.; Rondin, L.; Spinicelli, P.; Chipaux, M.; Debuisschert, T.; Roch, J.F.; Jacques, V. Magnetic-field-dependent photodynamics of single NV defects in diamond: an application to qualitative all-optical magnetic imaging. *New Journal of Physics* **2012**, *14*, 103033. https://doi.org/10.1088/1367-2630/14/10/103033.

[23] Zhou, T.X.; Stöhr, R.J.; Yacoby, A. Scanning diamond NV center probes compatible with conventional AFM technology. *Applied Physics Letters* **2017**, *111*. https://doi.org/10.1063/1.4995813.

[24] Floch, J.M.L.; Bradac, C.; Nand, N.; Castelletto, S.; Tobar, M.E.; Volz, T. Addressing a single NV^- spin with a macroscopic dielectric microwave cavity **2014**. https://doi.org/10.48550/ARXIV.1412.8327.

[25] Maksymov, I.S.; Kostylev, M. Impact of eddy currents on the dispersion relation of surface spin waves in thin conducting magnetic films. *Journal of Physics D: Applied Physics* **2013**, *46*, 495001. https://doi.org/10.1088/0022-3727/46/49/495001.

[26] Rogers, L.J.; McMurtrie, R.L.; Sellars, M.J.; Manson, N.B. Time-averaging within the excited state of the nitrogen-vacancy centre in diamond. *New Journal of Physics* **2009**, *11*, 063007. https://doi.org/10.1088/1367-2630/11/6/063007.

[27] Fedotov, I.; Amitonova, L.; Sidorov-Biryukov, D.; Safronov, N.; Blakley, S.; Levchenko, A.; Zibrov, S.; Fedotov, A.; Kilin, S.; Scully, M.; et al. Fiber-optic magnetic-field imaging. *Optics Letters* **2014**, *39*. https://doi.org/10.1364/OL.39.006954.

[28] Paone, D.; Pinto, D.; Kim, G.; Feng, L.; Kim, M.J.; Stöhr, R.; Singha, A.; Kaiser, S.; Logvenov, G.; Keimer, B.; et al. All-optical and microwave-free detection of Meissner screening using nitrogen-vacancy centers in diamond. *Journal of Applied Physics* **2021**, *129*, 024306. https://doi.org/10.1063/5.0037414.

[29] Anishchik, S.V.; Vins, V.G.; Yelisseyev, A.P.; Lukzen, N.N.; Lavrik, N.L.; Bagryansky, V.A. Low-field feature in the magnetic spectra of N-V centers in diamond. *New Journal of Physics* **2015**, *17*, 023040. https://doi.org/10.1088/1367-2630/17/2/023040.

[30] Wickenbrock, A.; Zheng, H.; Bougas, L.; Leefer, N.; Afach, S.; Jarmola, A.; Acosta, V.M.; Budker, D. Microwave-free magnetometry with nitrogen-vacancy centers in diamond. *Applied Physics Letters* **2016**, *109*, 053505, [https://doi.org/10.1063/1.4960171]. https://doi.org/10.1063/1.4960171.

[31] Zheng, H.; Sun, Z.; Chatzidrosos, G.; Zhang, C.; Nakamura, K.; Sumiya, H.; Ohshima, T.; Isoya, J.; Wrachtrup, J.; Wickenbrock, A.; et al. Microwave-Free Vector Magnetometry with Nitrogen-Vacancy Centers along a Single Axis in Diamond. *Phys. Rev. Applied* **2020**, *13*, 044023. https://doi.org/10.1103/PhysRevApplied.13.044023.

[32] Wunderlich, R.; Staacke, R.; Knolle, W.; Abel, B.; Meijer, J. Magnetic field and angle-dependent photoluminescence of a fiber-coupled nitrogen vacancy rich diamond. *Journal of Applied Physics* **2021**, *130*, 124901. https://doi.org/10.1063/5.0059330.

[33] Dhungel, O.; Lenz, T.; Omar, M.; Rebeirro, J.S.; Ivady, V.; Gali, A.; Wickenbrock, A.; Budker, D. Zero-field microwave-free magnetometry with ensembles of nitrogen-vacancy centers in diamond **2023**. [arXiv:cond-mat.mes-hall/2301.09666]. https://doi.org/10.48550/arXiv.2301.09666.

[34] Akhmedzhanov, R.A.; Gushchin, L.A.; Zelensky, I.V.; Kupaev, A.V.; Nizov, V.A.; Nizov, N.A.; Sobgayda, D.A. Quantum Magnetometer Based on Cross-Relaxation Resonances in Ensembles of NV-Centers in Diamond. *Technical Physics* **2024**, *69*, 121–128. https://doi.org/10.1134/s1063784224010018.

[35] Duan, D.; Du, G.X.; Kavatamane, V.K.; Arumugam, S.; Tzeng, Y.K.; Chang, H.C.; Balasubramanian, G. Efficient nitrogen-vacancy centers' fluorescence excitation and collection from micrometer-sized diamond by a tapered optical fiber in endoscope-type configuration. *Optics Express* **2019**, *27*, 6734. https://doi.org/10.1364/oe.27.006734.

[36] Chatzidrosos, G.; Rebeirro, J.S.; Zheng, H.; Omar, M.; Brenneis, A.; Stürner, F.M.; Fuchs, T.; Buck, T.; Rölver, R.; Schneemann, T.; et al. Fiberized Diamond-Based Vector Magnetometers. *Frontiers in Photonics* **2021**, *2*. https://doi.org/10.3389/fphot.2021.732748.

[37] Bian, C.; Yang, P.; Wang, H.; Wen, R.; Li, M.; Song, C.; Yang, K.; Huang, Y. Research on a Fiber Optic Magnetic Field Sensor Based on Fuze Platform. In Proceedings of the 2024 IEEE 7th International Conference on Electronic Information and Communication

Technology (ICEICT). IEEE, 2024, pp. 780–782. https://doi.org/10.1109/iceict61637.2024.10671121.

[38] Ziegler, S.; Woodward, R.C.; Iu, H.H.C.; Borle, L.J. Current Sensing Techniques: A Review. *IEEE Sensors Journal* **2009**, *9*, 354–376. https://doi.org/10.1109/jsen.2009.2013914.

[39] Sun, H.; Huang, S.; Peng, L. High-Current Sensing Technology for Transparent Power Grids: A Review. *IEEE Open Journal of the Industrial Electronics Society* **2024**, *5*, 326–358. https://doi.org/10.1109/ojies.2024.3387432.

[40] Crescentini, M.; Syeda, S.F.; Gibiino, G.P. Hall-Effect Current Sensors: Principles of Operation and Implementation Techniques. *IEEE Sensors Journal* **2022**, *22*, 10137–10151. https://doi.org/10.1109/jsen.2021.3119766.

[41] Xu, F.; Wang, L.; Wang, K., Integrated Design and Optimization of SSPC Current Measurement Module Based on AMR. In *The proceedings of the 18th Annual Conference of China Electrotechnical Society*; Springer Nature Singapore, 2024; pp. 582–589. https://doi.org/10.1007/978-981-97-1072-0_59.

[42] Schreiber-Prillwitz, W.; Nebeling, A.; von Manteuffel, G.; Nau, C. P5.3 - Architecture of an Integrated AMR Current Sensor (IACS) System for a Wide Range of Automotive Applications. In Proceedings of the Proceedings SENSOR 2011. AMA Service GmbH, Von-Münchhausen-Str. 49, 31515 Wunstorf, Germany, 2011, pp. 774–779. https://doi.org/10.5162/sensor11/sp5.3.

[43] Hall, E.H. On a new action of the magnet on electric currents. *American Journal of Science* **1880**, *s3-19*, 200–205. https://doi.org/10.2475/ajs.s3-19.111.200.

[44] Thomson, W. On the electro-dynamic qualities of metals: Effects of magnetization on the electric conductivity of nickel and of iron. *Proceedings of the Royal Society of London* **1857**, *8*, 546–550. https://doi.org/10.1098/rspl.1856.0144.

[45] Dietmayer, K.C. Magnetische Sensoren auf Basis des AMR-Effekts (Magnetic Sensors Based on the AMR-Effect). *teme* **2001**, *68*, 269. https://doi.org/10.1524/teme.2001.68.6.269.

[46] Wang, S.; Gao, J. Overview of Magnetic Field Sensor. *Journal of Physics: Conference Series* **2023**, *2613*, 012012. https://doi.org/10.1088/1742-6596/2613/1/012012.

[47] Griffith, W.C.; Knappe, S.; Kitching, J. Femtotesla atomic magnetometry in a microfabricated vapor cell. *Optics Express* **2010**, *18*, 27167. https://doi.org/10.1364/oe.18.027167.

[48] Tumanski, S. Induction coil sensors—a review. *Measurement Science and Technology* **2007**, *18*, R31–R46. https://doi.org/10.1088/0957-0233/18/3/r01.

[49] Stepanov, V.; Cho, F.H.; Abeywardana, C.; Takahashi, S. High-frequency and high-field optically detected magnetic resonance of nitrogen-vacancy centers in diamond. *Applied Physics Letters* **2015**, *106*. https://doi.org/10.1063/1.4908528.

[50] Wolf, T.; Neumann, P.; Nakamura, K.; Sumiya, H.; Ohshima, T.; Isoya, J.; Wrachtrup, J. Subpicotesla Diamond Magnetometry. *Physical Review X* **2015**, *5*. https://doi.org/10.1103/physrevx.5.041001.

[51] Takada, K.; Katsumi, R.; Yatsui, T. Sensitivity improvement of a single-NV diamond magnetometer using a chiral waveguide. *Optics Express* **2023**, *32*, 795. https://doi.org/10.1364/oe.509860.

[52] Degen, C.; Reinhard, F.; Cappellaro, P. Quantum sensing. *Reviews of Modern Physics* **2017**, *89*, 035002. https://doi.org/10.1103/revmodphys.89.035002.

[53] Wei, L.; Kuo, P.K.; Thomas, R.L.; Anthony, T.R.; Banholzer, W.F. Thermal conductivity of isotopically modified single crystal diamond. *Physical Review Letters* **1993**, *70*, 3764–3767. https://doi.org/10.1103/physrevlett.70.3764.

[54] Jelezko, F.; Wrachtrup, J. Single defect centres in diamond: A review. *physica status solidi (a)* **2006**, *203*, 3207–3225. https://doi.org/10.1002/pssa.200671403.

[55] Zaitsev, A.M. *Optical Properties of Diamond*; Springer Berlin Heidelberg, 2001. https://doi.org/10.1007/978-3-662-04548-0.

[56] Doherty, M.W.; Manson, N.B.; Delaney, P.; Jelezko, F.; Wrachtrup, J.; Hollenberg, L.C. The nitrogen-vacancy colour centre in diamond. *Physics Reports* **2013**, *528*, 1–45. https://doi.org/10.1016/j.physrep.2013.02.001.

[57] Acosta, V.; Hemmer, P. Nitrogen-vacancy centers: Physics and applications. *MRS Bulletin* **2013**, *38*, 127–130. https://doi.org/10.1557/mrs.2013.18.

[58] Childress, L.; Hanson, R. Diamond NV centers for quantum computing and quantum networks. *MRS Bulletin* **2013**, *38*, 134–138. https://doi.org/10.1557/mrs.2013.20.

[59] Mamin, H.J.; Kim, M.; Sherwood, M.H.; Rettner, C.T.; Ohno, K.; Awschalom, D.D.; Rugar, D. Nanoscale Nuclear Magnetic Resonance with a Nitrogen-Vacancy Spin Sensor. *Science* **2013**, *339*, 557–560. https://doi.org/10.1126/science.1231540.

[60] Yang, Y.; Vallabhapurapu, H.H.; Sewani, V.K.; Isarov, M.; Firgau, H.R.; Adambukulam, C.; Johnson, B.C.; Pla, J.J.; Laucht, A. Observing hyperfine interactions of NV- centers in diamond in an advanced quantum teaching lab. *American Journal of Physics* **2022**, *90*, 550–560. https://doi.org/10.1119/5.0075519.

[61] Bürgler, B.; Sjolander, T.F.; Brinza, O.; Tallaire, A.; Achard, J.; Maletinsky, P. All-optical nuclear quantum sensing using nitrogen-vacancy centers in diamond. *npj Quantum Information* **2023**, *9*. https://doi.org/10.1038/s41534-023-00724-6.

[62] Hall, L.; Simpson, D.; Hollenberg, L. Nanoscale sensing and imaging in biology using the nitrogen-vacancy center in diamond. *MRS Bulletin* **2013**, *38*, 162–167. https://doi.org/10.1557/mrs.2013.24.

[63] Schirhagl, R.; Chang, K.; Loretz, M.; Degen, C.L. Nitrogen-Vacancy Centers in Diamond: Nanoscale Sensors for Physics and Biology. *Annual Review of Physical Chemistry* **2014**, *65*, 83–105, [https://doi.org/10.1146/annurev-physchem-040513-103659]. PMID: 24274702, https://doi.org/10.1146/annurev-physchem-040513-103659.

[64] Webb, J.L.; Troise, L.; Hansen, N.W.; Achard, J.; Brinza, O.; Staacke, R.; Kieschnick, M.; Meijer, J.; Perrier, J.F.; Berg-Sørensen, K.; et al. Optimization of a Diamond Nitrogen Vacancy Centre Magnetometer for Sensing of Biological Signals **2020**. *8*. https://doi.org/10.3389/fphy.2020.522536.

[65] Fujiwara, M.; Shikano, Y. Diamond quantum thermometry: from foundations to applications. *Nanotechnology* **2021**, *32*, 482002. https://doi.org/10.1088/1361-6528/ac1fb1.

[66] Loubser, J.H.N.; Wyk, J.A.v. Electron spin resonance in the study of diamond. *Reports on Progress in Physics* **1978**, *41*, 1201–1248. https://doi.org/10.1088/0034-4885/41/8/002.

[67] Meara, C.J.; Rayson, M.J.; Briddon, P.R.; Goss, J.P. Density functional theory study on magnetically detecting positively charged nitrogen-vacancy center in diamond. *Physical Review B* **2019**, *100*, 104108. https://doi.org/10.1103/physrevb.100.104108.

[68] Grotz, B.; Hauf, M.V.; Dankerl, M.; Naydenov, B.; Pezzagna, S.; Meijer, J.; Jelezko, F.; Wrachtrup, J.; Stutzmann, M.; Reinhard, F.; et al. Charge state manipulation of qubits in diamond. *Nature Communications* **2012**, *3*. https://doi.org/10.1038/ncomms1729.

[69] Giri, R.; Jensen, R.H.; Khurana, D.; Bocquel, J.; Radko, I.P.; Lang, J.; Osterkamp, C.; Jelezko, F.; Berg-Sorensen, K.; Andersen, U.L.; et al. Charge Stability and Charge-State-Based Spin Readout of Shallow Nitrogen-Vacancy Centers in Diamond. *ACS Applied Electronic Materials* **2023**, *5*, 6603–6610. https://doi.org/10.1021/acsaelm.3c01141.

[70] Hong, S.; Grinolds, M.S.; Pham, L.M.; Le Sage, D.; Luan, L.; Walsworth, R.L.; Yacoby, A. Nanoscale magnetometry with NV centers in dia-

mond. *MRS Bulletin* **2013**, *38*, 155–161. https://doi.org/10.1557/mrs.2013.23.

[71] Fuchs, G.D.; Dobrovitski, V.V.; Hanson, R.; Batra, A.; Weis, C.D.; Schenkel, T.; Awschalom, D.D. Excited-State Spectroscopy Using Single Spin Manipulation in Diamond. *Physical Review Letters* **2008**, *101*, 117601. https://doi.org/10.1103/physrevlett.101.117601.

[72] Batalov, A.; Zierl, C.; Gaebel, T.; Neumann, P.; Chan, I.Y.; Balasubramanian, G.; Hemmer, P.R.; Jelezko, F.; Wrachtrup, J. Temporal Coherence of Photons Emitted by Single Nitrogen-Vacancy Defect Centers in Diamond Using Optical Rabi-Oscillations. *Physical Review Letters* **2008**, *100*, 077401. https://doi.org/10.1103/physrevlett.100.077401.

[73] Fuchs, G.D.; Dobrovitski, V.V.; Toyli, D.M.; Heremans, F.J.; Weis, C.D.; Schenkel, T.; Awschalom, D.D. Excited-state spin coherence of a single nitrogen–vacancy centre in diamond. *Nature Physics* **2010**, *6*, 668–672. https://doi.org/10.1038/nphys1716.

[74] Robledo, L.; Bernien, H.; van der Sar, T.; Hanson, R. Spin dynamics in the optical cycle of single nitrogen-vacancy centres in diamond. *New Journal of Physics* **2011**, *13*, 025013. https://doi.org/10.1088/1367-2630/13/2/025013.

[75] Gupta, A.; Hacquebard, L.; Childress, L. Efficient signal processing for time-resolved fluorescence detection of nitrogen-vacancy spins in diamond. *Journal of the Optical Society of America B* **2016**, *33*, B28. https://doi.org/10.1364/josab.33.000b28.

[76] Stürner, F.M.; Liu, Y.; Colard, P.O.; Markham, M.; Jelezko, F. Magnetometry based on the excited-state lifetimes of a single nitrogen-vacancy center in diamond. *Applied Physics Letters* **2021**, *119*, 134001. https://doi.org/10.1063/5.0070639.

[77] Kurtsiefer, C.; Mayer, S.; Zarda, P.; Weinfurter, H. Stable Solid-State Source of Single Photons. *Physical Review Letters* **2000**, *85*, 290–293. https://doi.org/10.1103/physrevlett.85.290.

[78] Sewani, V.K.; Vallabhapurapu, H.H.; Yang, Y.; Firgau, H.R.; Adambukulam, C.; Johnson, B.C.; Pla, J.J.; Laucht, A. Coherent control of NV- centers in diamond in a quantum teaching lab. *American Journal of Physics* **2020**, *88*, 1156–1169. https://doi.org/10.1119/10.0001905.

[79] Rogers, L.J.; Armstrong, S.; Sellars, M.J.; Manson, N.B. Infrared emission of the NV centre in diamond: Zeeman and uniaxial stress studies. *New Journal of Physics* **2008**, *10*, 103024. https://doi.org/10.1088/1367-2630/10/10/103024.

[80] Rogers, L.J.; Doherty, M.W.; Barson, M.S.J.; Onoda, S.; Ohshima, T.; Manson, N.B. Singlet levels of the NV- centre in diamond. *New Journal of Physics* **2015**, *17*, 013048. https://doi.org/10.1088/1367-2630/17/1/013048.

[81] Acosta, V.M.; Jarmola, A.; Bauch, E.; Budker, D. Optical properties of the nitrogen-vacancy singlet levels in diamond **2010**. https://doi.org/10.48550/ARXIV.1009.0032.

[82] Ulbricht, R.; Loh, Z.H. Excited-state lifetime of the NV- infrared transition in diamond. *Physical Review B* **2018**, *98*, 094309. https://doi.org/10.1103/physrevb.98.094309.

[83] Acosta, V.M.; Bauch, E.; Ledbetter, M.P.; Santori, C.; Fu, K.M.C.; Barclay, P.E.; Beausoleil, R.G.; Linget, H.; Roch, J.F.; Treussart, F.; et al. Diamonds with a high density of nitrogen-vacancy centers for magnetometry applications. *Physical Review B* **2009**, *80*, 115202. https://doi.org/10.1103/physrevb.80.115202.

[84] El-Ella, H.A.R.; Ahmadi, S.; Wojciechowski, A.M.; Huck, A.; Andersen, U.L. Optimised frequency modulation for continuous-wave optical magnetic resonance sensing using nitrogen-vacancy ensembles. *Optics Express* **2017**, *25*, 14809. https://doi.org/10.1364/oe.25.014809.

[85] Edmonds, A.M.; Hart, C.A.; Turner, M.J.; Colard, P.O.; Schloss, J.M.; Olsson, K.S.; Trubko, R.; Markham, M.L.; Rathmill, A.; Horne-Smith, B.; et al. Characterisation of CVD diamond with high concentrations of nitrogen for magnetic-field sensing applications. *Materials for Quantum*

Technology **2021**, *1*, 025001. https://doi.org/10.1088/2633-4356/abd88a.

[86] Jeong, K.; Parker, A.J.; Page, R.H.; Pines, A.; Vassiliou, C.C.; King, J.P. Understanding the magnetic resonance spectrum of nitrogen vacancy centers in an ensemble of randomly-oriented nanodiamonds, 2017. https://doi.org/10.48550/ARXIV.1707.07205.

[87] Patel, A.; Chowdhry, Z.; Prabhakar, A.; Rathi, A.; Bhallamudi, V.P. Single and double quantum transitions in spin-mixed states under photoexcitation, 2023. https://doi.org/10.48550/ARXIV.2306.17531.

[88] Welter, P.; Rhensius, J.; Morales, A.; Wörnle, M.S.; Lambert, C.H.; Puebla-Hellmann, G.; Gambardella, P.; Degen, C.L. Scanning nitrogen-vacancy center magnetometry in large in-plane magnetic fields. *Applied Physics Letters* **2022**, *120*. https://doi.org/10.1063/5.0084910.

[89] Happacher, J.; Bocquel, J.; Dinani, H.T.; Tschudin, M.A.; Reiser, P.; Broadway, D.A.; Maze, J.R.; Maletinsky, P. Temperature-Dependent Photophysics of Single NV Centers in Diamond. *Physical Review Letters* **2023**, *131*, 086904. https://doi.org/10.1103/physrevlett.131.086904.

[90] Doherty, M.W.; Dolde, F.; Fedder, H.; Jelezko, F.; Wrachtrup, J.; Manson, N.B.; Hollenberg, L.C.L. Theory of the ground-state spin of the NV-center in diamond. *Physical Review B* **2012**, *85*, 205203. https://doi.org/10.1103/physrevb.85.205203.

[91] Homrighausen, J.; Hoffmann, F.; Pogorzelski, J.; Glösekötter, P.; Gregor, M. Microscale fiber-integrated vector magnetometer with on-tip field biasing using N - V ensembles in diamond microcrystals. *Physical Review Applied* **2024**, *22*, 034029. https://doi.org/10.1103/physrevapplied.22.034029.

[92] Zhang, H.; Belvin, C.; Li, W.; Wang, J.; Wainwright, J.; Berg, R.; Bridger, J. Little bits of diamond: Optically detected magnetic resonance of nitrogen-vacancy centers. *American Journal of Physics* **2018**, *86*, 225–236. https://doi.org/10.1119/1.5023389.

[93] Dix, S.; Lönard, D.; Barbosa, I.C.; Gutsche, J.; Witzenrath, J.; Widera, A. A miniaturized magnetic field sensor based on nitrogen-vacancy centers **2024**. [arXiv:physics.app-ph/2402.19372].

[94] Acosta, V.M.; Bauch, E.; Ledbetter, M.P.; Waxman, A.; Bouchard, L.S.; Budker, D. Temperature Dependence of the Nitrogen-Vacancy Magnetic Resonance in Diamond. *Physical Review Letters* **2010**, *104*, 070801. https://doi.org/10.1103/physrevlett.104.070801.

[95] Chen, Y.; Li, Z.; Guo, H.; Wu, D.; Tang, J. Simultaneous imaging of magnetic field and temperature using a wide-field quantum diamond microscope. *EPJ Quantum Technology* **2021**, *8*. https://doi.org/10.1140/epjqt/s40507-021-00097-9.

[96] Zhu, X.; Wu, H.; Chen, B.; Yu, T.; Qian, P.; Fan, J.W.; Chen, B. Joint quantum sensing of vector magnetic field and temperature with nitrogen-vacancy centers in diamond. *Applied Physics Letters* **2023**, *123*. https://doi.org/10.1063/5.0174016.

[97] Fescenko, I.; Jarmola, A.; Savukov, I.; Kehayias, P.; Smits, J.; Damron, J.; Ristoff, N.; Mosavian, N.; Acosta, V.M. Diamond magnetometer enhanced by ferrite flux concentrators. *Physical Review Research* **2020**, *2*, 023394. https://doi.org/10.1103/physrevresearch.2.023394.

[98] Choi, J.; Choi, S.; Kucsko, G.; Maurer, P.C.; Shields, B.J.; Sumiya, H.; Onoda, S.; Isoya, J.; Demler, E.; Jelezko, F.; et al. Depolarization Dynamics in a Strongly Interacting Solid-State Spin Ensemble. *Physical Review Letters* **2017**, *118*, 093601. https://doi.org/10.1103/physrevlett.118.093601.

[99] Schloss, J.M.; Barry, J.F.; Turner, M.J.; Walsworth, R.L. Simultaneous Broadband Vector Magnetometry Using Solid-State Spins. *Physical Review Applied* **2018**, *10*, 034044. https://doi.org/10.1103/physrevapplied.10.034044.

[100] Akhmedzhanov, R.; Gushchin, L.; Nizov, N.; Nizov, V.; Sobgayda, D.; Zelensky, I.; Hemmer, P. Microwave-free magnetometry based on cross-relaxation resonances in diamond nitrogen-vacancy centers. *Physical Re-*

view A **2017**, *96*, 013806. https://doi.org/10.1103/physreva.96.013806.

[101] Donati, S. Photodetectors, 2021. Includes bibliographical references and index.

[102] Guggenmos, J. Minimization Of Laser Diode Relative Intensity Noise (RIN). In Proceedings of the SPIE Proceedings; Seery, B.D., Ed. SPIE, jul 1989. https://doi.org/10.1117/12.951301.

[103] Joindot, I. Measurements of relative intensity noise (RIN) in semiconductor lasers. *Journal de Physique III* **1992**, *2*, 1591–1603. https://doi.org/10.1051/jp3:1992201.

[104] Hobbs, P.C.D. Ultrasensitive laser measurements without tears. *Applied Optics* **1997**, *36*, 903. https://doi.org/10.1364/ao.36.000903.

[105] Allan, D.W. Should the classical variance be used as a basic measure in standards metrology? *IEEE Transactions on Instrumentation and Measurement* **1987**, *IM–36*, 646–654. https://doi.org/10.1109/tim.1987.6312761.

[106] Marinov, M.B.; Ganev, B.; Djermanova, N.; Tashev, T.D. Analysis of Sensors Noise Performance Using Allan Deviation. In Proceedings of the 2019 IEEE XXVIII International Scientific Conference Electronics (ET). IEEE, 2019. https://doi.org/10.1109/et.2019.8878552.

[107] Hobbs. *Electro-Optical Systems 2e*; John Wiley & Sons, 2009.

[108] Schottky, W. Über spontane Stromschwankungen in verschiedenen Elektrizitätsleitern. *Annalen der Physik* **1918**, *362*, 541–567. https://doi.org/10.1002/andp.19183622304.

[109] Johnson, M. *Photodetection and Measurement*; McGraw-Hill Education - Europe, 2003.

[110] Mackowiak, V.; Peupelmann, J.; Ma, Y.; Gorges, A. NEP – Noise Equivalent Power. Technical report.

[111] Margan, E. Transimpedance Amplifier Analysis. http://www-f9.ijs.si/~margan/Articles/trans_z_amplifier.pdf, 2012. Accessed: 2021-07-02.

[112] Nyquist, H. Thermal Agitation of Electric Charge in Conductors. *Physical Review* **1928**, *32*, 110–113. https://doi.org/10.1103/physrev.32.110.

[113] Hooge, F. 1/f noise sources. *IEEE Transactions on Electron Devices* **1994**, *41*, 1926–1935. https://doi.org/10.1109/16.333808.

[114] Horowitz, P. *The art of electronics*, third edition, 19th printing ed.; Cambridge University Press: New York, 2022. Auf Einband und Buchrücken: Third edition improved.

[115] Alem, M. Time-Domain Response of Lock-in Filters. https://www.zhinst.com/europe/en/blogs/time-domain-response-lock-filters, 2017. [Online; accessed 13-August-2023].

[116] Van Baak, D.A.; Herold, G. Response of a lock-in amplifier to noise. *American Journal of Physics* **2014**, *82*, 785–797. https://doi.org/10.1119/1.4873915.

[117] Karras, T.J. Equivalent noise bandwidth analysis from transfer functions. Technical report, 1965.

[118] Heinzel, G.; Rüdiger, A.; Schilling, R. Spectrum and spectral density estimation by the Discrete Fourier transform (DFT), including a comprehensive list of window functions and some new flat-top windows. Technical report, Max-Planck-Institut für Gravitationsphysik (Albert-Einstein-Institut) Teilinstitut Hannover, 2002.

[119] Alem, M. Noise Analysis of Signal Components. https://www.zhinst.com/europe/en/blogs/noise-analysis-signal-components, 2017. [Online; accessed 18-December-2023].

[120] Haykin, S.S. *Communication systems*, 4. ed. ed.; Wiley: New York, NY, 2001. Previous ed.: 1994.

[121] Dharmawansa, P.; Rajatheva, N.; Tellambura, C. Envelope and phase distribution of two correlated gaussian variables. *IEEE Transactions on Communications* **2009**, *57*, 915–921. https://doi.org/10.1109/tcomm.2009.04.070065.

[122] The mpmath development team. mpmath: a Python library for arbitrary-precision floating-point arithmetic (version 1.3.0). https://mpmath.org/, 2023.

[123] Meade, M.L. *Lock-in amplifiers*, reprin. ed.; Number 1 in IEE electrical measurement series, Peregrinus: London, 1989.

[124] Uddin, K.; Moore, A.D.; Barai, A.; Marco, J. The effects of high frequency current ripple on electric vehicle battery performance. *Applied Energy* **2016**, *178*, 142–154. https://doi.org/10.1016/j.apenergy.2016.06.033.

[125] Manson, N.B.; Harrison, J.P.; Sellars, M.J. Nitrogen-vacancy center in diamond: Model of the electronic structure and associated dynamics. *Physical Review B* **2006**, *74*, 104303. https://doi.org/10.1103/physrevb.74.104303.

[126] Masuyama, Y.; Shinei, C.; Ishii, S.; Abe, H.; Taniguchi, T.; Teraji, T.; Ohshima, T. Columnar excitation fluorescence microscope for accurate evaluation of quantum properties of color centers in bulk materials. *Scientific Reports* **2024**, *14*. https://doi.org/10.1038/s41598-024-68610-5.

[127] Welch, P. The use of fast Fourier transform for the estimation of power spectra: A method based on time averaging over short, modified periodograms. *IEEE Transactions on Audio and Electroacoustics* **1967**, *15*, 70–73. https://doi.org/10.1109/tau.1967.1161901.

[128] Oppenheim, A.V.; Schafer, R.W. *Discrete-Time Signal Processing (3rd Edition) (Prentice-Hall Signal Processing Series)*; Pearson, 2009.

[129] Smith, J.O. *Spectral audio signal processing*; Stanford University, CCRMA: Stanford, Calif., 2011.

[130] Liu, Q.; Xie, F.; Peng, X.; Hu, Y.; Wang, N.; Zhang, Y.; Wang, Y.; Li, L.; Chen, H.; Cheng, J.; et al. Millimeter-Scale Temperature Self-Calibrated Diamond-Based Quantum Sensor for High-Precision Current Sensing. *Advanced Quantum Technologies* **2023**, *6*. https://doi.org/10.1002/qute.202300210.

[131] Liu, Q.; Xie, F.; Peng, X.; Zhang, Y.; Wang, N.; Hu, Y.; Wang, L.; Liu, Y.; Wang, Y.; Nie, S.; et al. Closed-Loop Diamond Quantum Sensor for Large Range and High Precision Current Measurement. *IEEE Sensors Journal* **2024**, *24*, 4356–4364. https://doi.org/10.1109/jsen.2023.3348161.

[132] Stürner, F.M.; Brenneis, A.; Kassel, J.; Wostradowski, U.; Rölver, R.; Fuchs, T.; Nakamura, K.; Sumiya, H.; Onoda, S.; Isoya, J.; et al. Compact integrated magnetometer based on nitrogen-vacancy centres in diamond **2019**. *93*, 59–65. https://doi.org/10.1016/j.diamond.2019.01.008.

[133] Doherty, M.W.; Acosta, V.M.; Jarmola, A.; Barson, M.S.J.; Manson, N.B.; Budker, D.; Hollenberg, L.C.L. Temperature shifts of the resonances of the NV-center in diamond. *Physical Review B* **2014**, *90*, 041201. https://doi.org/10.1103/physrevb.90.041201.

[134] Attrash, M.; Shtempluck, O.; Buks, E. High temperature spectroscopy of ensembles of nitrogen-vacancy centers in diamond. *Journal of Applied Physics* **2023**, *133*, 094401, [https://pubs.aip.org/aip/jap/article-pdf/doi/10.1063/5.0128069/16775144/094401_1_online.pdf]. https://doi.org/10.1063/5.0128069.

[135] Fujiwara, M.; Sun, S.; Dohms, A.; Nishimura, Y.; Suto, K.; Takezawa, Y.; Oshimi, K.; Zhao, L.; Sadzak, N.; Umehara, Y.; et al. Real-time nanodiamond thermometry probing in vivo thermogenic responses. *Science Advances* **2020**, *6*. https://doi.org/10.1126/sciadv.aba9636.

[136] Zhang, Z.; Wen, H.F.; Li, L.; Cao, B.; Liu, Y.; Guo, H.; Li, Z.h.; Ma, Z.; Li, X.; Tang, J.; et al. Temperature dependence of magnetic sensitivity in ensemble NV centers. *Japanese Journal of Applied Physics* **2024**, *63*, 062001. https://doi.org/10.35848/1347-4065/ad483c.

[137] Sarkar, S.; Agrawal, N.; Shishir, D.; Saha, K. Real-time Simultaneous Dual Sensing of Temperature and Magnetic Field using NV-based Nanodiamonds **2024**. [arXiv:quant-ph/2408.17418]. https://doi.org/10.48550/ARXIV.2408.17418.

[138] Plakhotnik, T.; Aman, H.; Chang, H.C. All-optical single-nanoparticle ratiometric thermometry with a noise floor of 0.3 K Hz-1/2. *Nanotechnology* **2015**, *26*, 245501. https://doi.org/10.1088/0957-4484/26/24/245501.

[139] Fukami, M.; Yale, C.; Andrich, P.; Liu, X.; Heremans, F.; Nealey, P.; Awschalom, D. All-Optical Cryogenic Thermometry Based on Nitrogen-Vacancy Centers in Nanodiamonds. *Physical Review Applied* **2019**, *12*, 014042. https://doi.org/10.1103/physrevapplied.12.014042.

[140] Dong, B.; Shi, C.; Xu, Z.; Wang, K.; Luo, H.; Sun, F.; Wang, P.; Wu, E.; Zhang, K.; Liu, J.; et al. Temperature dependence of optical centers in Ib diamond characterized by photoluminescence spectra. *Diamond and Related Materials* **2021**, *116*, 108389. https://doi.org/10.1016/j.diamond.2021.108389.

[141] Plakhotnik, T.; Gruber, D. Luminescence of nitrogen-vacancy centers in nanodiamonds at temperatures between 300 and 700 K: perspectives on nanothermometry. *Physical Chemistry Chemical Physics* **2010**, *12*, 9751. https://doi.org/10.1039/c001132k.

[142] Pedroza-Montero, F.A.; Santacruz-Gomez, K.J.; Meléndrez-Amavizca, R.; Barboza-Flores, M. Commercial nanodiamonds for precise fluorescence-based temperature sensing. *Applied Physics Letters* **2024**, *125*. https://doi.org/10.1063/5.0219532.

[143] Bommidi, D.K.; Pickel, A.D. Temperature-dependent excited state lifetimes of nitrogen vacancy centers in individual nanodiamonds. *Applied Physics Letters* **2021**, *119*. https://doi.org/10.1063/5.0072357.

[144] Toyli, D.M.; Christle, D.J.; Alkauskas, A.; Buckley, B.B.; de Walle, C.G.V.; Awschalom, D.D. Persistence of Single Spin Coherence above 600K in Diamond **2012**. [arXiv:cond-mat.mes-hall/1201.4420]. https://doi.org/https://doi.org/10.48550/arXiv.1201.4420.

[145] Hatano, Y.; Shin, J.; Nishitani, D.; Iwatsuka, H.; Masuyama, Y.; Sugiyama, H.; Ishii, M.; Onoda, S.; Ohshima, T.; Arai, K.; et al. Simultaneous thermometry and magnetometry using a fiber-coupled quantum diamond sensor **2021**. *118*, 034001. https://doi.org/10.1063/5.0031502.

[146] Blanchard, H.; de Raad Iseli, C.; Popovic, R.S. Compensation of the temperature-dependent offset drift of a Hall sensor. *Sensors and Actuators A: Physical* **1997**, *60*, 10–13. https://doi.org/10.1016/s0924-4247(96)01411-2.

[147] Paun, M.A.; Sallese, J.M.; Kayal, M. Hall Effect Sensors Design, Integration and Behavior Analysis. *Journal of Sensor and Actuator Networks* **2013**, *2*, 85–97. https://doi.org/10.3390/jsan2010085.

[148] Lai, N.D.; Zheng, D.; Jelezko, F.; Treussart, F.; Roch, J.F. Influence of a static magnetic field on the photoluminescence of an ensemble of nitrogen-vacancy color centers in a diamond single-crystal. *Applied Physics Letters* **2009**, *95*, 133101. https://doi.org/10.1063/1.3238467.

[149] Lakowicz, J.R. *Principles of fluorescence spectroscopy*, third edition, corrected at 4. printing ed.; Springer: New York, NY, 2010.

[150] Laube, C.; Temme, R.; Prager, A.; Griebel, J.; Knolle, W.; Abel, B. Fluorescence Lifetime Control of Nitrogen Vacancy Centers in Nanodiamonds for Long-Term Information Storage. *ACS Nano* **2023**, *17*, 15401–15410. https://doi.org/10.1021/acsnano.3c00328.

[151] Laube, C.; Oeckinghaus, T.; Lehnert, J.; Griebel, J.; Knolle, W.; Denisenko, A.; Kahnt, A.; Meijer, J.; Wrachtrup, J.; Abel, B. Controlling the fluorescence properties of nitrogen vacancy centers in nanodiamonds. *Nanoscale* **2019**, *11*, 1770–1783. https://doi.org/10.1039/c8nr07828a.

[152] Fraczek, E.; Savitski, V.G.; Dale, M.; Breeze, B.G.; Diggle, P.; Markham, M.; Bennett, A.; Dhillon, H.; Newton, M.E.; Kemp, A.J. Laser spectroscopy of NV- and NV0 colour centres in synthetic diamond. *Optical*

Materials Express **2017**, *7*, 2571. https://doi.org/10.1364/ome.7.002571.

[153] Storteboom, J.; Dolan, P.; Castelletto, S.; Li, X.; Gu, M. Lifetime investigation of single nitrogen vacancy centres in nanodiamonds. *Optics Express* **2015**, *23*, 11327. https://doi.org/10.1364/oe.23.011327.

[154] Newville, M.; Stensitzki, T.; Allen, D.B.; Ingargiola, A. LMFIT: Non-Linear Least-Square Minimization and Curve-Fitting for Python, 2014. https://doi.org/10.5281/ZENODO.11813.

[155] Collins, A.T.; Thomaz, M.F.; Jorge, M.I.B. Luminescence decay time of the 1.945 eV centre in type Ib diamond. *Journal of Physics C: Solid State Physics* **1983**, *16*, 2177–2181. https://doi.org/10.1088/0022-3719/16/11/020.

[156] Lenef, A.; Brown, S.W.; Redman, D.A.; Rand, S.C.; Shigley, J.; Fritsch, E. Electronic structure of the N-V center in diamond: Experiments. *Physical Review B* **1996**, *53*, 13427–13440. https://doi.org/10.1103/physrevb.53.13427.

[157] Robledo, L.; Bernien, H.; van Weperen, I.; Hanson, R. Control and Coherence of the Optical Transition of Single Nitrogen Vacancy Centers in Diamond. *Physical Review Letters* **2010**, *105*, 177403. https://doi.org/10.1103/physrevlett.105.177403.

[158] Khalid, A.; Chung, K.; Rajasekharan, R.; Lau, D.W.; Karle, T.J.; Gibson, B.C.; Tomljenovic-Hanic, S. Lifetime Reduction and Enhanced Emission of Single Photon Color Centers in Nanodiamond via Surrounding Refractive Index Modification. *Scientific Reports* **2015**, *5*. https://doi.org/10.1038/srep11179.

[159] Epstein, R.J.; Mendoza, F.M.; Kato, Y.K.; Awschalom, D.D. Anisotropic interactions of a single spin and dark-spin spectroscopy in diamond. *Nature Physics* **2005**, *1*, 94–98. https://doi.org/10.1038/nphys141.

[160] Smith, B.R.; Gruber, D.; Plakhotnik, T. The effects of surface oxidation on luminescence of nano diamonds. *Diamond and Related Materials* **2010**, *19*, 314–318. https://doi.org/10.1016/j.diamond.2009.12.009.

[161] Laporte, G.; Psaltis, D. STED imaging of green fluorescent nanodiamonds containing nitrogen-vacancy-nitrogen centers. *Biomed. Opt. Express* **2016**, *7*, 34–44. https://doi.org/10.1364/BOE.7.000034.

[162] Inam, F.A.; Edmonds, A.M.; Steel, M.J.; Castelletto, S. Tracking emission rate dynamics of nitrogen vacancy centers in nanodiamonds. *Applied Physics Letters* **2013**, *102*. https://doi.org/10.1063/1.4812711.

[163] Wee, T.L.; Tzeng, Y.K.; Han, C.C.; Chang, H.C.; Fann, W.; Hsu, J.H.; Chen, K.M.; Yu, Y.C. Two-photon Excited Fluorescence of Nitrogen-Vacancy Centers in Proton-Irradiated Type Ib Diamond. *The Journal of Physical Chemistry A* **2007**, *111*, 9379–9386. https://doi.org/10.1021/jp073938o.

[164] Magaletti, S.; Mayer, L.; Roch, J.F.; Debuisschert, T. A quantum radio frequency signal analyzer based on nitrogen vacancy centers in diamond. *Communications Engineering* **2022**, *1*. https://doi.org/10.1038/s44172-022-00017-4.

[165] Hartung, J. *Statistical meta-analysis with applications*; Wiley: Hoboken, NJ, 2008. Includes bibliographical references and index.

[166] Roberts, D.A.; Yaida, S.; Hanin, B. *The Principles of Deep Learning Theory: An Effective Theory Approach to Understanding Neural Networks*; Cambridge University Press, 2022. https://doi.org/10.1017/9781009023405.

[167] Rumelhart, D.E.; Hinton, G.E.; Williams, R.J., (1986) D. E. Rumelhart, G. E. Hinton, and R. J. Williams, "Learning internal representations by error propagation," Parallel Distributed Processing: Explorations in the Microstructures of Cognition, Vol. I, D. E. Rumelhart and J. L. McClelland (Eds.) Cambridge, MA: MIT Press, pp. 318-362. In *Neurocomputing, Volume 1*; The MIT Press, 1988; pp. 675–695. https://doi.org/10.7551/mitpress/4943.003.0128.

[168] Abadi, M.; Agarwal, A.; Barham, P.; Brevdo, E.; Chen, Z.; Citro, C.; Corrado, G.S.; Davis, A.; Dean, J.; Devin, M.; et al. TensorFlow: Large-Scale Machine Learning on Heterogeneous Systems, 2015. Software available from tensorflow.org.

[169] Guyon, I.; Weston, J.; Barnhill, S.; Vapnik, V. *Machine Learning* **2002**, *46*, 389–422. https://doi.org/10.1023/a:1012487302797.

[170] Breiman, L. *Machine Learning* **2001**, *45*, 5–32. https://doi.org/10.1023/a:1010933404324.

[171] Fisher, A.; Rudin, C.; Dominici, F. All Models are Wrong, but Many are Useful: Learning a Variable's Importance by Studying an Entire Class of Prediction Models Simultaneously. *Journal of Machine Learning Research* **2019**, *20*, 1–81.

[172] Fanselau, G. Die Erzeugung weitgehend homogener Magnetfelder durch Kreisstroeme. *Zeitschrift fuer Physik* **1929**, *54*, 260–269. https://doi.org/10.1007/bf01339844.

[173] Depold, A.; Erhardt, S.; Weigel, R.; Lurz, F. A 10 kHz to 6 GHz Low-Cost Vector Network Analyzer. *Advances in Radio Science* **2021**, *19*, 17–22. https://doi.org/10.5194/ars-19-17-2021.

[174] Verhaevert, J.; Van Torre, P. A Low-cost Vector Network Analyzer: Design and Realization. In Proceedings of the Loughborough Antennas; Propagation Conference (LAPC 2017). Institution of Engineering and Technology, 2017. https://doi.org/10.1049/cp.2017.0225.

[175] Han, K.Y.; Wildanger, D.; Rittweger, E.; Meijer, J.; Pezzagna, S.; Hell, S.W.; Eggeling, C. Dark state photophysics of nitrogen–vacancy centres in diamond. *New Journal of Physics* **2012**, *14*, 123002. https://doi.org/10.1088/1367-2630/14/12/123002.

[176] Bai, D.; Huynh, M.H.; Simpson, D.A.; Reineck, P.; Vahid, S.A.; Greentree, A.D.; Foster, S.; Ebendorff-Heidepriem, H.; Gibson, B.C. Fluorescent diamond microparticle doped glass fiber for magnetic field sensing. *APL Materials* **2020**, *8*. https://doi.org/10.1063/5.0013473.

[177] Stoica, P.G.; Moses, R. *Spectral analysis of signals*; Pearson, Prentice Hall: Upper Saddle River, NJ, 2005. Includes bibliographical references (p. 423-434) and index.